Characteristics of the Liquid Film in Horizontal Two-Phase Flow

T. A. Shedd and T. A. Newell

ACRC TR-179 March 2001

For additional information:

Air Conditioning and Refrigeration Center
University of Illinois
Mechanical & Industrial Engineering Dept.
1206 West Green Street
Urbana, IL 61801

(217) 333-3115

Prepared as part of ACRC Project #113
Flow Visualization of Refrigerant/Oil Flows in Tubes, Microchannels, Flat Plates, and Tube Bends
T. A. Newell, Principal Investigator

The Air Conditioning and Refrigeration Center was founded in 1988 with a grant from the estate of Richard W. Kritzer, the founder of Peerless of America Inc. A State of Illinois Technology Challenge Grant helped build the laboratory facilities. The ACRC receives continuing support from the Richard W. Kritzer Endowment and the National Science Foundation. The following organizations have also become sponsors of the Center.

Amana Refrigeration, Inc.
Arçelik A. S.
Brazeway, Inc.
Carrier Corporation
Copeland Corporation
Dacor
Daikin Industries, Ltd.
DaimlerChrysler Corporation
Delphi Harrison Thermal Systems
Frigidaire Company
General Electric Company
General Motors Corporation
Hill PHOENIX
Honeywell, Inc.
Hussmann Corporation
Hydro Aluminum Adrian, Inc.
Indiana Tube Corporation
Invensys Climate Controls
Kelon Electrical Holdings Co., Ltd.
Lennox International, Inc.
LG Electronics, Inc.
Modine Manufacturing Co.
Parker Hannifin Corporation
Peerless of America, Inc.
Samsung Electronics Co., Ltd.
The Trane Company
Thermo King Corporation
Valeo, Inc.
Visteon Automotive Systems
Wolverine Tube, Inc.
York International, Inc.

For additional information:

Air Conditioning & Refrigeration Center
Mechanical & Industrial Engineering Dept.
University of Illinois
1206 West Green Street
Urbana, IL 61801

217 333 3115

CHARACTERISTICS OF THE LIQUID FILM IN HORIZONTAL TWO-PHASE FLOW

Timothy Allen Shedd, Ph.D.
Department of Mechanical and Industrial Engineering
University of Illinois at Urbana-Champaign, 2001
Professor Ty A. Newell, Advisor

Horizontal annular two-phase flow is a very important condition in many common applications, including power generation, air-conditioning, and refrigeration. The purpose of this investigation is to present a broad survey of detailed liquid film thickness results for a variety of geometries for which film thickness data is not currently available. Measurements for round tubes, square tubes in two orientations, and a triangle tube in two orientations are presented. Beyond the fundamental importance of these data sets, the results are used to show that the base liquid layer tends to behave in a manner analogous to wall-bounded turbulent single-phase flow; that a limiting film thickness exists below which the wall dries out; and that pressure drop can be predicted for all geometries using vertical flow interfacial shear correlations. Flow through the square tubes shows strong evidence of the impact of secondary flows on the liquid profile, and a theory for the origins of secondary flows under two-phase annular conditions is developed. Another important class of tubing analyzed are tubes with 0.2 mm microgrooves of varying helix angles in the walls. Film thickness data indicate that these grooves act to rotate and redistribute the film, providing a basis for understanding the heat transfer enhancement these types of tubes exhibit. An experimental study of the effects of the angle and number of grooves is also presented. Key findings show that relatively few grooves are necessary to redistribute the film and that the grooves act on the film in such away as to increase the surface fluctuations and lower the mean film thickness, both of which could have significant impact on heat transfer. Finally, a new diagnostic technique, thin film particle image velocimetry, is described with results providing evidence for strong upflows of liquid during the passage of waves and relatively smooth, draining flows in between. Together, the results of this study have enhanced the understanding of two-phase annular flow and have laid the groundwork for improved models to predict heat and mass transfer in systems important to daily life.

Contents

List of Figures

List of Tables

Definitions of Symbols Used

This list contains the list of symbols used throughout the text. The location of the first definition is listed in parenthesis. Occasionally, a definition will temporarily change, and symbol is re-listed with the chapter where this occurs.

A Cross-sectional area (Chapter 2)

A_{Dh} Cross-sectional area of round tube with the diameter equal to the hydraulic diameter of the non-round tube (Chapter 2)

$A_{1,2}(n)$ Correlation functions for the γ relation (Chapter 6)

$B_{1,2}(n)$ Correlation functions for the γ relation (Chapter 6)

C_1 Laurinat et al.'s correlation constant (Chapter 1)

C_1 Fukano and Ousaka's correlation constant (Chapter 1)

C_D Fukano and Ousaka's disturbance wave velocity (Chapter 1)

D Diameter (Chapter 1)

D_h Hydraulic diameter (Chapter 2)

f Friction factor (Chapter 1)

f_i Interfacial friction factor (Chapter 1)

Fr_l Liquid Froude number (Chapter 3)

Ft Froude rate parameter (Chapter 2)

g Gravitational acceleration (Chapter 2)

G Mass flux [$\frac{kg}{m^2 s}$] (Chapter 1)

h Local film thickness (Chapter 1)

h^+ Local film thickness non-dimensionalized by u_i^* and ν_l (Chapter 3)

k Butterworth's correlation parameter (Chapter 1)

k Troniewski and Ulbricht's aspect ratio of rectangle (Chapter 3)

L Length; distance in the axial direction (Chapter 2)

$\dot{m}$ Mass flow rate [kg/s] (Chapter 1)

n Number of grooves (Chapter 6)

p Local static pressure [N/m^2] (Chapter 1)

P Inner tube wall perimeter (Chapter 2)

P Mean Pressure (Chapter 4)

R Tube radius

Re_{LF} Liquid film Reynolds number ($\frac{4\dot{m}_L}{\pi D \mu_L}$) (Chapter 1)

Re_{SG} Reynolds number based on superficial gas velocity: $\frac{U_{SG}D}{\nu}$ (Chapter 1)

u_{G2} Fukano and Ousaka's superficial vapor velocity (Chapter 1)

u_{G1} Fukano and Ousaka's vapor velocity at wave surface (Chapter 1)

$u_i\bar{v}_j$ Turbulent Reynolds stress (Chapter 4)

U_i, U_j Average velocity components (Chapter 4)

U_{sg} Common notation for superficial gas velocity (Chapter 2)

U_{sl} Common notation for superficial liquid velocity (Chapter 2)

U_{SG} Superficial gas velocity [m/s] (Chapter 1)

u_i^* Liquid friction velocity based on τ_i (Chapter 3)

x Mass quality of vapor (Chapter 1)

x Circumferential coordinate (Chapter 1)

X_{tt} Lockhart-Martinelli parameter (Chapter 2)

α Void fraction (Chapter 1)

γ Angle of liquid film rotation (Chapter 6)

Γ Butterworth's circumferential mass flow term (Chapter 1)

ν Kinematic viscosity $[m^2/s]$ (Chapter 1)

$\phi = \frac{\mu_l}{\mu_g}\left(\frac{\rho_g}{\rho_l}\right)^{0.5}$

ρ Density $[kg/m^3]$ (Chapter 1)

τ_i Interfacial shear stress (Chapter 3)

τ_s Vapor shear over smooth wall (Chapter 1)

τ_{xx} Circumferential normal Reynolds stress (Chapter 1)

Υ Film uniformity parameter (Chapter 2)

$\omega(k)$ Troniewski and Ulbricht's velocity correction factor for flows through rectangular pipes (Chapter 3)

1

Introduction

Liquid-vapor two-phase flows exist in many common processes and domestic products. Some examples include air-conditioning and refrigeration systems, both nuclear and conventional steam-driven power plants, and chemical processing systems. Patterns of flow which persist in many of these processes when pipes are horizontal are stratified annular and annular distributions of the liquid phase, as shown in Figure 1.1.

In the stratified annular and annular flow regimes, turbulent vapor flows down the center of the pipe while a thin liquid film flows along the pipe wall. Prediction of the distribution and behavior of this liquid layer is important in the modeling of pressure drop, heat transfer, and the mass flow of fluid needed for a required heat load. After several decades of work, however, the prediction of film distribution is still an active field of research. Complicating the work are the complexities of the

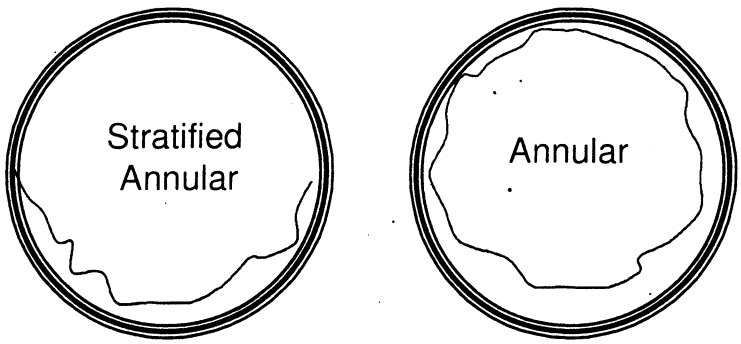

Figure 1.1: Typical distributions of gas and liquid phases in stratified annular and annular two-phase flow.

interactions between a turbulent vapor core and the liquid film, the added effect of gravity on flows in horizontal or angled pipes, the effects of heat and mass transfer occurring continually, and the behavior of different wave structures at the vapor-liquid interface.

The goal of this research is to provide a broad survey of detailed liquid film measurements in horizontal annular flow through a variety of geometries. This will provide a broader base on which to build our understanding of annular two-phase flow.

To begin, an overview of the issues involved in understanding the liquid film distribution will be discussed in some detail.

1.1 Two-phase flow in horizontal tubes

Horizontal two-phase vapor-liquid flow is best understood in smooth, round tubes; this knowledge will serve as a base for later excursions into non-circular and micro-grooved tubes. In a typical refrigeration or air conditioning evaporator, for instance, refrigerant will enter as primarily liquid.[1] As heat is added, some refrigerant evaporates, possibly causing bubbly flow, but, most likely, transitioning to plug flow as the bubbles of vapor will coalesce at the top of the tube due to buoyancy. As more vapor forms (vapor quality increases), the flow may transition to stratified flow. This would occur at relatively low mass fluxes[2] where vapor velocities are low.

In this case, the kinetic energy of the vapor in these flows is insufficient to cause the liquid to climb the tube walls. At higher mass fluxes, truly stratified flow may not exist, or may exist only briefly. Instabilities at the liquid surface cause waves to form leading to the classification of wavy stratified flow. If some of these waves bridge the entire tube, they form slugs – masses of liquid that travel along the tube at the vapor velocity. As the vapor velocity increases further due to increased evaporation, the vapor interacts with the liquid in such a way that the liquid is pushed up the walls to some extent and the thick liquid at the bottom of the tube has a curved, rather than flat, interface with the vapor. This condition may also fall under the stratified wavy flow classification if the liquid flowing on

[1] Vapor quality, x, the ratio of the mass of vapor to the total mass of refrigerant, may equal about 0.2 due to some vaporization in passing through the expansion valve.

[2] G, mass flow rate per unit cross-sectional area of the tube [$\frac{kg}{m^2 s}$], also sometimes called mass velocity

the bottom is significantly thicker than the film on the side walls. If a continuous film exists around the tube but the film at the top is very thin compared to the bottom, the condition is generally called stratified annular flow. Further increases in vapor velocity induce forces which somehow distribute the liquid as a thin film that completely coats the wall. This is called annular flow as it may be described as an annulus of liquid flowing about a core of vapor. As quality increases further, eventually too little liquid remains to completely coat the wall, resulting in what some refer to as stratified annular flow, though this condition may more closely resemble uniform annular flow with incomplete wall wetting.

In general, the reverse of this process may be imagined for a flow of vapor with condensation. However, particularly at low mass fluxes, it is likely that a mainly stratified condition could occur with a thin film of condensate covering the upper surface of the tube. This condition has served as the basis for some important early modeling efforts.

For the engineer, the most important quantities in a refrigeration system design are likely to be system work input (energy required for the compressor to drive the cycle), size of the heat exchangers needed for a given heat load, and the amount of refrigerant needed in the system (the refrigerant charge). The energy required by the system is governed by the rate at which heat must be transferred and the pressure difference through which the refrigerant must flow. Thus, predicting pressure losses in the components of the system are a high priority.

The sizes of the heat exchangers required are determined primarily by their efficiencies. The more heat that can be transferred per length of tube in the heat exchanger, the less tube is necessary and less refrigerant charge is required. Hence, predicting the heat transfer characteristics of a tube is of fundamental importance. While convective heat transfer is a very complicated process which is still best predicted using empirical correlations, knowledge of the fundamental fluid mechanics is essential for applying the appropriate correlation. For example, a different correlation procedure will apply for annular flow than for stratified annular flow where part of the tube wall is in direct contact with vapor. Once the fluid behavior is understood well enough, physical models of heat transfer can be constructed.

Finally, knowledge of the fluid mechanics of the refrigerant flow can more directly be used to predict the void fraction[3] in the tube. This, in turn, leads directly to

[3] α, the ratio of the cross sectional area occupied by the vapor to the total cross sectional area of

the total volume occupied by the refrigerant at a given flow condition and hence the required mass of refrigerant needed to sustain that condition in an operating system.

1.2 Horizontal, annular two-phase flow

Annular and stratified annular flows occupy the largest percentage of the length of an evaporator or condenser. This work, then, will focus on the fluid mechanics of two-phase vapor-liquid flow in the annular and stratified annular regimes to provide a basis for better models for pressure loss, heat transfer and void fraction in tubes of complex geometries.

Some important characteristics of horizontal, annular two-phase flow are the asymmetrical distribution of the liquid film, the complex interaction between the turbulent vapor and the liquid film, and the existence of disturbance waves in the liquid flow. The asymmetry is a fairly intuitive result of the action of gravity on the liquid. A thicker liquid flows along the bottom of a tube than on the top, although the amount of asymmetry is dependent on the mass flow rates of liquid and vapor. Film thicknesses vary widely, of course, but in conditions that might be typical in an air conditioner evaporator, films ranging from 50 to 300 μm would not be uncommon.

Local interaction between vapor and liquid is not well understood, so local values of interfacial shear stress are usually inferred from correlations developed for vertical annular flow, horizontal flow in rectangular channels, or horizontal stratified flow in round tubes. Flow visualization has revealed that, in general, the flow between disturbance waves is relatively smooth. Small waves are apparent, ranging from what appear to be small ripples to a fairly uniform pebbled structure, depending on liquid and vapor flow rates. Studies of two-phase shear stresses are legion; a typical and frequently used treatment is given in Wallis' book [Wallis, 1969]. A more recent work, and one that has been applied to horizontal annular flow, was performed by Asali et al. [1985].

Disturbance waves, sometimes referred to as roll waves, are highly turbulent masses of liquid that flow as relatively coherent, relatively long-lived structures along the tube with a velocity typically on the order of 1/5 to 1/10 of the vapor velocity and average thicknesses about 5 times that of the local base film thickness.

---

the tube

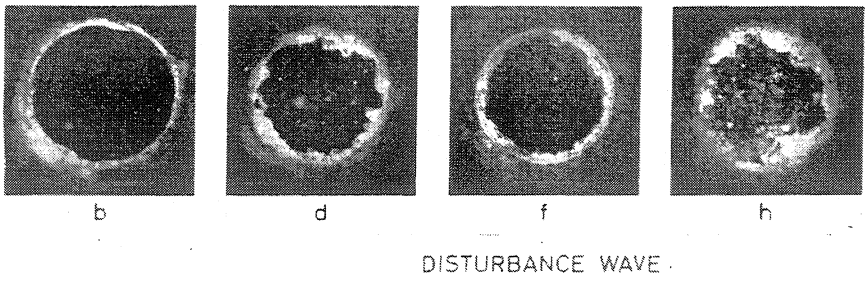

Figure 1.2: Axial views of annular flow in a vertical pipe. From Arnold and Hewitt [1967].

Photography by Cooper et al. [1964] and Arnold and Hewitt [1967] show very graphically the nature of these waves. Some sample images are shown in Figures 1.2 and 1.3. Disturbance waves are known to be important for the generation of droplets entrained in the vapor flow (see, for example, Woodmansee [1968]) and are thought by some to be the driving force for maintaining the liquid film on the tube wall in annular flow[Fukano et al., 1997]. Due to their complex nature, however, detailed knowledge of disturbance wave behavior is still lacking. Studies such as those by Chung and Murgatroyd [1965], Miya [1970] and Azzopardi [1986] in vertical annular flow and Paras and Karabelas [1991] and Jayanti et al. [1990a] in horizontal flow have produced information about the shear stresses induced by the waves as well as statistical descriptions of frequency and spacing.

The experimental work seems to indicate that two-phase annular flow can be described by a thin, laminar substrate film on which disturbance waves appear to slide. (See, for example, Hewitt et al. [1990].) Recent computational models indicate that this is, in fact, the most likely physical reality [Jayanti and Hewitt, 1997]. Initial results from a new particle image velocimetry (PIV) technique for two-phase annular flow appear to confirm this (see Chapter 7).

1.3 Summary of modeling research

Research into the development of a model to predict the liquid film distribution of horizontal annular two-phase flow has been active for over 40 years. Initially, McManus [1961] approached the problem with an empirical correlation based on a modified Lockhart-Martinelli set of parameters. A later empirical correlation was

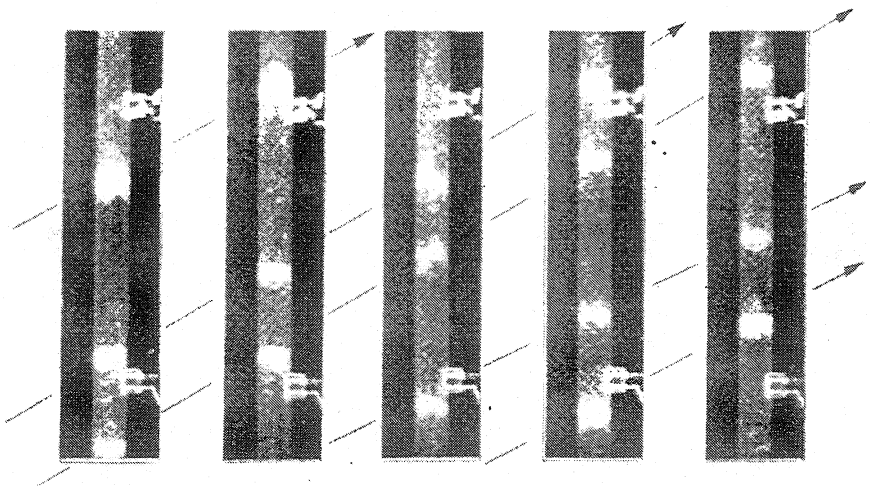

Figure 1.3: Disturbance waves in vertical annular flow viewed through the pipe wall. Arrows show the progression of waves from frame to frame. From Cooper et al. [1964].

presented by Dallman [1978].

To look at the problem from a more physically based view, researchers began inferring which behaviors were most important for maintaining the liquid film distribution from experimental measurements and observations. Some of these important observations were made in the works of McManus [1961], Jacowitz and Brodkey [1964], Anderson and Russell [1970], Darling and McManus [1968], Butterworth [1972], Hewitt et al. [1990], Sutharshan et al. [1995], and Fukano et al. [1997]. Butterworth is generally credited with delineating the four possible physical mechanisms important to the circumferential liquid film thickness distribution as

- Surface tension,
- Entrainment–deposition,
- Secondary vapor flows,
- Redistribution due to wave behavior.

Two additional factors, the coupling to the vapor through the interfacial shear stress and the velocity profile within the draining film, play important roles as well.

Models built by many researchers have included some or all of these effects, thus permitting the evaluation of which physical mechanisms are dominant in maintaining the liquid film on the tube wall.

1.3.1 Surface tension

Surface tension was included in the models of Jacowitz and Brodkey [1964] and Butterworth [1972]. Jacowitz and Brodkey did not attempt to isolate these effects on the output, but Butterworth found that surface tension forces were negligible compared to the forces required to hold the film against gravity in the diameters of the tubes he was studying. Laurinat et al. [1985] carried out an order of magnitude analysis and also found surface tension to be negligible. As a general rule, surface tension seems to play only an indirect role until tube diameters fall to about 6 mm. Recent visualization studies clearly show the impact of surface tension on the flow of refrigerants in small tubes with the presence of altered (though still asymmetrical) film distributions and transitions in flow regimes when compared with larger tube data [Coleman and Garimella, 1999, Begg et al., 1999, Triplett et al., 1999].

1.3.2 Secondary vapor flows

Pletcher and McManus [1965] were apparently the first to propose that, because of the asymmetrical film thicknesses, the vapor would be exposed to an asymmetrical roughness and thus the possibility existed for the generation of secondary flows. Their model indicated a minimal influence of secondary flow ($< 5\%$ change in bottom film thickness, $< 1\%$ change in top film thickness), and this influence appeared to diminish as the flow developed. Soon after, Darling and McManus [1968] reported the results of velocity measurements in a tube with an eccentric thread, mimicking the asymmetrical wall roughness of annular flow. These measurements clearly indicated the existence of a secondary flow. Butterworth [1972] analyzed the effects of secondary flow on the liquid distribution and concluded that forces present in his model were great enough to influence the liquid distribution.

Laurinat et al. [1985] and Lin et al. [1985] both considered circumferential interfacial shear stress due to secondary flows to be important factors in the liquid distribution. However, as admitted by these authors, due to the nature of fitting model parameters to empirical data, it was not possible to clearly determine the

significance of secondary flow effects with respect to other modeled forces. In fact, James et al. [1987] performed an order of magnitude analysis based on the models of Laurinat et al. and Lin et al. and determined that secondary flow effects were negligible relative to other factors.

Fukano and Ousaka [1989] constructed a model ignoring secondary flow which predicted film profiles well. To justify their decision, studies were performed with another group to observe the flow of liquid before, during and after the passage of a disturbance wave [Sutharshan et al., 1995]. This study found that, in the smooth regions between disturbance waves, the liquid appears to drain continuously due to gravity with no apparent upflow or shear due to circumferential vapor flow. Further, Fukano et al. [1997], noted that the temporal behavior of the liquid film at a given axial position could be accurately modeled with a simple laminar gravitational draining model, further evidence that secondary flow was not affecting the liquid. Additionally, Dykhno et al. [1994] found velocity measurements in flows with high levels of entrainment that indicated occurrences of secondary flows moving opposite (downward at the wall) to the direction necessary for maintaining a liquid film.

Jayanti et al. [1990a] have argued that secondary flows have little influence on the liquid film based on their experimental observations. Additional confirmation was provided when numerical simulations performed by Jayanti et al. [1990b] demonstrated that secondary vapor flow was unable to sustain a liquid layer on the walls of a horizontal tube. They further showed that, consistent with the prevailing theory on the origin of secondary flows, the circumferential interfacial shear stress is dependent on the gradient of the axial shear stress, and thus may have widely varying values depending on the local liquid surface structure.

Flores et al. [1995] performed a unique experiment to confirm the existence of secondary flows in two-phase horizontal annular flow. They inserted two paddle wheels, one in each vertical half of the tube, and noted the rotation of the wheels under different flow conditions. When air alone flowed in the tube, no rotation was observed. However, with liquid flowing concurrently with the vapor, rotation speed proportional to the liquid and vapor flow rates was observed. They proceeded to develop a film thickness model which depended solely on the circumferential shear stress of the secondary flows. No comparison to experimental data was given, but agreement is expected to be poor for two reasons. First, the interfacial shear

correlation they used to represent the circumferential shear was created from axial shear data. It is unlikely that the two shear stresses are of the same order. Second, using this model, the maximum film thickness that could be supported at the 90 degree point (where, according to experimental correlations, the secondary flow is strongest) in a 2.54 cm tube with vapor flow of 25 m/s is 4 μm. This does not agree with any of the reported experimental data. Hence, although the experimental work was significant in that it conclusively showed the existence of secondary flows in two-phase annular flow, the modeling effort further supported the theory of Fukano et al. that secondary flows play no direct role in distributing the liquid film.

In summary, then, it appears that secondary flows do not play a direct role in maintaining the liquid film distribution on the tube wall. However, the presence of secondary vapor motion may play significant roles in the deposition patterns of entrained droplets and in the redistribution of axial momentum, thus affecting local shear stress values. This may be particularly important in understanding the liquid film distribution in non-circular channels, as will be discussed in Chapters 2 and 4.

1.3.3 Entrainment–deposition

The first model to consider the entrainment and deposition of liquid droplets was generated by Russell and Lamb [1965]. Rather than modeling film profiles directly, they modeled the distribution of the concentration of an injected species to see which mechanisms acted to distribute the species throughout the liquid. They found that measured concentration profiles could be predicted with almost equal accuracy using entrainment-deposition alone with empirical multipliers, or with a general film diffusion term which could account for wave effects together with entrainment-deposition.

Butterworth [1972], based on the experimental work of Anderson and Russell [1970], found that entrainment and deposition was probably only a minor factor in the liquid distribution, possibly accounting for changes on the order of 10% in the local film thicknesses. He later constructed a model for condensation ignoring entrainment [Butterworth, 1974].

The model by Fisher and Pearce [1979] was based almost entirely on entrainment and deposition. Rather poor agreement with experiment was achieved, with errors of 30% or greater common. Another model based solely on net deposition was created by James et al. [1987]. When the model results were compared with

experimental data it achieved very poor agreement in most cases. Film thicknesses at the top of the tube were consistently over-predicted while the bottom thicknesses were generally significantly too low. The mass flux of entrained droplets was consistently over-predicted, in some cases by more than 100%.

Laurinat et al. [1985] found that deposition of droplets had a minimal effect on their film thickness predictions, and that the inclusion of deposition could make the predictions worse compared with experimental data. Lin et al. [1985] compared a modified form of this model to one derived from work of Butterworth comprising entrainment and deposition only. They too found that net deposition of droplets was a very poor predictor of liquid film distribution. In addition, work of Fukano and Ousaka [1989] and Tso and Sugawara [1990] both indicated that droplet deposition plays an insignificant role in the maintenance of the annular film.

Thus, it appears that, as implemented in these works, entrainment and deposition play only minimal roles in predicting the liquid film distribution. These models were based on experimental conditions for air and water in tubes ranging from 19 to 76.4 mm, with the majority of models tested for diameters of either 25.4, 31.8 or 50.8 mm. The maximum vapor velocity used was about 70.3 m/s, but most of the models were tested for vapor velocities of 50 m/s or below. Net droplet deposition may be an important factor in tubes of larger diameter or in higher speed flows. For instance, the work of Dallman [1978] found entrained liquid fractions $\left(\frac{\dot{m}_{L\text{ent}}}{\dot{m}_{L\text{total}}}\right)$ of 0.5 and greater with vapor velocities of 60 m/s and higher. Both the work of Dallman and of Williams [1989] indicate that flows with vapor velocities below about 30 m/s have small entrained liquid fractions and that entrainment at higher velocities is highly dependent on liquid flow rate. Film thickness data obtained by Williams appeared to indicate a change in wetting mechanisms at the top of a 95.3 mm pipe once vapor velocities exceeded about 45 m/s, so he suggested that droplet deposition becomes important under these flow conditions.

1.3.4 Redistribution due to wave behavior

In developing his earliest model, Butterworth [1969] used a single circumferential flow term representing unknown forces acting within the film that balanced the downward flow due to gravity. This term, Γ_x, the circumferential volumetric flow

rate up the tube wall, was defined

$$\Gamma_x = -\frac{k}{R}\frac{\partial \Gamma_z}{\partial x}, \tag{1.1}$$

where Γ_z is the local axial volumetric flow rate, k is a correlation parameter and R is the tube radius. When this term balances a laminar gravitational draining flow, good agreement with experiment was found for k ranging from 2 mm to 20 mm depending on the flow conditions. (Note that Butterworth's notation has been changed slightly to conform with the common use of x, rather than θ, for the circumferential coordinate.)

After further study, Butterworth connected this circumferential flow term with two mechanisms, wave-spreading and circumferential mixing [Butterworth, 1972]. The wave spreading effect is a vertical flow due to upward forces on the waves from the vapor that exists when the waves are sloped with respect to the vertical. Circumferential mixing was just a label given to an unknown amount of net turbulent transport within disturbance waves. He concluded that this term, though not well understood, was a dominant factor in the liquid film distribution.

Laurinat et al. [1985] modeled the stress driving the circumferential flow against gravity using both a circumferential pressure gradient due to gravity and a gradient in the turbulent normal Reynolds stress, $\frac{\partial \tau_{xx}}{\partial x}$. They found that the pressure gradient had a minimal effect, but that the $\frac{\partial \tau_{xx}}{\partial x}$ term was quite significant. To further simplify the model, they assumed that τ_{xx} could be represented by a term similar to that used by Butterworth,

$$\tau_{xx} = -C_1 \left(\frac{\Gamma_z}{h}\right)^2,$$

where h is the local film thickness. Through comparison with their experimental data, C_1 was found to be related to the gas and liquid film Reynolds numbers,

$$C_1 = 3.36 \times 10^{-6} \left[\frac{Re_{SG}}{Re_{LF}}\right]^{1.74},$$

with Re_{SG} defined using the superficial gas velocity (the velocity of the gas assuming it filled the entire area of the pipe) and the pipe diameter, and Re_{LF} defined by

$$Re_{LF} = \frac{4\dot{m}_L}{\pi D \mu_L}.$$

An experimental program carried out by Jayanti et al. [1990a] found that redistribution of liquid by disturbance waves was the dominant factor in maintaining

the liquid film. Statistical analysis of conductance probe traces allowed them to determine that at relatively large liquid flow rates and lower air velocities, the surging observed by Coney [1974] appeared to dominate and disturbance waves did not generally reach the top of the tube. However, at higher air flow rates, disturbance waves were circumferentially coherent and moved down the tube with a vertically sloping profile. This sloping was actually due to a width variation from the bottom to the top of the tube. Since the wave was being pushed forward by the vapor at the rear, the rear of the wave was essentially vertical. At the front, the wave extended further forward at the bottom than the top. They proposed that this sloping front acted as a shovel of sorts, pushing liquid film up the wall in front of it. The model of Adechy and Issa [1999] includes such a wave lift force.

Similarly to Laurinat et al., Fukano and Ousaka [1989] considered $\frac{\partial \tau_{xx}}{\partial x}$ to be the dominant mechanism for maintaining the film against gravity and modeled it based on their "pumping action of disturbance waves" hypothesis. This hypothesis stated that a pressure gradient was created within a disturbance wave due to the fact that vapor would impact more wave frontal area at the bottom of the pipe than the top because of its asymmetry. Thus, liquid was pumped from the bottom of the tube to the top within a disturbance wave and then drained essentially undisturbed in between waves. From this manner of thought, they assumed

$$\tau_{xx} = -C_1 \frac{\Delta p}{\tau_s} \tag{1.2}$$

$$= -C_1 \frac{\rho_g[(u_{G1} - C_D)^2 - (u_{G2} - C_D)^2]}{4\tau_s} \tag{1.3}$$

where u_{G2} was the superficial gas velocity and u_{G1} was the gas velocity at the wave location where flow separation takes place; this was determined by a correlation derived by the authors. C_D was the disturbance wave velocity and τ_s was the gas shear stress at a smooth wall. C_1 ranged over two orders of magnitude without obvious trends, leading the authors to acknowledge that, while their model gave good predictions, they could not explain the precise meaning or physical representation of the normal stress term.

To better understand the circumferential redistribution, Sutharshan et al. [1995] conducted an extensive set of studies using photochromic dye activation and high speed video. These data indicated that the circumferential flow of liquid was upward in a disturbance wave and always downward in the thin film between waves.

In addition, observations of the dye during and after the passage of a disturbance wave indicated little random mixing of the dye; thus the redistribution of liquid in the disturbance is not due to a mixing mechanism. An additional study was performed, which indicated that disturbance waves tend to move as relatively coherent structures [Fukano et al., 1997]. Although the wave is wider at the bottom than the top, the wave tends to move with a common velocity all around the circumference of the tube. Hence, the wave spreading mechanism, as envisioned by Butterworth, was not observed to occur.

Recently, Hurlburt and Newell [2000] constructed a model based on a simplified form of that created by Laurinat et al. Ignoring secondary flows, as well as other terms in the model that Laurinat et al. found negligible, and treating liquid entrainment only in as much as it decreases the total liquid flow rate, the circumferential momentum equation became a balance between gravitational forces and forces due to $\frac{\partial \tau_{xx}}{\partial x}$. Rather than use an experimental parameter with the normal Reynolds stress as was done previously, they derived a correlation for it from data collected by Dallman [1978]. Model calculations were compared with the film thickness measurements of several researchers. Agreement was generally good, although the model did not always follow the experimental profile, especially as symmetry decreased. This was noted by the authors and attributed to the dependence on a film symmetry correlation. However, the model appears to be applicable to a very wide range of flows and tube sizes, and thus provides strong support for concluding that it is the gradient in the turbulent circumferential normal Reynolds stress that is the primary force maintaining the film profile balanced by gravity.

Conceptually, the $\frac{\partial \tau_{xx}}{\partial x}$ term is a measure of the change in magnitude of lateral turbulent fluctuations around the circumference of the tube. At the bottom of a smooth, round tube, the film tends to be thicker and liquid movement is less constrained by the wall. With this theory, then, lateral fluctuation magnitudes are greatest at the bottom and decrease with film thickness along the circumference. A gradient in fluctuation intensity implies a net transfer of momentum, leading to a force in the direction of momentum transfer. This is the force which, on average, is thought to balance the downward pull of gravity. It is important to note that, in reality, the $\frac{\partial \tau_{xx}}{\partial x}$ is $\frac{\partial \tau_{xx}}{\partial h}$. In smooth, round tubes, perhaps no distinction is necessary. However, when non-circular geometries or grooves are present, the two are no longer equivalent.

In summary, experimental observations and modeling results both indicate that the Reynolds stress gradient, $\frac{\partial \tau_{xx}}{\partial x}$, is the dominant mechanism in the annular flow liquid film thickness distribution. Experimentally, it appears that this mechanism operates primarily within disturbance waves with the liquid film draining freely in between. Every model, however, implements this mechanism as a time-averaged effect, with both gravitational draining and upward flow due to the stress gradient balancing each other in time so no net flow occurs. Very little is known on the nature of turbulence within the liquid film, so it has not been possible to construct a quantitative model for $\frac{\partial \tau_{xx}}{\partial x}$. Also, disturbance wave behavior is quite complicated, and although many have studied it, still not enough is known to be able to predict such parameters as wave frequency or width.

1.3.5 Interfacial shear

Wallis noted that the experimental interfacial shear in vertical annular flow could be correlated by a friction factor of the form

$$f_i = 0.005\left(1 + 300\frac{h}{D}\right),$$

where h is the mean film thickness [Wallis, 1969]. He also noted that friction factors for roughened pipes with a grain size of ϵ of could be correlated by the very similar

$$f = 0.005\left(1 + 75\frac{\epsilon}{D}\right),$$

so that annular flow could be conceptualized as flow in a roughened pipe with grain size of four times the mean film thickness.

This type of correlation has been used frequently in horizontal annular flow by assuming that the local interfacial shear stress can be predicted using the value from a vertical flow with the mean thickness set equal to the local horizontal film thickness. The Wallis correlation, or one similar to it, was used by Pletcher and McManus [1965], Fisher and Pearce [1979], James et al. [1987] and Flores et al. [1995].

Laurinat et al. [1985] used a correlation based on work in horizontal stratified flows while Fukano and Ousaka derived their own correlation from horizontal flow in a rectangular duct.

A Prandtl mixing length type of correlation derived from vertical flow data worked well for Tso and Sugawara [1990]. (This was quite a bit more complex

than correlations used by other researchers, but this model on the whole was quite complex.)

Finally, the correlation of vertical flow data by Asali et al. [1985] was incorporated by Hurlburt and Newell [2000].

In general, it appears that the interfacial shear stress in vertical annular flow tends to show a leveling off as vapor velocity becomes high enough to begin to entrain droplets. Some of the later correlations incorporate this while the Wallis-type do not. However, as noted earlier, much of the modeling was developed for flow conditions with relatively low levels of entrainment, so it is possible that the linear shear stress relations are adequate. Since most authors did not provide pressure drop results or perform comparisons of different interfacial shear stress relations, this survey of modeling efforts does not provide sufficient information to determine the whether one method of correlating shear stress is superior to another.

1.3.6 Gravitational draining profile

The one element common to all models was the action of gravity on the liquid film. However, the manner in which the draining liquid was modeled varied. Some chose to use a laminar velocity profile while others chose a Law of the Wall type of turbulent profile based on the axial flow characteristics. All of the more recent models chose the turbulent approach with generally quite good results.

On the other hand, as mentioned earlier, the liquid film in annular flow has been shown to behave much more like isolated turbulent bursts flowing on top of a thin laminar base layer [Chung and Murgatroyd, 1965, Jayanti and Hewitt, 1997]. Experiments by Fukano et al. [1997] indicate that the film draining after the passage of a disturbance wave can be modeled very accurately by assuming a laminar profile. In addition, other studies have shown that the time averaged behavior of the film does not always follow a turbulent Law of the Wall profile [Hewitt et al., 1990, Paras and Karabelas, 1991]. Perhaps, then, the model equations for the circumferential force balance could be simplified by using a laminar profile without loss of accuracy in the predictions produced.

1.4 Overview of the thesis

In what follows, experimental results will be presented, analyzed and discussed with respect to the annular flow issues just presented. In Chapter 2, unique film thickness profiles of annular flow through square and triangular tubes will be presented. Analysis of these results in Chapter 3 allows for the testing of traditional assumptions made about the velocity profile in the liquid film and the use of interfacial shear correlations from vertical flow data in horizontal flow models. Chapter 4 discusses the generation and behavior of secondary flows in two-phase systems in some detail, drawing on insight from the liquid film profiles in the square tubes. Attention will then turn to micro-grooved tubes in Chapter 5. In this chapter, the film profiles in 0, 9 and 18 degree helix tubes will be compared with an extensive review of the heat transfer literature in an attempt to explain the unique behaviors these tubes exhibit. Chapter 6 then presents the results of experimental evaluation of the effects of the groove angle and the number of grooves on the liquid film behavior. Finally, Chapter 7 presents a new experimental techinique, Thin Film PIV, which was inspired by the need to obtain more detailed information about the liquid film flow in these tubes.

1.5 References

D. Adechy and R. I. Issa. Numerical modelling of horizontal annular flows. In G. P. Celata, P. Di Marco, and R. K. Shah, editors, *Two-Phase Flow Modelling and Experimentation 1999*, volume 3, pages 1607–1615, Rome, Italy, May 1999. Edizioni ETS, Pisa.

R. J. Anderson and T. W. F. Russell. Film formation in two-phase annular flow. *AIChE Journal*, 16(4):626–633, 1970.

C. R. Arnold and G. F. Hewitt. Further developments in the photography of two-phase gas-liquid flow. *The Journal of Photographic Science*, 15:97–114, 1967.

J. C. Asali, T. J. Hanratty, and P. Andreussi. Interfacial drag and film height for vertical annular flow. *AIChE Journal*, 31(6):895–902, 1985.

B. J. Azzopardi. Disturbance wave frequencies, velocities and spacing in vertical annular two-phase flow. *Nuclear Engineering and Design*, 92(2):121–133, April 1986.

E. Begg, D. Khrustalev, and A. Faghri. Complete condensation of forced convection two-phase flow in a miniature tube. *Journal of Heat Transfer – Transactions of the ASME*, 121:904–915, 1999.

D. Butterworth. Note on fully-developed, horizontal, annular two-phase flow. *Chemical Engineering Science*, 24:1832–1834, 1969.

D. Butterworth. Air-water annular flow in a horizontal tube. *Progress in Heat and Mass Transfer*, 6:235–251, 1972.

D. Butterworth. An analysis of film flow and its application to condensation in a horizontal tube. *International Journal of Multiphase Flow*, 1:671–682, 1974.

H. S. Chung and W. Murgatroyd. Studies of the mechanism of roll wave formation on thin liquid films. In *Proceedings of the Symposium on Two-Phase Flow*, volume 2, pages A201–A214, University of Exeter, 1965.

J. W. Coleman and S. Garimella. Characterization of two-phase flow patterns in small diameter round and rectangular tubes. *International Journal of Heat and Mass Transfer*, 42:2869–2881, 1999.

M. W. E. Coney. The analysis of a mechanism of liquid replenishment and draining in horizontal two-phase flow. *International Journal of Multiphase Flow*, 1:647–669, 1974.

K. D. Cooper, G. F. Hewitt, and B. Pinchin. Photography of two-phase gas/liquid flow. *The Journal of Photographic Science*, 12:269–278, 1964.

J. C. Dallman. *Investigation of Separated Flow Model in Annular Gas-Liquid Two-Phase Flows*. PhD thesis, University of Illinois at Urbana-Champaign, Urbana, IL, February 1978.

R. S. Darling and H. N. McManus. Flow patterns in circular ducts with circumferential variation of roughness: a two-phase flow analog. *Proceedings of the 11th Mid-Western Mechanics Conference (Developments in Mechanics)*, 5:153–170, 1968.

L. A. Dykhno, L. R. Williams, and T. J. Hanratty. Maps of mean gas velocity for stratified flows with and without atomization. *International Journal of Multiphase Flow*, 20(4):691–702, 1994.

S. A. Fisher and D. L. Pearce. A theoretical model for describing horizontal annular flows. In F Durst, G V Tsiklauri, and N H Afghan, editors, *Two-Phase Momentum, Heat and Mass Transfer*, volume 1, pages 327–337. Hemisphere Publishing Corporation, 1979.

A. G. Flores, K. E. Crowe, and P. Griffith. Gas-phase secondary flow in horizontal, stratified and annular two-phase flow. *International Journal of Multiphase Flow*, 21(2):207–221, 1995.

T. Fukano, H. Nakagawa, Y. Mori, and M. Watanabe. Liquid film formation on the inner surface of the horizontal channel. *Nuclear Engineering and Design*, 175: 3–13, 1997.

T. Fukano and A. Ousaka. Prediction of the circumferential distribution of film thickness in horizontal and near-horizontal gas-liquid annular flows. *International Journal of Multiphase Flow*, 15(3):403–419, 1989.

G. F. Hewitt, S. Jayanti, and C. B. Hope. Structure of thin liquid films in gas–liquid horizontal flow. *International Journal of Multiphase Flow*, 16(6):951–957, 1990.

E. T. Hurlburt and T. A. Newell. Prediction of the circumferential film thickness distribution in horizontal annular gas-liquid flow. *Journal of Fluids Engineering – Transactions of the ASME*, 122:1–7, 2000.

L. A. Jacowitz and R. S. Brodkey. An analysis of geometry and pressure drop for the horizontal, annular, two-phase flow of water and air in the entrance region of a pipe. *Chemical Engineering Science*, 19:261–274, 1964.

P. W. James, N. S. Wilkes, W. Conkie, and A. Burns. Developments in the modelling of horizontal annular two-phase flow. *International Journal of Multiphase Flow*, 13(2):173–198, 1987.

S. Jayanti and G. F. Hewitt. Hydrodynamics and heat transfer in wavy annular gas-liquid flow: a computational fluid dynamics study. *International Journal of Heat and Mass Transfer*, 40(10):2445–2460, 1997.

S. Jayanti, G. F. Hewitt, and S. P. White. Time-dependent behavior of the liquid film in horizontal annular flow. *International Journal of Multiphase Flow*, 16(6): 1097–1116, 1990a.

S. Jayanti, N. S. Wilkes, D. S. Clarke, and G. F. Hewitt. The prediction of turbulent flows over roughened surfaces and its application to interpretation of mechanisms of horizontal annular flow. *Proceedings of the Royal Society of London A*, 431: 71–88, 1990b.

J. E. Laurinat, T. J. Hanratty, and W. P. Jepson. Film thickness distribution for gas-liquid annular flow in a horizontal pipe. *PhysioChemical Hydrodynamics*, 6(1,2): 179–195, 1985.

T. F. Lin, O. C. Jones, R. T. Lahey, R. C. Block, and M. Murase. Film thickness measurements and modelling in horizontal annular flows. *PCH: PhysicoChemical Hydrodynamics*, 6(1/2):197–206, 1985.

H. N. McManus, Jr. Local liquid distribution and pressure drops in annular two-phase flow. In *ASME–EIC Hydraulic Conference*, Montreal, Canada, 1961. Paper 61-HYD-20.

M. Miya. *Properties of Roll Waves*. PhD thesis, University of Illinois at Urbana-Champaign, Urbana, IL, June 1970.

S. V. Paras and A. J. Karabelas. Properties of the liquid layer in horizontal annular flow. *International Journal of Multiphase Flow*, 17(4):439–454, 1991.

R. H. Pletcher and H. N. McManus, Jr. The fluid dynamics of three dimensional liquid films with free surface shear: A finite difference approach. *Proceedings of the 9th Mid-Western Conference on Mechanics (Developments in Mechanics)*, 3: 305–318, 1965.

T. W. F. Russell and D. E. Lamb. Flow mechanism of two-phase annular flow. *The Canadian Journal of Chemical Engineering*, 43:237–245, 1965.

B. Sutharshan, M. Kawaji, and A. Ousaka. Measurement of circumferential and axial liquid film velocities in horizontal annular flow. *International Journal of Multiphase Flow*, 21(2):193–206, 1995.

K. A. Triplett, S. M. Ghiaasiaan, S. I. Abdel-Khalik, and D. L. Sadowski. Gas-liquid two-phase flow in microchannels. *International Journal of Multiphase Flow*, 25: 377–394, 1999.

C. P. Tso and S. Sugawara. Film thickness prediction in a horizontal annular two-phase flow. *International Journal of Multiphase Flow*, 16(5):867–884, 1990.

G. B. Wallis. *One-dimensional Two-phase Flow*. McGraw-Hill, Inc., New York, 1969.

L. R. Williams. *Effect of Pipe Diameter on Horizontal Annular Two-Phase Flow*. PhD thesis, University of Illinois at Urbana-Champaign, Urbana, IL, 1989.

D. E. Woodmansee. *Atomization from a Flowing Horizontal Water Film by a Parallel Air Flow*. PhD thesis, University of Illinois at Urbana-Champaign, Urbana, IL, 1968.

2

Liquid film distribution during horizontal annular flow through round, square and triangular tubes

2.1 Introduction

Flow through non-circular passages is quite common, and it has been known for nearly a century that the behavior of these flows is somewhat different from those in circular passages. Pressure losses are typically greater, and heat and mass transfer are not uniform along the walls. While a large number of studies have been made of turbulent single-phase flow in square and triangular geometries, very little has been done with two-phase flow. No previous work on two-phase pressure loss or liquid film distribution in triangular passages could be located.

The lack of work in this area is somewhat surprising, given the large number of non-circular flow passages in the nuclear power generation industry and the growing number of heat exchangers constructed with square, rectangular and triangular channels [Leung and Probert, 1997, Mayinger and Klas, 1992]. In addition, Zietlow and Pedersen [1995] and others have found that heat transfer and pressure loss predictions for relatively large channels scale well to the microchannel regime. Microchannel heat exchangers are now quite widely used. An understanding annular flow through channels with corners may also help improve the state of knowledge of flow through internally finned tubes, plate-fin exchangers, and flow in turbine blade cooling channels [Webb, 1990].

Fukano et al. [1984] obtained information about two-phase horizontal flow in

square and rectangular channels, focusing primarily on the film flow along the bottom wall. They obtained mean film thickness measurements and used a unique method to obtain film flow information in 8 zones across the bottom wall. Although visual observations were used to generate a flow-regime map, no detailed film thickness measurements were obtained in this study. Fukano et al. [1987] and Fukano et al. [1997] studied two-phase stratified annular flow in square and rectangular channels, but their publications were concerned primarily with the gross behavior of the liquid film and did not report two-phase pressure gradient or detailed film distribution information. A flow regime map has been generated for horizontal and vertical flows through rectangular channels by Troniewski and Ulbrich [1984] as well.

This work presents a survey of annular air-water flow through varying geometries. Specifically, the effect of corners on the liquid distribution is investigated using square and triangular tubes with comparison to round tubes. Two different sizes of both the square and round tubes are tested to determine behaviors associated with tube size. In addition, two different orientations of both the square and triangular tubes were examined to delineate the effect of gravity on the flows. The results of these experiments will be discussed with respect to the effects of geometry and orientation on film profiles, dryout and pressure drop.

2.2 Experimental

A schematic of the flow loop used in this work is shown in Figure 2.1. A 6.0 HP (4470 W) wet-vacuum was used to generate suction on one end of the test section. Air entered the apparatus through a long, smooth, round pipe with a valve at its opening to control air flow. Liquid was introduced from a gravity-fed tank through the holes in the test section wall.

Test sections were all constructed of acrylic. Two round tube sections, one 12.7 mm I.D. and one 25.4 mm I.D., were cast acrylic with excellent dimensional consistency. Each had 3.1 mm walls and were 6.5 m long. The square sections were of extruded acrylic with inner sidewalls measuring 15.2 mm and 22.7 mm, respectively. The walls were 1.5 mm thick and these test sections were also 6.5 m in length. To achieve the long test section, the ends of shorter tube lengths were sanded plane with a final polishing of 1500 grit sandpaper. The tube section ends

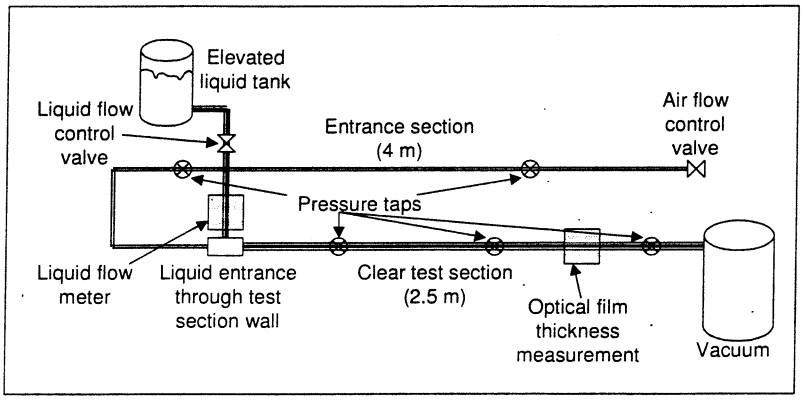

Figure 2.1: Schematic of the two-phase flow loop used in this set of experiments.

were secured in PVC flanges. For the square test sections, alignment tabs were affixed to two sides of each end so that two test section ends would mate and self-align. The sections were then bolted together and leak tested. While seamless joints were not achieved, very little flow disturbance was observed at the joints. Pressure drop results, presented later, confirm that, in the least, the joints of all test sections were of a consistent roughness.

The triangular test sections were formed from three 2.5 m long, 40 mm wide sheets of cast acrylic, each 3 mm thick. These were held together with a circular form at each end while the corners were sealed with silicon sealant. Once dried, a layer of tape was applied externally to protect the sealant. The triangular section was coupled to round entrance and exit sections via round rubber adapter fittings and silicon sealant. In this case only, liquid was injected through the wall of a round section preceding the test section, rather than directly through the test section walls.

The air flow rate was determined by measuring the pressure drop across a 3 m length of the entrance tube. The Colebrook correlation for friction factor, along with the definitions of friction factor, Reynolds number and mass flow rate, are then solved simultaneously to provide the mass flow rate of air in the loop. This process was simplified by using the Engineering Equation Solver (EES) from F-Chart Software. Comparison of this method with an inline spring-loaded mass flow meter gave agreement to within 10%.

Liquid flow rates were initially determined by timing the dropping liquid level with a stopwatch. Later, rotameters by King Industries were installed. A pump in the wet-vacuum tank recirculated the water, but the level in the feed tank was

not kept constant. The operator adjusted the liquid flow as needed to maintain a constant flow rate for the duration of the test (about 5 minutes), compensating for the variations in liquid level. This was only a concern at the highest liquid flow rate. Measurements of the liquid flow were precise to about 0.00025 Kg/s, or about 10% of the lowest flows. Repeatability of the flow settings was poor before the installation of the rotameters. Deviations of up to 50% occurred in Flows E, F, and G of the large square (LS) and large diamond (LD) trials, primarily in the 5 data points along the bottom(right bottom of diamond). The remaining liquid flows determined in this manner were generally within 10%.

All pressure drops were measured using U-tube water manometers. Vertical manometers could be read to a precision of 1 mm (9.8 Pa) at low liquid flow rates. At higher liquid flows, pressure fluctuations in the test section caused significant variation in the manometer levels. The resulting measurements were mentally "averaged" by the operator and recorded. For each test section, at least 16 pressure measurements were made and averaged together. The resulting averages had standard deviations ranging from 30 Pa to 160 Pa, generally well correlated by inverse mass quality. Thus, as a rule, the total estimated error in the pressure gradient measurements are about 60 Pa for Flows A-C and about 130 Pa for Flows D-F of any given geometry.

An angled manometer was used for the inlet pressure difference because the pressure drops were often quite small. The manometer was mounted to give 10 times the sensitivity of the vertical position. Hence, the inlet pressures were determined to a precision of 0.1 mmH_2O (0.98 Pa).

Local liquid film thicknesses were obtained using an optical measurement system described in Shedd [1998] and Shedd and Newell [1998]. The time averaged liquid film thicknesses presented here were measured to within ± 0.003 mm ($\pm$ one standard error). Due to the nature of the measurement, the experimental results exclude the large liquid waves from the calculated average thickness, so the thicknesses reported reflect only the thin base film that exists between the large liquid waves. It is important to take this into consideration when comparing the results of this experiment with measurements made by various impedance-based methods. The film thicknesses were measured at about 200 L/D from the point where liquid was introduced for the large round and square tubes; about 400 L/D for the small round and square tubes. The triangular test sections were much shorter, so

measurements were made at only about 75 L/D from the liquid entrance.

To obtain a set of film thickness measurements, the test section was mounted, then the film thickness apparatus mounted and calibrated at the initial location. A series of flow conditions were then established and film thickness measurements were made for each condition at that position. The test section was then allowed to dry out while the camera was repositioned and calibrated (zeroed) at the next measurement location. The same set of flow conditions were then re-established and new measurements taken. The repeatability of the flow conditions was quite good in general.

2.3 Results

In addition to the film profiles and pressure drop data, two additional significant quantities will be presented: film uniformity and film distribution. Film uniformity is defined as

$$\text{Film Uniformity} = 1 - \frac{\text{standard deviation of film thickness measurements}}{\text{mean film thickness}}$$

$$\Upsilon = 1 - \left.\frac{\sigma(h)}{\bar{h}}\right|_{\text{wetted perimeter}}$$

This is parameter quantifies the symmetry of the film, much as h_o/h_{avg} (where h_o is the film thickness at the bottom center of the tube) was used by Williams [1989] and Hurlburt and Newell [2000]. This definition, however, was based on horizontal flow through smooth tubes where the thickest film clearly flows along the bottom. In flows through tubes with corners it is not clear whether this sort of symmetry makes sense. Additionally, for flows through tubes with microgrooves, reported in Chapter 5, the liquid film is not always symmetrical with respect to the vertical plane through the axis. The film uniformity parameter captures the symmetry where it exists, (in the limit, a perfectly symmetrical film will have $\Upsilon = 1$), as well as providing information about how evenly the liquid is distributed along the wetted tube wall regardless of the geometry or enhancement.

The film distribution is defined as the film uniformity, Υ, multiplied by the wetted percentage of the tube wall perimeter, P,

$$\text{Dist} = \frac{P_{wet}}{P}\Upsilon.$$

The film distribution is expected to better correlate with the local heat transfer coefficient along a tube in either evaporation and condensation as it includes both film thickness and dryout behaviors.

The Froude rate, Ft, and the Lockhart-Martinelli parameter, X_{tt}, will be used frequently in reporting and plotting the results. The Froude rate is a non-dimensional group that essentially represents the ratio of the rate of kinetic energy flowing in the vapor to the power required to pump liquid from the bottom to the top of the tube at its axial flow rate. It is defined by

$$\begin{aligned} \text{Ft} &= \sqrt{\frac{\dot{m}_g}{\dot{m}_l}}\text{Fr} \\ &= \sqrt{\frac{\dot{m}_g}{\dot{m}_l}}\left(\frac{U_{sg}}{\sqrt{gd}}\right) \\ &\sim \frac{\text{gas phase power}}{\text{liquid phase pumping power}}, \end{aligned} \tag{2.1}$$

where the subscripts g and l represent vapor and liquid quantities, respectively, U_{sg} is the superficial vapor velocity (the velocity of vapor if it occupied the entire tube at the same mass flow rate), g is the gravitational acceleration and d is the tube diameter. Ft has been found to be a useful parameter for correlating some two-phase flow quantities [Hurlburt and Newell, 2000, Yashar et al., 2001].

The Lockhart-Martinelli parameter, the ratio of the liquid-only to vapor-only pressure drops in a given tube, is calculated by

$$X_{tt} = \left(\frac{1-x}{x}\right)^{0.9}\left(\frac{\rho_g}{\rho_l}\right)^{0.5}\left(\frac{\mu_l}{\mu_g}\right)^{0.1}. \tag{2.2}$$

2.3.1 Round

Film profiles for the round tube flows may be found in Figures 2.2 and 2.3. The corresponding flow conditions are given in Tables 2.1 and 2.2. These represent the average of the measurements taken for each of the 16 runs required to obtain the full set of film thickness data. Tabulated film thickness values may be found in Appendix A.

The flow conditions were established in a consistent and straightforward manner. First, the vacuum was turned on to generate air flow and dry the tube. The film thickness measurement apparatus was then positioned and calibrated. Once ready,

the liquid was added and the flow allowed to stabilize for about one minute before film thickness measurements were made. After the measurement was complete, the liquid flow was incremented and again allowed to settle. After flows LR-C and SR-C, with the liquid still flowing, a valve at the air inlet was closed to a predetermined setting and a new film thickness measurement was made. The liquid was then decreased as needed to obtain the remaining measurements. The flow conditions were found to be very repeatable, even over the span of several weeks.

Tables 2.3 and 2.4 present ensemble-averaged two-phase flow quantities for the flow conditions examined. Examining these tables together with the plots, several noteworthy behaviors are apparent. The liquid in both LR-A and SR-A only partially wets the tube. However, this is not stratified or stratified annular flow in the sense normally discussed in the literature. The value of the Froude rate would tend to indicate highly symmetrical film flow in a smooth round tube based on the correlation of previously reported data [Hurlburt and Newell, 2000]. Both inspection of the plots and the large values of Υ (0.87 and 0.78) indicate, as well, that the film is very uniform, not like the asymmetrical profiles associated with the stratified and stratified annular flow regimes. Thus, this appears to be a profile of what is termed high-quality dryout in the heat transfer literature. An appropriate designation might be shear-driven dryout, as it appears that a film has been sheared into a uniform film that lacks sufficient liquid to completely coat the tube wall. Further, it is interesting to note that the mean film thickness values for the film are within 0.01 mm of each other for both the 12.7 mm and 25.4 mm tubes. This indicates, perhaps, that some physical limit of film thickness is being approached.

Although the void fraction, α, never falls below 0.94, the mass quality (the ratio of the vapor mass flow to the total mass flow) in this data set ranges from 0.22 to 0.84. The film profiles remain quite symmetrical throughout this quality range, with the lowest qualities beginning to approach a stratified-annular description. Once the wall is fully wetted, there is a fairly strong correlation between quality and film uniformity. Weaker correlations between Froude rate and uniformity and X_{tt} and uniformity are apparent as well.

Finally, the corresponding values of h_{avg}/h_{bot} have been included in Tables 2.3 and 2.4 for comparison with Υ. From this it is clear the new film uniformity parameter corresponds closely to the more familiar measure of symmetry.

Flow Conditions – Large Round Tube					
Flow	$\dot{m}_g$ kg/s	$\dot{m}_l$ kg/s	U_{sg} m/s	U_{sl} m/s	G_{tot} kg/sm^2
LR-A	0.0248	0.0048	49	0.0095	58
LR-B	0.0219	0.0138	43	0.027	71
LR-C	0.0174	0.0340	34	0.067	101
LR-D	0.0141	0.0498	28	0.098	126
LR-E	0.0156	0.0229	31	0.045	76

Table 2.1: Flow conditions for the data obtained in the 25.4 mm round tube.

Flow Conditions – Small Round Tube					
Flow	$\dot{m}_g$ kg/s	$\dot{m}_l$ kg/s	U_{sg} m/s	U_{sl} m/s	G_{tot} kg/sm^2
SR-A	0.0052	0.0021	41	0.017	58
SR-B	0.0045	0.0042	35	0.033	68
SR-C	0.0036	0.0084	29	0.066	95
SR-D	0.0032	0.0074	25	0.058	83
SR-E	0.0035	0.0063	27	0.050	77
SR-F	0.0038	0.0037	30	0.029	59

Table 2.2: Flow conditions for the data obtained in the 12.7 mm round tube.

Two-Phase Flow Measurements – Large Round Tube										
Flow	α	x	Ft	X_{tt}	Wet %	Υ	h_{avg}/h_{bot}	Dist	dP/dx N/m^2	h_{avg} mm
LR-A	0.98	0.84	198	0.011	0.63	0.87	0.92	0.54	1188	0.161
LR-B	0.97	0.61	96	0.031	1.00	0.84	0.87	0.84	1343	0.191
LR-C	0.96	0.34	44	0.086	1.00	0.67	0.70	0.67	1530	0.273
LR-D	0.95	0.22	26	0.147	1.00	0.54	0.62	0.54	1169	0.310
LR-E	0.96	0.40	46	0.067	1.00	0.57	0.62	0.57	944	0.253

Table 2.3: Measured two-phase quantities for the specified flow conditions in the 25.4 mm round tube.

Two-Phase Flow Measurements – Small Round Tube										
Flow	α	x	Ft	X_{tt}	Wet %	Υ	h_{avg}/h_{bot}	Dist	dP/dx N/m^2	h_{avg} mm
SR-A	0.98	0.71	160	0.021	0.75	0.78	0.74	0.58	1991	0.152
SR-B	0.96	0.51	87	0.045	1.00	0.76	0.68	0.76	2010	0.133
SR-C	0.94	0.30	46	0.101	1.00	0.65	0.60	0.65	2048	0.182
SR-D	0.95	0.30	42	0.101	1.00	0.65	0.62	0.65	1902	0.173
SR-E	0.95	0.36	51	0.081	1.00	0.65	0.62	0.65	1913	0.156
SR-F	0.96	0.50	76	0.047	1.00	0.78	0.73	0.78	1876	0.127

Table 2.4: Measured two-phase quantities for the specified flow conditions in the 12.7 mm round tube.

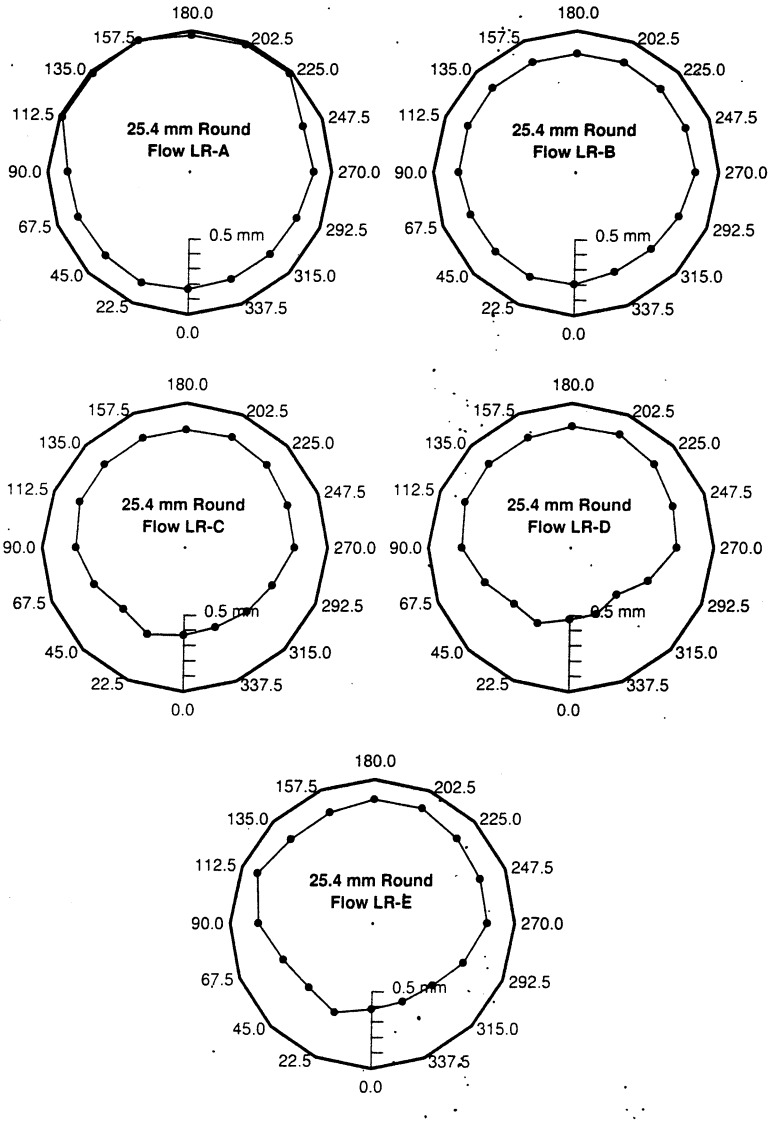

Figure 2.2: Film thickness profiles in a 25.4 mm round tube.

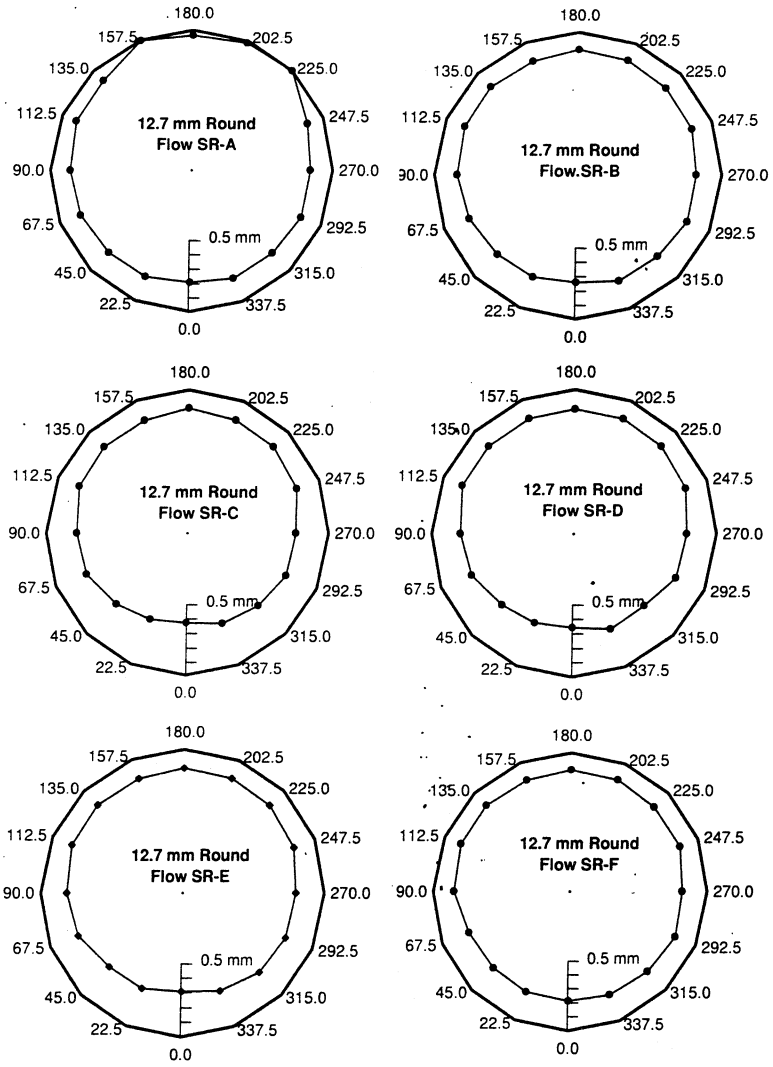

Figure 2.3: Film thickness profiles in a 12.7 mm round tube.

2.3.2 Square

Data for flow in the large and small square test sections are presented similarly to the round tube data above. Flow through the square tubes exhibited several unique behaviors. For example, a definite threshold was qualitatively observed in flow quantities before the top side of the tube would fully wet. For a given air flow rate (below that required for significant atomization), as liquid flow increased, the film would climb the wall until the upper corners were approached. Then, although rivulets might exist along the top, the liquid flow could be increased some amount further without a visible change in film behavior. At some level, however, the top would suddenly wet and fully annular flow would persist. This transition can be visualized with plots LS-A, LS-B and LS-B in Figure 2.5. In the reverse direction, as liquid flow decreased, first the upper corners would dry and a rivulet would form down the center of the tube, thinning rapidly with reduction in flow rate.

Like the round tube flows, the highest quality flows have relatively uniform, partially wetting films. The uniformity parameter is equivalent for both the large and small tubes at the highest quality examined and the mean film thickness results lie within 0.014 mm. However, unlike the round tubes, once the walls are completely wetted, the correlation between quality and uniformity does not appear to be very strong.

As liquid flow increases, a very noticeable thinning of the film in the corners of the tube with respect to the wall center locations becomes evident. The difference in thickness between the bottom center point of the LS data and the bottom corner points is generally between 0.05 and 0.1 mm, much greater than the average error of 0.005 mm. In addition, the measurements were very repeatable.

Other researchers have noticed similar effects when studying turbulent flow through rectangular and square channels. An experimental study of the liquid film in horizontal two-phase annular flow through a 4 cm square and 1 cm by 8 cm rectangular duct was carried out by Fukano et al. [1984]. As a result of their work, they generated a flow regime map based on the volumetric flow of water normalized by the channel width (m^3/sm) and the superficial gas velocity. The present data agree well with their findings as shown in Figure 2.4. Note that the flows with dryout tend to fall in the region of transition to annular flow from the ripple regime.

To better understand the liquid distribution, Fukano et al. measured mean liquid film thickness using a conductance method and divided the bottom wall at the outlet

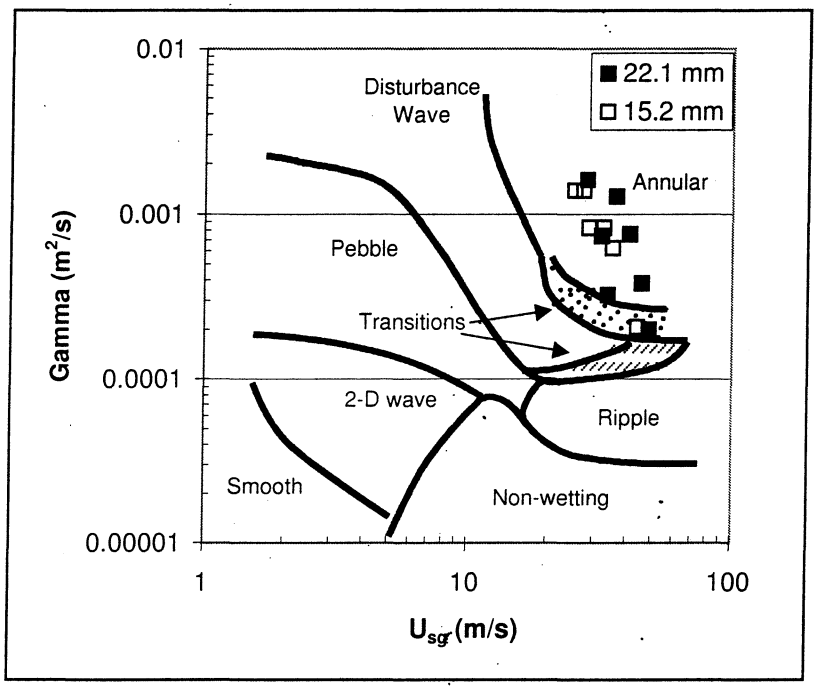

Figure 2.4: Flow map for two-phase horizontal flow through square tubes interpreted and redrawn from Figure 3 of Fukano et al. [1984]. Flow regime designations are from Fukano et al. Gamma (Γ) is the volumetric flow rate of liquid normalized by the channel width.

Flow Conditions – Large Square Tube					
Flow	$\dot{m}_g$ kg/s	$\dot{m}_l$ kg/s	U_{sg} m/s	U_{sl} m/s	G_{tot} kg/sm^2
LS-A	0.0231	0.0044	49	0.0093	53
LS-B	0.0217	0.0084	46	0.018	58
LS-C	0.0196	0.0168	41	0.035	70
LS-D	0.0173	0.0282	36	0.059	87
LS-E	0.0135	0.0356	28	0.075	94
LS-F	0.0153	0.0164	32	0.035	61
LS-G	0.0161	0.0072	34	0.015	45

Table 2.5: Flow conditions for the data obtained in the 22.1mm square tube.

Flow Conditions – Small Square Tube					
Flow	$\dot{m}_g$ kg/s	$\dot{m}_l$ kg/s	U_{sg} m/s	U_{sl} m/s	G_{tot} kg/sm^2
SS-A	0.0102	0.0032	44	0.014	58
SS-B	0.0082	0.0095	35	0.041	76
SS-C	0.0076	0.0126	33	0.054	87
SS-D	0.0064	0.0211	27	0.091	118
SS-E	0.0059	0.0211	25	0.091	116
SS-F	0.0067	0.0126	29	0.0543	83

Table 2.6: Flow conditions for the data obtained in the 15.2 mm square tube.

into 8 channels using very thin copper dividers, recording the flow rate collected in each of these sections. In interpreting this data, the fact that liquid is pushed up the side walls and across the top must be taken into account. For instance, it appears from the presentation of flow results in the 1cm by 8 cm channel that a very thick film appears in the corners when, in reality, this is an indication of flow along the side walls, not flow in the corners themselves. Unfortunately, these authors chose not to present their data for the 4 cm by 4 cm channel, so direct comparison of their work with the current is not possible. However, the 1 cm by 8 cm results do show the same trends that are found in Figures 2.5 - 2.7 with a higher mass flow of liquid in the center, diminishing toward the corners, then peaking in the corners due to the flow on the side walls.

2.3.3 Diamond

The rotated square, or "diamond", results are presented in Tables 2.9 - 2.12 and Figures 2.8 - 2.10. The high quality uniformity is again generally apparent, as well as the thinning in the corners – even the bottom corner to which liquid tended to

Two-Phase Flow Measurements – Large Square Tube									
Flow	α	x	Ft	X_{tt}	Wet %	Υ	Dist	dP/dx N/m^2	h_{avg} mm
LS-A	0.99	0.84	217	0.011	0.50	0.75	0.37	1337	0.141
LS-B	0.98	0.72	143	0.020	0.75	0.78	0.59	1398	0.158
LS-C	0.97	0.54	85	0.041	1.00	0.73	0.73	1472	0.173
LS-D	0.97	0.38	54	0.073	1.00	0.72	0.72	1496	0.197
LS-E	0.97	0.27	33	0.113	1.00	0.62	0.58	1177	0.219
LS-F	0.97	0.48	60	0.050	0.85	0.67	0.57	1014	0.181
LS-G	0.98	0.69	103	0.023	0.55	0.63	0.35	887	0.175

Table 2.7: Measured two-phase quantities for the specified flow conditions in the 22.1 mm square tube. h_{avg} the average liquid film thickness over the wetted perimeter.

Two-Phase Flow Measurements – Small Square Tube									
Flow	α	x	Ft	X_{tt}	Wet %	Υ	Dist	dP/dx N/m^2	h_{avg} mm
SS-A	0.98	0.76	176	0.017	0.50	0.74	0.37	1719	0.127
SS-B	0.97	0.46	73	0.054	0.94	0.65	0.61	1922	0.137
SS-C	0.96	0.38	56	0.075	1.00	0.65	0.65	1968	0.146
SS-D	0.96	0.23	33	0.140	1.00	0.67	0.67	2021	0.168
SS-E	0.96	0.22	30	0.150	1.00	0.64	0.64	1748	0.174
SS-F	0.96	0.35	46	0.085	1.00	0.62	0.62	1601	0.149

Table 2.8: Measured two-phase quantities for the specified flow conditions in the 15.2 mm square tube. h_{avg} the average liquid film thickness over the wetted perimeter.

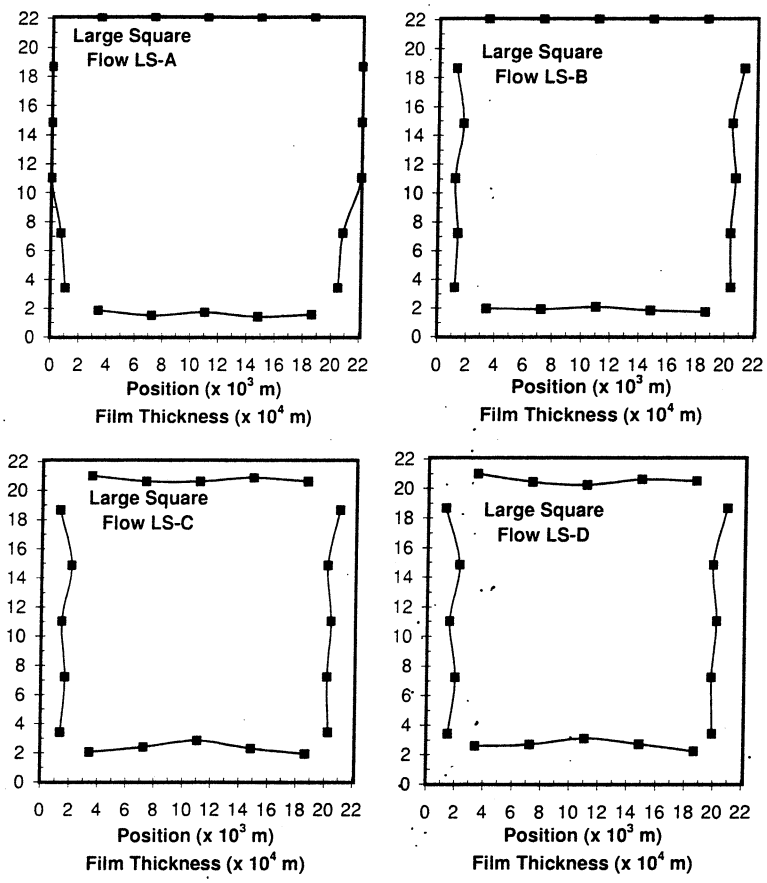

Figure 2.5: Film thickness profiles in the 22.1 mm square tube for flows A – D.

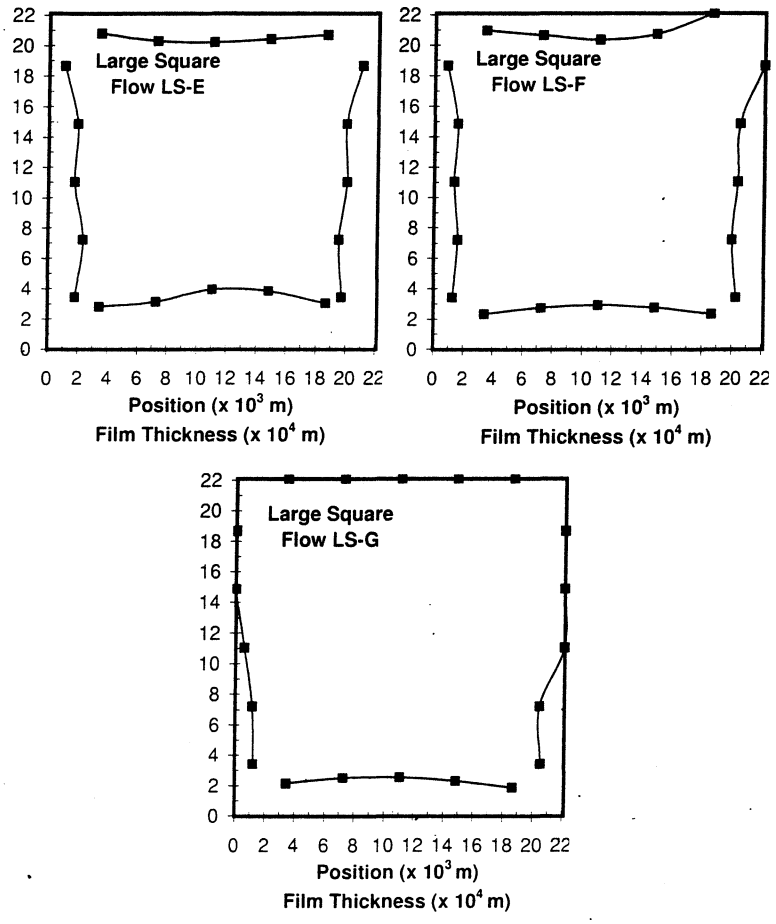

Figure 2.6: Film thickness profiles in the 22.1 mm square tube for flows E – G.

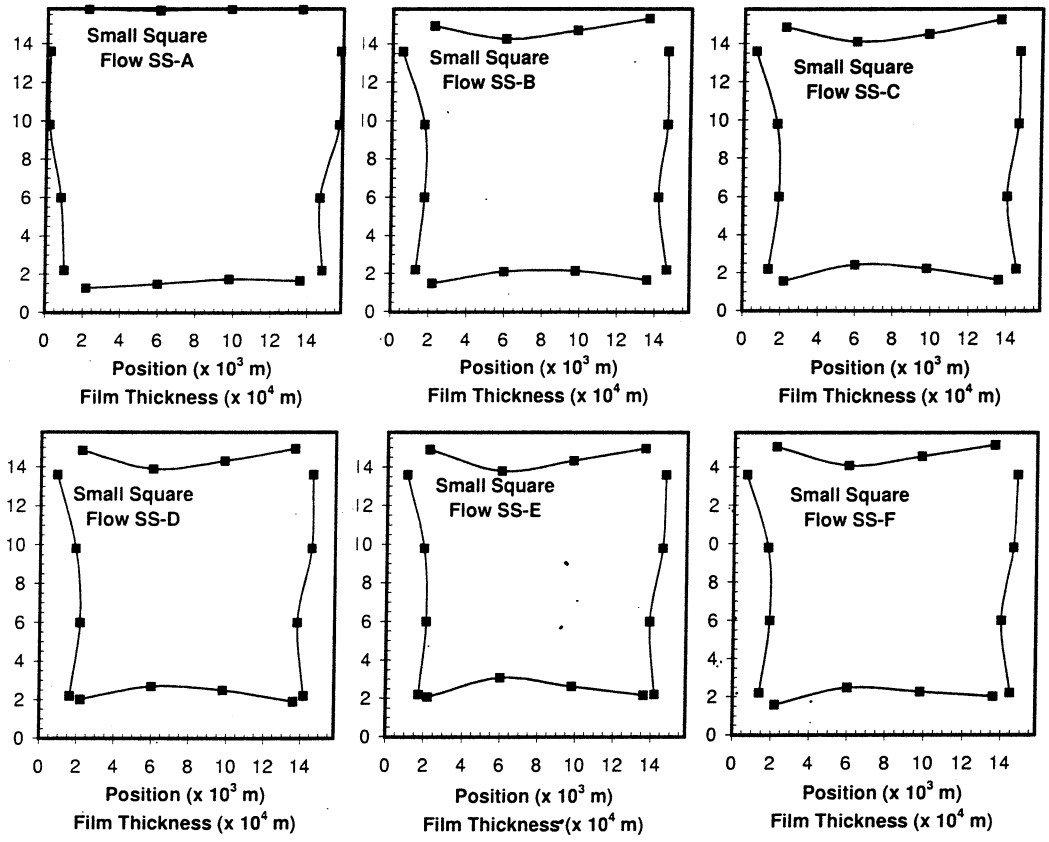

Figure 2.7: Film thickness profiles in 15.8 mm square tube.

Flow Conditions – Large Diamond Tube					
Flow	$\dot{m}_g$ kg/s	$\dot{m}_l$ kg/s	U_{sg} m/s	U_{sl} m/s	G_{tot} kg/sm^2
LD-A	0.0232	0.0053	49	0.0111	55
LD-B	0.0224	0.0080	47	0.017	58
LD-C	0.0199	0.0178	42	0.038	72
LD-D	0.0177	0.0289	37	0.061	89
LD-E	0.0151	0.0320	32	0.067	90
LD-F	0.0168	0.0126	35	0.027	56
LD-G	0.0181	0.0059	38	0.012	46

Table 2.9: Flow conditions for the data obtained in the 22.1mm diamond tube.

Flow Conditions – Small Diamond Tube					
Flow	$\dot{m}_g$ kg/s	$\dot{m}_l$ kg/s	U_{sg} m/s	U_{sl} m/s	G_{tot} kg/sm^2
SD-A	0.0103	0.0032	44	0.014	58
SD-B	0.0081	0.0095	35	0.041	75
SD-C	0.0075	0.0126	32	0.054	87
SD-D	0.0064	0.0210	27	0.091	118
SD-E	0.0056	0.0210	24	0.091	115
SD-F	0.0064	0.0126	27	0.054	82

Table 2.10: Flow conditions for the data obtained in the 15.2 mm diamond tube.

drain. However, in general, the change in orientation appeared to have a noticeable impact on the uniformity of the film as liquid drained into the bottom corner. Interestingly, the overall dryout characteristics, as quantified by the "Wet %" column of the data tables, appear to be little affected by the rotation. Also unaffected, within experimental error, was the pressure gradient.

Comparing the film profiles, especially for LD-A, B and LS-A, B, it would appear that there exists an equilibrium base film flow which distributes itself to cover the same perimeter regardless of orientation.

2.3.4 Triangle

Tables 2.13 - 2.16 and Figures 2.11 and 2.12 give the results of the measurements for triangle tube flow. Although the flows were carefully matched for both the apex-up and apex-down trials, several significant differences in flow behavior are apparent. For example, it was much easier to wet the walls of the tube in the apex-down configuration. Though flow TU-D indicates 100% wet walls, in reality, the walls near the apex of the upward pointing triangle never appeared to maintain a steady film. Thus, dryout is significantly affected by the tube orientation. In addition, because

Two-Phase Flow Measurements – Large Diamond Tube									
Flow	α	x	Ft	X_{tt}	Wet %	Υ	Dist	dP/dx N/m^2	h_{avg} mm
LD-A	0.99	0.81	200	0.012	0.55	0.71	0.39	1329	0.151
LD-B	0.98	0.74	153	0.019	0.75	0.78	0.58	1385	0.155
LD-C	0.97	0.53	86	0.043	0.95	0.75	0.71	1480	0.183
LD-D	0.97	0.38	57	0.073	1.00	0.69	0.69	1576	0.213
LD-E	0.96	0.32	43	0.093	0.95	0.60	0.57	1150	0.245
LD-F	0.98	0.57	83	0.036	0.65	0.67	0.44	978	0.197
LD-G	0.99	0.75	135	0.017	0.35	0.91	0.32	827	0.186

Table 2.11: Measured two-phase quantities for the specified flow conditions in the 22.1 mm diamond tube.

Two-Phase Flow Measurements – Small Diamond Tube									
Flow	α	x	Ft	X_{tt}	Wet %	Υ	Dist	dP/dx N/m^2	h_{avg} mm
SD-A	0.99	0.76	178	0.016	0.44	0.59	0.26	1723	0.098
SD-B	0.97	0.46	72	0.055	0.94	0.72	0.68	1906	0.141
SD-C	0.96	0.37	56	0.076	0.94	0.73	0.68	1944	0.156
SD-D	0.95	0.23	34	0.139	0.94	0.70	0.65	1989	0.198
SD-E	0.95	0.21	28	0.156	0.94	0.64	0.60	1643	0.212
SD-F	0.96	0.33	43	0.088	0.94	0.69	0.65	1472	0.170

Table 2.12: Measured two-phase quantities for the specified flow conditions in the 15.2 mm diamond tube.

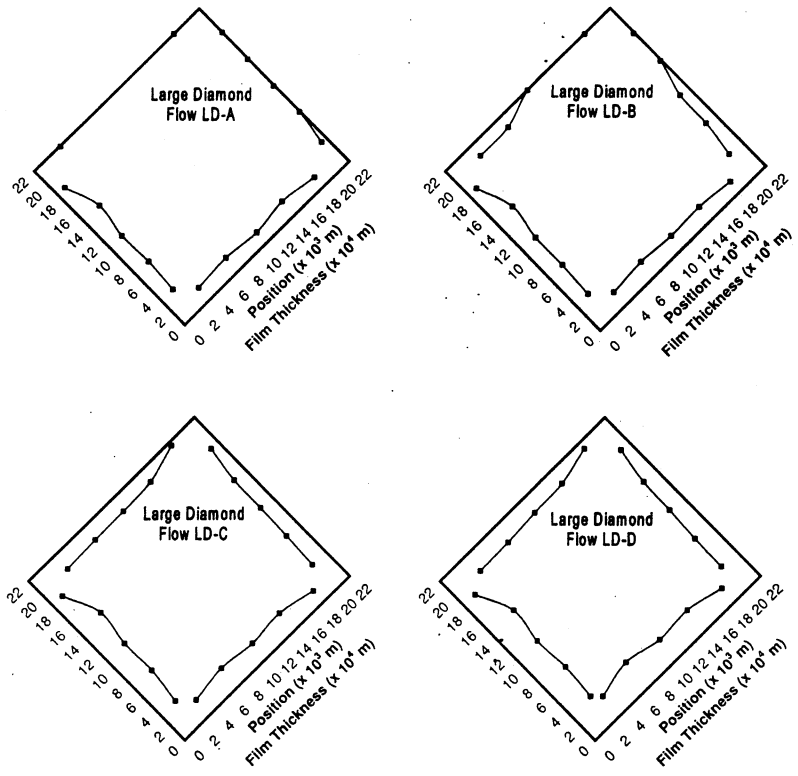

Figure 2.8: First set of film thickness profiles in the 22.1 mm square tube rotated 45 degrees. Note that the labeled flow conditions, A – D, correspond closely with the A – D flow conditions for the unrotated 22.1 mm square results presented above.

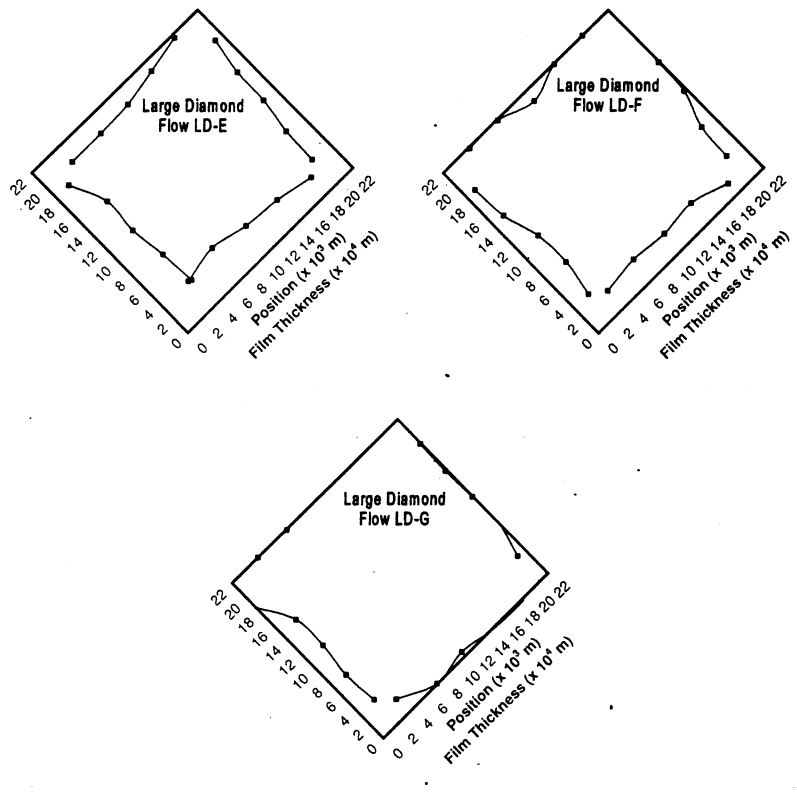

Figure 2.9: Remaining film thickness profiles in the 22.1 mm square tube rotated 45 degrees. Note that the labeled flow conditions, E – G, correspond closely with the E – G flow conditions for the unrotated 22.1 mm square results presented above.

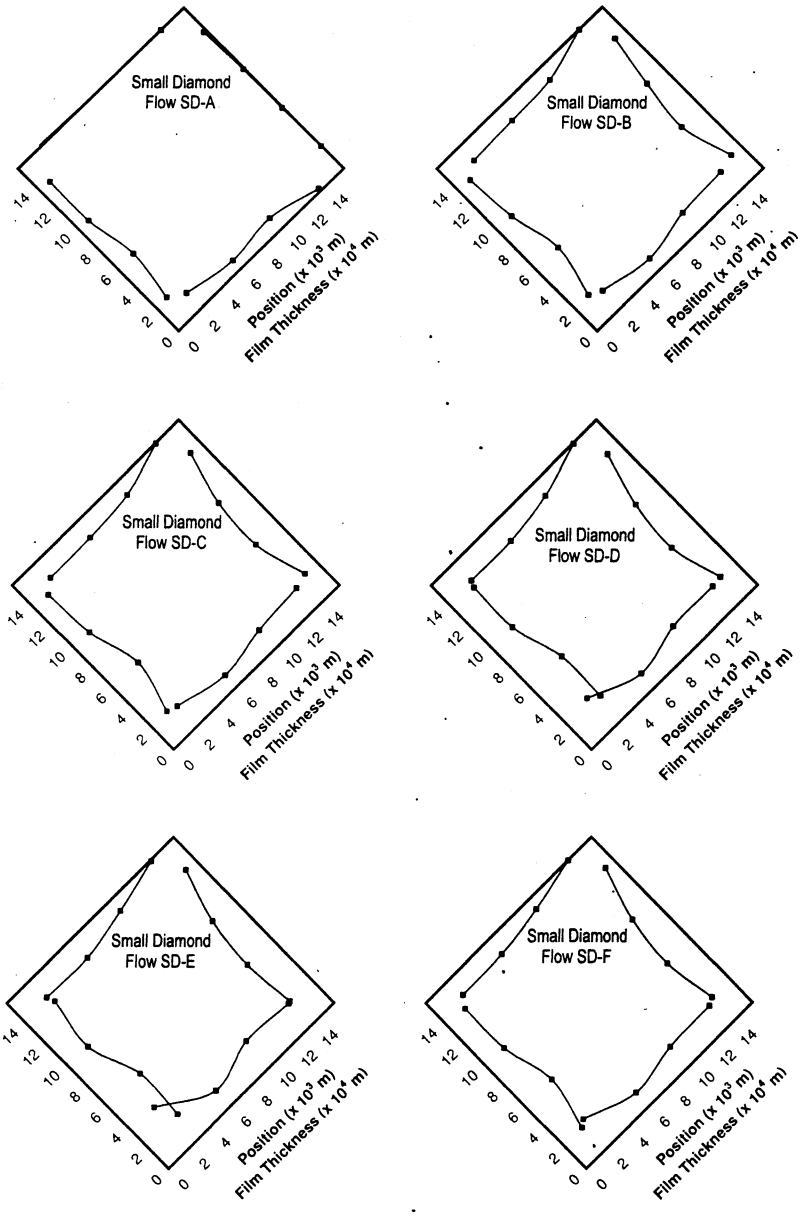

Figure 2.10: Film thickness profiles in the 15.8 mm square tube rotated 45 degrees. Note that the labeled flow conditions, A-F, correspond closely with the A-F flow conditions for the unrotated 15.8 mm square results presented above.

Flow Conditions – Triangle, Apex Down					
Flow	$\dot{m}_g$ kg/s	$\dot{m}_l$ kg/s	U_{sg} m/s	U_{sl} m/s	G_{tot} kg/sm^2
TD-A	0.0251	0.0042	36	0.0061	42
TD-B	0.0231	0.0126	33	0.018	57
TD-C	0.0221	0.0210	32	0.030	68
TD-D	0.0206	0.0314	30	0.045	83
TD-E	0.0174	0.0314	25	0.045	78
TD-F	0.0183	0.0210	26	0.030	62

Table 2.13: Flow conditions for the data obtained in the apex down triangle tube.

the liquid was distributed around less of the tube perimeter, the mean wetted film thickness measurements are generally greater in the apex-up configuration.

Apparently because liquid was more likely to drain to the downward-pointing apex, the apex-up data show consistently higher film uniformities. Flow TU-A with a film only along the bottom of the tube achieved the highest uniformity of any profile measured in this work, being very nearly constant at 0.190 mm. The fairly uniform film that forms on the top wall of the apex-down flows is interesting as well. The mean thickness of this film ranges from about 0.100 mm to 0.160 mm.

In spite of these differences, pressure drop is not significantly affected by orientation, as was noted with the square tube flows. The apex-up data are consistently higher, but these differences fall within the error in the pressure measurement. This is somewhat surprising as it could be expected that pressure losses would be lower in a tube with less of its wall wetted at the same vapor flow condition; the smooth wall should present significantly less resistance than the liquid film. Perhaps this increase in smooth wall area is compensated for by the presence of the thicker films which many have associated with greater interfacial shear.

Secondary flows are well documented in single-phase flow through triangular ducts. As in the square tubes, they appear to have an impact on the liquid film, especially in TU-D, TU-F, TD-D and TD-F flows. The thinning effect is somewhat smaller in the triangle, perhaps in this case due to the lower vapor velocities used in the triangle versus the square runs.

2.3.5 Pressure drop

As shown in Figure 2.13, the pressure drop data for all geometries are well-correlated by the Lockhart-Martinelli parameter, X_{tt}. The friction factor was defined in the

Flow Conditions – Triangle, Apex Up					
Flow	$\dot{m}_g$ kg/s	$\dot{m}_l$ kg/s	U_{sg} m/s	U_{sl} m/s	G_{tot} kg/sm^2
TU-A	0.0256	0.0042	37	0.006	43
TU-B	0.0237	0.0126	34	0.018	52
TU-C	0.0219	0.0210	32	0.030	62
TU-D	0.0205	0.0314	30	0.045	75
TU-E	0.0177	0.0314	26	0.045	71
TU-F	0.0190	0.0210	27	0.030	58

Table 2.14: Flow conditions for the data obtained in the apex up triangle tube.

Two-Phase Flow Measurements – Triangle, Apex Down									
Flow	α	x	Ft	X_{tt}	Wet %	Υ	Dist	dP/dx N/m^2	h_{avg} mm
TD-A	0.99	0.86	161	0.009	0.50	0.80	0.40	976	0.150
TD-B	0.98	0.65	82	0.027	0.92	0.64	0.59	1057	0.150
TD-C	0.97	0.51	59	0.045	1.00	0.69	0.69	1171	0.174
TD-D	0.97	0.40	44	0.068	1.00	0.75	0.75	1220	0.205
TD-E	0.97	0.36	34	0.079	1.00	0.55	0.55	878	0.202
TD-F	0.97	0.47	45	0.053	0.83	0.59	0.49	789	0.199

Table 2.15: Measured two-phase quantities for the specified flow conditions in the apex down triangle tube.

Two-Phase Flow Measurements – Triangle, Apex Up									
Flow	α	x	Ft	X_{tt}	Wet %	Υ	Dist	dP/dx N/m^2	h_{avg} mm
TU-A	0.99	0.86	168	0.009	0.33	0.97	0.32	975	0.191
TU-B	0.98	0.65	86	0.026	0.67	0.80	0.54	1137	0.182
TU-C	0.98	0.51	59	0.045	0.83	0.65	0.54	1251	0.185
TU-D	0.97	0.39	44	0.068	1.00	0.55	0.55	1284	0.193
TU-E	0.97	0.36	35	0.078	0.75	0.66	0.50	975	0.245
TU-F	0.98	0.48	48	0.051	0.67	0.74	0.49	845	0.228

Table 2.16: Measured two-phase quantities for the specified flow conditions in the apex up triangle tube.

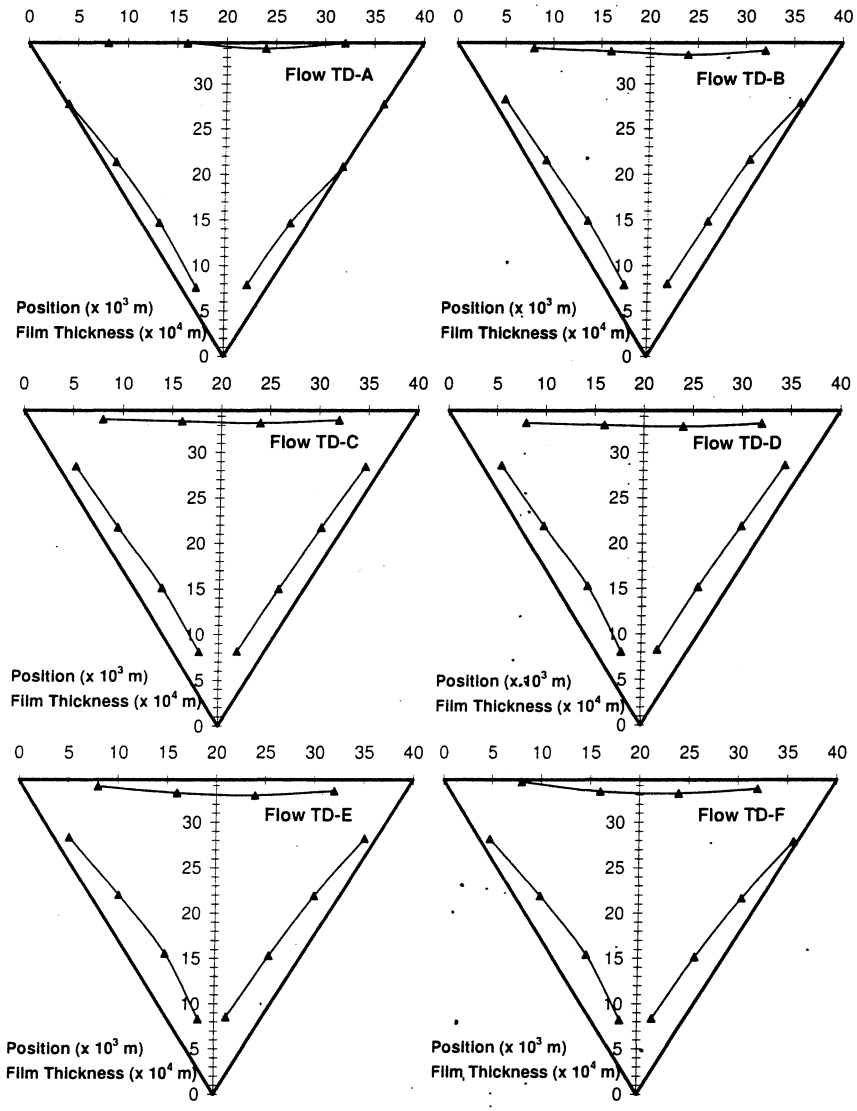

Figure 2.11: Film thickness profiles in an equilateral triangular tube with 40 mm sides and the apex down.

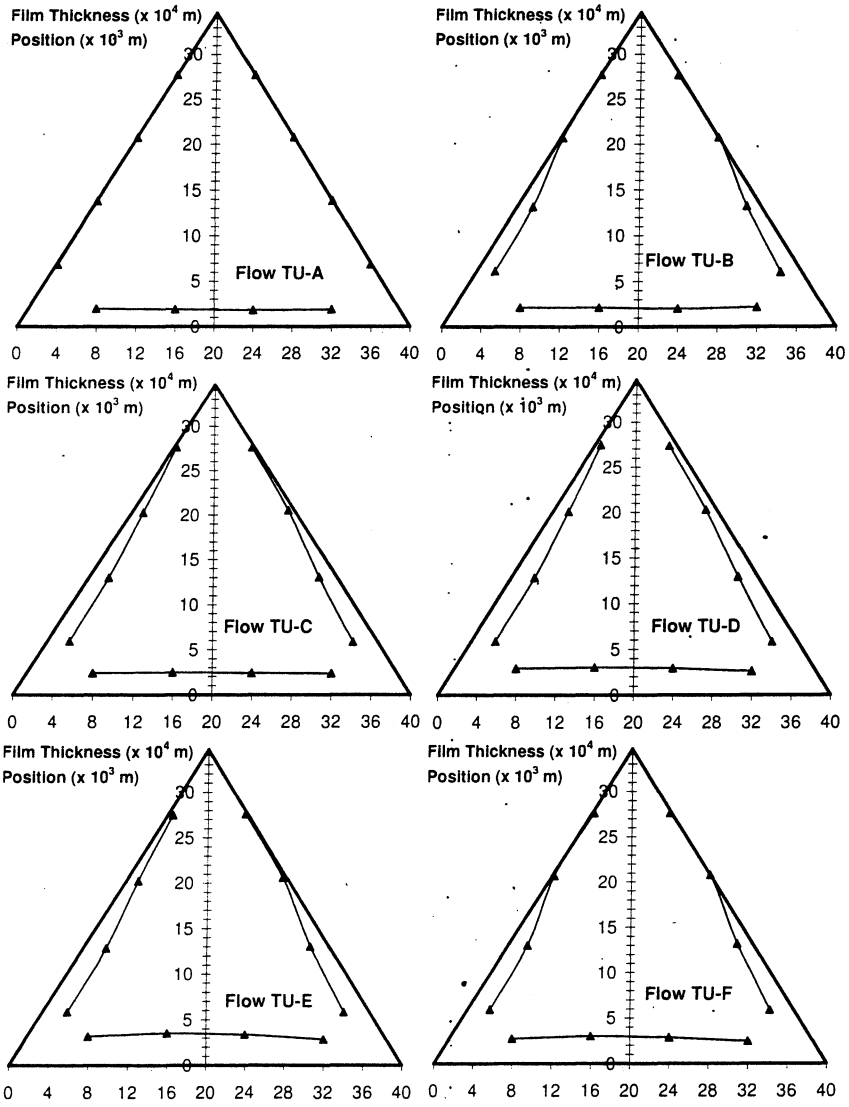

Figure 2.12: Film thickness profiles in an equilateral triangular tube with 40 mm sides and the apex up.

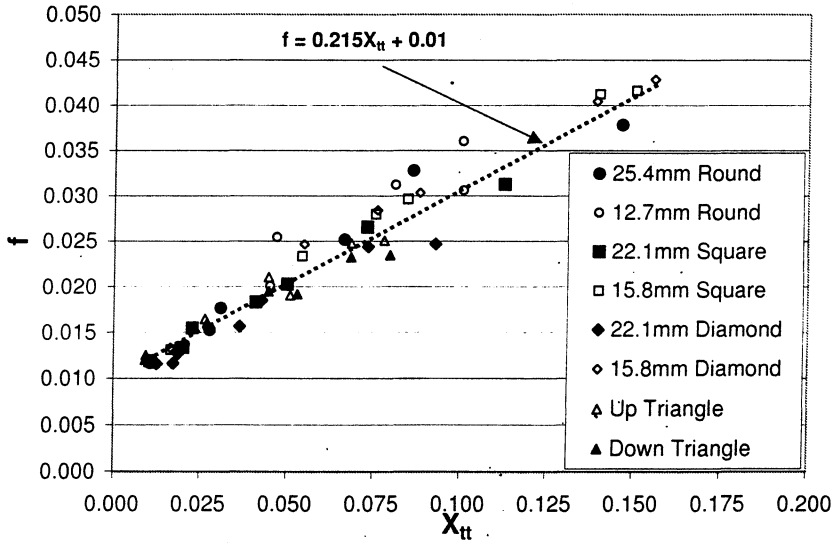

Figure 2.13: Friction factor versus the Lockhart-Martinelli parameter, X_{tt}, compiled from the two-phase pressure gradients measured for all of the geometries and flow conditions.

standard manner as

$$f = \frac{\Delta p}{(L/D_H)(\rho_g U_{sg}^2)/2} \tag{2.3}$$

where U_{sg} is the superficial gas velocity and D_H is the hydraulic diameter, $4A/P$.

The superficial velocity used in calculating the triangle tube friction factor is defined as

$$U_{sg} = \frac{\dot{m}_g}{\rho_g A_{Dh}}, \tag{2.4}$$

where

$$A_{Dh} = \frac{\pi D_H^2}{4} \tag{2.5}$$

is the area of the circle defined by the hydraulic diameter. This has the effect of significantly increasing the gas velocity in the calculations for the non-circular tubes, bringing these friction factors in line with the round tube data.

2.4 Discussion

The purpose of this investigation was to obtain a broad set of film thickness data for annular flow through round, square and triangle tubes and observe influences

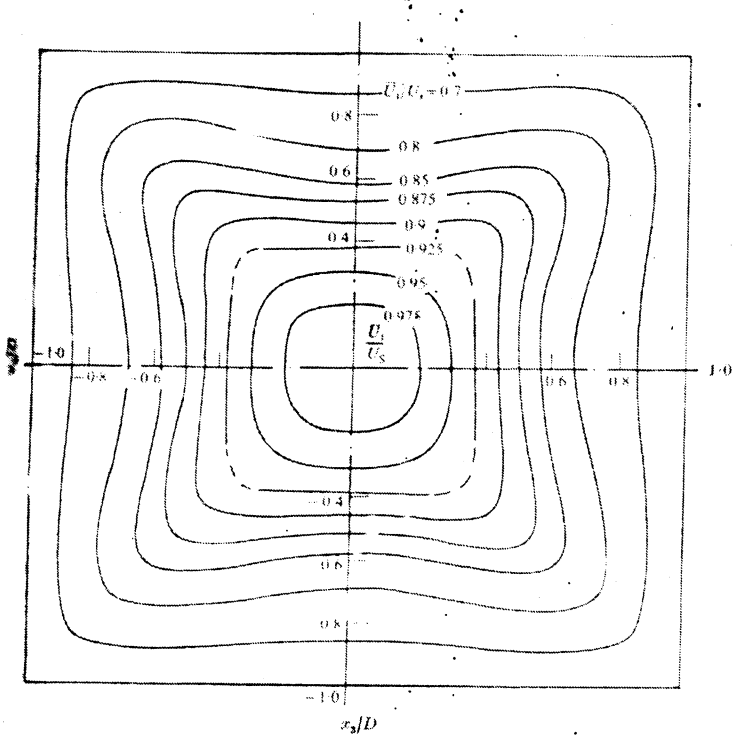

Figure 2.14: Axial velocity contours (isotachs) of turbulent fluid flow in a square duct. Taken from Melling and Whitelaw [1976].

on flow behavior due to tube size, shape and orientation. Tube size had very little impact overall. Pressure gradients increased with smaller cross section, as expected.

Rotating the square tubes had surprisingly little impact on the flow behavior. Dryout behavior was essentially unaffected as was the mean film thickness. The film did become less uniform, however. Unlike the square, the triangular channel was significantly affected by orientation.

The liquid film profiles in the square tubes are remarkably similar to the profiles of isotachs (lines of equal velocity) found in single phase turbulent flow through these geometries as shown in Figure 2.14. The results of Fukano et al. [1984], discussed above, as well as mass transfer studies by Goldstein et al. [1992] further verify this unique behavior. No known attempts have been made to accurately model the liquid film of annular flow in non-circular tubes, either horizontal or vertical. However, the experimental results just presented appear to suggest that forces act upon the film in such a way that the film tends to follow curves of constant velocity (isotachs) in the vapor. Secondary flows are responsible for the distorted isotachs,

so it is apparent that secondary flows may play an important role in two-phase flow as well. As well, it is likely that the additional roughness and asymmetry of the liquid film act to enhance secondary flows in the vapor.

A possible mechanism for the thinning in the corners is the action of redistributed axial shear on the film. Secondary flow in the vapor carries axial momentum from the center of the tube into the corners. This increased momentum will contribute to increased interfacial shear in the corner regions versus central regions at the same distance from the wall, which could act to thin the liquid film in the corners. As the film thins in the corner with respect to the center, the interfacial shear will tend to approach a constant value across the side. This agrees with the single-phase work of Leutheusser [1963] who found that the secondary flows acted to equalize the axial wall shear in turbulent flow.

The generation and interactions of secondary vapor flows in two-phase annular flow is discussed in detail in Chapter 4.

An important observation should be reported at this point. First, the film profiles reported in this work were easily reproducible on the apparatus described earlier (each flow condition was repeated at least 16 times). However, when an attempt was made to recreate the partially-wetted profile in a round tube on a flow loop where the air flow was provided by a compressed air supply (see Chapter 5 for a complete description of the facility), the flow could not be reproduced. A high-quality dryout condition was obtained, but at significantly higher vapor flow and significantly lower liquid flow than in the loop used for this work. When the same vacuum equipment was attached to the second loop, however, it was possible to recreate the reported flow configuration with ease.

It seems likely that this is due in part to the variation in density of the air in the test section. The average pressure in the test section when driven by compressed air for a certain flow condition corresponds to a density for air of about 1.3 kg/m^3. At the same mass flow being driven by the vacuum equipment, the corresponding density of air was about 1.0 kg/m^3, nearly a 30% change. This does not seem to fully explain why a similar dryout condition could not be obtained in the compressor-driven loop until the air flow reached over 3 times, and the water flow 1/5, the conditions for the vacuum driven loop, however.

It was also observed that the two-phase flow through the flexible vacuum tubing tended to cause noticeable fluctuations in the air flow drawn through the system.

Perhaps these additional fluctuations induce further instabilities in the annular flow through the test section, making the liquid film unstable at the same conditions where the compressor-driven system is stable.

2.5 References

T. Fukano, H. Akenaga, M. Ikeda, A. Itoh, T. Kuriwaki, and Y. Takamatsu. Liquid film flowing concurrently with air in horizontal duct (4th report, effect of the geometry of duct cross-section on liquid film flow). *Bulletin of JSME*, 27(230): 1644–1651, August 1984.

T. Fukano, H. Nakagawa, Y. Mori, and M. Watanabe. Liquid film formation on the inner surface of the horizontal channel. *Nuclear Engineering and Design*, 175: 3–13, 1997.

T. Fukano, T. Sakamoto, A. Tominaga, and E. Katoh. Experimental study on the flow mechanism of a thin liquid film flowing concurrently with a high speed gas flow in a horizontal rectangular duct. *Proceedings of the 1987 ASME-JSME Thermal Engineering Joint Conference*, 5:351–357, 1987.

R. J. Goldstein, M. Y. Jabbari, and J. P. Brekke. The near-corner mass transfer associated with turbulent flow in a square duct. *Wärme- und Stoffübertragung*, 27:265–272, 1992.

E. T. Hurlburt and T. A. Newell. Prediction of the circumferential film thickness distribution in horizontal annular gas-liquid flow. *Journal of Fluids Engineering – Transactions of the ASME*, 122:1–7, 2000.

C. W. Leung and S. D. Probert. Forced-convective turbulent-flows through horizontal ducts with isosceles-triangular internal cross-sections. *Applied Energy*, 57(1): 13–24, May 1997.

H. J. Leutheusser. Turbulent flow in rectangular ducts. *Journal of the Hydraulics Division, Proceedings of the ASCE*, HY3:1–19, 1963.

F. Mayinger and J. Klas. Compact heat exchangers. In *Heat Transfer; 3rd UK National Conference*, volume 1, pages 35–49. Institute of Chemical Engineers, Warwickshire, UK, 1992. Also incorporating the 1st European Conference on Thermal Sciences.

A. Melling and J. H. Whitelaw. Turbulent flow in a rectangular duct. *Journal of Fluid Mechanics*, 78(2):289–315, 1976.

T. A. Shedd. An automated optical liquid film thickness measurement method. Master's thesis, University of Illinois at Urbana-Champaign, Urbana, IL, 1998.

T. A. Shedd and T. A. Newell. Automated optical liquid film thickness measurement method. *Review of Scientific Instruments*, 69(12):4205–4213, December 1998.

L. Troniewski and R. Ulbrich. Flow regime maps and pressure drop in two-phase gas-liquid flow in a rectangular channel. In T. N. Veziroğlu and A. E. Bergles, editors, *Multi-Phase Flow and Heat Transfer III. Part A: Fundamentals*, pages 155–166. Elsevier Science Publishers B.V., Amsterdam, 1984.

R. L. Webb. *Principles of Enhanced Heat Transfer*. John Wiley & Sons, Inc., New York, 1990.

L. R. Williams. *Effect of Pipe Diameter on Horizontal Annular Two-Phase Flow*. PhD thesis, University of Illinois at Urbana-Champaign, Urbana, IL, 1989.

D. A. Yashar, M. J. Wilson, H. R. Kopke, D. M. Graham, J. C. Chato, and T. A. Newell. An investigation of refrigerant void fraction in horizontal, microfin tubes. *To be published in HVAC& R Research*, 2001.

D. C. Zietlow and C. O. Pedersen. Heat transfer and flow characteristics of condensing refrigerants in small-channel cross-flow heat exchangers. Technical Report TR-73, Air Conditioning and Refrigeration Center, University of Illinois at Urbana-Champaign, Urbana, IL, April 1995.

3

Characteristics of the liquid film, dryout and pressure drop in horizontal annular flow

3.1 Introduction

Understanding the thin liquid film that flows together with vapor in concurrent annular two-phase flow is of vital importance to the understanding and design of many common industrial and commercial systems. Key parameters are pressure drop, related to the energy required to drive the system, heat transfer efficiency, which dictates the size and design of heat exchangers, and the void fraction or hold-up, which determines the mass flows necessary to transfer a given amount of energy.

In this work, a large set of detailed liquid film thickness data for horizontal flow through tubes of round, square and triangular geometries is analyzed to determine fundamental properties of the film, particularly how they relate to heat transfer and pressure drop. Some important aspects of adiabatic dryout will be discussed and several pressure drop and interfacial shear correlations will be examined in light of the data. In addition, the applicability of vertical interfacial shear correlations to horizontal flow modeling will be addressed.

3.2 Experimental

The data used in this analysis were obtained on a horizontal air/water flow loop that has been described in detail elsewhere (Chapter 2). All pressure drops were

measured using U-tube water manometers. Vertical manometers could be read to a precision of 1 mm (9.8 Pa) at low liquid flow rates. At higher liquid flows, pressure fluctuations in the test section caused significant variation in the manometer levels. The resulting measurements were mentally "averaged" by the operator and recorded. For each test section, at least 16 pressure measurements were made and averaged together. The resulting averages had standard deviations ranging from 30 Pa to 160 Pa. In general, the error increased as mass quality decreased.

Local liquid film thicknesses were obtained using an optical measurement system described in Shedd [1998] and Shedd and Newell [1998]. The time averaged liquid film thicknesses presented here were measured to within ± 0.003 mm ($\pm$ one standard error). Briefly, a point light source is placed on a transparent test section wall which has a translucent, diffusing coating on it. The light travels through the wall and liquid layer, but when it reaches the vapor/liquid interface, any light arriving at an angle greater than or equal to the critical angle for the substances will be reflected back from the interface, creating a ring of light around the light source. The diameter of this light ring is directly proportional to the vertical distance traveled by the light. It is sampled at regular intervals and the mean liquid film thickness is determined from several hundred samples. If the surface is highly disturbed, the light will be significantly scattered and no measurement will be possible. Thus, due to the nature of the measurement system, the experimental results presented here exclude large liquid waves from the calculated average thickness; the thicknesses reported reflect only the thin base film that exists between the large liquid waves. This is an important consideration as several of the correlations for pressure drop and film distribution in the literature assume time averaged values obtained with electrical impedance methods which include the waves.

Five different tubes were used: 25.4 mm I.D. round (LR), 12.7 mm round (SR), 22.1 mm square (LS), 15.2 mm square (SS), 40 mm equilateral triangle. The square tubes were tested at 45 degree rotation as well to obtain the "diamond" sets, LD and SD. The triangle was examined with its apex upward (TU) and downward (TD).

Film thicknesses were measured at 16 equally spaced circumferential locations on the round tubes. Four equally spaced points were used on each of the four sides of the 15.2 mm square and 5 equally spaced points were used on each side of the 22.1 mm square. Four equally-spaced points were used on each side of the triangle. Thus, film thickness from 16 points for each flow condition comprise the LR, SR,

SS and SD data sets; 20 points the LS and LD sets; and 12 points the TU and TD sets.

Another useful quantity is the standard error of the individual light ring diameter measurements which are averaged together. The standard error not only indicates the expected range within which the actual measurement lies, but also gives an indication of the fluctuations of the liquid surface. Since large waves are excluded, the resulting standard errors are primarily due to the fluctuations on the surface of the base film in between the waves. The standard error will include the systematic measurement errors, electrical noise, etc., as well, but these contributions are small compared to the variations due to the liquid surface structure.

Because the system uses noise-averaged sampling (often referred to as dithering in the signal processing literature), the standard error is strongly influenced by the resolution of the imaging system used to capture the light ring. For example, if only one sample is taken, the error would be ±one pixel width. As more samples are averaged, however, for a signal with variations within a pixel width, the standard error will approach this mean variance within the pixel. Although a theory exists which could provide the means to calculate number of samples required to reach this limit [Vanderkooy and Lipshitz, 1989, 1984, Lipshitz et al., 1992], the effort was not undertaken to do so. Over 1000 samples were used in each average film thickness reported, and this is thought to be sufficient to render the resolution bias insignificant.

3.3 General characteristics of the liquid film

Figures 3.1 - 3.4 display the relationship between the non-dimensional film thickness, h^+, and the standard errors of the local film thickness measurements. The film thickness measurements are non-dimensionalized following a procedure commonly used with the perpendicular coordinate in wall-bounded turbulent shear flows:

$$h^+ = \frac{h u_i^*}{\nu_l}. \tag{3.1}$$

In this case, the friction velocity,

$$u_i^* = \sqrt{\frac{\tau_i}{\rho_l}}, \tag{3.2}$$

is based on the mean interfacial shear between the liquid and the vapor. Since the interfacial shear and the shear between the liquid and the wall must, on average, balance each other in a steady flow, τ_i is determined experimentally from the measured pressure drop by a force balance for flow through a round tube,

$$\tau_i = \frac{\Delta p}{L}\frac{D}{4}, \tag{3.3}$$

where L is the length between pressure taps and D is the diameter of the tube.

Looking first at Figure 3.1, several trends are evident. Clearly, standard error, or the amount of surface fluctuation, increases with film thickness, and in a fairly linear manner. The spread in the data points offers further insight when flow variables are taken into account.

Table 3.1 gives the vapor and liquid film Reynolds numbers for each of the flow conditions represented. The vapor Reynolds number, Re_{sg}, is based on the mean superficial gas velocity, U_{sg},

$$Re_{sg} = \frac{U_{sg} D_h}{\nu_g}, \tag{3.4}$$

where D_h is the hydraulic diameter. The liquid film Reynolds number is defined by

$$Re_{lf} = \frac{G_l D_h}{\mu_l} \tag{3.5}$$

$$= \frac{\dot{m}_l D_h}{A \mu_l}, \tag{3.6}$$

which, for a round tube, is

$$Re_{lf} = \frac{4\dot{m}_l}{\pi D_h \mu_l}.$$

(G_l is the liquid mass flux, or mass flow per unit area, and A is the tube cross sectional area.)

Referring again to Figure 3.1, with the aid of Table 3.1, dimensionless film thickness is found to increase with increased Re_{lf}, noting as well that in this case, $h^+ < 20$ for $Re_{lf} < 400$. Standard error tends to increase, for a given film thickness, with Re_{sg} and Re_{lf}, thus indicating that surface fluctuations increase with either increased vapor or liquid flow.

Now looking at the remaining plots and tables, it is apparent that very similar trends exist across the different geometries. $Re_{lf} = 400$ appears to be some sort of transition for these flows as h^+ remains below 20 in this regime. The vast majority of the h^+ data lies between 5 and 30. The LR-C and LR-D flows are

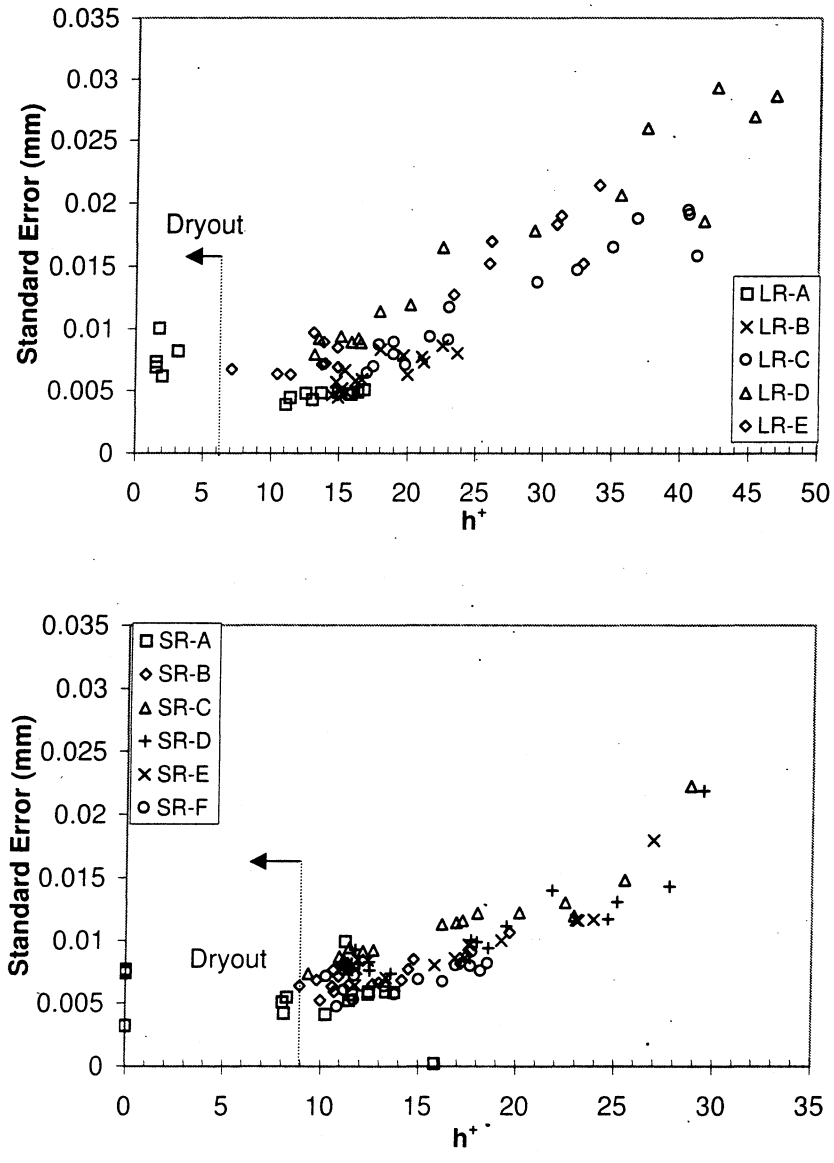

Figure 3.1: Standard error plotted against the non-dimensional film thickness measurements for the 25.4 mm and 12.7 mm round tubes.

Flow	Re_{sg}	Re_{lf}
LR-A	67000	240
LR-B	59000	690
LR-C	47000	1720
LR-D	38000	2510
LR-E	42000	1150
SR-A	28000	195
SR-B	24000	390
SR-C	20000	790
SR-D	17000	800
SR-E	18500	690
SR-F	20000	400

Table 3.1: Vapor and liquid film Reynolds numbers for the round tube flows.

Flow	Re_{sg}	Re_{lf}
LS-A	57000	210
LS-B	53000	390
LS-C	48000	780
LS-D	42500	1320
LS-E	33000	1660
LS-F	37500	760
LS-G	40000	330
SS-A	36500	180
SS-B	29500	550
SS-C	27000	730
SS-D	23000	1220
SS-E	21000	1220
SS-F	29000	730

Table 3.2: Vapor and liquid film Reynolds numbers for the square tube flows.

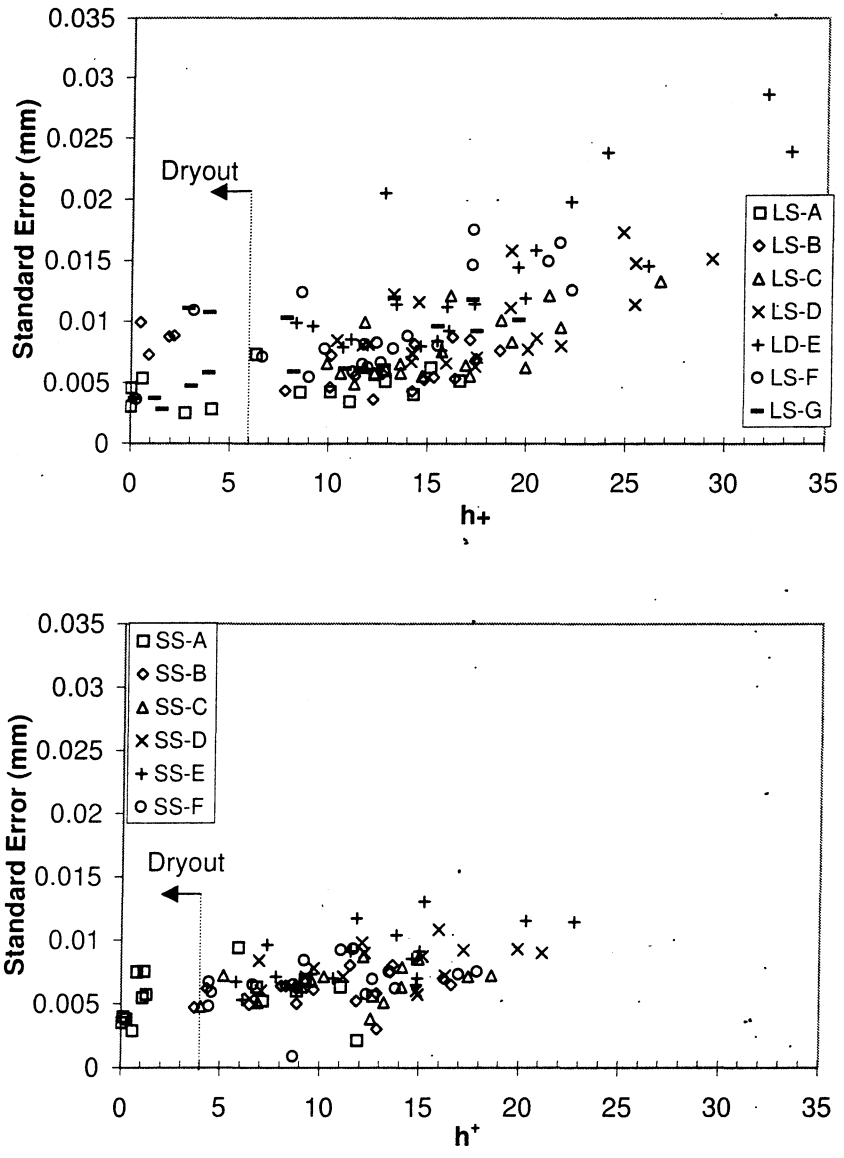

Figure 3.2: Standard error plotted against the non-dimensional film thickness measurements for the 22.1 mm and 15.2 mm square tubes.

Flow	Re_{sg}	Re_{lf}
LD-A	51500	240
LD-B	55500	370
LD-C	49000	820
LD-D	44000	1330
LD-E	37500	1480
LD-F	42000	580
LD-G	45000	270
SD-A	36500	190
SD-B	28500	580
SD-C	26500	770
SD-D	22500	1290
SD-E	20000	1290
SD-F	22500	770

Table 3.3: Vapor and liquid film Reynolds numbers for the diamond tube flows.

strong exceptions, from which it would appear that another transition may occur near $Re_{lf} = 1700$ with a new type of wave structure and thicker base films.

In general, smaller tube size appears to suppress wave activity. Higher standard errors are evident at lower h^+ in the square and diamond data compared to the round, with the diamond having the largest increase. One of the effects of geometry, then, may be an increase in wave activity, though not necessarily an increase in wave height. Thicker liquid films are allowed to form on the walls of the downward apex triangle (Cf. Chapter 2), and increased surface fluctuation compared with the upward apex configuration is evident.

3.4 Dryout

Dryout is a condition where the film on the wall breaks down. Prediction of dryout is important in situations where a heat flux is present and damage to the tube itself may occur if phase-change heat transfer ceases. This condition has been studied with respect to high heat flux and is frequently called "burnout" in the literature. Dryout is very significant to air conditioning and refrigeration applications as well, as overall heat transfer coefficients are significantly degraded when dryout occurs. Because of its importance in these heat transfer situations, the majority of the research in this area has been performed in the presence of relatively high applied

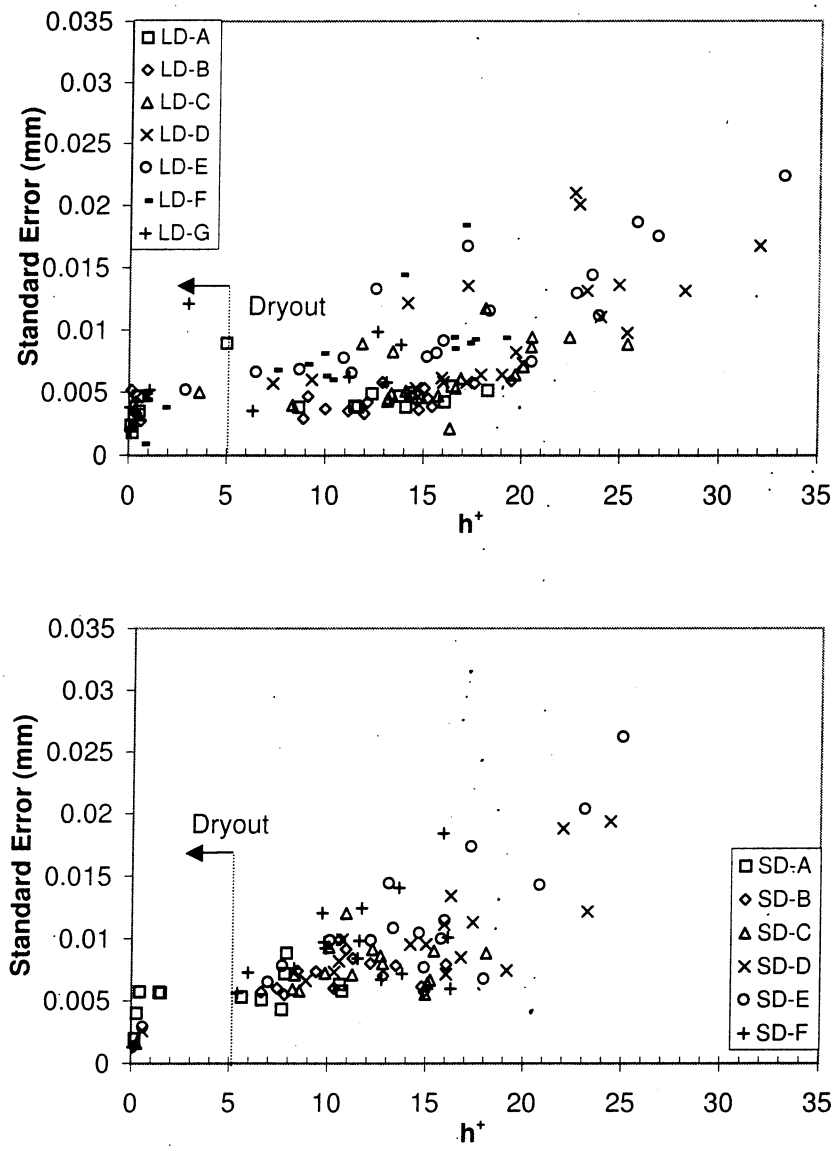

Figure 3.3: Standard error plotted against the non-dimensional film thickness measurements for the rotated 22.1 mm and 15.2 mm square (diamond) tubes.

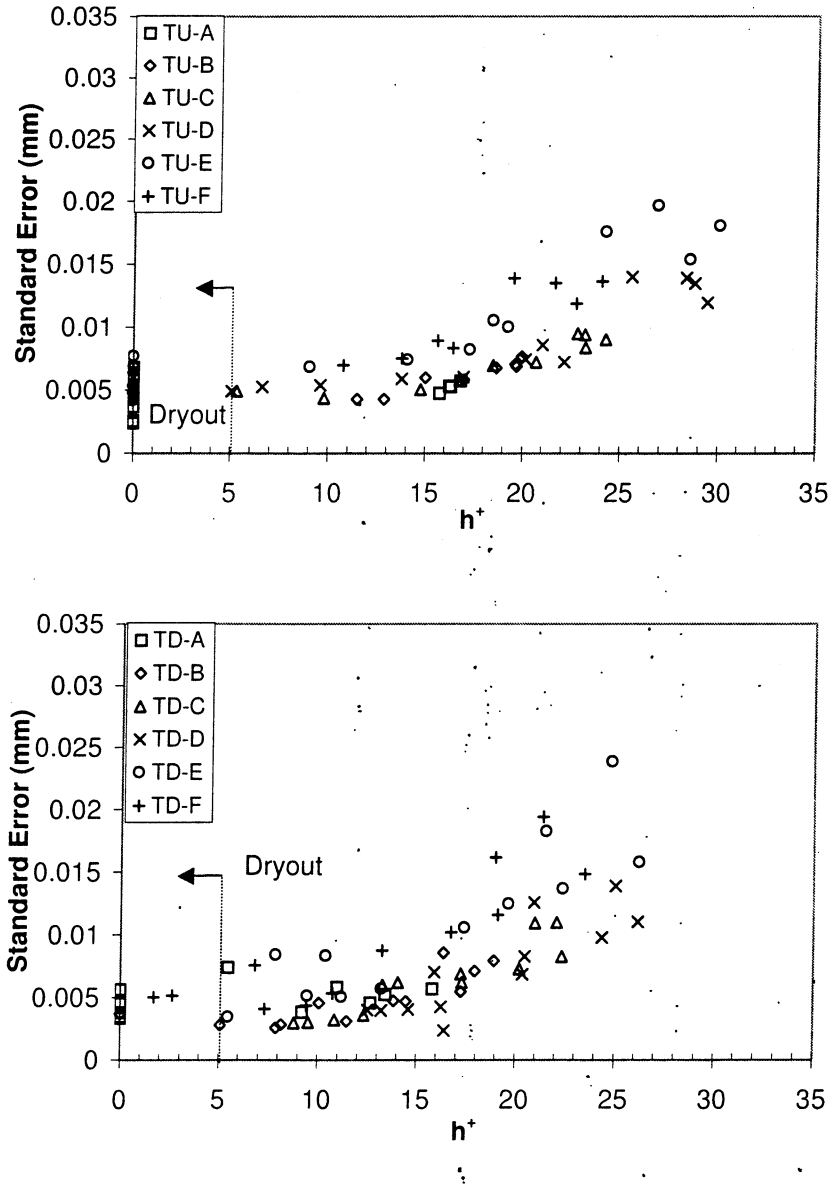

Figure 3.4: Standard error plotted against the non-dimensional film thickness measurements for the triangle tube in both the apex-up and apex-down orientations.

Flow	Re_{sg}	Re_{lf}
TD-A	45000	150
TD-B	42000	460
TD-C	40000	770
TD-D	37000	1150
TD-E	31000	1150
TD-F	33000	770
TU-A	46000	160
TU-B	42000	480
TU-C	39000	800
TU-D	37000	1200
TU-E	32000	1200
TU-F	34000	800

Table 3.4: Vapor and liquid film Reynolds numbers for the triangle tube flows.

heat flux. However, little has apparently been done to understand the adiabatic conditions under which dryout occurs in shear driven annular flow. This could provide insight into the influence of two-phase fluid dynamics on film continuity. Examples of some previous work includes Hartley and Murgatroyd [1964], Murgatroyd [1965] and Penn and Lopez de Bertodano [1998].

Each of the plots in Figures 3.1 - 3.4 is marked approximately where visual observation determined that dryout conditions existed for all thicknesses below that point. Any film thickness measurement reported was due to transient droplets or rivulets. Thus, $h^+ \approx 5$ appears to mark a limit below which the liquid film cannot be sustained. This agrees with the extensive data set compiled by Hewitt and Lacey [1965] who examined the minimum liquid flow required to re-wet an artificially-induced dry spot in annular vertical upflow. The limiting liquid thickness at this minimum flow lay consistently between $h^+ = 4.75$ and $h^+ = 6.5$.

Fukano et al. [1985] studied the flow of a liquid film through rectangular channels, with the primary focus on the dryout of the film flowing along the bottom of a channel. This is not a condition studied in the present work, but Fukano et al. went further and noted transitions from annular to separated flow in their experimental runs. They noted two different relations. First, when plotting their data as liquid Froude number ($Fr_l = U_{sl}/gD_h$) versus the Lockhart-Martinelli parameter, X_{tt}, they found the demarcation between the annular and separated flow regimes occurred at $Fr_l = X_{tt}$ when averaged values were used. A modified form applied

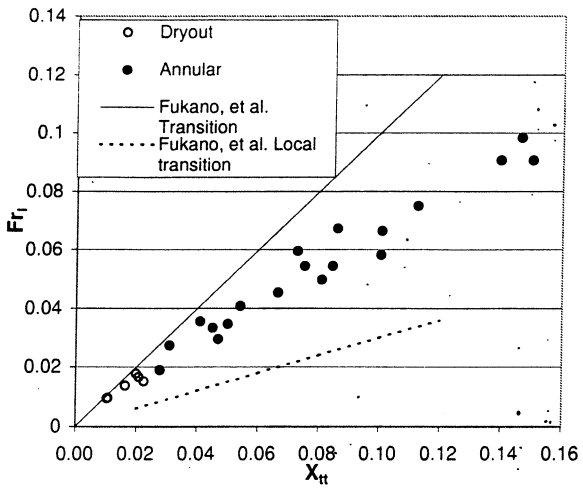

Figure 3.5: Current data plotted on a liquid Froude number versus Lockhart-Martinelli parameter flow map. Open symbols indicate dryout. Transition boundaries suggested by Fukano et al. are shown as well.

when "local" values were used, though this was not clearly defined. Data for the 22.1 mm and 15.2 mm square tubes from the current experiment is plotted in this manner, together with the Fukano et al. boundaries in Figure 3.5.

The present data are not well-represented on this plot compared with the Fukano et al. data. In their work, all of the annular flow data points fell to the left of the $Fr_l = X_{tt}$ line, but the opposite occurs in Figure 3.5. The "local" transition is marked on the plot as well, and the current data do fall to the left of this. Second, their separated flow data points fell solidly to the right of their annular flow points, clearly showing a transition in flow regimes. The present data, on the other hand, appears to continue along the same trend as it moves from the annular flow data into the dryout data.

In addition, Fukano et al. found that their data fit well onto a flow map with the superficial liquid and vapor velocities as the coordinates. The data for the large and small square tubes are plotted on this map, together with the transition between annular and separated flow specified by Fukano et al. in Figure 3.6. Again, it appears that the current data exhibit a different behavior where the annular flow transitions to dryout in a smooth manner, as if the data points from the runs with dryout are an extension of the annular flow regime. This seems quite plausible when the liquid film profiles for these flows are examined (see Chapter 2). It was

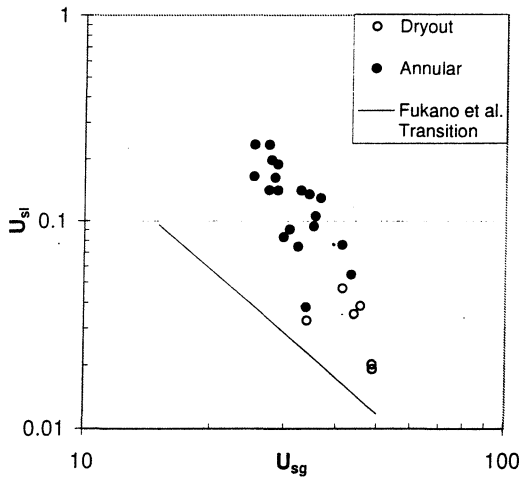

Figure 3.6: Current experimental data plotted on a superficial liquid velocity vs. superficial gas velocity flow map. Open symbols denote dryout. The transition line suggested by Fukano et al. is shown.

noted in Chapter 2 that the profiles of the film with dryout appeared to be those of a uniform annular flow where insufficient liquid was available to completely wet the tube walls.

3.5 Structure of the liquid film

In reviewing the data presented, it seems that perhaps the film flow follows the same general behavior as wall-bounded single-phase flow, i.e.

$$\begin{array}{rc} \text{viscous region:} & h^+ < 5 \\ \text{transition region:} & 5 < h^+ < 30 \\ \text{log region:} & h^+ > 30 \end{array}$$

From this experimental work, it appears that a continuous film can not be sustained in annular flow when it reaches a thickness where viscous forces dominate. The fact that the majority of the data tends to fall within $5 < h^+ < 30$ could be interpreted to mean that the liquid film in annular flow is comprised of a fluctuating base film, with properties similar to the buffer region in wall-bounded turbulent shear flow. Additional liquid beyond that needed to fill out this buffer layer then tends to go into highly turbulent waves which move over the base film.

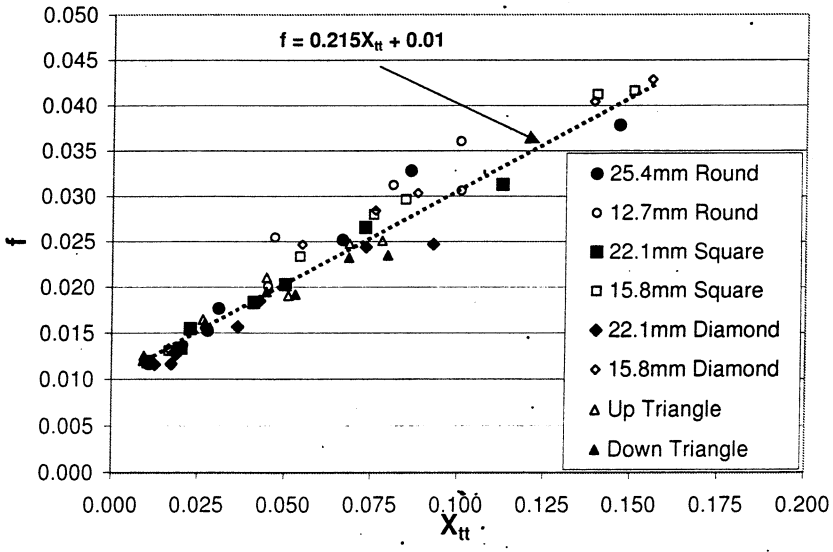

Figure 3.7: Friction factor versus the Lockhart-Martinelli parameter, X_{tt}, compiled from the two-phase pressure gradients measured for all of the geometries and flow conditions.

This turbulent wall-bounded profile is a popular assumption made in modeling the liquid film, but Dobran [1983, 1985] has shown that a model modifying this profile by reducing the turbulent mixing somewhat as the gas-liquid interface is approached gives much better agreement to physical behavior. This was noted independently by Leuthner et al. [1999] as well.

3.6 Pressure drop

As shown in Figure 3.7, the pressure drop data for all geometries are well correlated by the Lockhart-Martinelli parameter, X_{tt}, as defined by

$$X_{tt} = \left(\frac{1-x}{x}\right)^{0.9} \left(\frac{\rho_g}{\rho_l}\right)^{0.5} \left(\frac{\mu_l}{\mu_g}\right)^{0.1} \tag{3.7}$$

The friction factor was defined in the standard manner as

$$f = \frac{\Delta p}{(L/D_H)(\rho_g U_{sg}^2)/2} \tag{3.8}$$

where

$$U_{sg} = \frac{\dot{m}_g}{\rho_g A}$$

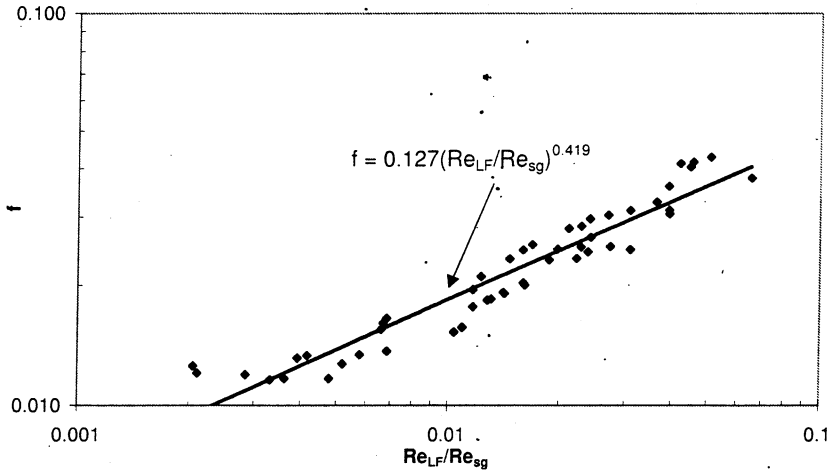

Figure 3.8: Friction factor versus the ratio of liquid film Reynolds number to vapor Reynolds number for all of the geometries and flow conditions.

is the superficial gas velocity (A is the cross-sectional area of the tube) and D_H is the hydraulic diameter, $4A/P$, (P is the tube perimeter). A modified definition of U_{sg} is used for the triangle tubes as discussed below.

Using this method with the current data set produces a simple correlation for two-phase friction factor for any of the three geometries and orientations tested:

$$f = 0.215X_{tt} + 0.01 \tag{3.9}$$

It is expected that this will work with any arbitrary orientation of the horizontal square and triangular tubes. However, caution should be used in applying this to flows with larger X_{tt} values or in rectangles with aspect ratios greater than 1. In addition, the validity of this correlation cannot be assured outside the quality range between 0.2 and 0.85. The dependence of the Lockhart-Martinelli parameter on mass quality limits its applicability at very low and very high quality conditions as well.

Henstock and Hanratty [1976] correlated interfacial drag with a term analogous to the Martinelli parameter,

$$F = g\left(\frac{Re_{LF}}{Re_g}\right)\frac{\nu_l}{\nu_g}\sqrt{\frac{\rho_l}{\rho_g}},$$

where $g()$ is a specified function. As seen in Figure 3.8, the ratio Re_{LF}/Re_g correlates the geometrical data well. Once simplified, this ratio is similar to the Martinelli

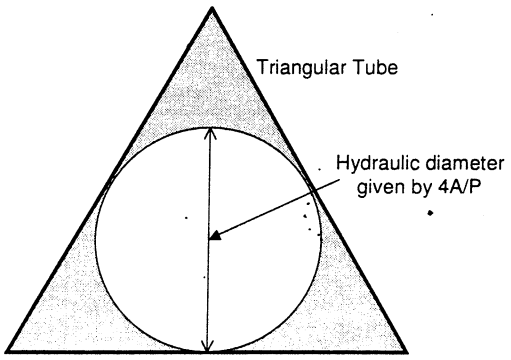

Figure 3.9: Sketch of the definition of the hydraulic diameter in a triangular tube.

parameter, X_{tt}, as given in Equation 3.7:

$$\begin{aligned} \frac{Re_{LF}}{Re_g} &= \frac{\dot{m}_g}{\dot{m}_l}\frac{\mu_l}{\mu_g} \\ &= \left(\frac{1-x}{x}\right)\frac{\mu_l}{\mu_g}. \end{aligned}$$

For this data set, X_{tt} predicts the friction factors somewhat better.

Many other two-phase pressure drop correlations exist in the literature, and it is not the intent here to review them. The reader is referred to Collier and Thome [1994] and Wilson [2001] for current, detailed reviews.

3.6.1 Pressure drop in triangular tubes

Correlating experimental pressure drop measurements of single phase turbulent flow through triangular pipes has confounded researchers for some time. (See, for example, Altemani and Sparrow [1980] and Obot and Adu-Wusu [1985].) The two-phase data obtained in this study was no different. Consistent with many previous investigations, use of the hydraulic diameter alone was found to over predict the triangular friction factors. However, in reviewing the works of Hanks and Brooks [1970] and Bandopadhayay and Hinwood [1973], among others, who investigated single-phase turbulence in triangular ducts, it was noted that extended regions where viscous effects become important exist near a corner, dampening turbulent fluctuations. The hydraulic diameter for a triangular duct specifies the largest circle which will fit in the triangle, as illustrated in Figure 3.9. Hence, if it is assumed that, at high Reynolds numbers, turbulent flow is somewhat restricted outside of this diameter, then the majority of the fluid mass can be thought of as flowing through

a round tube with the triangle's hydraulic diameter. Thus, the superficial velocity used in calculating the triangle's friction factor is defined as

$$U_{sg} = \frac{\dot{m}_g}{\rho_g A_{Dh}}, \tag{3.10}$$

where

$$A_{Dh} = \frac{\pi D_H^2}{4} \tag{3.11}$$

is the area of the circle defined by the hydraulic diameter. This has the effect of significantly increasing the gas velocity in the calculations for the triangular tubes, bringing these friction factors in line with the round tube data.

It appears, however, that the success of this correction is coincidental. This method tends to significantly under predict (give superficial velocities that are too high) for the single phase turbulent friction factor data of Eckert and Irvine [1960], Carlson and Irvine [1961], Aly et al. [1978] and Hurst and Rapley [1991] whose results include data from equilateral, scalene and isosceles triangles of varying apex angle. Thus, no extension can be made to the method's effectiveness in two-phase flow through triangular tubes in general.

3.6.2 Pressure drop in square tubes

Previous work related to pressure drop in square tubes includes that of Hosler [1968] who presented flow regime data for high-pressure steam-water flows in a vertical rectangular channel, as well as an excellent bibliography of earlier related work. No other studies in horizontal rectangular channels were cited in this research, however. Fukano et al. [1987] and Fukano et al. [1997] have studied two-phase stratified annular flow in square and rectangular channels, but their publications were concerned primarily with the gross behavior of the liquid film and did not report two-phase pressure gradient or detailed film distribution information.

One previous study performed in rectangular tubes (defined here as passages with length to width ratios between 1 and 3; greater ratios tend to be considered flat plate passages) was that of Troniewski and Ulbrich [1984a,b]. They provided some flow regime and pressure loss data for tubes with aspect ratios from 1 to 3 and found that a modified Lockhart-Martinelli method predicted pressure loss to within about 20% . Based on derivations of single phase laminar velocity profiles in rectangular tubes, they proposed a correction factor for the mean velocity related to the aspect

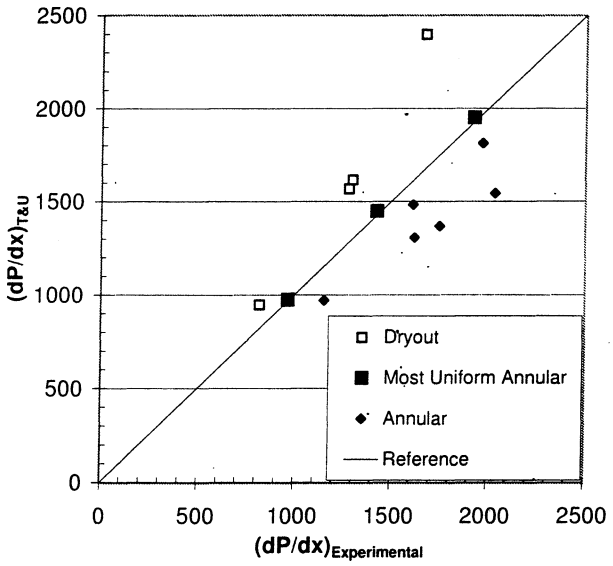

Figure 3.10: Comparison of predictions using the correlation of Troniewski and Ulbrich versus experimental data for the 25.4 mm and 12.7 mm square tubes.

ratio of the sides of the tube. Using this to calculate the liquid-only and vapor-only pressure drops from correlations for round tubes (even for turbulent flows), the two phase pressure drop was determined based on the calculated Lockhart-Martinelli parameter. A more general description of the use of the Lockhart-Martinelli method can be found in either Wallis [1969] or Collier and Thome [1994].

Troniewski and Ulbrich applied a formal analysis to the laminar velocity profiles of single phase flow through round and rectangular pipes, and determined that the ratio of the mean velocity in a rectangular duct to that in a round tube can be approximated by

$$\omega(k) = \left(\frac{k}{2}\right)^{0.16}$$

where k is the aspect ratio (height/width) of the rectangle. They recommend calculating two-phase pressure drops using a modified Lockhart-Martinelli correlation. The single-phase liquid-only friction factor is calculated based on the turbulent Blasius correlation but using a velocity adjusted by the round-to-rectangular velocity ratio,

$$U_{2p} = \frac{U_{sg}}{\omega(k)}.$$

A comparison of this correlation with the current experimental data for the 25.4

mm and 12.7 mm square tubes is shown in Figure 3.10. The correlation generally predicts within 25%, although it belies its derivation from vertical upflow data. As noted in the figure, the correlation is most accurate when the liquid film is most uniform as would be the general situation in vertical upflow. When dryout occurs, the correlation over predicts, while it under predicts in situations where the film is annular, but less uniform.

3.7 Interfacial shear correlations

A frequent practice in horizontal annular flow modeling is to apply a correlation developed for the average interfacial shear in vertical flow locally to each circumferential computational point. This assumption has been made without verification because, to this point, insufficient data had been obtained to test its validity.

As a starting point for developing interfacial shear predictions, several researchers have used the Wallis correlation, [Wallis, 1969]

$$\tau_i = \tau_s \left[1 + 300\left(\frac{h}{D}\right)\right], \tag{3.12}$$

where τ_s is the smooth tube friction factor given by the Blasius correlation,

$$\tau_s = 0.079 Re_{sg}^{-0.25}(1/2\rho_g U_{sg}^2), \tag{3.13}$$

h is the local film thickness and D is the tube diameter. When applied to the current set of round tube data, however, it over predicted the experimental results by 2 to 3 times. It is unclear why this should happen. The correlation is based on both vertical and horizontal annular flows and, according to Wallis, fits the data fairly well. Given the method of measuring h used in this experiment (electrical conductance probes), Equation 3.12 should tend to under predict the measured drag.

Hurlburt and Newell [2000] implemented a horizontal annular flow model which incorporated an interfacial shear correlation based on that developed for vertical upflow by Asali et al. [1985].

$$\tau_i = \tau_s \left[1 + 0.45 Re_{sg}^{-0.2}(\phi h^+ - 4)\right], \tag{3.14}$$

where

$$\phi = \frac{\mu_l}{\mu_g}\left(\frac{\rho_g}{\rho_l}\right)^{0.5}, \tag{3.15}$$

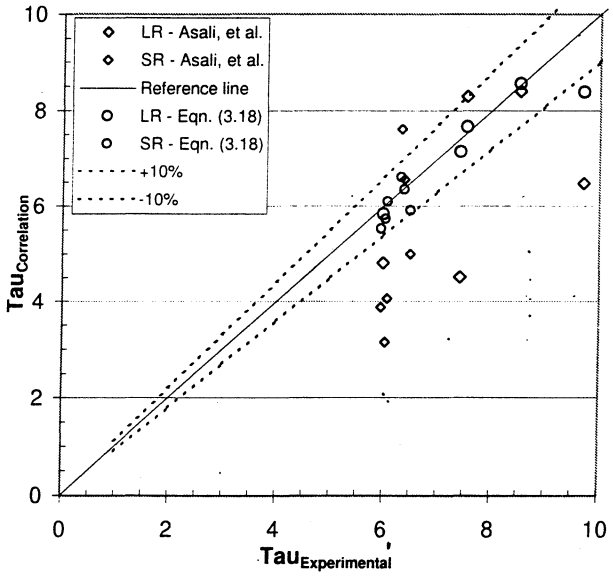

Figure 3.11: Comparison of shear stress values calculated using the correlation of Asali et al. as implemented by Hurlburt and Newell with experimental data. Also shown are the results of a modified form of the Asali et al. correlation.

h^+ and u^* are defined as given in Equations. 3.1 and 3.2, respectively, and

$$\tau_s = 0.046 Re_{sg}^{-0.2} (1/2 \rho_g U_{sg}^2). \tag{3.16}$$

To extend the application of this correlation to films outside the range used to develop Equation 3.14, Hurlburt and Newell approximated the interfacial shear with

$$\tau_i = \tau_s \left[1 + 10 \left(1 - \exp \left[-\frac{\phi h^+}{250} \right] \right) \right]. \tag{3.17}$$

The model of Asali et al. (Eqs. 3.14 - 3.16) was implemented and compared with the current experimental results for the round tubes. The correlation was applied locally to each of the 16 film thickness measurements. The average of these 16 values was compared to the experimental interfacial shear as shown in Figure 3.11. Equation 3.17 was also used, but the results were very similar and thus are not shown in the figure.

As can be seen, this correlation significantly under predicts the experimental results. This is to be expected, however. The Asali et al. correlation was developed based on film thickness measurements made using conductance methods, and thus incorporate large waves in the average of the film thickness measurements. As was

noted earlier, the optical method used in this work excludes the large waves so the resulting base film average thickness should be somewhat smaller. Hence, when the optically measured film thicknesses are used, the correlation should return smaller shear stresses. No clear explanation is apparent for the large scatter in the calculated results.

To compensate for the lack of wave information in the film thickness measurements, it is proposed that a modified form of the Asali et al. correlation be used. Beginning with Equation 3.14, replacing $0.45Re_{sg}^{-0.2}$ with τ_o gives

$$\tau_i = \tau_s \left[1 + \tau_o(\phi h^+ - 4)\right]. \tag{3.18}$$

Expressions for τ_o used for the best fit of the data are given in Table 3.5. Next, to include the full liquid flow in the film thickness used to calculate the shear, a local film Reynolds number, $Re_{lf,loc}$, is defined by

$$Re_{lf,loc} = \frac{h}{h_{avg}} Re_{lf},$$

where

$$Re_{lf} = \frac{4\dot{m}_l}{\pi D_h \mu_l},$$

for the round and square tubes, with D_h equal to hydraulic diameter, and

$$Re_{lf} = \frac{4\dot{m}_l}{3s\mu_l},$$

for the equilateral triangular tube, s being the length of a side. Thus, the local flow is adjusted for the change in film thickness at each measurement location and the entire mass flow of liquid is accounted for.

Asali et al. found that

$$h^+ = 0.19Re_{lf}^{0.7}$$

was an appropriate expression for the mean film thickness in vertical flow in the roll wave regime, or when $Re_{lf} > Re_{lf,crit}$. For smaller Re_{lf},

$$h^+ = 0.34Re_{lf}^{0.6}$$

was to be used. It is likely that a slightly more sophisticated model where the correct h^+ expression is chosen based on $Re_{lf,loc}$ might be more accurate, however, it appears that, in general, the expression recommended for the roll wave regime

Flow	τ_o	h^+
LR	$0.45Re_{sg}^{-0.25}$	$0.19Re_{lf,loc}^{0.7}$
SR	$0.45Re_{sg}^{-0.25}$	$0.19Re_{lf,loc}^{0.7}$
LS	$0.45Re_{sg}^{-0.25}$	$0.34Re_{lf,loc}^{0.6}$
SS	$0.45Re_{sg}^{-0.25}$	$0.19Re_{lf,loc}^{0.7}$
LD	$0.45Re_{sg}^{-0.25}$	$0.34Re_{lf,loc}^{0.6}$
SD	$0.45Re_{sg}^{-0.25}$	$0.19Re_{lf,loc}^{0.7}$
TU	$0.45Re_{sg}^{-0.18}$	$0.34Re_{lf,loc}^{0.6}$
TD	$0.45Re_{sg}^{-0.20}$	$0.34Re_{lf,loc}^{0.6}$

Table 3.5: Optimal expressions for predicting the experimental interfacial shear for all geometries investigated.

produced good predictions. It is not clear why the large square, large diamond and triangle flows were better correlated by the subcritical h^+, but this was true even though disturbance waves (roll waves) were present at all flows examined. The optimum expressions for h^+ and τ_o are summarized in Table 3.5.

When averaged interfacial shear stresses are calculated based on this model and the optimal expressions given in the table, the results agree with the experimental data within about 10%, as shown in Figure 3.12. The round and square tube predictions may be calculated using $h^+ = 0.19Re_{lf}^{0.7}$ for all the tubes, but this tends to over predict the large square (diamond) data by up to 15%. As was noted above when correlating the triangular tube friction factors with X_{tt}, flows in these tubes are apparently unique. Significant errors are incurred using expressions for τ_o other than those specified.

The success of the modified Asali et al. correlation is encouraging. This indicates that a correlation derived from vertical annular flow can be applied locally to the film in horizontal annular flow, though care must be taken in implementing any such model. In this case, the limits of applicability placed on the various terms used in the correlation appear to remain relevant to horizontal flow (i.e. transitions based on $Re_{lf,crit}$), and some minor modification of the correlation was necessary to achieve good agreement with the experimental data. It is recommended that a much larger set of data in round, square and equilateral triangles be analyzed before the modifications made here are assumed to apply generally in horizontal flow.

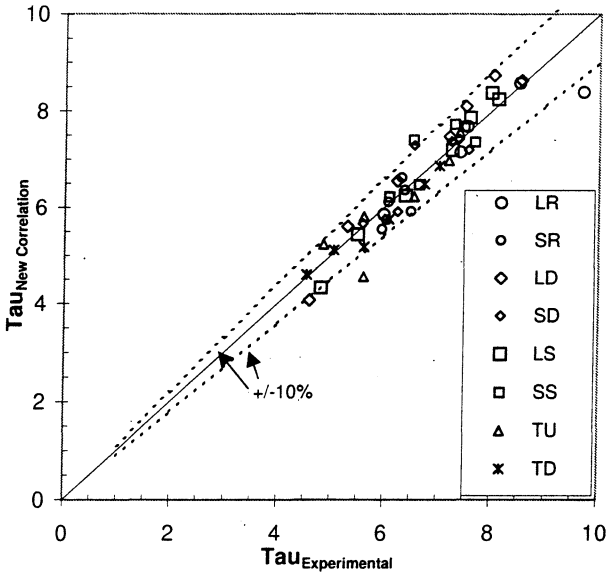

Figure 3.12: Comparison of shear stress values calculated using the modified correlation of Asali et al. with experimental data.

3.8 Conclusion

A large set of detailed film thickness data for horizontal annular flow through round, square and triangular tubes has been analyzed with the emphasis of understanding the basic film behavior and validating assumptions often made in modeling this system.

When film surface fluctuations, as indicated by the standard errors of film thickness measurements, are viewed with respect to non-dimensional film thickness, clear trends evolve. First, $h^+ \approx 5$ appears to be a limit below which a stable, continuous film can not be maintained. In addition, most of the data for the base film tends to fall within the range of $5 < h^+ < 30$. These two points together lend credence to the general assumption that the liquid film can be modeled using the methods of single-phase wall-bounded turbulent shear flows, for which $h^+ = 5$ is the approximate boundary between the viscous and buffer layers, and the buffer layer extends approximately from $h^+ = 5$ to $h^+ = 30$.

With respect to pressure drop, the present data for round, square and triangular tube was found to be well-correlated by

$$f = 0.215 X_{tt} + 0.01,$$

with appropriate modifications to the triangular data. Other correlations for averaged frictional drag in two-phase flow through round and rectangular tubes, usually generated from vertical flow data, were compared to the present data set and found to be consistently unable to predict the horizontal flow.

Significantly, a modified form of a vertical flow interfacial shear correlation was found to be valid for predicting the current pressure drop data in each of the geometries. This is important as it is a relatively common practice to apply the vertical flow correlations locally to horizontal flow without the ability to verify their appropriateness.

Issues still remain as to the applicability of these analyses to tubes of significantly larger or smaller diameters, rectangles of different aspect ratios and non-equilateral triangles. Further study is recommended before these results are extended to more general cases.

3.9 References

C. A. C. Altemani and E. M. Sparrow. Turbulent heat transfer and fluid flow in an unsymmetrically heated triangular duct. *Journal of Heat Transfer-Transactions of the ASME*, 120(4):590–596, November 1980.

A. M. M. Aly, A. C. Trupp, and A. D. Gerrard. Measurements and prediction of fully developed turbulent flow in an equilateral triangular duct. *Journal of Fluid Mechanics*, 85.1:57–83, March 1978.

J. C. Asali, T. J. Hanratty, and P. Andreussi. Interfacial drag and film height for vertical annular flow. *AIChE Journal*, 31(6):895–902, 1985.

P. C. Bandopadhayay and J. B. Hinwood. On the coexistence of laminar and turbulent flow in a narrow triangular duct. *Journal of Fluid Mechanics*, 59(4):775–783, August 1973.

L. W. Carlson and T. F. Irvine, Jr. Fully developed pressure drop in triangular shaped ducts. *Journal of Heat Transfer*, 83:441–444, November 1961. Paper No. 60-WA-100.

J. G. Collier and J. R. Thome. *Convective Boiling and Condensation.* Oxford University Press, Oxford, third edition, 1994.

F. Dobran. Hydrodynamic and heat transfer analysis of two-phase annular flow with a new liquid film model of turbulence. *International Journal of Heat and Mass Transfer*, 26(8):1159–1171, 1983.

F. Dobran. Heat transfer in an annular two-phase flow. *Journal of Heat Transfer – Transactions of the ASME*, 107:472–476, 1985.

E. R. G. Eckert and T. F. Irvine, Jr. Pressure drop and heat transfer in a duct with triangular cross section. *Journal of Heat Transfer, Transactions of the ASME*, 82: 125–138, May 1960.

T. Fukano, A. Itoh, and A. Ousaka. Breakdown of a liquid film flowing concurrently with gas in a horizontal line. *PCH: PhysicoChemical Hydrodynamics*, 6(1/2):23–47, 1985.

T. Fukano, H. Nakagawa, Y. Mori, and M. Watanabe. Liquid film formation on the inner surface of the horizontal channel. *Nuclear Engineering and Design*, 175: 3–13, 1997.

T. Fukano, T. Sakamoto, A. Tominaga, and E. Katoh. Experimental study on the flow mechanism of a thin liquid film flowing concurrently with a high speed gas flow in a horizontal rectangular duct. *Proceedings of the 1987 ASME-JSME Thermal Engineering Joint Conference*, 5:351–357, 1987.

R. W. Hanks and J. C. Brooks. Birefringent flow visualization of transitional flow phenomena in an isosceles triangular duct. *AICHE Journal*, 16(3):483–489, May 1970.

D. E. Hartley and W. Murgatroyd. Criteria for the break-up of thin liquid layers flowing isothermally over solid surfaces. *International Journal of Heat and Mass Transfer*, 7:1003–10015, 1964.

W. H. Henstock and T. J. Hanratty. The interfacial drag and the height of the wall layer in annular flows. *AIChE Journal*, 22(6):990–1000, 1976.

G. F. Hewitt and P. M. C. Lacey. The breakdown of the liquid film in annular two-phase flow. *International Journal of Heat and Mass Transfer*, 8:781 – 791, 1965.

E R Hosler. Flow patterns in high pressure two-phase (steam-water) flow with heat addition. *Chemical Engineering Progress Symposium Series; Heat Transfer–Seattle*, 64(82):54–66, 1968.

E. T. Hurlburt and T. A. Newell. Prediction of the circumferential film thickness distribution in horizontal annular gas-liquid flow. *Journal of Fluids Engineering – Transactions of the ASME*, 122:1–7, 2000.

S. K. Hurst and C. W. Rapley. Turbulent flow measurements in a 30/60 degree right triangular duct. *International Journal of Heat and Mass Transfer*, 34(3): 739–748, March 1991.

S. Leuthner, A. H. Maun, and H. Auracher. Influence of waves on heat transfer to falling films of a binary mixture. In G. P. Celata, P. Di Marco, and R. K. Shah, editors, *Two-Phase Flow Modelling and Experimentation 1999*, volume 2, pages 1241–1247, Rome, Italy, May 1999. Edizioni ETS, Pisa.

S. P. Lipshitz, R. A. Wannamaker, and J. Vaderkooy. Quantization and dither: A theoretical survey. *Journal of the Audio Engineering Society*, 40(5):355–375, May 1992.

W. Murgatroyd. The role of shear and form forces in the stability of a dry patch in two-phase film flow. *International Journal of Heat and Mass Transfer*, 8: 297–301, 1965.

N. T. Obot and K. Adu-Wusu. The flow pattern in a scalene triangular duct having two rounded corners. *Journal of Fluids Engineering – Transactions of the ASME*, 107(4):455–459, December 1985.

D. G. Penn and M. A. Lopez de Bertodano. Breakdown of the liquid film in annular flow: dry patch. *Transactions of the American Nuclear Society*, 79:354–356, 1998.

T. A. Shedd. An automated optical liquid film thickness measurement method. Master's thesis, University of Illinois at Urbana-Champaign, Urbana, IL, 1998.

T. A. Shedd and T. A. Newell. Automated optical liquid film thickness measurement method. *Review of Scientific Instruments*, 69(12):4205–4213, December 1998.

L. Troniewski and R. Ulbrich. Flow regime maps and pressure drop in two-phase gas-liquid flow in a rectangular channel. In T. N. Veziroğlu and A. E. Bergles, editors, *Multi-Phase Flow and Heat Transfer III. Part A: Fundamentals*, pages 155–166. Elsevier Science Publishers B.V., Amsterdam, 1984a.

L. Troniewski and R. Ulbrich. Two-phase gas-liquid flow in rectangular channels. *Chemical Engineering Science*, 39(4):751–765, 1984b.

J. Vanderkooy and S. P. Lipshitz. Resolution below the least significant bit in digital systems with dither. *Journal of the Audio Engineering Society*, 32(3):106–113, March 1984.

J. Vanderkooy and S. P. Lipshitz. Digital dither: Signal processing with resolution far below the least significant bit. *Proceedings of the AES 7th International Conference: Audio in Digital Times*, pages 87–96, May 1989.

G. B. Wallis. *One-dimensional Two-phase Flow*. McGraw-Hill, Inc., New York, 1969.

M. J. Wilson. *Two-phase flow through flattened tubes*. PhD thesis, University of Illinois at Urbana-Champaign, Urbana, IL, 2001.

4

Generation and influence of secondary vapor flow in horizontal annular flow

4.1 Introduction

Liquid/vapor two-phase flows exist in many common processes and domestic products. Some examples include air conditioning and refrigeration systems, both nuclear and conventional steam-driven power plants, and chemical processing systems. Patterns of flow which persist in most of these processes are stratified annular and annular distributions of the liquid phase, as shown in Figure 4.1.

In the stratified annular and annular flow regimes, turbulent vapor flows down the center of the pipe while a thin liquid film flows along the pipe wall. Prediction of

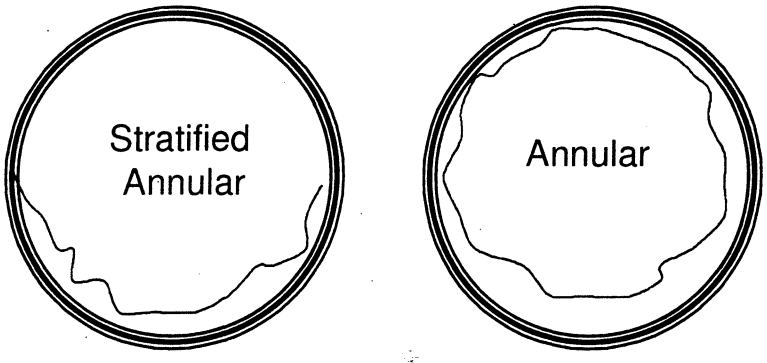

Figure 4.1: Typical distributions of gas and liquid phases in stratified annular and annular two-phase flow.

the distribution of this liquid layer is important for predictions of pressure drop, heat transfer, and, for refrigeration, the amount of refrigerant needed for a required heat load. After several decades of work, however, the prediction of film distribution is still an active field of research. Complicating the work are the complexities of the interactions between a turbulent vapor core and a turbulent liquid film, the added effect of gravity on flows in horizontal or angled pipes, the effects of heat and mass transfer occurring continually, and the behavior of different wave structures at the vapor-liquid interface.

If the pipe is horizontal, gravity will act on the film, causing an asymmetric distribution of liquid. Several researchers have observed that wave heights are proportional to the thickness of the liquid film, and have documented that waves on the bottom of a horizontal tube are larger than those on the top. This asymmetry in roughness in a round tube gives rise to secondary flows, flows normal to the axial direction, in the turbulent vapor core, as first shown by Darling and McManus [1968], and confirmed by Paras et al. [1998], Dykhno et al. [1994], Jayanti et al. [1990] and Flores et al. [1995]. In addition, it has been known at least since the work of Nikuradse [1930] that flows in non-round passages exhibit secondary flows, and significant efforts have been made to document and model these behaviors in single-phase flow.

Some controversy exists, however, on the role of secondary vapor flows in horizontal two-phase flow through round pipes. Laurinat et al. [1985], Lin et al. [1985] and Flores et al. [1995] consider secondary flows to be a significant factor in the development of their liquid film distribution models. On the other hand, Coney [1974], Butterworth [1974], Fisher and Pearce [1993], Fukano and Ousaka [1989], and Hurlburt and Newell [2000] all have developed models without direct consideration of secondary flow in the vapor. It is unclear from these works whether secondary flow plays any significant role in the liquid film distribution. In fact, Dykhno et al. [1994] found that, under certain flow conditions, there was evidence of secondary flows with movement opposite to that which is assumed in the former set of models.

This work will revisit the role of secondary flows in annular two-phase flow. First, a survey of experimental evidence of secondary flows in two-phase vapor-liquid annular flows will be presented. Next, the role of secondary flow in modeling will be discussed. A discussion of the mechanisms which generate secondary flows

follows with an extension of the concepts developed in single-phase flow to two-phase flows.

4.2 Secondary flows in two-phase annular flow: experimental evidence

Darling and McManus [1968] conducted an experiment using pipe with an eccentric thread, the thread being deeper on the bottom than the top, to simulate the conditions of a non-uniform liquid film. Hot-wire velocity data indicated an axial velocity profile skewed toward the bottom of the tube as well as the existence of secondary flow velocity vectors. These measurements further indicated that the secondary flow is of the form of two counter-rotating vortices, one in each vertical half, with flow down the center and up the walls.

Dykhno et al. [1994] took detailed velocity measurements in an air-water stratified annular flow. These also appear to imply, using Prandtl's interpretation of curved isotachs, that secondary flows exist in actual gas-liquid flows. However, the direction of the secondary motion varies with the atomization, or droplet entrainment, rate. At air velocities where very little entrainment occurs, the secondary flows were similar to those observed by Darling et al. However, at higher velocities, the secondary motions, again inferred from the curvature of isotachs, actually appeared to be turning the opposite direction, i.e. downward at the walls and upward at the center. The theory presented to explain this was that the downward secondary motion is established due to pressure gradients created by the cross-sectional variation in droplet concentration.

Figures 4 and 7 of Dykhno et al. [1994] are reproduced here as Figures 4.2 and 4.3 with a new interpretation of possible secondary motions in these flows. These new contours are based on the application of Prandtl's interpretation of the curvature of isotachs and the heuristic rule of Hinze that secondary flows will carry turbulence rich fluid out of regions of high turbulence generation as guides. These theories are discussed in greater detail below. Noting first that wave height is roughly proportional to film thickness, the area near the bottom of the tube will be a region of relatively high turbulence generation. Secondly, in each of these flows, the liquid never covers the entire tube. As is frequently observed, the liquid edge moves erratically along the wall as the liquid interacts with the vapor. From this observation

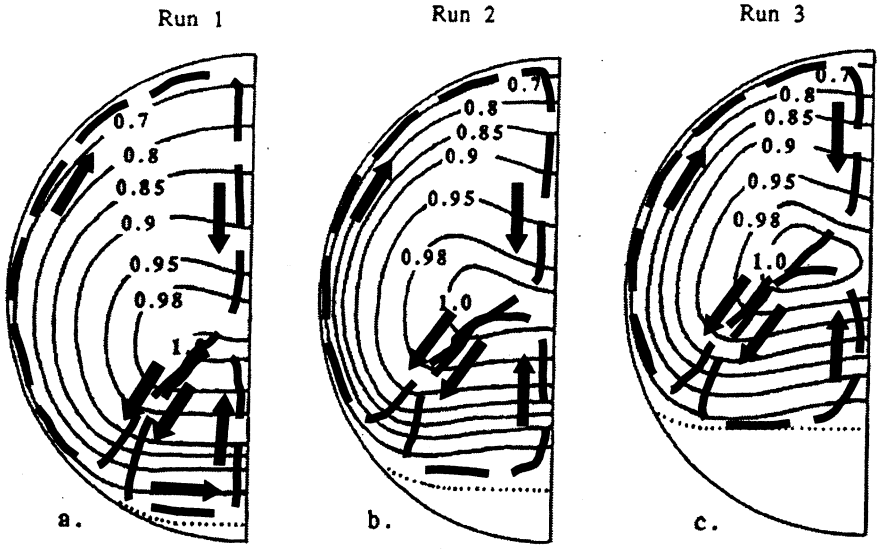

Figure 4.2: Isotach patterns in two-phase stratified-annular flow without droplet entrainment. Dashed secondary flow lines added based on assumptions described in the text. Taken from Dykhno et al. [1994].

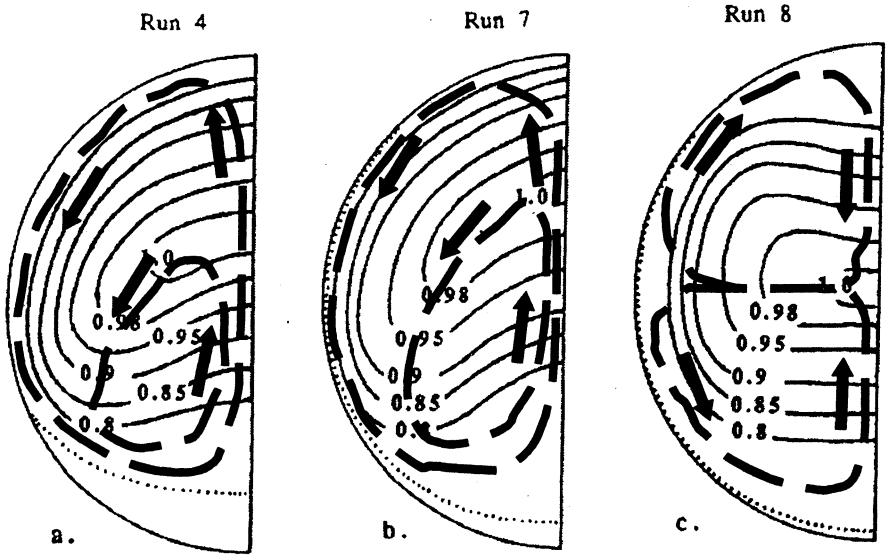

Figure 4.3: Isotach patterns in two-phase stratified-annular flow with droplet entrainment. Dashed secondary flow lines added based on assumptions described in the text. Taken from Dykhno et al. [1994].

it is assumed that the area near where the film no longer wets the wall will also be a region of relatively high turbulence generation. In addition, the stratified layer of liquid in Figure 4.2 creates a somewhat flat region with "corners". This geometry is known to generate secondary flow into the corner regions, as was discussed in the previous section, and is implied for round tubes with solid inserts by further measurements of Dykhno et al. The orientations of secondary flows shown in Figures 4.2 and 4.3 are one possible interpretation based on these observations.

Using Figure 4.3, a possible explanation of the secondary movement in flows with entrainment is that droplets are created from the tops of waves, the highest generation being at the thickest part of the film where the waves are largest. These droplets are initially carried upward by a flow from the higher to lower pressure regions (due to the droplet concentration gradient), but gravity pulls them down away from the center until they rejoin the liquid. This droplet flow does not preclude the existence of a vapor secondary flow in the opposite direction, but since a fairly high proportion of the momentum of the vapor is transferred by the droplets, the droplet flow dictates the shifts in velocities observed in the isotachs. Plot (c) of Figure 4.3 could possibly suggest this superposition of flows, or at least what appears to be a strong interaction between an upper vapor flow and a lower droplet-dominated flow. CFD modeling of annular flow with entrainment performed by Adechy and Issa [1999] produced secondary flow patterns similar to those shown in Figure 4.3a,b.

It should be noted that Azzopardi [1987] has observed no such spiraling motion of droplets, as has been hypothesized here, in an experiment using high-speed cine films. However, his study was apparently only able to track fairly large droplets, while the effects seen in the Dykhno et al. data may be generated by the large numbers of droplets less than 1 mm in diameter.

Perhaps the clearest confirmation of secondary flows in two-phase annular vapor-liquid flow in horizontal round tubes is in the work of Flores et al. [1995]. Two small paddle wheels were placed at the midline in the center of each vertical half of a 5.08 cm tube as shown in Figure 4.4. When air only flowed, the paddle wheels did not turn. However, when liquid flow was initiated, both wheels turned in a direction indicating secondary flow downwards at the center and upwards at the walls. Video measurements indicated that the velocity of the secondary flow was on the order of 2-4% of the axial flow, in accord with measurements in square and rough-

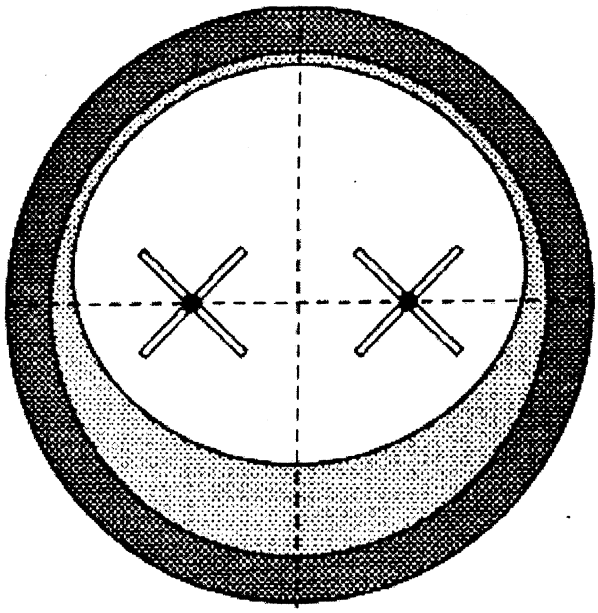

Figure 4.4: Vorticity meters used by Flores et al. to visually verify the existence of secondary flow in annular air-water flow. Taken from Flores et al. [1995].

ened round tubes in single phase flow. In addition, studies performed by the same authors in tubes where the lower half was roughened by varying amounts showed both that secondary flows may be initiated by asymmetric roughness and that these secondary velocities are proportional to the roughness.

Although Flores et al. did not present the exact flow conditions at which the observations were made, they indicated a maximum air velocity of about 21 m/s, which is below the velocity generally seen to initiate significant droplet generation. Thus, these observations do not contradict those of Dykhno et al. The fact that Flores et al. observed fully annular flow while Dykhno et al. only stratified flow is due to the large difference in tube diameters, 5.08 cm vs. 9.53 cm. Further studies of the type conducted by Flores et al. in larger tubes and higher velocities may be useful.

An additional experiment performed by Flores et al. used a solid, smooth cast of a previously measured liquid profile inside a round pipe. Secondary flows were seen to exist initially with this setup, but to die out with distance down the pipe. The flow condition modeled by the cast was created by air flows about three times the velocities used in the experiment described above. The cast was smooth, and as such secondary motion must have been initiated by geometrical effects alone. However,

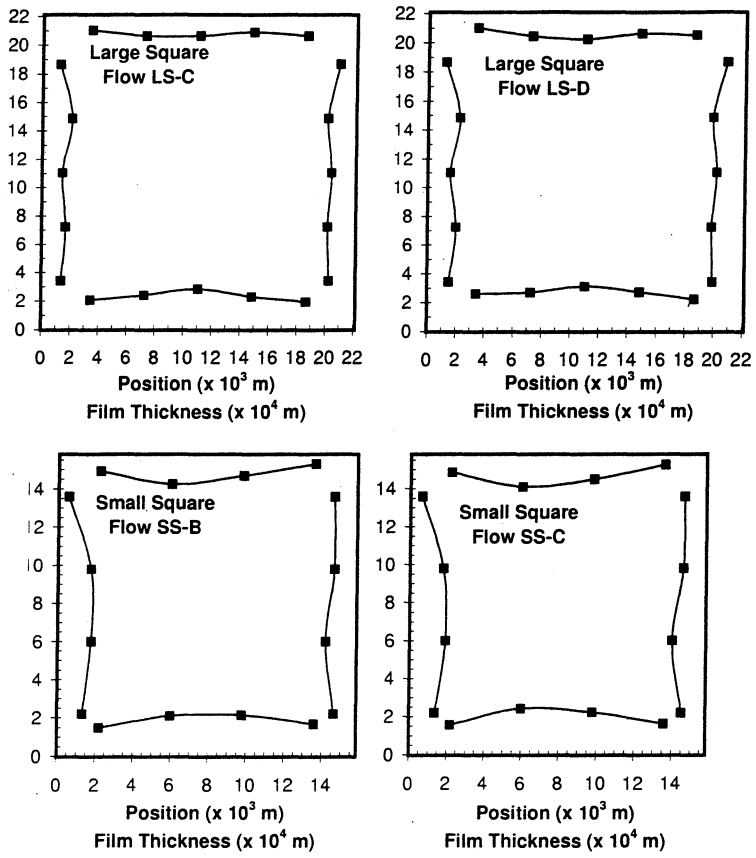

Figure 4.5: Film thickness profiles in a 22.1 mm and a 15.7 mm square tube for horizontal annular flow.

the cast does not present the gas flow with defined "corners" or regions that would force significant isotach distortion, so the turbulent stress gradients associated with secondary flows will be relatively weak. Hence, it seems that the Reynolds numbers of this experiment were not high enough to sustain the turbulent stresses necessary for secondary flow

The detailed liquid film thickness measurements (presented in Chapter 2) obtained for air/water flows in square and triangular tubes, appear to indicate that secondary flows may have a noticeable affect on the distribution of the liquid film. Figure 4.5 present two sets of this data. The liquid film profiles may be partially explained, not by shearing due to the secondary flow, as these velocities are quite small, but by the convection of mean axial momentum from the center of the pipes toward the corners and away from the centers of the sides. Interpretation of the interaction between the gas and liquid film along the vertical sides is complicated by

gravitational effects. The dips in the side profiles occur consistently in the data for the 22.1 mm pipe at different flow rates, but do not seem to exist in data taken for a smaller, 15.7 mm pipe. Mass transfer data for naphthalene in a turbulent air flow give similar profiles with slight thinning at the midline as well [Goldstein et al., 1992].

4.3 Secondary flows in two-phase annular flow: modeling

Pletcher and McManus [1965] appear to be the first to consider secondary flow effects on the distribution of the liquid film in horizontal two-phase annular flow. Based on earlier work showing that the axial velocity profile in a round tube could be skewed toward the bottom of the tube by a non-uniform film, Pletcher and McManus hypothesized that secondary flows could be present. They constructed a computer model assuming a laminar liquid film which demonstrates a clear, though small, redistribution of liquid from the bottom toward the top as the result of the secondary flow. The film thickness results obtained, however, were significantly in error when compared to the data available at the time of this work.

Many others have constructed two-phase annular flow models, but relatively few directly included the effects of secondary flows. Of fairly recent models that directly calculate the film thickness distribution, Laurinat et al. [1985] and Lin et al. [1985] explicitly included secondary flow effects. Flores et al. [1995] generated a model that depends almost exclusively on secondary flows, but they did not publish any calculated results or comparisons with experiments.

The model of Laurinat et al. incorporated droplet exchange, varying circumferential normal stress mechanisms, and a circumferential shear stress due to secondary flow based on the work of Darling et al. This shear is applied uniformly along the wall from the bottom to the top of the pipe, and it turns out to be quite small – about 0.01 N/m^2. A closely related model developed by Lin et al. incorporated only the droplet exchange and secondary flow mechanisms to distribute liquid to the top of the pipe. In this implementation, shear stresses due to secondary flows were more than an order of magnitude greater than those seen in Laurinat's model, though still quite small. Comparison with experimental film thickness measurements shows good agreement over a wide range of flows.

In contrast, Fukano and Ousaka [1989] and Hurlburt and Newell [2000] both generate predictions that compare well with experiment without explicitly including secondary flows. Fukano and Ousaka found that Laurinat's model failed to predict film distributions for flows in smaller pipes with lower vapor velocities, and concluded that secondary flow effects may be ignored. Hurlburt and Newell did not attempt to define the external physical mechanisms which maintain the film distribution, but rather focused on correctly modeling the stresses internal to the film. With this approach, they were able to model a wide range of flow conditions and working fluids while gaining insight as to the mechanisms which may contribute to the generation of internal film stresses. Their work did not seem to imply a circumferential shear due specifically to secondary flow.

Several difficulties exist in assuming that secondary flows generate significant circumferential interfacial shear. First, as has been noted several times, the absolute values of these stresses are quite small, on the order of a few percent of the mean axial shear, and can not, in themselves, support a liquid film of any significant thickness. Secondly, Jayanti et al. [1990] show computationally that the circumferential shear is not uniform, but varies with position along the wall. Further, they demonstrate that the magnitude of this shear is related to the circumferential gradient of the axial shear. Thus, the greatest circumferential shear stress occurs where the greatest circumferential variation in axial shear occurs. None of the aforementioned models take these effects into account. Finally, all of the circumferential shear stress models assume that this shear may be modeled as some percentage of the axial shear calculated from experimental correlations. There does not seem to be strong justification for this assumption, as the behavior and shape of the gas-liquid interface in the axial direction will surely be quite different than in the circumferential direction.

4.4 Generation of secondary flows

Secondary flows are essentially a mechanism originating in a flow to compensate for imbalances in local pressures or sheer stresses. For instance, secondary flow occurs in laminar flow through a bend in a circular pipe. The momentum of the fluid entering the bend tends to force it to the outside wall of the pipe, creating a higher pressure at the center of the outer wall and a lower pressure in the center of the inner wall. The mean flow momentum causes flow from the inner to the outer

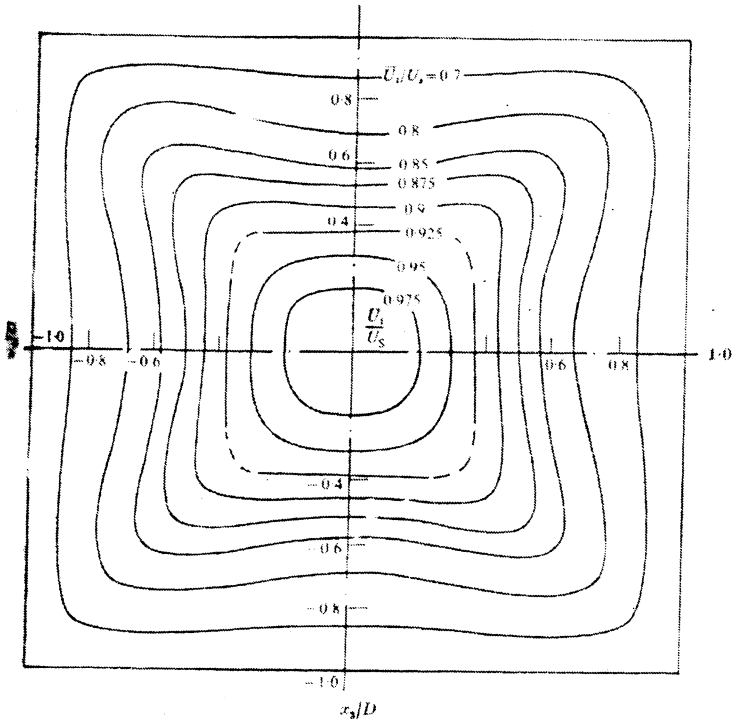

Figure 4.6: Axial velocity contours (isotachs) of turbulent fluid flow in a square duct. Taken from Melling and Whitelaw [1976].

walls along the centerline while the pressure gradient drives fluid along the top and bottom of the pipe from the outer wall to the inner, completing two semi-circular flow patterns. (See p. 84 of Vol. 1 of Goldstein [1938], for instance.)

In general, however, laminar flow through a straight closed passage of any geometry will not give rise to a secondary flow. In a square tube, for instance, frictional losses are greater in the corners of the tube than elsewhere, giving rise to a pressure imbalance. Viscosity resists non-axial motion, however, and no other driving force exists to sustain a secondary flow. In turbulent flow, on the other hand, it is possible for Reynolds' stresses to provide the energy necessary to sustain secondary motion, as is observed in turbulent flow in any non-circular geometry. Figure 4.6 shows typical contours of constant volicity in turbulent flow through a square duct.

A more precise picture of secondary flow mechanisms requires considerably greater sophistication, and is a topic of continuing research. The first detailed observations of turbulent secondary flow were made by Nikuradse and Prandtl. Nikuradse used both flow visualization with a dye and Pitot tube measurements to map

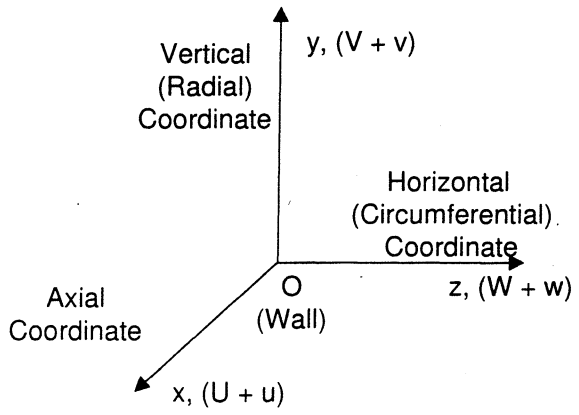

Figure 4.7: Primary coordinate system.

velocity contours [Nikuradse, 1930] while Prandtl was apparently the first to conclude that the shape of the measured axial velocity contours implied the existence of secondary motion [Prandtl, 1927]. Prandtl theorized that turbulent velocity fluctuations exist tangent to the curved contours of constant mean axial velocity (isotachs), and that these fluctuations are not only greater than the fluctuations in the axial direction, but that they increase with increased curvature of the isotachs. The resulting Reynolds' stresses, $\overline{u^2}$, $\overline{uw}$ and $\overline{w^2}$, will generate forces on the convex side of the isotachs, giving rise to the secondary flow. (Refer to Figure 4.7 for the definition of coordinate directions.) While this explanation is satisfactory to first order, Brundrett and Baines [1964] have pointed out easily reproducible flows in rectangular passages where the secondary flow does not correspond closely to the isotach curvature. Hinze has also reported that isotach curvature alone can be a misleading guide to secondary flows [Hinze, 1973]. In addition, Melling and Whitelaw [1976] present detailed data of air flow in a square duct and show that fluctuations in the axial direction are significantly greater than the transverse fluctuations.

Another approach to the source of secondary flows is the analysis of the vorticity in the flow. Speziale [1982] argues that streamwise vorticity is an indicator of secondary flow movement based on the definition

$$\int_A \omega_x dA = \oint_C \mathbf{U}_s \cdot d\mathbf{s} \tag{4.1}$$

where $\mathbf{U}_s$ is the velocity of the secondary flow along a differential length, $d\mathbf{s}$, of the

curve C. Following this line of argument, Speziale gives the criteria that secondary flow must occur whenever

$$\overline{v^2} - \overline{w^2} \neq 0. \tag{4.2}$$

While this appears to be true from experiment [Melling and Whitelaw, 1976], Gessner [1973] contends that this can not be used as an explanation for the initiation, or even the maintenance, of secondary flows due to the small values associated with the streamwise vorticity compared with ω_y and ω_z. For example, while $\omega_y \approx \frac{\partial U}{\partial z}$, $\omega_x \approx 0.05Uh$, where h is the length of one side of a square duct. U changes quickly with z, and this gradient will most certainly be much larger than $0.05U$. Hinze has experimentally confirmed the smallness of the difference in (4.2) relative to other terms in the equations of flow [Hinze, 1973].

In an effort to identify the behaviors in the flow that are able to initiate and sustain secondary motion, Hinze [1973] begins with the equation of turbulent kinetic energy, given here in its general form for steady flow, [Hinze, 1975]

$$\begin{array}{ccccc} \frac{U_j}{2}\frac{\partial \overline{u_i u_i}}{\partial x_j} & + & \frac{\partial}{\partial x_i}\overline{u_i\left(\frac{p}{\rho}+\frac{1}{2}u_j u_j\right)} & = & (-\overline{u_i u_j})\frac{\partial U_j}{\partial x_i} \\ I & & II & & III \\ & + & \nu\frac{\partial}{\partial x_i}\overline{u_j\left(\frac{\partial u_i}{\partial x_j}+\frac{\partial u_j}{\partial x_i}\right)} & - & \nu\overline{\left(\frac{\partial u_i}{\partial x_j}+\frac{\partial u_j}{\partial x_i}\right)\frac{\partial u_j}{\partial x_i}} \\ & & IV & & V \end{array} \tag{4.3}$$

where capital letters (U_j) represent mean values and lower case variables (u_i and p) represent fluctuating values. Term (I) gives the rate at which turbulent kinetic energy is convected by the mean motion. Term (II) represents the rate of work done by the total turbulent dynamic pressure. Term (III) is the rate at which the turbulent stresses perform work of deformation on the mean motion, while (IV) gives the rate of work done by the viscous shear stresses and (V) is the viscous dissipation of the turbulent motion. All terms are per unit mass.

Hinze expands Equation (4.3) for the flow normal to, and in the center of, the bottom wall of a rectangular duct. For this case, it is assumed that derivatives with respect to z (the direction parallel to the bottom wall and transverse to the flow) are small and that $W \approx 0$ due to symmetry. Away from the wall, turbulent diffusion terms are small and it is assumed that $\overline{v^2} \approx \overline{w^2}$. Further, if second derivatives of turbulent kinetic energy are small, (4.3) reduces to

$$V\frac{\partial}{\partial y}\frac{\overline{u_i u_i}}{2} \approx -\overline{uv}\frac{\partial U}{\partial y} - \nu\overline{\left(\frac{\partial u_j}{\partial x_i}\right)^2}, \tag{4.4}$$

which may be interpreted as,

convection of turbulent energy $\approx$ *production - dissipation.*

Thus, he states that in any region where production is much greater than viscous dissipation of turbulent kinetic energy, turbulence-poor fluid must be convected toward that region by a secondary flow. This interpretation is quite broad and may be applied not only to flows in tubes with corners, but to flows in roughened round tubes, open channels or over flat plates. Hinze supports the assumptions made above with experimental data.

Darling and McManus [1968] infer from the data they obtained in a roughened round tube that it is the gradients of turbulent Reynolds stresses that drive secondary motion. Gessner [1973] analyzes the turbulent flow along a corner to show this is true. He begins with the equation of mean flow kinetic energy, [Hinze, 1975]

$$\begin{array}{ccccccc} \frac{\partial}{\partial x_i}U_i\left(\frac{P}{\rho}+\frac{1}{2}U_jU_j\right) & = & -(-\overline{u_iu_j})\frac{\partial U_i}{\partial x_j} & + & \frac{\partial}{\partial x_j}(-\overline{u_iu_j}U_i) & & \\ I & & II & & III & & \\ & + & \nu\frac{\partial}{\partial x_i}U_j\left(\frac{\partial U_i}{\partial x_j}+\frac{\partial U_j}{\partial x_i}\right) & - & \nu\left(\frac{\partial U_i}{\partial x_j}+\frac{\partial U_j}{\partial x_i}\right)\frac{\partial U_i}{\partial x_j} & & \\ & & IV & & V & & \end{array} \tag{4.5}$$

where capital letters (U_i and P) represent mean values and lower case variables (u_i) represent fluctuating values. Term I signifies the rate of work done by the total dynamic pressure. Term II represents the rate of work of deformation by the turbulence stresses. Term III is the rate of flow work done by the turbulence stresses. Term IV gives the rate of work done by the viscous stresses and Term V is the dissipation rate. All terms are per unit mass.

Using axes oriented along, and orthogonal to, the corner bisector (as shown in Figure 4.8), and employing the boundary layer approximations, Gessner simplifies (4.5) to

$$\begin{array}{ccccccc} \frac{U}{\rho}\frac{\partial P_0}{\partial x} & + & \frac{V}{\rho}\frac{\partial P_0}{\partial y} & = & (\overline{uv})\frac{\partial U}{\partial y} & & \\ IA & & IB & & II & & \\ & & & - & \frac{\partial}{\partial y}(U\overline{uv}) & - & \frac{\partial}{\partial z}(U\overline{uw}) \\ & & & & IIIA & & IIIB \\ & & & + & \nu\left[\frac{\partial}{\partial y}\left(U\frac{\partial U}{\partial y}\right)\right. & + & \left.\frac{\partial}{\partial z}\left(U\frac{\partial U}{\partial z}\right)\right] \\ & & & & IVA & & IVB \\ & & & - & \nu\left(\frac{\partial U}{\partial y}\right)^2, & & \\ & & & & V & & \end{array} \tag{4.6}$$

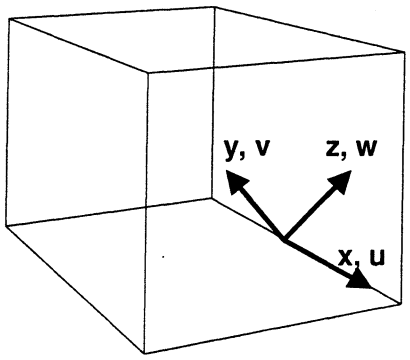

Figure 4.8: Diagram of coordinate system oriented along the corner bisector used to simplify the analysis of secondary flow into the corner.

where

$$P_0 \equiv p + \frac{1}{2}\rho(U^2 + V^2 + W^2),$$

and the y-axis follows the diagonal bisector with its origin at the corner.

(IA) and (IB) in (4.5) represent the convective transport of mean flow energy into the corner bisector by the primary and secondary flows, respectively. Terms (III) give the work done by the mean flow against the gradients in turbulent shear stresses, while (IV) applies analogously to the viscous shear stresses. Production of turbulent energy from the mean flow is represented by (II) and viscous dissipation by (V).

To determine which of the terms in Equation (4.6) are most likely to effect secondary motions, note that all of the terms but (IB), $(IIIB)$ and (IVB) would be present in two-dimensional flow. Since secondary motions can not exist in two-dimensional flow, the B terms alone must be of interest in this case. Note also that (IVB) will be significant only in the near vicinity of the wall where viscous effects are dominant, and thus could not help maintain secondary flow in the body of the flow. Hence, it is possible to interpret Equation (4.6) as providing the following balance for secondary flow into a corner as,

$$\frac{V}{\rho}\frac{\partial P_0}{\partial y} \approx -\frac{\partial}{\partial z}(U\overline{uw}), \tag{4.7}$$

or

convection of mean flow energy	$\approx$	*working of mean flow against transverse Reynolds stress gradients.*

Gessner provides experimental evidence that these terms do indeed dominate for flow along a corner. Similar analysis shows that a flow away from the wall at the wall bisector will result from the balance of the convection of mean flow energy and the gradients of turbulent Reynolds stresses as well. In fact, this analysis, though using the mean flow kinetic energy rather than the turbulent kinetic energy, arrives at a conclusion similar to Hinze's, outlined above. This is expected, as Hinze examined the cause of flow at the wall bisector.

Experimentally, the data of both Hinze and Gessner indicate that the secondary convective flow away from the wall along the center line is significantly smaller than the flow into the corner. In addition, the data support Gessner's assertion that the convection of turbulent kinetic energy is small compared with the convection of mean flow energy, and thus is considered a second order effect and not one of the prime drivers of secondary flow.

4.5 Generation of secondary flows in round tubes

From this work, it appears that the terms containing the gradients of the turbulent shear stresses are the primary factors in the creation and maintenance of secondary flow. Now these concepts will be generalized to any turbulent flow system with curved isotachs.

Consider terms III from the mean flow kinetic energy equation derived by Gessner, Equation (4.6),

$$\frac{\partial}{\partial y}(-U\overline{uv}) + \frac{\partial}{\partial z}(-U\overline{uw}), \tag{4.8}$$

which can be rewritten as

$$\underset{IA}{-\left(U\tfrac{\partial}{\partial y}\overline{uv}\right)} \quad \underset{IB}{+\left(\overline{uv}\tfrac{\partial U}{\partial y}\right)} \quad \underset{IIA}{-\left(U\tfrac{\partial}{\partial z}\overline{uw}\right)} \quad \underset{IIB}{+\left(\overline{uw}\tfrac{\partial U}{\partial z}\right)}. \tag{4.9}$$

The (B) terms represent turbulence production. Away from the wall, these terms tend to be rather small because the gradient of mean axial velocity becomes relatively small. Each of the (A) terms provides an indication of how much of the mean flow energy is removed from, or accumulated at, a given point in the flow through the action of Reynolds stresses. These terms are directly related to the curvature and spacing of the axial flow isotachs and can be quite significant throughout the flow field. This can be seen qualitatively through the following examples.

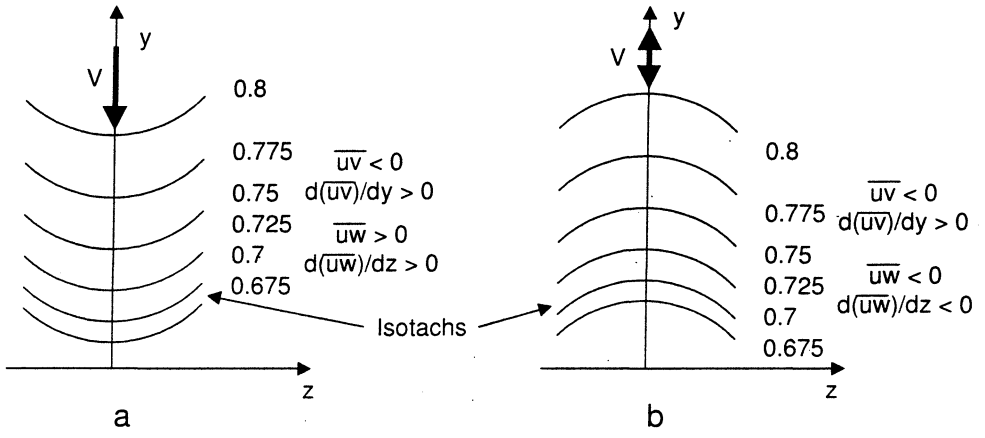

Figure 4.9: Examples of isotach configurations presenting different Reynolds' stress gradients.

1. First, consider flow along a line through convex, progressively separated isotachs. From Figure 4.9a, it can be determined that $\overline{uv}$ is negative using reasoning similar to that used in turbulent boundary layers: A positive fluctuation in v will tend to produce a negative fluctuation in u. Because the spacing between isotachs increases with y, a fluctuation in v at large y will tend to produce a less negative fluctuation in u than that at small y, so $\partial\overline{uv}/\partial y$ is positive. Since both $\overline{uv}$ and $\partial U/\partial y$ are relatively small,

$$\frac{\partial}{\partial y}(U\overline{uv}) \approx U\frac{\partial \overline{uv}}{\partial y},$$

this term represents a loss of flow energy along the y-axis due to the work expended to overcome the transfer of axial momentum in the negative y direction.

In the z-direction, a positive w fluctuation will tend to produce a positive u fluctuation, implying that $\overline{uw}$ is positive. Since the isotachs have an upward curvature and are progressively further apart with increasing y, a fluctuation in w near $z = 0$ will tend to induce a smaller u fluctuation than it would at larger z; $\partial\overline{uw}/\partial z$ must be positive. Near $z = 0$, $\partial U/\partial z \approx 0$, so

$$\frac{\partial}{\partial z}(U\overline{uw}) \approx U\frac{\partial \overline{uw}}{\partial z},$$

and this gradient indicates a loss of flow energy along the y-axis due to the

work needed to counteract the transfer of axial momentum away from the y-axis in the positive z direction by $\overline{uw}$.

Referring to Equation (4.9), both terms (I) and (II) are positive, giving a negative sum which must be balanced on the right side of Equation (4.6) by a mean velocity V in the negative y direction.

2. Now consider the flow along a line through a series of concave, progressively separated isotachs as shown in Figure 4.9b. Along the y-axis, the same discussion applies for the $\overline{uv}$ stresses as above. Note that a fluctuation of w in the positive z direction will tend to produce a negative fluctuation of u, and thus $\overline{uw}$ is negative. The concave curvature and varied spacing of the isotachs dictate that a fluctuation in w close to the axis will produce a less negative fluctuation in u than the same movement at more positive z; thus, $\partial\overline{uw}/\partial z$ is less than zero. Now, since

$$\frac{\partial}{\partial z}(U\overline{uw}) \approx U\frac{\partial\overline{uw}}{\partial z},$$

the gradient of $\overline{uw}$ indicates an accumulation of mean flow energy along the y-axis; i.e. mean flow energy is expended to transfer momentum toward the y-axis since $\overline{uw} < 0$.

Again referring back to (4.9), term (I) is now negative while (II) is positive. A secondary flow, if any exists, will be determined by the relative strengths of these two terms. At the wall bisector in a square or rectangle, (II) dominates, requiring velocity V to flow from the wall to the center. This flow is likely to be less than flow into a corner because of the competing stress gradients.

It is now possible to explain the origin of secondary flows in turbulent flow with some confidence. In passageways with corners, laser-Doppler anemometry data indicate that developing single-phase flow contains significant Reynolds shear stress gradients of the type in Equation (4.9) [Melling and Whitelaw, 1976]. DNS simulations of square-duct flow by Huser and Biringen [1993] indicate mushroom-like eruptions of turbulence from the walls which may contribute to the development of these stress gradients.

The origins of secondary flows in round tubes are not so obvious and, to the author's knowledge, have not been previously explained. Numerous experiments

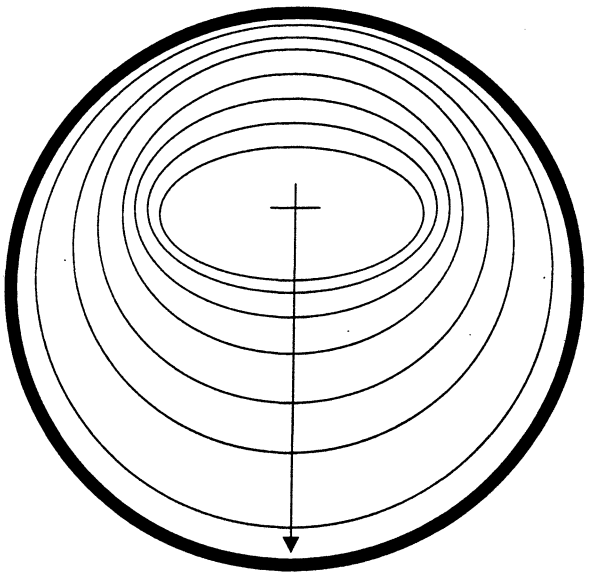

Figure 4.10: Examples of isotach configuration for developing turbulent flow in a round pipe with circumferentially varying roughness. This idealization assumes the bottom of the pipe is roughest.

have shown that uniformly smooth or rough tubes have symmetrical velocity profiles with the peak velocity in the center. However, if the tube is non-uniformly rough, as has been shown to be the case for annular air-water flow [Paras and Karabelas, 1991], limited experimental evidence shows that the location of the peak velocity will move away from the rough side toward the smoother side [Hanratty and Engen, 1957, Darling and McManus, 1968, Fukano et al., 1987]. This will produce a set of mean axial velocity contours idealized in Figure 4.10. From this representation, it is apparent that along the vertical axis of the pipe, a situation exists analogous to that in Figure 4.9b, described above. Gradients are created in the $\overline{uw}$ Reynolds stresses which may initiate a secondary flow from the center of the pipe to the bottom. This secondary current will begin to convect axial momentum downward. Once the flow develops, the location of the peak velocity is lowered below the horizontal axis [Dykhno et al., 1994, Darling and McManus, 1968, Jayanti et al., 1990, Paras et al., 1998].

Jayanti et al. [1990] have performed computer simulations of single-phase flow in pipes with circumferentially varied roughness. The resulting velocity contours and secondary flow vectors are shown in Figures 4.11 and Figure 4.12. Qualitative

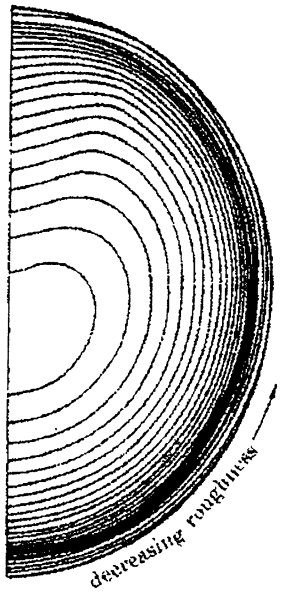

Figure 4.11: Velocity contours computed by Jayanti et al., in a round pipe with asymmetrical roughness. Taken from Jayanti et al. [1990].

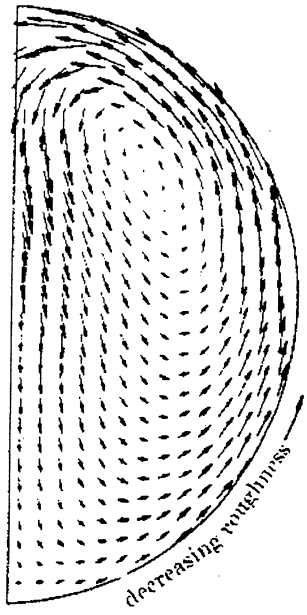

Figure 4.12: Secondary flow vectors for turbulent flow in a round pipe with asymmetrical wall roughness as computed by Jayanti et al. Taken from Jayanti et al. [1990].

analysis of the isotachs from this computational study, using the methods described in Example 2 above, can explain the relative velocities within the secondary flow along the vertical axis, further validating this theory and its application to turbulent secondary flows in pipes of arbitrary shape and roughness.

Finally, it should be noted that Prandtl's assertion that gradients in the transverse turbulent fluctuations normal to isotach curvature are the driving force of secondary flows has essentially been validated. When velocity gradients along the isotach normals are taken into account, Prandtl's correlations between isotach curvature and secondary movement tend to give good first-order approximations.

4.6 Conclusion

The role of gradients in tangential Reynolds shear stresses in the initiation and maintenance of secondary flow has been demonstrated. This theory has been applied to single-phase flow in asymmetrically roughened round pipes as well as ducts with corners by many investigators. In this work, it has been shown how these stresses may lead to the development of secondary flow in horizontal round tubes with gas and liquid flowing concurrently.

A survey of experimental evidence for the existence of secondary flows in two-phase flow through pipes of different shapes has been presented. Secondary motion in the vapor has been clearly demonstrated for horizontal two-phase flow in round pipes. However, its direct effect on the distribution of the liquid phase is uncertain. Mean liquid film profiles in horizontal square and triangle pipes appear to indicate that mean axial momentum is convected by secondary flow to the wall region where it contributes to an increased axial interfacial shear stress on the film.

Models developed for horizontal, annular, two-phase flow have taken various approaches to secondary flows. While it has been presented that circumferential interfacial shear stresses due to secondary flows are very unlikely to have a significant impact on the liquid film distribution, the convection of mean flow momentum by secondary motion is important. Thus, while circumferential shear stresses have not been modeled correctly to date, their inclusion in some models may have, in effect, modeled the redistribution of mean flow momentum, and thus have improved film thickness predictions. A recommendation for further modeling efforts is to relate the redistribution of mean axial momentum by secondary flows to mean flow

properties, then apply interfacial shear stress models to the liquid film using these redistributed values. Although this may already be accounted for in some round tube annular flow models through adjustable parameters, it may become more important to consider this mechanism separately as models for flows in non-round geometries are developed.

4.7 References

D. Adechy and R. I. Issa. Numerical modelling of horizontal annular flows. In G. P. Celata, P. Di Marco, and R. K. Shah, editors, *Two-Phase Flow Modelling and Experimentation 1999*, volume 3, pages 1607–1615, Rome, Italy, May 1999. Edizioni ETS, Pisa.

B. J. Azzopardi. Observations of drop motion in horizontal annular flow. *Chemical Engineering Science*, 42(8):2059–2062, 1987.

E. Brundrett and W. D. Baines. The production and diffusion of vorticity in duct flow. *Journal of Fluid Mechanics*, 19:375–394, 1964.

D. Butterworth. An analysis of film flow and its application to condensation in a horizontal tube. *International Journal of Multiphase Flow*, 1:671–682, 1974.

M. W. E. Coney. The analysis of a mechanism of liquid replenishment and draining in horizontal two-phase flow. *International Journal of Multiphase Flow*, 1:647–669, 1974.

R. S. Darling and H. N. McManus. Flow patterns in circular ducts with circumferential variation of roughness: a two-phase flow analog. *Proceedings of the 11th Mid-Western Mechanics Conference (Developments in Mechanics)*, 5:153–170, 1968.

L. A. Dykhno, L. R. Williams, and T. J. Hanratty. Maps of mean gas velocity for stratified flows with and without atomization. *International Journal of Multiphase Flow*, 20(4):691–702, 1994.

S. A. Fisher and D. L. Pearce. An annular flow model for predicting liquid carryover into austenitic superheaters. *International Journal of Multiphase Flow*, 19(2): 295–307, 1993.

A. G. Flores, K. E. Crowe, and P. Griffith. Gas-phase secondary flow in horizontal, stratified and annular two-phase flow. *International Journal of Multiphase Flow*, 21(2):207–221, 1995.

T. Fukano and A. Ousaka. Prediction of the circumferential distribution of film thickness in horizontal and near-horizontal gas-liquid annular flows. *International Journal of Multiphase Flow*, 15(3):403–419, 1989.

T. Fukano, T. Sakamoto, A. Tominaga, and E. Katoh. Experimental study on the flow mechanism of a thin liquid film flowing concurrently with a high speed gas flow in a horizontal rectangular duct. *Proceedings of the 1987 ASME-JSME Thermal Engineering Joint Conference*, 5:351–357, 1987.

F. B. Gessner. The origin of secondary flow in turbulent flow along a corner. *Journal of Fluid Mechanics*, 58(1):1–25, March 1973.

R. J. Goldstein, M. Y. Jabbari, and J. P. Brekke. The near-corner mass transfer associated with turbulent flow in a square duct. *Wärme- und Stoffübertragung*, 27:265–272, 1992.

S. Goldstein, editor. *Modern Developments in Fluid Dynamics*, volume 1. Oxford University Press, Oxford, 1938.

T. J. Hanratty and J. M. Engen. Interaction between a turbulent air stream and a moving water surface. *AIChE Journal*, 3(3):299–304, September 1957.

J. O. Hinze. Experimental investigation on secondary currents in the turbulent flow through a straight conduit. *Applied Scientific Research*, 28:453–465, December 1973.

J. O. Hinze. *Turbulence*. McGraw-Hill, Inc., New York, second edition, 1975.

E. T. Hurlburt and T. A. Newell. Prediction of the circumferential film thickness distribution in horizontal annular gas-liquid flow. *Journal of Fluids Engineering – Transactions of the ASME*, 122:1–7, 2000.

A. Huser and S. Biringen. Direct numerical simulation of turbulent flow in a square duct. *Journal of Fluid Mechanics*, 257:65–95, 1993.

S. Jayanti, N. S. Wilkes, D. S. Clarke, and G. F. Hewitt. The prediction of turbulent flows over roughened surfaces and its application to interpretation of mechanisms of horizontal annular flow. *Proceedings of the Royal Society of London A*, 431: 71–88, 1990.

J. E. Laurinat, T. J. Hanratty, and W. P. Jepson. Film thickness distribution for gas-liquid annular flow in a horizontal pipe. *PhysioChemical Hydrodynamics*, 6(1,2): 179–195, 1985.

T. F. Lin, O. C. Jones, R. T. Lahey, R. C. Block, and M. Murase. Film thickness measurements and modelling in horizontal annular flows. *PCH: PhysicoChemical Hydrodynamics*, 6(1/2):197–206, 1985.

A. Melling and J. H. Whitelaw. Turbulent flow in a rectangular duct. *Journal of Fluid Mechanics*, 78(2):289–315, 1976.

J. Nikuradse. Untersuchungen über turbulente strömungen in nicht kreisförmigen rohren. *Ingenieur–Archiv*, 1:306–332, 1930.

S. V. Paras and A. J. Karabelas. Properties of the liquid layer in horizontal annular flow. *International Journal of Multiphase Flow*, 17(4):439–454, 1991.

S. V. Paras, N. A. Vlachos, and A. J. Karabelas. LDA measurements of local velocities inside the gas phase in horizontal stratified/atomization two-phase flow. *International Journal of Multiphase Flow*, 24(4):651–661, 1998.

R. H. Pletcher and H. N. McManus, Jr. The fluid dynamics of three dimensional liquid films with free surface shear: A finite difference approach. *Proceedings of the 9th Mid-Western Conference on Mechanics (Developments in Mechanics)*, 3: 305–318, 1965.

L. Prandtl. Turbulent flow. Technical Memorandum 435, NACA, October 1927.

C. G. Speziale. On turbulent secondary flows in pipes of noncircular cross-section. *International Journal of Engineering Science*, 20(7):863–872, 1982.

5

Visualization of two-phase flow through micro-grooved tubes for understanding enhanced heat transfer

5.1 Introduction

Microgrooved (also called micro-fin) tubes play a very significant role in modern, high-efficiency refrigerators and air conditioners. These tubes generally have grooves approximately 0.2 mm deep with about a 0.5 mm pitch which may be arranged in a variety of patterns around the inner walls. Currently, tubes with axial, helical, crosshatched and herringbone patterns are available. With their introduction about twenty years ago, it was found that microgrooved tubes demonstrate significantly increased heat transfer coefficients over smooth tubes with only a minor addition to pressure loss. This effect is most dramatic at low mass fluxes. Evidence from heat transfer data and flow visualization experiments indicate that the enhancement is due in large part to increased wetting of the tube perimeter, and various theories have been advanced to explain this. In this work, background on what has been learned about two-phase heat transfer in refrigerant systems will be discussed, followed by a description of previous efforts to explain the mechanics of heat transfer in enhanced tubes through inference from heat transfer data and visualization studies. Experimental liquid film distribution results will then be presented and used to provide additional physical insight for the fluid mechanics behavior underlying the heat transfer data reported in the literature.

5.2 Background – two-phase heat transfer

Whether evaporating or condensing, the liquid fraction of the fluid will assume either annular, stratified annular or stratified configurations for a large percentage of the length of the heat transfer device. Annular flow, which can form in both horizontal and vertical tubes, exists when a thin layer of liquid coats the tube wall with vapor flowing through the center of the tube. In horizontal flow, the liquid will tend to be drawn to the bottom of the tube, and significant asymmetry may exist. When energy from the vapor is not sufficient to push liquid around the tube wall against gravity, stratified flow will exist. Here, liquid pools at the bottom of the tube with little or no liquid on the top. The condition named stratified annular flow generally refers to flow where a thick liquid layer flows along the bottom of the tube with a very thin layer completely coating the remaining wall; this is common in condensation. Finally, a situation can occur in which a fairly uniform film that does not coat the entire tube at high qualities or when a portion of the film dries out due to evaporation. Patterns of this sort were discussed in Chapter 2.

Boiling heat transfer in annular flow is dominated by film evaporation. The thinness of the films determines that, for a wide range of heat flux, the temperature gradient within the liquid is too small to allow nucleate boiling to be sustained. To contrast this behavior with nucleate or pool boiling, some authors describe this regime as shear driven or forced convection heat transfer.

In condensation, drop-wise condensing yields very high heat transfer coefficients. This behavior, however, is difficult to sustain as additional liquid forms on the cooled surface. Therefore, in most practical applications, film condensation dominates, and the thermal resistance posed is that due to movement of heat across the film.

The behavior of the thin film in annular flow is quite complex, and can not as yet be described with certainty. Waves readily form on the film and appear to take on many forms. While the smaller waves certainly contribute to the interfacial shear, it is thought that large waves play an important role in both the liquid behavior and the heat transfer. Disturbance waves, sometimes referred to as roll waves, are highly turbulent masses of liquid that flow as relatively coherent, relatively long-lived structures along the tube with a velocity typically on the order of 1/5 to 1/10 of the vapor velocity and average thicknesses about 5 times that of the local base

film thickness. The experimental work seems to indicate that two-phase annular flow can be described by a thin, laminar substrate film on which disturbance waves appear to slide. (See, for example, Hewitt et al. [1990].) Recent computational models indicate that this is, in fact, the most likely physical reality [Jayanti and Hewitt, 1997a].

Hence, it is important to focus on the physics of heat transfer in thin flowing films, long a subject of research. In shear driven annular flow, it has been frequently assumed that the film is turbulent with significant mixing causing an enhanced heat transfer over that in a laminar film. The behavior of the liquid film, though very complex, does not lend itself to traditional turbulent descriptions, however. Models for heat transfer assuming a Law of the Wall, or Von Karman, type of velocity profile tend to significantly over predict the measured heat transfer. Several possible reasons for this discrepancy are noted by Yang [1999]. Dobran [1983, 1985] has shown that a model reducing the turbulent mixing somewhat as the gas-liquid interface is approached gives much better agreement to physical behavior. This was noted independently by Leuthner et al. [1999] as well. Jayanti and Hewitt [1997b] demonstrated through computational work that the heat transfer in a wavy laminar film was predominantly due to conduction through a base film, with waves serving to enhance this primarily as a result of the decreased liquid mass flowing in the film when waves are present. A similar approach applied to shear-driven disturbance waves showed that heat transfer is enhanced by the passage of the turbulent mass, but not significantly over the rate of heat transfer in a laminar base film [Jayanti and Hewitt, 1997a].

In summary, then, it appears that the heat transfer behavior within evaporating and condensing annular flow is dominated by the viscous base film. Hence, the measurements of the circumferential film thickness which are presented in this work should provide some explanation for the experimental heat transfer measurements that have been made in many previous investigations.

5.3 Theories of enhancement from heat transfer experiments

An important and frequently cited theory for heat transfer enhancement in microgrooved tubes is that capillary forces are responsible for driving liquid from

the bottom of the tube to the top. Ito and Kimura [1979] and Kimura and Ito [1981] were among the earliest to suggest this behavior and performed experiments with grooved flat plates to support it. They claimed that additional enhancement, particularly at higher mass flux, is due to the formation of Görtler vortices in the grooves (see Panton [1996], p. 743) as well as an increased velocity of liquid within the grooves, although no experimental evidence is offered for these explanations. Numerical studies by Benhalilou and Kasagi [1999] confirm that streamwise vortices can occur in fluid flow through a microgroove, but their work assumed films that were much thicker and at much higher Reynolds numbers than generally occur in annular refrigerant flows.

The importance of capillary forces is suggested by several other researchers as well, including Yoshida et al. [1987, 1988] who measured heat transfer coefficients circumferentially and found that boiling heat transfer in a micro-fin tube is much more uniform around the tube than in a smooth tube. Based on this and on fiber-scope observations of two-phase refrigerant flow inside micro-fin tubes, they suggest that at low mass flux, liquid is essentially pooled in the bottom of the tube and the upper surfaces are wetted by capillary action. As mass flux increases, the grooves act together with the vapor shear to generate annular flow. They suggest that the relatively constant heat transfer coefficient at high mass fluxes is due to a suppression of turbulence in the liquid film by some action of the grooves.

Boiling heat transfer data led Cui et al. [1992] to infer that at mass flux greater than 100 $\frac{kg}{m^2 s}$ for R-502, annular flow prevails composed of both circumferential (spiral) and axial components. The spiral flow enhances tube wall wetting while the axial flow generates boundary layer separation at the micro-fin tips.

Experimental work of Khanpara et al. [1988] and Schlager et al. [1990] led these researchers to suggest that increased turbulence in the liquid film provides the mechanism for increased heat transfer. The decreased enhancement at higher mass fluxes is explained by the hypothesis that turbulence in the smooth tube film increases more rapidly with mass flux than in the finned tube.

The importance of flow pattern transitions, both accelerated and delayed, in the heat transfer behavior of enhanced tubes has been reported by more recent heat transfer research in both condensation and evaporation. Graham et al. [1999] studied condensation in an axially finned tube and compared this with the condensation data of Ponchner and Chato [1995] for an 18 degree helically finned tube. These

data suggest that at low mass flux the helical grooves may be enhancing the drainage of condensate from the top of the tube to the bottom, allowing more of the tube wall surface area to be available for heat transfer. The axial fins, however, may inhibit this drainage, decreasing condensation effectiveness. At higher mass flux, the helical tube appears to transition to annular flow somewhat sooner than a smooth tube, but otherwise tends to show only an enhancement approximately equal to the percentage increase in surface area. The axial tube, however, by comparison with smooth tube data, seems to establish an annular flow pattern at very low qualities and thus shows significant enhancement in this region of operation.

Other researchers have suggested that flow pattern transitions had dominant influences on their data as well. In condensation, Koyama et al. [1990] inferred what appeared to be transitions from annular to stratified flow from their circumferential temperature data. Sight glass observations allowed Singh et al. [1996] to correlate improved evaporation heat transfer with a transition to annular flow. A similar transition was postulated by Zürcher et al. [1998a] based on comparison of R134a and R407C flow boiling data.

Chamra and Webb [1995] found that their heat transfer measurements in both condensation and evaporation, together with the work of Yang and Webb [1995], suggest that flow pattern transition is instrumental in the heat transfer behavior of both condensation and evaporation. At lower mass fluxes ($< 150\ \frac{kg}{m^2 s}$) and qualities of R-22, gravitational effects are significant, with liquid draining to a stratified layer in the tube. However, at higher qualities and moderate to high mass flux, the liquid flow transitions to annular flow where they suspect both surface tension and vapor shear forces are important. These authors expect that vapor shear forces dominate in this case, but suggest that more experimentation is needed to confirm this. Surface tension forces would tend to become significant when the tips of the fins are exposed and this was not addressed in the study performed.

5.4 Previous flow visualization efforts

Flow visualization by several researchers has provided additional insight. Much of this work has been performed using clear tubes with wire inserts. Ravigururajan and Bergles [1994] performed single phase flow visualization in this manner. In this case, dye was injected at various points to observe the water flow behavior.

The authors note that rotational flow is established by the inserts in both laminar and turbulent flow, and that the thickness of the rotational layer decreases with increasing Reynolds number. The rotating fluid tends to follow the rib angle better as Reynolds number decreases.

Two-phase air-water studies carried out in horizontal transparent tubes with helical wire inserts were reported in Weisman et al. [1994]. These investigators mapped transitions between flow behaviors and found that the transition from separated (stratified or wavy) to annular flow occurred at much lower superficial liquid and vapor velocities than in a smooth tube. As well, bubbly dispersed flow did not occur in the enhanced tube due to the swirling motion which forced bubbles to coalesce in the center and extended the annular regime. A subsequent study by the same authors [Weisman et al., 1996] showed qualitatively similar behavior using refrigerant, R-113. The R-113 system was more affected by the number of helical wires used, however, and exhibited a prolonged intermittent slug-annular behavior during the transition to annular flow.

To better understand refrigerant and refrigerant-oil mixture flows, Manwell and Bergles [1990] used a smooth tube sight glass placed between two sections of microgrooved tube. Using R-12, a dramatic shift toward lower quality and mass flux was noted in the transition from stratified to annular flow in the enhanced tube. With the addition of oil, increased wetting of the upper wall of the tube was found at low qualities. The enhanced tube showed some reduction in foaming compared to the smooth tube when oil was present.

Yoshida et al. [1988] used a boroscope to observe R-22 flow inside of microgrooved tubing. Liquid was observed in the grooves around the entire circumference at all mass flux conditions. Where the liquid was thicker than the groove depth, it appeared to flow axially over the tops of the grooves. The liquid flowing in the grooves appeared to flow "slowly and rather smoothly along the grooves." At a mass flux of 50 $\frac{kg}{m^2 s}$, the liquid at the top of the tube appeared stagnant, with liquid in the grooves along the sides showing some oscillation. At mass flux conditions greater than 200 $\frac{kg}{m^2 s}$, the flow appeared to be annular, and, for qualities less than 0.8, the liquid film was thicker than the groove depth and the flow was generally axial.

A similar visualization technique was employed by Nozu and Honda [1997], with the addition of a view looking axially down the tube near the exit of the test

section. Observations of R-11 flow appear to show wavy stratified flow at 80 $\frac{kg}{m^2 s}$, annular flow with significant droplet entrainment at 110 $\frac{kg}{m^2 s}$ and nearly uniform annular flow with fins continually submerged for a wide range of vapor quality at 175 $\frac{kg}{m^2 s}$. There is some possible indication of swirling or rotated flow of waves passing over the grooves, but this can not be confirmed from the images presented. The exit pictures show that liquid tends to pool slightly asymmetrically with respect to the vertical; i.e. the liquid at the bottom of the tubes in these images tends to exit shifted counter-clockwise, the direction of groove rotation, when viewed from the flow direction.

Each of these heat transfer and flow visualization experiments have made significant contributions to the understanding of this complex two-phase flow. Limitations on materials and technology, however, have not allowed for quantitative measurements of the liquid distribution and flow behavior in tubes with groove depths and helix angles close to those commonly used in commercial applications. As a result, somewhat conflicting or inconsistent explanations for the heat transfer enhancement exist in the literature, as noted above.

The objective of this work is to accurately determine the distribution of liquid in annular horizontal flow through tubes with microgrooves using a recently developed non-intrusive, optical film thickness measurement system. Three transparent test sections with 20 microgrooves approximately 0.2 mm deep have been fabricated with 0 (axial), 9 and 18 degree helix angles. Detailed distributions of the mean liquid film thickness have been obtained for air-water horizontal annular flow. The results of this experimental work will then be used to provide a context for the numerous heat transfer studies performed to date on enhanced tubes.

5.5 Experimental setup

5.5.1 Test sections

The test sections were constructed of 0.5 inch schedule 40 clear PVC tubing. The actual inner diameter of the tubes was 15.1 mm. The total observable length was about 6 m including a 3 m smooth flow development section. The grooved test sections were fabricated by pulling 0.8 m lengths of tube over a die with four orthogonal cutting points which were set to cut grooves 200 microns deep. After completing the grooves, the ends of these short lengths were milled square and were joined

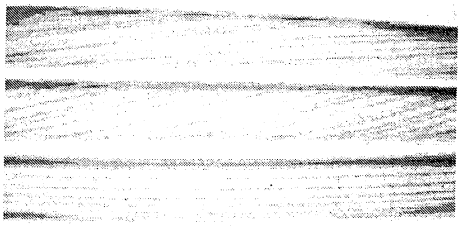

Figure 5.1: Photo of the grooved tubes used in this experiment.

flush using a modified clear PVC coupling adapter such that the grooves aligned as closely as possible. A guide sleeve slotted with the appropriate helix angle was used to rotate the tube during the cutting. This process was manual and prone to some inconsistency; the resulting grooves were not perfectly spaced nor as smooth as production quality copper tubes, as can be seen in Figure 5.1. In addition, only 20 grooves (as opposed to 60 in commercial tube of about this diameter) were cut into each tube to allow space for visualization between the grooves. In spite of these differences the resulting data show trends that correspond to heat transfer observations made in commercial copper and aluminum tubing.

5.5.2 Flow loop

The primary experimental apparatus is shown in Figure 5.2. Laboratory compressed air was regulated and passed through a 3 m entrance tube. The mass flow rate of the air was determined by measuring the pressure drop across this entrance tube. The Colebrook correlation for friction factor along with the definitions of friction factor, Reynolds number and mass flow rate were then solved simultaneously to provide the mass flow rate of air in the loop. This process was simplified by using the Engineering Equation Solver (EES) from F-Chart Software. Water from the laboratory main passed through a volumetric flow meter before entering the test section through several 1/16" holes drilled in the test section wall. Both the water and air are filtered to 5 microns prior to entering the apparatus.

Pressure gradients are measured using solid state differential pressure transducers. The inlet pressure transducer has a sensitivity of ± 1.7 Pa while the test section transducers are sensitive to ± 6.8 Pa. Gauge pressures in the entrance and test sections were monitored with Bourdon-style gauges.

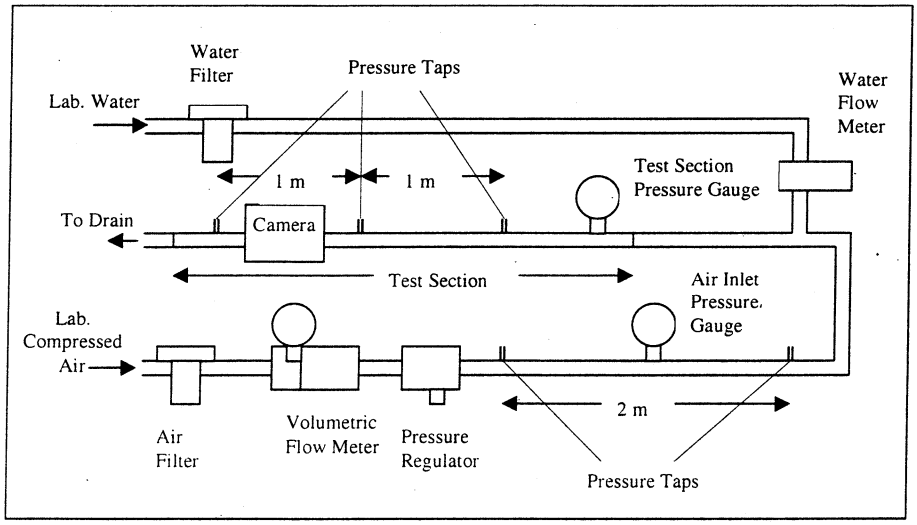

Figure 5.2: Experimental air/water test loop.

5.5.3 Film thickness measurement

Local liquid film thicknesses were obtained using an optical measurement system described by Shedd and Newell [1998]. The time averaged liquid film thicknesses presented here were measured to within ± 0.003 mm ($\pm$ one standard error). Due to the nature of the measurement, the experimental results exclude the large liquid waves from the calculated average thickness, so the thicknesses reported reflect only the thin base film that exists between the large liquid waves. This is significant since, as noted above, it is this thin base film that apparently plays the most active role in heat transfer. The film thicknesses were measured at about 390 L/D from the point where liquid was introduced. The actual grooved length of each test section varied due to the nature of their fabrication. Film thickness was measured at 170 L/D, 140 L/D and 120 L/D from the beginning of the 0, 9 and 18 degree grooved sections, respectively.

5.6 Experimental results

The flow conditions examined are shown in Table 5.1.

The Froude rate is a non-dimensional group that essentially represents the ratio of the rate of kinetic energy flowing in the vapor to the power required to pump

Name	$\dot{m}_g$ kg/s	$\dot{m}_l$ kg/s	Ft	x	G kg/sm^2
T	0.0048	0.0032	70	0.6	44
U	0.0067	0.0032	120	0.68	55
V	0.0099	0.0032	210	0.76	73
Q	0.0047	0.0063	50	0.42	61
R	0.0079	0.0063	105	0.56	79
F	0.0110	0.0063	165	0.64	97
G	0.0152	0.0063	250	0.71	120

Table 5.1: Details of the experimental flow conditions. Ft is the Froude rate, x is quality and G is mass flux. See text for an explanation of the Froude rate parameter.

liquid from the bottom to the top of the tube at its axial flow rate. It is defined by

$$\begin{aligned} \text{Ft} &= \sqrt{\frac{\dot{m}_g}{\dot{m}_l}}\text{Fr} \\ &= \sqrt{\frac{\dot{m}_g}{\dot{m}_l}}\left(\frac{U_{sg}}{\sqrt{gd}}\right) \\ &\sim \frac{\text{gas phase power}}{\text{liquid phase pumping power}}, \end{aligned} \tag{5.1}$$

where the subscripts g and l represent vapor and liquid quantities, respectively, U_{sg} is the superficial vapor velocity (the velocity of vapor if it occupied the entire tube at the same mass flow rate), g is the gravitational acceleration and d is the tube diameter. Ft has been found to be a useful parameter for correlating some two-phase flow quantities [Hurlburt and Newell, 2000, Yashar et al., 2001].

5.6.1 Pressure drop

Figure 5.3 plots the friction factors of the various tubes against the vapor Reynolds number. This plot reaffirms that the presence of grooves only generates a mild increase in pressure loss over smooth tubes in two-phase annular flow.

5.6.2 Film thickness

The liquid film thickness data at 16 circumferential locations for each of the 7 flows are presented in Appendix B for reference and direct comparison with other experimental and modeling results.

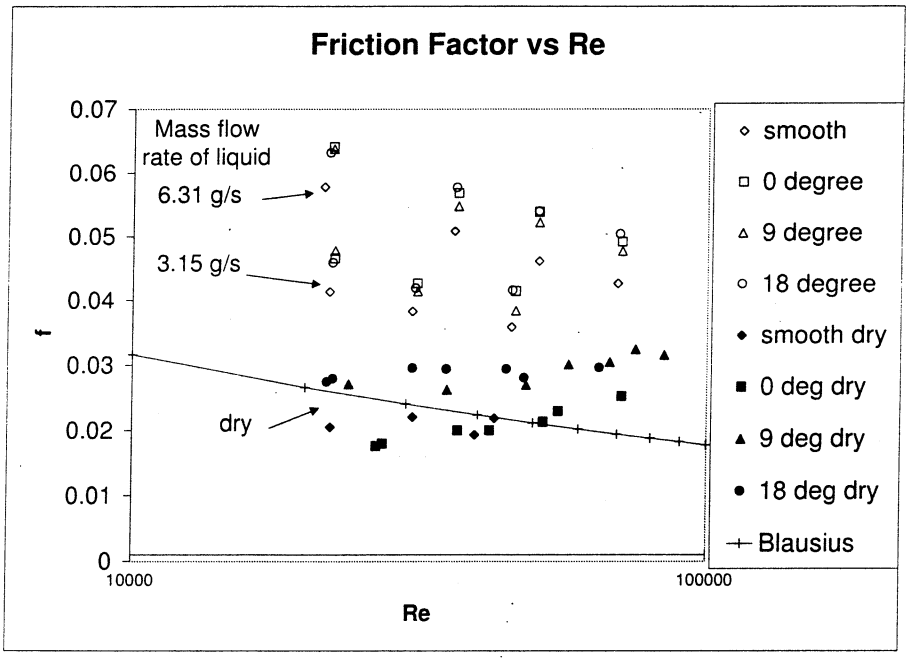

Figure 5.3: Friction factor versus Reynolds number for various flow conditions in the four different tubes.

Liquid film thickness profiles for annular flow through the 9 and 18 degree helix tubes are presented in Figures 5.4 – 5.9. In each of these plots, the smooth tube profiles are shown by dotted lines while the grooved tube profiles are solid. The smooth tube profiles are essentially symmetrical left to right, but show the effects of gravity with thicker liquid on the bottom. Contrast with these the profiles of the helically grooved tubes. First, the thickest parts of these films appears to have been rotated counterclockwise (the same direction as the groove helix), so that these films seem to be symmetrical about a line passing through the center of the tube at some angle from upper left to lower right. Second, the amount of wetted tube periphery is substantially increased. In the lowest flow approximately 62% of the smooth tube is wetted versus 81% of the 9 degree and 94% of the 18 degree tubes.

The profiles of the 9 and 18 degree tubes seem quite similar to that which is found when liquid is placed inside a rotating cylinder. Or, in other words, that a circumferential shear, due to the grooves, occurs at the wall. To test this theory, a term representing rotation at the tube wall was added to a simplified form of the horizontal annular flow model developed by Hurlburt and Newell [2000], and the

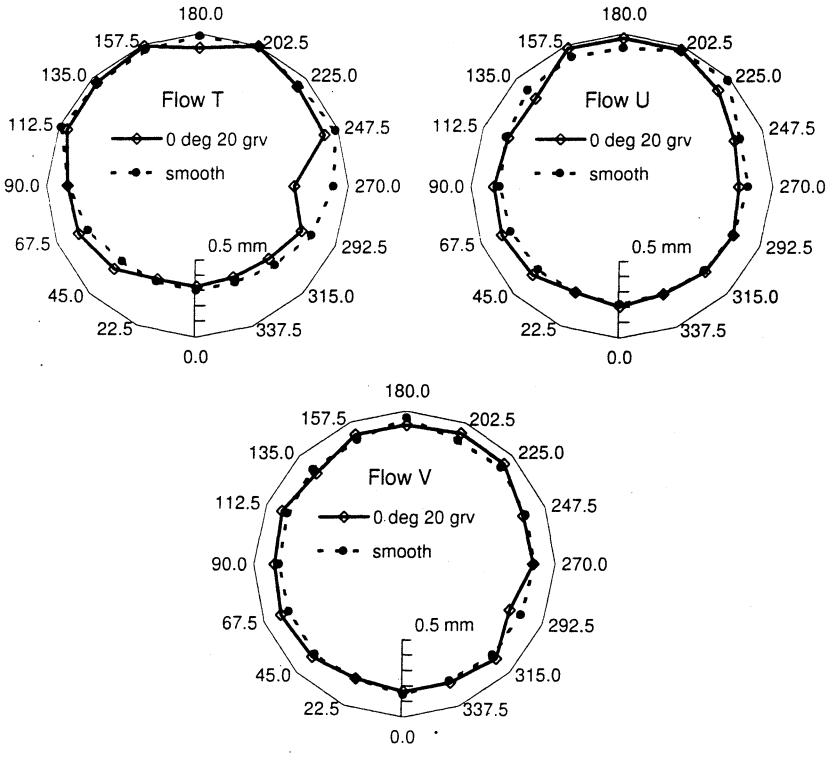

Figure 5.4: Film thickness profiles in tube with 0 degree helix grooves compared with the smooth tube profiles with liquid flow of 0.003 Kg/s.

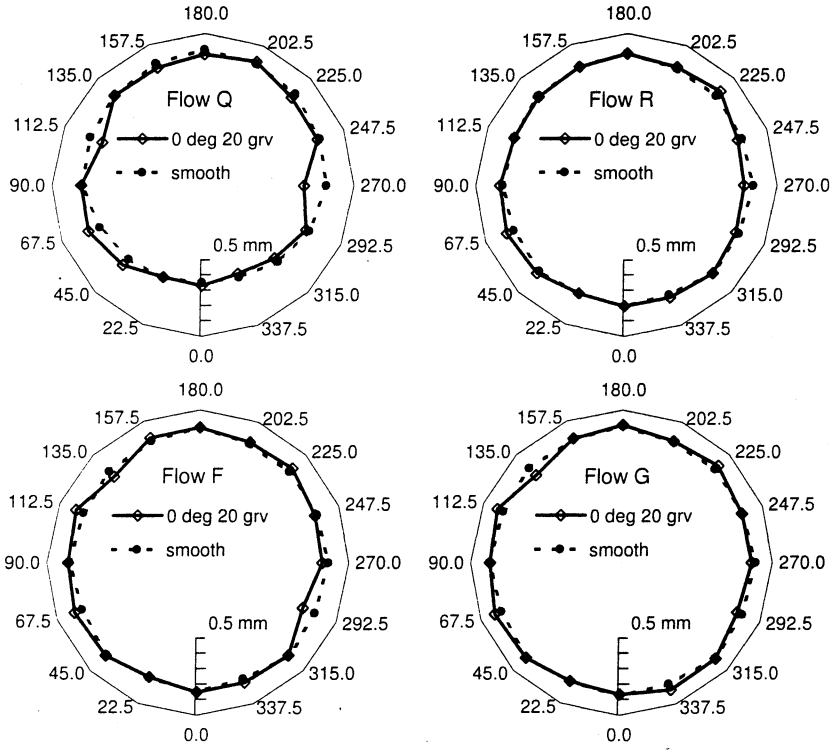

Figure 5.5: Film thickness profiles in tube with 0 degree helix grooves compared with the smooth tube profiles with liquid flow 0.006 Kg/s.

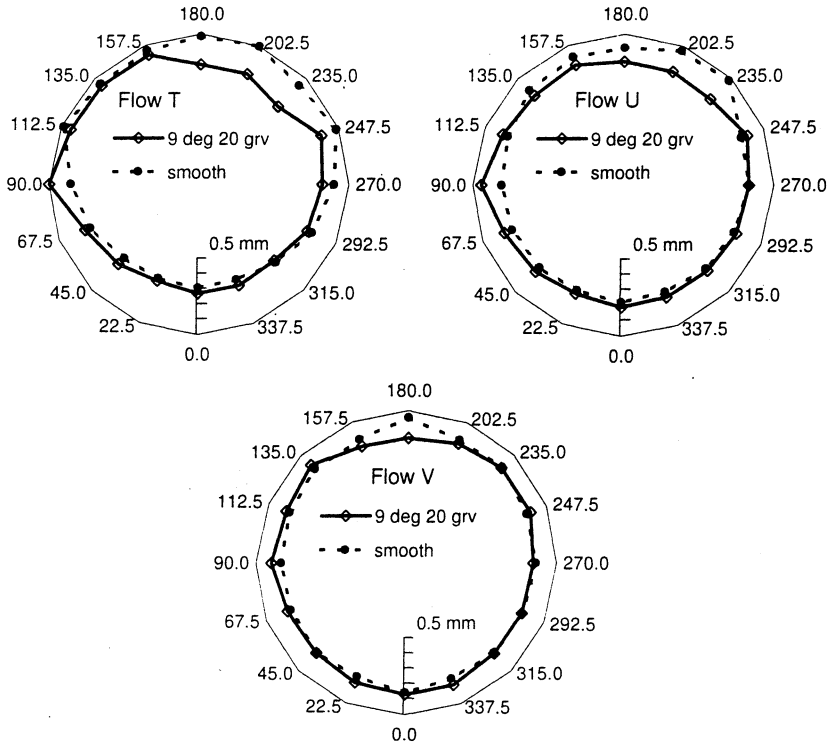

Figure 5.6: Film thickness profiles in tube with 9 degree helix grooves compared with the smooth tube profiles with liquid flow of 0.003 Kg/s.

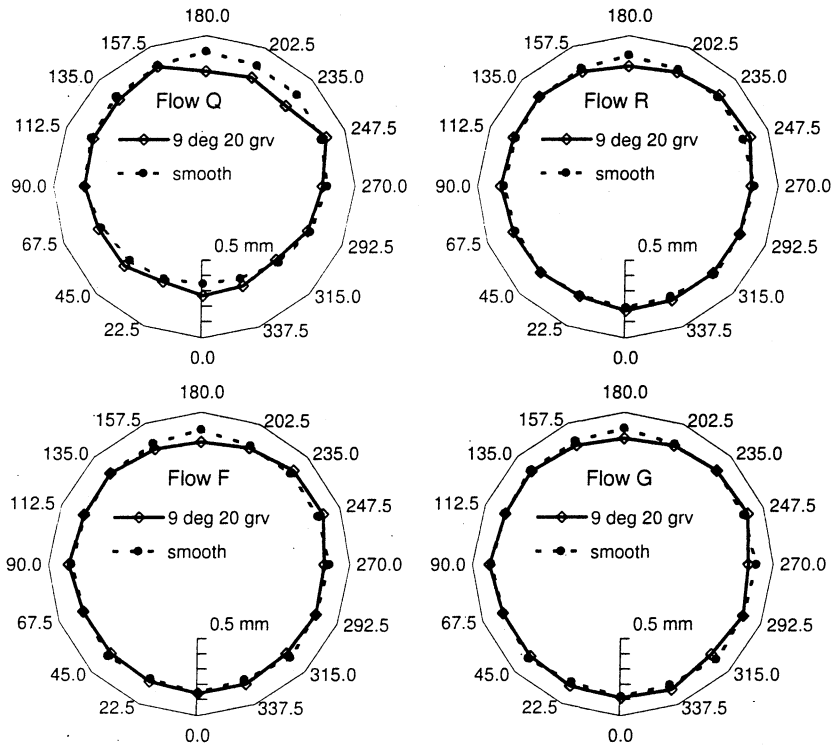

Figure 5.7: Film thickness profiles in tube with 9 degree helix grooves compared with the smooth tube profiles with liquid flow 0.006 Kg/s.

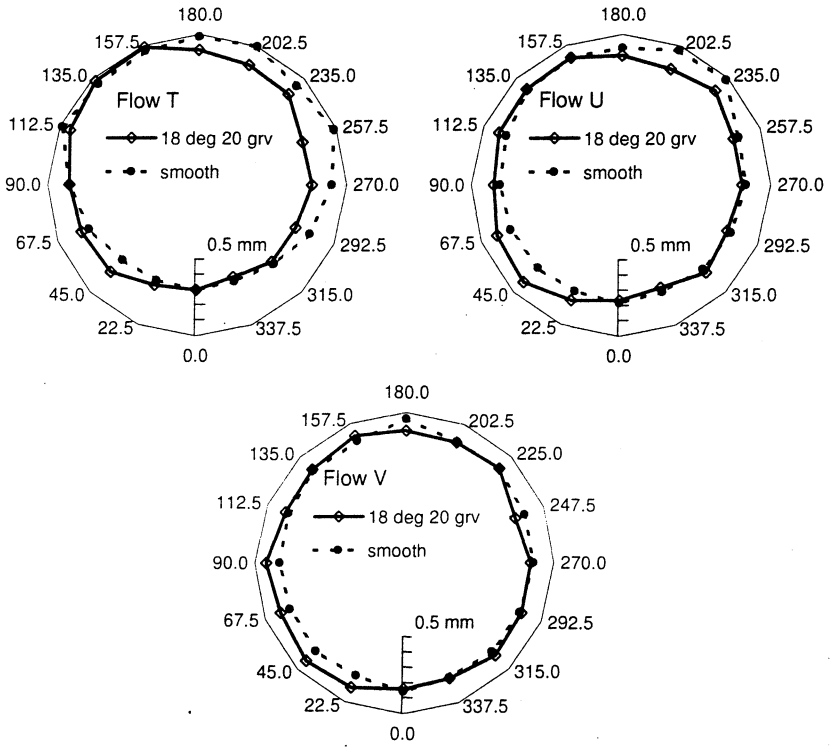

Figure 5.8: Film thickness profiles in tube with 18 degree helix grooves compared with the smooth tube profiles with liquid flow of 0.003 Kg/s.

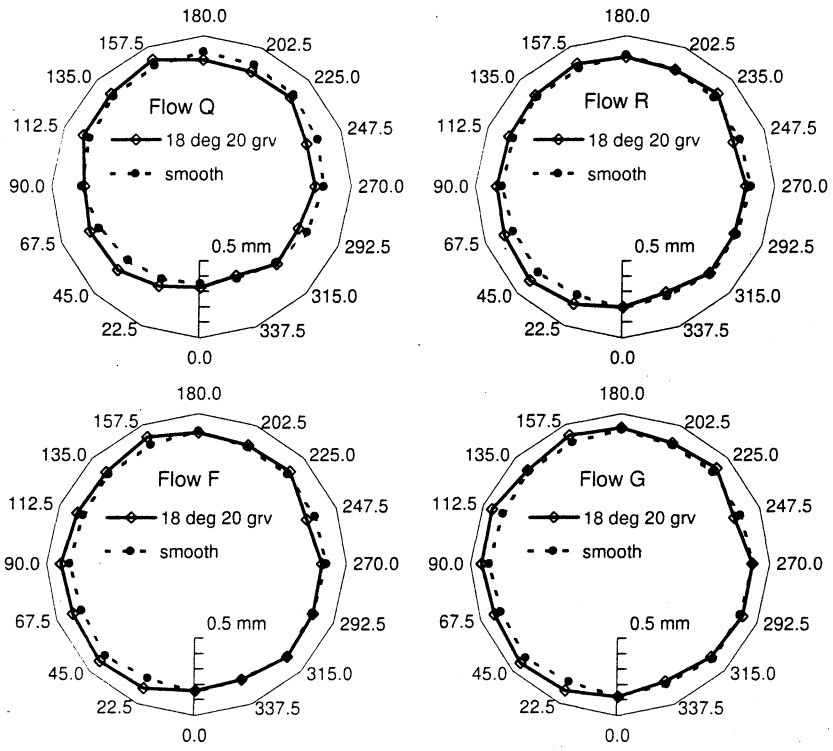

Figure 5.9: Film thickness profiles in tube with 18 degree helix grooves compared with the smooth tube profiles with liquid flow 0.006 Kg/s.

comparison with experimental data was good for the flow conditions tested. To achieve this agreement, the average film thickness for the given run was provided to the model and the wall rotation was adjusted until the calculation approaches the experiment.

Here it should be noted, however, that this rotation, if it exists, acts in combination with several other mechanisms to generate the steady profiles shown above. Observation of the film gave no real indication of a rotation or swirling motion propagating into the bulk of the film layer. At low mass flux conditions, steady profiles would form with sections of the tube dried out. These dryout patches did not follow the grooves for long lengths. Typically, the film would dryout in a roughly rectangular region that was more or less horizontal, cutting across several grooves, rather than following the groove angle. If the film were swirling (having a helical trajectory), the dryout patches should follow some helical pattern, which was not observed. These dry patches were quite stable, lasting several minutes, and the overall dryout pattern was reproducible, indicating that the film is in some sort of mechanical equilibrium.

The 0 degree, or axially grooved, tube behaves differently than the other two. Most noticeable are the regions on the sides of the tube where a stable, thicker film appears to form. These may be indications that forces pushing liquid up the wall meet resistance in the groove; these locations may reflect the equilibrium reached between the upward forces and gravity in the presence of the horizontal grooves.

5.7 Application to heat transfer measurements

At this point, it is important to define two terms frequently used in the enhanced heat transfer literature: the enhancement factor (EF) and the penalty factor (PF). The enhancement factor is the ratio of the heat transfer in an enhanced tube to that in a smooth tube at the same flow condition. The penalty factor is the ratio of the pressure drop in the enhanced tube to that in a smooth tube at the same flow condition. The terms will be used frequently in the following discussion.

Effects of diameter and fin geometry

To begin with, consider the influence of geometrical factors not accounted for in the present work, including tube diameter, the number of grooves (fin pitch or spacing),

and the groove (fin) shape. Limited information on the influence of groove angle may be inferred from the data presented and this will be discussed in detail in the following chapter.

The impact of groove depth and spacing on evaporation was studied at length by Ito and Kimura [1979]. The greatest gain in heat transfer performance was found to come as fin heights were increased to 0.2 mm. Beyond this, enhancement does not increase rapidly but pressure drop does. For this groove depth, a width of 0.5 mm, fin peak to fin peak, gave an optimum heat transfer coefficient.

Extensive comparisons of fin geometries were carried out by Khanpara et al. [1986] and Eckels et al. [1992]. The Khanpara et al., study investigated 8 different fin geometries for evaporation. Under the conditions examined, the heat transfer data for all the tubes generally fell within 10% of one another, though some trends were evident. Based on these trends, rounded-tip fins, round valleys, groove depth of about 0.17 mm and a pitch (groove width) of 0.38 mm were recommended for evaporation.

In their work, Eckels et al. [1992] also investigated several different fin geometries for evaporation of R-22 in tubes with two different diameters. In the end, slight variations in performance were noted, but no geometry appeared significantly better or worse. The smaller diameter tubes (7.94 mm vs. 9.52 mm) had higher HTCs by about 20%, which is about the same as the percent difference in the diameters. This could be because the cross sectional area to perimeter ratio changes linearly with diameter, so a 20% increase in diameter will cause a 20% increase in the area to perimeter ratio, indicating that less heat transfer surface area exists per unit of cross sectional area.

Additional work by Eckels et al. [1998a] compared the performance of a 9.52 mm tube with that of a 12.7 mm tube in both condensation and evaporation. It was found that the enhancement factor was greater for a 9.52 mm tube than for the 12.7 mm on average in condensation, but little change was noted in evaporation. As the penalty factor also increased for the 9.52 mm tube in condensation, perhaps this indicates that it is the shear effects more that the surface area than give the additional enhancement.

However, Schlager et al. [1990] also compared evaporation and condensation in tubes of 12.7 mm and 9.52 mm diameters and found no significant performance difference between the two diameters. The 9.52 mm generally had the same en-

hancement as the 12.7 mm tube in condensation and slightly higher enhancement in evaporation.

In their review of heat transfer in micro-fin tubes, Newell and Shah [1999] report that, generally, heat transfer coefficients increase with a decrease in diameter, though not all literature is in agreement. They also note that changes in tube diameter do not appear to have a significant effect on void fraction.

In summary, the literature appears to indicate that, to first order, the shape of the fin and variation in tube diameter, within the range common for refrigeration applications, are minor factors in the heat transfer performance of the tube. Based on the literature, the tubes used in this study were fabricated with grooves that were approximately 0.2 mm deep and 0.5 mm wide at the opening. While far fewer grooves were used in these experiments, it appears that 20 grooves is sufficient to recreate significant fluid mechanical behavior, which was the intent of this work.

Condensation versus evaporation

In most commercial applications, condensation takes place at higher saturation temperatures and pressures than evaporation. Vapor densities at these conditions are frequently about 3 times greater than those at typical evaporation conditions. At the same mass flux, then, vapor velocities are lower. This impacts heat transfer in multiple ways. For example, slower vapor has less energy to push the liquid up the tube walls, creating more non-uniform liquid distributions. Pressure losses will also be lower per unit length. This is emphasized by the work of Yashar et al. [2001] who found that void fraction shows a dependence on mass flux in their lower mass flux condensation data compared with evaporation data at the same flow conditions. Apparently, the refrigerant flow in condensation indicated a transition from dominantly stratified to primarily annular flow as mass flux increased, while the evaporating refrigerant (at lower pressures) remained annular through all mass flux conditions.

Evidence of the impact of flow behavior on heat transfer is also shown by the studies of Schlager et al. and Eckels et al. Schlager et al. [1989b, 1988, 1989a, 1990, 1989c] found that, using R22, enhancement factors were greater for evaporation than for condensation, especially at the lowest mass flux conditions (125 $\frac{kg}{m^2 s}$). The differences in enhancement factors decreased as a mass flux of 400 $\frac{kg}{m^2 s}$ was approached.

On the other hand, Eckels et al. [1994a,b, 1998b] report that R134a gave much higher condensation enhancement factors than evaporation at both 200 $\frac{kg}{m^2 s}$ and 300 $\frac{kg}{m^2 s}$, even though these experiments were performed under very similar conditions. It appears that this difference from the R22 data could be due to the different refrigerant properties. Lower vapor densities in R134a suggest higher vapor velocities would exist than for a similar R22 flow, so it is likely that the liquid film transitions to annular flow earlier than with R22, so that enhancement appears to be less for evaporation when compared with condensation. In other words, for R22, because of the slower fluid flow, the liquid distribution in the smooth tubes probably remains stratified or very asymmetrically annular in both condensation and evaporation. Thus, the improved liquid distribution in the micro-fin tubes provides similar enhancements in both operations. With R134a, however, it is likely that flow during evaporation in a smooth tube makes the transition to primarily annular flow with relatively low mass flux, and thus liquid redistribution by the micro-fins appears to have less enhancement effect during evaporation than condensation. This behavior could explain the findings in Eckels et al. [1998a] for heat transfer in 12.7 mm tubes with R134a which show that at the lowest mass flux, 69 $\frac{kg}{m^2 s}$, evaporation enhancement began to approach the higher condensation enhancement levels.

A similar phenomenon appears in the work of Zürcher et al. [1998b] who noted from their evaporation data that while the microfin had appeared to force R134a into annular flow, at the same temperatures, R407C, operating at almost twice the pressure, appeared to remain in a wavy stratified flow.

This is also partially supported by condensation data provided by Fujii [1995] who compared enhancement factors of R22, R134a and R123. As working pressure increased with these fluids, the enhancement became less dependent on mass flux. And the greatest enhancements occurred at the higher qualities of the R123 tests. The values reported by Fujii are not as high as those reported by Eckels.

An analytical model for condensation heat transfer was constructed by Shikazono et al. [1998] assuming that the liquid distribution in micro-fin tubes is primarily a balance between gravity and the capillary forces. Based on the experimental film thickness observations presented above, it is expected that such a model would only apply at low qualities where stratified flow would dominate, and at high qualities, where the fin tips would be exposed through the annular film. Results of model calculations confirm this when compared with data taken using R22, R32

and R134a. Deviations of 50% or more in the calculated versus experimental heat transfer coefficient are indicated for the quality range of 0.1 – 0.6.

Yang [1999] provides a detailed review of condensation modeling efforts and the role of surface tension in condensation on enhanced surfaces. Yang observes that experimental evidence suggests that surface tension plays a significant role in condensation at higher quality flows when fin tips are exposed. As detailed in Yang and Webb [1995], it appears that condensate forming on the fin tip is drawn into the groove by surface tension, thus maintaining a very thin film of liquid on the upper surface of the fin resulting in very high rates of condensation. As quality decreases, fins become submerged in the liquid film and, as in evaporation, vapor shear becomes the dominant factor. This behavior was supported by the extensive review of Shah et al. [1999] as well.

The work of Chamra et al. [1996a,b] indicated that condensation heat transfer coefficients increase continually with groove depth and groove angle, along with the corresponding pressure penalty. Conversely, evaporation heat transfer peaked for tubes with a 20 degree helix angle. While they found numerically similar condensation and evaporation heat transfer coefficients for R-22 in enhanced tubes, the enhancement ratios were consistently larger for condensation. However, pressure penalties versus smooth tubes were also larger in condensation, though absolute values of pressure drop were less for condensation compared with evaporation.

Further work by Chamra and Webb [1995] showed that, when evaporation and condensation occur at the same temperature, heat transfer coefficients for both are almost equal. They concluded that the heat transfer in both processes was regulated by vapor shear, with the caveat that surface tension effects may be indicated by the lower mass flux data. Additionally, for the conditions reported, evaporation is more significantly influenced by mass flux, probably due to the presence of nucleate boiling and dryout.

It is possible, however, that other differences may exist between evaporation and condensation mechanisms in enhanced tubing. Ebisu and Torikoshi [1998] have found that, under the same conditions where helical tubes show very similar heat transfer coefficients in evaporation and condensation, tubes with a herringbone enhancement show very different behavior, with condensation heat transfer performance nearly twice that of evaporation. According to the previously cited works, both the evaporation and condensation behaviors should be driven by vapor shear

effects. Circumferential temperature measurements indicate high heat transfer coefficients exist at the sides of these tubes. From the correlation previously noted between film thickness and heat transfer coefficients, the liquid is likely drawn off the sides and to the top and bottom of the tube. Thus, it appears that more tube surface area is exposed for heat transfer than in the helical tubes. In condensation, the vapor will travel about 3 times more slowly, thus decreasing the effects of shear with perhaps surface tension beginning to play a more significant role. In addition, 30% of the increase is likely due to the 30 % increase in surface area of the herringbone tube over the helix tube.

Asymmetrical temperature and heat transfer coefficient distributions

To obtain accurate heat transfer coefficient data, most experimental setups have used three or four circumferential temperature measurements at a given axial location along the test section. In much of the literature, only the averages of these circumferential measurements are reported. Where the temperature variations around the tube are reported, however, they tend to indicate an asymmetrical distribution of liquid on the tube wall.

Yoshida et al. [1987] present circumferential heat transfer coefficient data for evaporation at two mass flux conditions and over a quality range from 0.1 to 1. For R-22 at 100 $\frac{kg}{m^2 s}$, the heat transfer coefficient at the top of a smooth tube is very near zero, while it is very high (reaches 8 kW/m^{2}K) at the top of the grooved tube. This indicates that the grooves are causing a thin film of refrigerant to form on the top of the grooved tube. These researchers do not measure both sides of the tube, but it is interesting that at low qualities, the heat transfer is greatest at the one measured side for the smooth tube, which may be expected because of a thin meniscus at the edges of the stratified layer or a thin film left behind by waves. In the grooved tube, however, the data consistently show the right side value in between the bottom and top, and the heat transfer is generally much more uniform over the tube throughout the whole quality range. Heat transfer coefficients in the grooved tube tend to be 3 or 4 times that in the smooth tube at low mass flux (100 - 200 $\frac{kg}{m^2 s}$).

At 300 $\frac{kg}{m^2 s}$, the heat transfer in the grooved tube is only about 1.3 times that in the smooth tube, and both sets of data indicate the flow is annular with a fairly uniform temperature distribution around the circumference of the tube. The scatter in the data is considerable, and probably due to the uncertainties in measuring the

small temperature differences that exist at these high heat transfer conditions.

Ebisu and Torikoshi [1998] recorded the circumferential heat transfer coefficients for 407C in both a helically grooved tube and a herringbone-enhanced tube in condensation and evaporation. The heat transfer coefficients for the helix tubes show almost identical trends with respect to mass quality as the Yoshida et al. study discussed above. Although the temperatures and pressures for condensation and evaporation were different, the data show similar uniformity as well as similar values for heat transfer coefficients.

A study of condensation of R22 and R22, R114 mixtures by Koyama et al. [1990] included circumferential temperature measurements during condensation of pure R22. These indicate highest heat transfer on the left side of the tube, with heat transfer decreasing on the bottom, top, and right side, respectively. These measurments suggested a liquid distribution with the thickest and thinnest regions rotated in the direction of the groove rotation.

Cho and Kim [1998] performed circumferential measurements in test sections with U-bends. At the entrance, the heat transfer coefficient distribution agrees well with the results of other researchers. However, flow through the bends appears to be able to induce an inversion of the patterns, and after three bends, the heat transfer coefficients are more uniformly distributed. Heat transfer coefficients for R-22 are consistently higher through the bends of the microfin tube than those of the smooth tube. It seems, perhaps, that the microfin tube tends to maintain annular flow through the bend while in the smooth tube liquid becomes highly disordered.

Heat transfer and pressure drop data for round and oval micro-fin tubes at mass flux conditions similar to those found in consumer refrigeration products were presented by Kim et al. [2000]. Their data show higher wall superheat temperatures on the bottom and right side of the tube with the top and left sides nearly equal. As quality increases, the temperature measurements converge. Similar trends are observed in the oval tube with the major axis either horizontal or vertical.

These studies bring out common behaviors in the circumferential measurements of heat transfer. First, at conditions where liquid flow in a smooth tube would be expected to be stratified with little heat transfer occurring through the top of the tube, the microfin tubes show very high heat transfer coefficients. Next, these heat transfer coefficients tend to be asymmetrical. The highest heat transfer takes place on the top or left side of the tube, the lowest to the bottom and right.

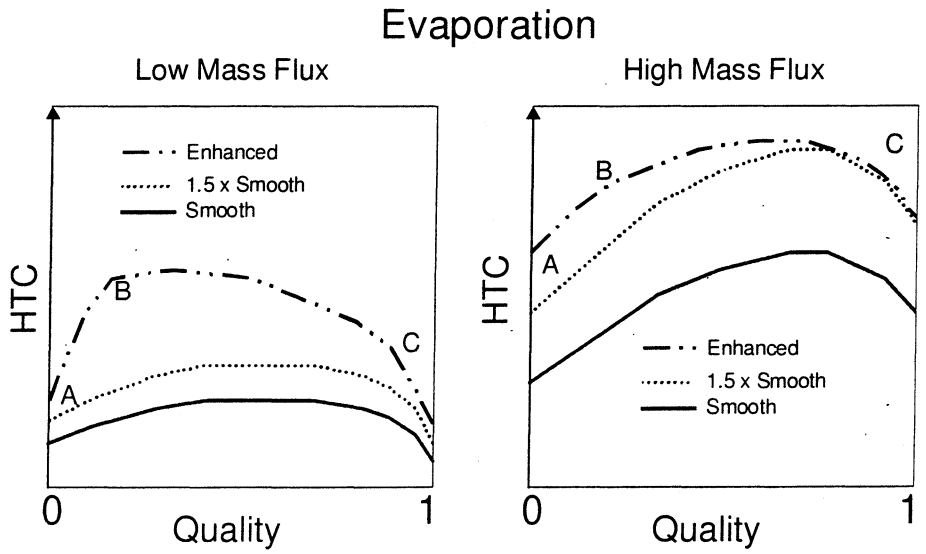

Figure 5.10: Generalized evaporative heat transfer behavior for smooth and helical microfin tubes. The 1.5 × Smooth curves represent the approximate enhancement due to the increased surface area alone. Fluid behavior in the regions marked A, B and C are discussed in the text.

This behavior appears to be well-described by the film thickness results obtained in this study. Looking at Figures 5.6 – 5.9, it is apparent that the grooves act to distribute liquid counterclockwise, from the bottom to the top. The profiles are also asymmetrical, being thinnest in the upper left and thickest in the lower right. It appears quite clear, then, that the grooves are contributing to heat transfer enhancement by assisting in the transition from stratified to annular flow, and that detailed knowledge of the liquid film distribution can lead to accurate predictions of circumferential heat transfer coefficients.

Heat transfer enhancement versus mass flux and mass quality

Substantial amounts of data have been gathered relating heat transfer behavior to system flow variables. Extensive reviews of pertinent heat transfer research in microfin tubes may be found in Newell and Shah [1999] and Webb [1990]. General trends are shown in Figures 5.10 and 5.11.

The behavior noted in region A in Figure 5.10 for evaporation has been studied in some detail. At very low quality, most of the fins are completely submerged by a thick, slow moving liquid. Here, nucleate boiling is significant. The heat transfer

coefficient is enhanced by more than just the additional surface area because, apparently, the grooves act to promote vapor nucleation [Webb, 1990, Carey, 1992, Koyama et al., 1995]. This situation occurs at both low and high mass flux, though the earlier transition to annular flow at higher mass flux limits this behavior.

New behavior appears as quality is increased slightly. At low mass flux, where flow in a smooth tube would be stratified with a thick liquid pool on the bottom, liquid is wicked up by surface tension in the microfins to form a very thin liquid layer around the top of the tube which is very effective for evaporation [Ito and Kimura, 1979, Kimura and Ito, 1981, Yoshida et al., 1987, 1988, Xu and Carey, 1990]. This leads to the sharp increase in heat transfer noted by several researchers.

As can be seen from the results of the current experiment in Figures 5.7 and 5.9, the grooves act to promote the transition from stratified to annular flow at low qualities, particularly as mass flux is increased. Hence, the high mass flux plot indicates that the heat transfer enhancement at B is due instead to the redistribution of the liquid by the grooves, and not by capillary wetting. The redistribution effect is active at lower mass flux, too, as can be seen from the results plotted in Figures 5.6 and 5.8. The enhancement seen at mid-qualities of the low mass flux is much greater than 1.5 times the smooth tube because, as noted in the current experiment, the *wetted* surface area is significantly increased in the microfin tube over the smooth tube. A similar explanation can be given for the additional enhancement of the high mass flux flow in region B of that plot.

No clear explanation for the decrease in heat transfer enhancement with increase mass flux has been offered in the literature. The current experimental results offer insight. As can be seen from the plots of film profiles in Figures 5.6–5.9, as mass flux and/or quality increases, the film profiles in the grooved tubes approach the profiles in the smooth tubes very closely. Based on this result, it can be said that, in evaporation, the heat transfer enhancement at high quality and/or high mass flux is due almost solely to the increased surface area offered by the grooves. Hence, the enhanced tube curves approach the 1.5 $\times$ Smooth curves in region C of the plots.

As discussed, fluid behavior under normal condensation conditions is somewhat different than that in evaporation, so it is expected that the nature of the heat transfer behavior will be different as well. At the beginning of the condensation process, drop-wise condensation dominates, leading to the very high heat transfer coefficients in the C regions of both the plots in Figure 5.11. The rather steep decline as

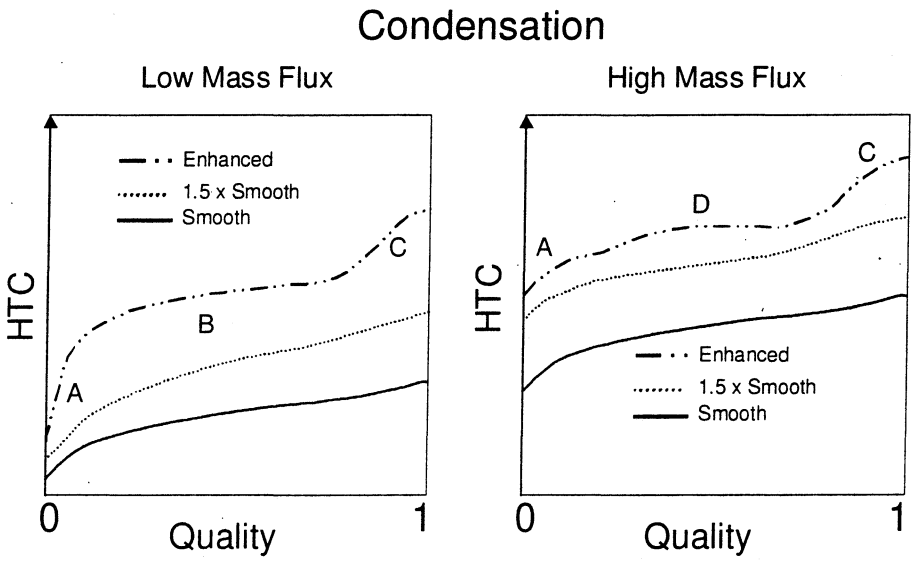

Figure 5.11: Generalized condensation heat transfer behavior for smooth and helical microfin tubes. The 1.5 × Smooth curves represent the approximate enhancement due to the increased surface area alone. Fluid behavior in the regions marked A, B, C and D are discussed in the text.

quality decreases marks the onset of film condensation.

At lower mass flux, due to the lower vapor velocities typical in condensation, the liquid in a smooth tube would tend to fall into a stratified flow. In the helical microgrooved tube, however, some balance of surface tension and shear forces act to significantly enhance the condensation heat transfer, as discussed in detail above. This explains the significant enhancement noted in region B of the low mass flux plot.

Region D of the high mass flux plot in Figure 5.11 is dominated by annular flow similar to that shown in the film profiles for Flows T, U, and Q of the current experiment. That the heat transfer remains higher than the surface area increase, as is consistently found in the literature, may be due to the more uniform film distribution, allowing more of the tube surface to play an active role in the condensation. In addition, as will be discussed in Chapter 6, the grooves appear to affect the wave behavior of the liquid film, which could further enhance the heat transfer.

As the condensation process nears completion, the heat transfer enhancement approaches that of the percentage increase in surface area, with some additional enhancement due to capillary or shear forces providing increased wetting of the

tube surface.

5.8 Pressure drop

Pressure drop data in smooth and microfin tubes have been attained by Khanpara et al. [1987], Schlager et al. [1989c,b, 1990], Eckels et al. [1998b], Eckels and Pate [1991], Eckels et al. [1994a,b, 1992], Kuo and Wang [1996], Chamra et al. [1996b,a]. Interpretation of pressure drop data is somewhat problematic due to the difficulty of performing accurate measurements. Data in the literature generally have uncertainties of 10% to 30%. In addition, most of the data presented are averaged values for evaporation or condensation over a quality range of 0.1 to 0.8. As will be noted, this can be misleading as the pressure drop behavior changes dramatically at the onset of dryout which frequently occurs at about x = 0.8.

That said, general trends are evident. Penalty factors, defined as the ratio of pressure drop in a microfin tube to that in a smooth tube, are approximately 1.2 to 1.3 for evaporation for the four refrigerants used in the survey (R12, R134a, R407C and R22), though penalty factors as high as 1.5 are found as well. In addition, the evaporation penalty factor is fairly insensitive to changes in mass flux. Condensation, on the other hand, tends to have penalty factors of 1.8 to 1.5. The data consistently show a decreasing trend with mass flux as well. For R22, the data generally show that the condensation penalty factor begins low at low mass flux (100 $\frac{kg}{m^2 s}$ or below), then increases to greater than 1.5 above G = 150 $\frac{kg}{m^2 s}$ after which it declines with increasing mass flux. This behavior indicates a possible transition from stratified to annular flow which is not apparent in the R134a data due to the much lower vapor densities (30% lower) in the latter. The condensation penalty factors are more sensitive to vapor density changes.

The most notable behavior in the pressure drop data is that microfin tubes generate on average only 10% to 80% additional pressure loss over smooth tubes. As noted above, the transition to annular flow is enhanced by the grooves, so the grooves remain completely covered by the liquid film for much of the quality range. Hence, the vapor does not directly interact with the grooves for much of the length of the heat exchanger. In addition, as noted by Ito and Kimura [1979], apparently grooves with angles less than 30 degrees do not behave as pure surface roughness.

Studies performed by Nidegger et al. [1997], Zürcher et al. [1997] and Zürcher

et al. [1998b,a] for evaporation of R134a and R407C in smooth and microfin tubes indicate a strong correlation between heat transfer data and pressure drop data, particularly at high qualities. As quality increases, heat transfer coefficients peak at qualities ranging from 0.75 to 0.95, depending on the mass flux; the pressure drop data show very similar peaks.

The peaks in both heat transfer and pressure drop mark the onset of dryout in the tube. This form of dryout was described in Chapter 2 and is apparently caused by vapor shearing the liquid layer to a point where the liquid can no longer maintain continuity. Just prior to this point, the film will be at its thinnest and most uniform distribution, leading to the lowest heat transfer resistance for that flow condition. In addition, the accelerational pressure drop will be greatest due to high velocity vapor interacting with a continuous liquid layer. Once dryout begins, heat transfer immediately falls. Pressure drop decreases as well because the dry wall, whether smooth or grooved, offers much less flow resistance than the liquid film.

This behavior is seen as well in the work of Reid et al. [1991] where the peaks in heat transfer coefficient and pressure drop coincide at much lower qualities as an applied heat flux causes dryout to occur much sooner.

5.9 Conclusion

Using the results of detailed film thickness measurements, a more complete picture of the mechanisms of heat transfer augmentation in enhanced tubes has been presented. These results show that helical grooves promote earlier transitions to to annular flow and give a rotated asymmetrical liquid film profile. These liquid profiles correspond to circumferential heat transfer measurements reported in the literature. In addition, the increased uniformity of the film at high qualities provides an explanation for the decrease in enhancement at higher mass flux and/or qualities seen in the literature.

Significant issues remain as to how exactly the grooves affect the liquid film. The effect of groove angle and the number of grooves on heat transfer is not clear. In addition, it will be important to quantify the forces acting on the liquid film in grooved tubes so that accurate models of heat transfer and pressure drop can be built. Finally, more investigation needs to be done before the unique behavior of the axially grooved tubes can be understood.

5.10 References

M. Benhalilou and N. Kasagi. Numerical prediction of heat and momentum transfer over micro-grooved surface with non-linear $\kappa - \epsilon$ model. *International Journal of Heat and Mass Transfer*, 42:2525–2541, 1999.

V. P. Carey. *Liquid-Vapor Phase-Change Phenomena.* Taylor & Francis, Hemisphere Publishing Corporation, Bristol, PA, 1992.

L. M. Chamra and R. L. Webb. Condensation and evaporation in micro-fin tubes at equal saturation temperatures. *Journal of Enhanced Heat Transfer*, 2(3):219–229, 1995.

L. M. Chamra, R. L. Webb, and M. R. Randlett. Advanced micro-fin tubes for condensation. *International Journal of Heat and Mass Transfer*, 39(9):1839–1846, 1996b.

L. M. Chamra, R. L. Webb, and M. R. Randlett. Advanced micro-fin tubes for evaporation. *International Journal of Heat and Mass Transfer*, 39(9):1827–1838, 1996a.

K. Cho and B. G. Kim. Heat transfer characteristics in the u-bend of a microfin tube evaporator using R-407c. *ASHRAE Transactions*, 105:1151–1158, 1998.

S. Cui, Y. Tan, and Y. Lu. Heat transfer and flow resistance of R-502 flow boiling inside horizontal ISF tubes. In X.-J. Chen, T. N. Veziroğlu, and C. L. Tien, editors, *Multiphase Flow and Heat Transfer: Second International Symposium*, volume 1, pages 662–670. Hemisphere Publishing Corp, 1992.

F. Dobran. Hydrodynamic and heat transfer analysis of two-phase annular flow with a new liquid film model of turbulence. *International Journal of Heat and Mass Transfer*, 26(8):1159–1171, 1983.

F. Dobran. Heat transfer in an annular two-phase flow. *Journal of Heat Transfer – Transactions of the ASME*, 107:472–476, 1985.

T. Ebisu and K. Torikoshi. Experimental study on evaporation and condensation heat transfer enhancement for r-407c using herringbone heat transfer tube. *ASHRAE Transactions*, 106:1044–1052, 1998.

S. J. Eckels, T. M. Doerr, and M. B. Pate. In-tube heat transfer and pressure drop of R-134a and ester lubricant mixtures in a smooth tube and a micro-fin tube: part i - evaporation. *ASHRAE Transactions*, 100(2):265–282, 1994a.

S. J. Eckels, T. M. Doerr, and M. B. Pate. In-tube heat transfer and pressure drop of R-134a and ester lubricant mixtures in a smooth tube and a micro-fin tube: part ii - condensation. *ASHRAE Transactions*, 100(2):283–294, 1994b.

S. J. Eckels, T. M. Doerr, and M. B. Pate. A comparison of the heat transfer and pressure drop performance of R-134a-lubricant mixtures in different diameter smooth tubes and micro-fin tube. *ASHRAE Transactions*, 104(1A):366–375, 1998a.

S. J. Eckels, T. M. Doerr, and M. B. Pate. Heat transfer coefficients and pressure drops for R-134a and an ester lubricant mixture in a smooth tube and a micro-fin tube. *ASHRAE Transactions*, 104(1A):366–375, 1998b.

S. J. Eckels and M. B. Pate. Evaporation and condensation of HFC-134a and CFC-12 in a smooth and a micro-fin tube. *ASHRAE Transactions*, 97(2):11 pages–Preprint, 1991.

S. J. Eckels, M. B. Pate, and C. H. Bemisderfer. Evaporation heat transfer coefficients for R-22 in micro-fin tubes of different configurations. *ASME HTD, Enhanced Heat Transfer*, 202:117–125, 1992.

T. Fujii. Enhancement to condensing heat transfer. *Journal of Enhanced Heat Transfer*, 2(1-2):127–137, 1995.

D. Graham, J. C. Chato, and T. A. Newell. Heat transfer and pressure drop during condensation of Refrigerant 134a in an axially grooved tube. *International Journal of Heat and Mass Transfer*, 42(11):1935–1944, June 1999.

G. F. Hewitt, S. Jayanti, and C. B. Hope. Structure of thin liquid films in gas–liquid horizontal flow. *International Journal of Multiphase Flow*, 16(6):951–957, 1990.

E. T. Hurlburt and T. A. Newell. Prediction of the circumferential film thickness distribution in horizontal annular gas-liquid flow. *Journal of Fluids Engineering – Transactions of the ASME*, 122:1–7, 2000.

M. Ito and H. Kimura. Boiling heat transfer and pressure drop in internal spiral-grooved tubes. *Bulletin of the JSME*, 22(171):1251–1257, September 1979.

S. Jayanti and G. F. Hewitt. Hydrodynamics and heat transfer in wavy annular gas-liquid flow: a computational fluid dynamics study. *International Journal of Heat and Mass Transfer*, 40(10):2445–2460, 1997a.

S. Jayanti and G. F. Hewitt. Hydrodynamics and heat transfer of wavy thin film flow. *International Journal of Heat and Mass Transfer*, 40(1):179–190, 1997b.

J. C. Khanpara, A. E. Bergles, and M. B. Pate. Augmentation of R-113 in-tube evaporation with micro-fin tubes. *ASHRAE Transactions*, 92(2B):506–524, 1986.

J. C. Khanpara, A. E. Bergles, and M. B. Pate. A comparison of in-tube evaporation of Refrigerant 113 in electrically heated and fluid heated smooth and inner-fin tubes. In *Advances in Enhanced Heat Transfer - 1987, Proceedings of the24th National Heat Transfer Conference*, volume HTD-68, pages 35–45, Pittsburgh, PA, 1987. ASME.

J. C. Khanpara, M. B. Pate, and A. E. Bergles. Local evaporation heat transfer in a smooth tube and a micro-fin tube using refrigerants 22 and 113. In *Boiling and Condensation in Heat Transfer Equipment. Presented at the Winter Annual Meeting of the American Society of Mechanical Engineers*, volume HTD-85, pages 31–39, Boston, MA, 1988. ASME.

M.-H. Kim, J.-S. Shin, and C. W. Bullard. Heat transfer and pressure drop characteristics during R22 evaporation in an oval micro-fin tube. In D. R. Tree, editor, *Eighth International Refrigeration Conference at Purdue University*, pages 1–8, West Lafayette, IN, 2000.

H. Kimura and M. Ito. Evaporating heat transfer in horizontal internal spiral-grooved tubes in the region of low flow rates. *Bulletin of the JSME*, 24(195): 1602–1607, September 1981.

S. Koyama, A. Miyara, H. Takamatsu, and T. Fujii. Condensation heat transfer of binary refrigerant mixtures of R22 and R114 inside a horizontal tube with internal spiral grooves. *International Journal of Refrigeration*, 13:256–263, 1990.

S. Koyama, J. Yu, S. Momoki, T. Fujii, and H. Honda. Forced convective flow boiling heat transfer of pure refrigerants inside a horizontal microfin tube. In John C Chen, editor, *Convective Flow Boiling: Proceedings of the International Conference on Convective Flow Boiling*, Banff, Alberta, Canada, April, May 1995. AIChE, ASME-HTD, Taylor and Francis.

C.-S. Kuo and C.-C. Wang. Horizontal flow boiling of R22 and R407C in a 9.52 mm micro-fin tube. *Applied Thermal Engineering*, 16(8/9):719–731, 1996.

S. Leuthner, A. H. Maun, and H. Auracher. Influence of waves on heat transfer to falling films of a binary mixture. In G. P. Celata, P. Di Marco, and R. K. Shah, editors, *Two-Phase Flow Modelling and Experimentation 1999*, volume 2, pages 1241–1247, Rome, Italy, May 1999. Edizioni ETS, Pisa.

S. P. Manwell and A. E. Bergles. Gas-liquid flow patterns in refrigerant-oil mixtures. *ASHRAE Transactions*, 96(2):456–464, 1990.

T. A. Newell and R. K. Shah. Refrigerant heat transfer, pressure drop and void fraction effects in microfin tubes. In G. P. Celata, P. Di Marco, and R. K. Shah, editors, *Two-Phase Flow Modelling and Experimentation 1999*, volume 3, pages 1623–1640, Rome, Italy, May 1999. Edizioni ETS, Pisa.

E. Nidegger, J. R. Thome, and D. Favrat. Flow boiling and pressure drop measurements for R-134a/oil mixtures, Part 1: Evaporation in a microfin tube. *HVAC&R Research*, 3(1):38–53, 1997.

S. Nozu and H. Honda. Flow characteristics of condensing two-phase flow in horizontal microfin tubes. *ASME Fluids Engineering Division*, 244:119–130, 1997.

R. Panton. *Incompressible Flow*. John Wiley & Sons, Inc., New York, second edition, 1996.

M. Ponchner and J. C. Chato. Condensation of HFC-134a in an 18° helix angle micro-finned tube. Technical Report TR-75, Air Conditioning and Refrigeration Center, University of Illinois at Urbana-Champaign, Urbana, IL, 1995.

T. S. Ravigururajan and A. E. Bergles. Visualization of flow phenomena near enhanced surfaces. *Journal of Heat Transfer-Transactions of the ASME*, 116(1): 54–57, February 1994.

R. S. Reid, M. B. Pate, and A. E. Bergles. A comparison of augmentation techniques during in-tube evaporation of R-113. *Journal of Heat Transfer – Transactions of the ASME*, 113:451–458, 1991.

L. M. Schlager, M. B. Pate, and A. E. Bergles. Evaporation and condensation of refrigerant-oil mixtures in a smooth tube and a micro-fin tube. *ASHRAE Transactions*, 93(1):149–166, 1988.

L. M. Schlager, M. B. Pate, and A. E. Bergles. A comparison of 150 and 300 sus oil effects on refrigerant evaporation and condensation in a smooth tube and a micro-fin tube. *AHSRAE Transactions*, 95:387–397, 1989a.

L. M. Schlager, M. B. Pate, and A. E. Bergles. Heat transfer and pressure drop during evaporation and condensation of R22 in horizontal micro-fin tubes. *International Journal of Refrigeration*, 12:6–14, January 1989c.

L. M. Schlager, M. B. Pate, and A. E. Bergles. Heat transfer and pressure drop performance of smooth and internally finned tubes with oil and refrigerant 22 mixtures. *ASHRAE Transactions*, 95(1):375–385, 1989b.

L. M. Schlager, M. B. Pate, and A. E. Bergles. Evaporation and condensation heat transfer and pressure drop in horizontal, 12.7-mm microfin tubes with refrigerant 22. *Journal of Heat Transfer – Transactions of the ASME*, 112:1041–1047, November 1990.

R. K. Shah, S. Q. Zhou, and K. A. Tagavi. The role of surface tension in film condensation in extended surface passages. *Journal of Enhanced Heat Transfer*, 6:179–216, 1999.

T. A. Shedd and T. A. Newell. Automated optical liquid film thickness measurement method. *Review of Scientific Instruments*, 69(12):4205–4213, December 1998.

N. Shikazono, M. Itoh, M. Uchida, T. Fukushima, and T. Hatada. An analytical model to predict the condesation heat transfer coefficient in horizontal microfin tubes. *ASHRAE Transactions*, 104(2):143–152, 1998.

A. Singh, M. M. Ohadi, and S. Dessiatoun. Flow boiling heat transfer coefficients of R-134a in a microfin tube. *Journal of Heat Transfer – Transactions of the ASME*, 118:497–499, 1996.

R. L. Webb. *Principles of Enhanced Heat Transfer*. John Wiley & Sons, Inc., New York, 1990.

J. Weisman, J. Lan, and P. Disimile. Two-phase (air-water) flow patterns and pressure drop in the presence of helical wire ribs. *International Journal of Multiphase Flow*, 20(5):885–899, 1994.

J. Weisman, J. Lan, and P. Disimile. The effect of fluid properties on two-phase (vapor-liquid) flow patterns in the presence of helical wire ribs. *International Journal of Multiphase Flow*, 22(3):613–619, 1996.

X. Xu and V. P. Carey. Film evaporation from a micro-grooved surface – an approximate heat transfer model and its comparison with experimental data. *Journal of Thermophysics*, 4(4):512–520, October 1990.

C.-Y. Yang. A critical review of condensation heat transfer predicting models – effects of surface-tension force. *Enhanced Heat Transfer*, 6:217–236, 1999.

C.-Y. Yang and R. L. Webb. Condensation of R-12 in small hydraulic diameter extruded aluminum tubes with and without microfins. *International Journal of Heat and Mass Transfer*, 39(4):791–800, 1995.

D. A. Yashar, M. J. Wilson, H. R. Kopke, D. M. Graham, J. C. Chato, and T. A. Newell. An investigation of refrigerant void fraction in horizontal, microfin tubes. *To be published in HVAC& R Research*, 2001.

S. Yoshida, T. Matsunaga, H. P. Hong, and K. Nishikawa. Heat transfer to refrigerants in horizontal evaporator tubes with internal, spiral grooves. In P J Marto, editor, *Proceedings of the 1987 ASME-JSME Thermal Engineering Joint Conference*, volume 5, pages 165–172, 1987.

S. Yoshida, T. Matsunaga, H. P. Hong, and K. Nishikawa. Heat transfer enhancement in horizontal, spirally grooved evaporator tubes. *JSME International Journal*, 31(3):505–512, 1988. Series II.

O. Zürcher, J. R. Thome, and D. Favrat. Flow boiling and pressure drop measurements for R-134a/oil mixtures, part 2: Evaporation in a plain tube. *HVAC&R Research*, 3(1):54–64, 1997.

O. Zürcher, J. R. Thome, and D. Favrat. In-tube flow boiling of R-407C and R-407C/oil mixtures part II: Plain tube results and predictions. *HVAC&R Research*, 4(4):373–399, 1998a.

O. Zürcher, J. R. Thome, and D. Favrat. In-tube flow boiling of R-407C and R-407C/oil mixtures part I: Microfin tube. *HVAC&R Research*, 4(4):347–372, 1998b.

6

The effects of the number and angle of microgrooves on the liquid film in annular two-phase flow

6.1 Introduction

Microfin tubes have become important components of modern air conditioning and refrigeration systems with their significantly enhanced heat transfer coefficients and low pressure loss characteristics. Though a substantial amount of data has been gathered and generalized predictive correlations have been generated with some success, a fundamental understanding of the two-phase vapor-liquid flow behavior through these tubes is still lacking. Looking at the patent documents for microfin tubes, it is apparent that the design process is generally one of trial-and-error, with optimum geometries determined by intensive experimentation (see, for example, Fujie et al. [1977] and Shinohara et al. [1987]). Not only is this a costly process, but the performance of these tubes varies with refrigerant and heat transfer mode (evaporation or condensation) making the design of more efficient tubing difficult.

To address these issues, a fundamental study of the two-phase vapor-liquid flow through tubes with microgrooves has been undertaken. In this work, detailed measurements of the liquid film distribution during the annular flow regime have been performed using a non-intrusive optical technique. In a previous work (Chapter 5) it was demonstrated that the grooves act to promote the transition from stratified to annular flow at lower qualities and/or liquid flow rates. In addition, it was noted that the steady-state film profiles tend to show a rotated symmetry; the thinnest and

thickest parts of the film tend to occur at locations shifted from the top or bottom center in the direction of the groove rotation.

Further observations indicated that the bulk of the film did not appear to be swirling or flowing along the grooves consistently. From these observations, it was hypothesized that the grooves, in effect, place a stress on the film at the wall in the circumferential direction in much the same manner as would a rotating tube. To test this idea, a simple model conceptually based on the annular flow model of Hurlburt and Newell [2000] and the circumferential flow model of Butterworth [1969], was constructed with such a constant circumferential stress at the wall and the results matched the experimental data examined.

This work describes the efforts to determine how the groove angle and the number of grooves affect the redistribution of the liquid film in annular flow and might relate to such a circumferential wall stress. First, a survey of research into groove angle effects will be presented followed by a description of the current experiment and results.

6.2 Background

Previous studies have focused on the effects of groove angle and number of grooves on heat transfer. As such, the majority present heat transfer results averaged over a range of qualities that generally lie between 0.15 and 0.8. The immediate difficulty with this is that in most cases, the tube wall does not begin to form dryout patches until qualities higher than 0.8, and since the wall enhancements likely have a pronounced effect on dryout, comparison of enhanced tube with plain tube performance may be misleading. As it directly pertains to this study, the averaged data are difficult to compare with the adiabatic data because the flow behavior at low qualities is markedly different than at high.

Hitachi's 1977 patent includes a plot of heat transfer performance versus groove angle as shown in Figure 6.1 [Fujie et al., 1977]. As described by Ito and Kimura [1979], the data for this plot were obtained by testing aluminum tubes with 0 (axial), 3, 7, 15, 30, and 75 degree grooves under varying mass and heat flux conditions. The data shown were for a mass flux of 121 $\frac{kg}{m^2 s}$ and heat flux of 18.3 $\frac{kW}{m^2}$ at an average quality of 0.6, though the inlet and outlet qualities were not given. The maximum at the low angles and subsequent decrease in performance as angle

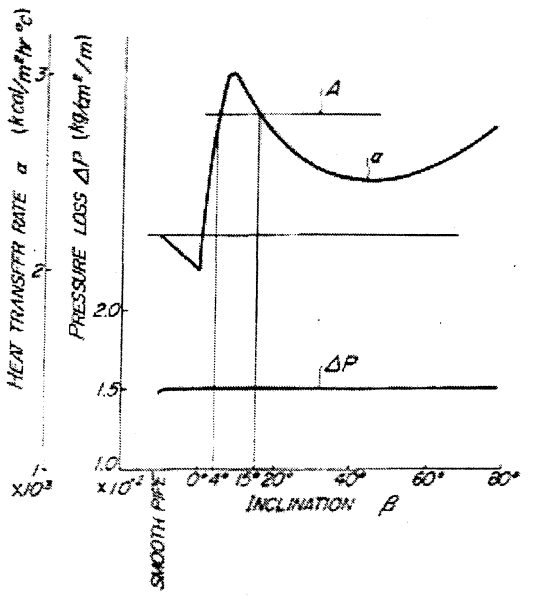

Figure 6.1: Heat transfer versus groove angle (inclination) as reported by Fujie et al. [1977].

increases is corroborated in a later study performed by Oh and Bergles [1998].

At a lower mass flux (50 $\frac{kg}{m^2 s}$), however, Oh and Bergles found that the best performing angle shifted higher to around 18 degrees with larger angles generally performing better than those below 12 degrees. This trend is shown in the data of Kimura and Ito [1981] and Yoshida et al. [1988] as well.

The work of Kimura et al. and Chamra et al. [1996a] shows that evaporation performance at a mass flux from about 100 - 200 $\frac{kg}{m^2 s}$ as a broad peak in tubes with angles ranging from about 18 to 25 degrees.

Averaged heat transfer coefficients obtained by Khanpara et al. [1986] and Schlager et al. [1989, 1990] for tubes with varying fin heights and shapes show that, in general, evaporation enhancement improves as the angle increases. The Schlager et al. data generally show the opposite trend for condensation, but this effect may be due to the variation in groove depth between the tubes. Condensation heat transfer is rather sensitive to groove depth due to the effects of surface tension on the film coating fins. Indeed, Chamra et al. [1996b] show the condensation heat transfer coefficient consistently to increase with fin angle.

Groove depth seemed to effect the pressure drop data of Schlager et al. as well. Groove depth appeared to be a greater factor than groove angle for a 9.52 mm tube.

Flows through a 12.7 mm tube behaved differently, with pressure drop proportional to groove angle, possibly because the groove depth relative to the diameter became less significant. In the data of Chamra et al., pressure drop in both condensation and evaporation rose linearly with groove angle. The small variation in groove number did not appear to influence either the heat transfer or pressure drop data.

Comparison of the performance of tubes with axial (0 degree helix) grooves to those with helical grooves is particularly interesting. Ito and Kimura [1979] found the performance of the axial tubes to be worse than any helical tube at all conditions tested in evaporation. Chiang [1993], on the other hand, tested condensation and evaporation at high mass flux and found that the axial tubes outperformed the helical at all flow and heat flux conditions but the lowest mass flux in evaporation. This difference may be explained completely or in part by the large differences in the geometries of the fins used in the axial and helical tubes tested. The helical tubes had fewer fins and a broader apex angle (40 to 50 degrees versus 15 degrees). The patent by Shinohara et al. [1987] documents that a tube with fins having 15 degree apex angles will outperform fins with 45 degree apex angles by almost 50% in both evaporation and condensation.

To address this geometrical discrepancy, Graham et al. [1999] undertook an experiment to compare the condensation performance of tubes with helical and axial fins of nearly identical geometries. They found that the axial tube outperformed the helical at mass flux conditions of 150 $\frac{kg}{m^2 s}$ and higher. The enhancement over the smooth tube was quality-dependent, however. When a simple flow regime indicator, the Froude rate, was applied to the data, it became apparent that the axial grooves appeared to maintain an annular flow condition to lower qualities than did a smooth or the helical tube.

Applying the same indicator to the Ito et al. data, it is seen that the poor axial performance around a quality of 0.6 may be due to the axial grooves delaying a transition to annular flow, or impeding the wetting of the tube wall by waves.

Less information has been published on the relationship between pressure loss and groove angle. Ito and Kimura, found that, for single phase flow, tubes with fins at 15 degrees or less generated only slightly larger pressure drops than smooth tubes. Fins at 30 degrees presented noticeable resistance, while the pressure drop increased to about 1.5 times the smooth tube at 45 degrees, about 2 times at 75 degrees and about 2.5 times at 90 degrees. Two-phase pressure drops were measured

Name	$\dot{m}_g$ kg/s	$\dot{m}_l$ kg/s	Ft	x	G kg/sm^2
T	0.0048	0.0032	70	0.6	44
U	0.0067	0.0032	120	0.68	55
V	0.0099	0.0032	210	0.76	73
Q	0.0047	0.0063	50	0.42	61
R	0.0079	0.0063	105	0.56	79
F	0.0110	0.0063	165	0.64	97
G	0.0152	0.0063	250	0.71	120

Table 6.1: Details of the experimental flow conditions. Ft is the Froude rate, x is quality and G is mass flux. See text for an explanation of the Froude rate parameter.

by Chamra et al. [1996b,a] for 15 to 27 degree fin angles and found to increase in a fairly linear manner with angle in both evaporation and condensation.

6.3 Experiment

The flow conditions examined are shown in Table 6.1.

The Froude rate, Ft, is a non-dimensional group that essentially represents the ratio of the rate of kinetic energy flowing in the vapor to the power required to pump liquid from the bottom to the top of the tube at its axial flow rate.

The test sections were constructed as described in Chapter 5. Three different tubes with 20 grooves were fabricated with angles of 0, 9 and 18 degrees. Three additional 18 degree helix tubes were made in the same manner with 4, 8 and 12 grooves.

An air/water flow loop, described in detail in Chapter 5, was used to establish the two-phase flow conditions. Filtered building water was used with filtered laboratory compressed air. The liquid mass flow rates were measured using floating-ball type rotameters while the air mass flow rate was determined using the pressure drop across a 3 m length of entrance tubing.

Film thickness measurements were obtained in the same manner as those reported in Chapter 5.

6.4 Influence of the helix angle on the liquid film profiles

Figures 6.2 through 6.5 show a direct comparison of the film profiles for all 7 flow conditions in the 0, 9 and 18 degree helix tubes, all with 20 grooves. The most striking behavior for the 9 and 18 degree helix tubes is the film rotation. The thinnest and thickest regions of these films appear to be rotated from the top and bottom center locations, respectively. From casual inspection, it is not clear which of the 9 or 18 degree helix rotate the film more.

The 0 degree, or axially grooved, tube behaves differently than the other two. Most noticeable are the regions on the sides of the tube where a stable, thicker film appears to form. These may be indications that forces pushing liquid up the wall meet resistance in the grooves and these locations reflect the equilibrium reached between the upward forces and gravity in the presence of the horizontal grooves. The rivulet at the top of the axial tube in Flow T (Figure 6.2 reflects the observed behavior that droplets landing on the upper surfaces of the axial tube tend to "stick" and combine to form rivulets flowing along the grooves. This could be a mechanism of enhanced wetting and film formation for the axial tubes in conditions where entrainment of liquid droplets is significant.

6.5 Influence of the number of grooves on the liquid film profiles

The film profiles in the 4, 8, 12 and 20 groove 18 degree helix tubes for Flows T, V, Q and F are presented in Figures 6.6 - 6.9. The remaining film profiles, along with tables of the local film thickness values, can be found in Appendix C. Though the profiles contain irregularities, the effect of increasing the number of grooves is readily apparent. In Flow Q, for instance, the thinnest and thickest parts of the film are not significantly offset from the smooth tube film for the 4 groove tube. As the number of grooves increases, an increasing amount of liquid appears to be drawing from the left side to the right side of the tube. Thus, the degree of rotation of the film profile appears to be directly related to the number of grooves, at least for these low numbers.

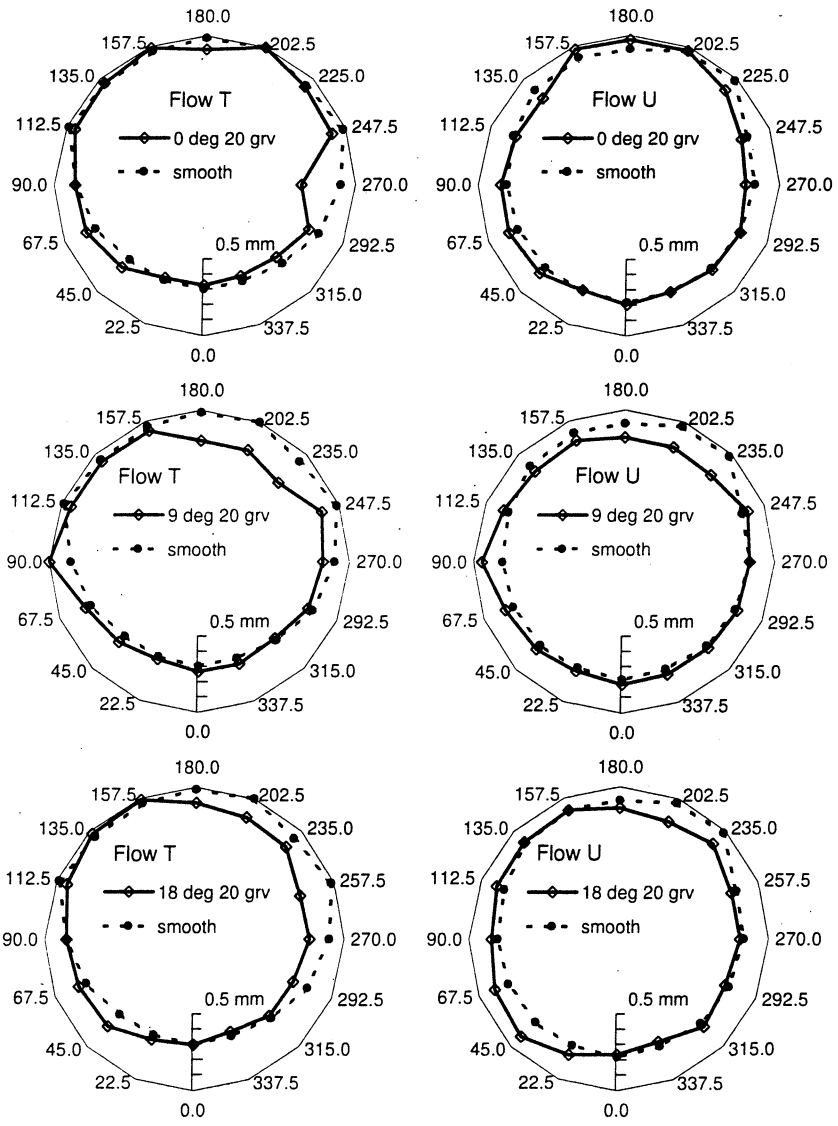

Figure 6.2: Film thickness profiles in the 0, 9 and 18 degree helix tubes for Flows T and U.

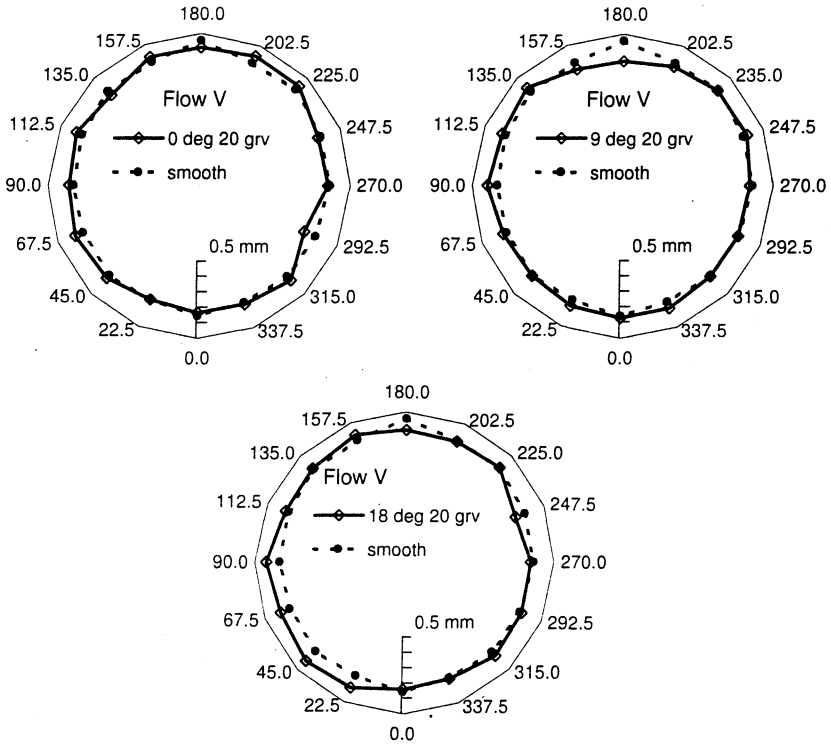

Figure 6.3: Film thickness profiles in the 0, 9 and 18 degree helix tubes for Flow V.

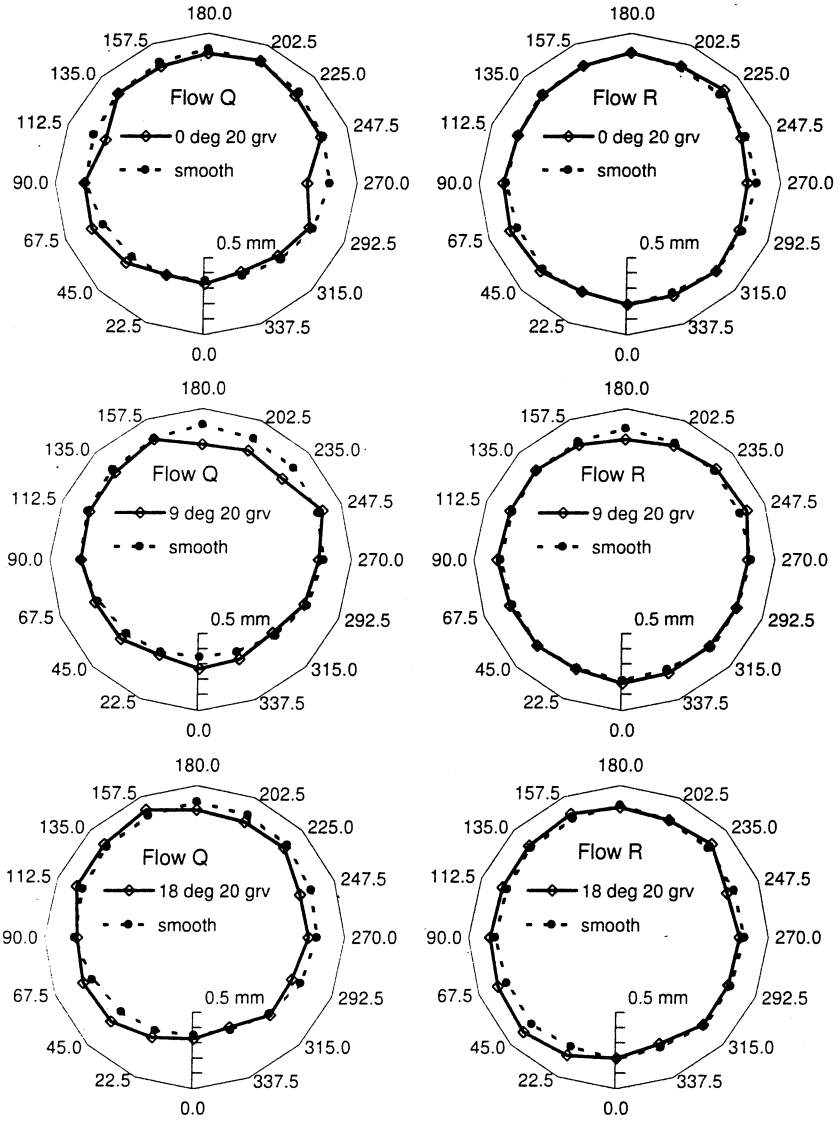

Figure 6.4: Film thickness profiles in the 0, 9 and 18 degree helix tubes for Flows Q and R.

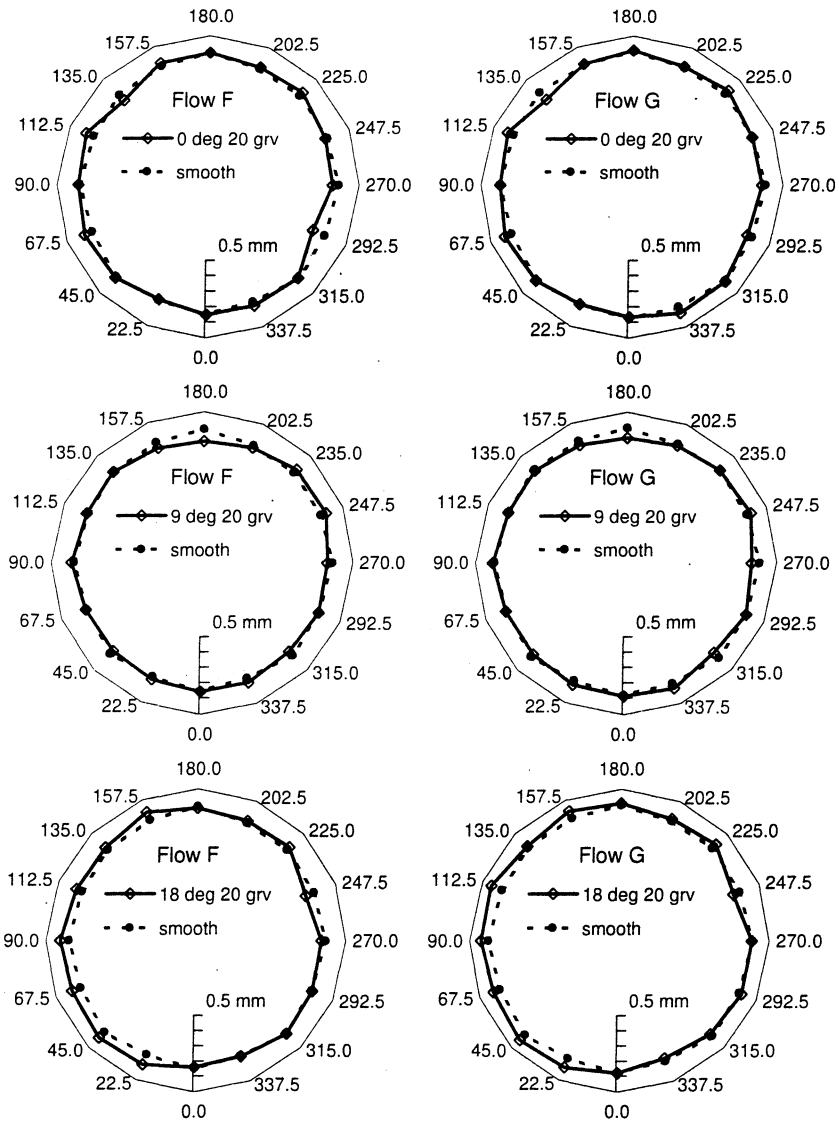

Figure 6.5: Film thickness profiles in the 0, 9 and 18 degree helix tubes for Flows F and G.

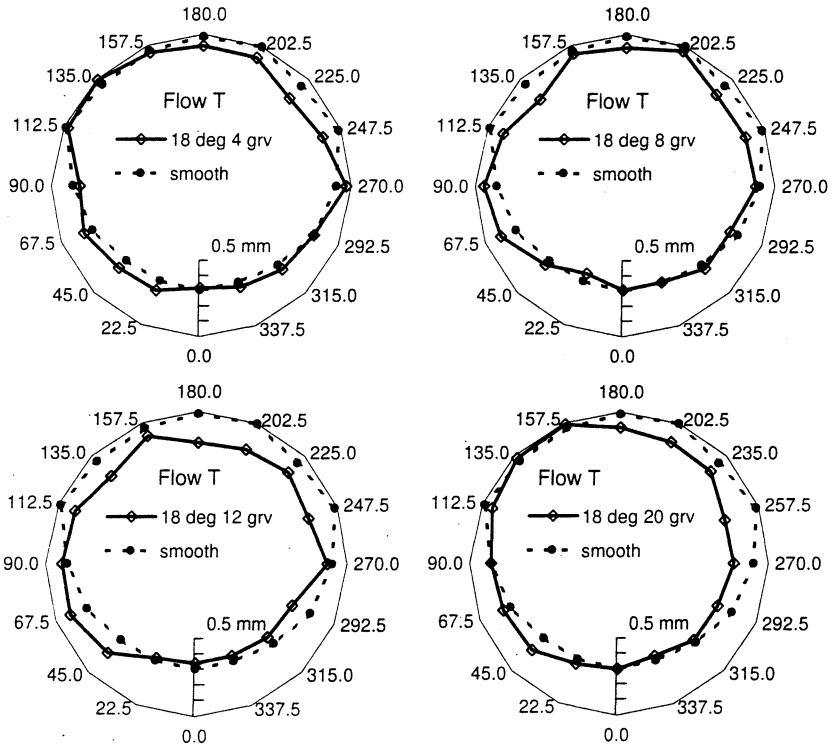

Figure 6.6: Film thickness profiles in tubes with 4, 8, 12 and 20 18 degree helix grooves for Flow T.

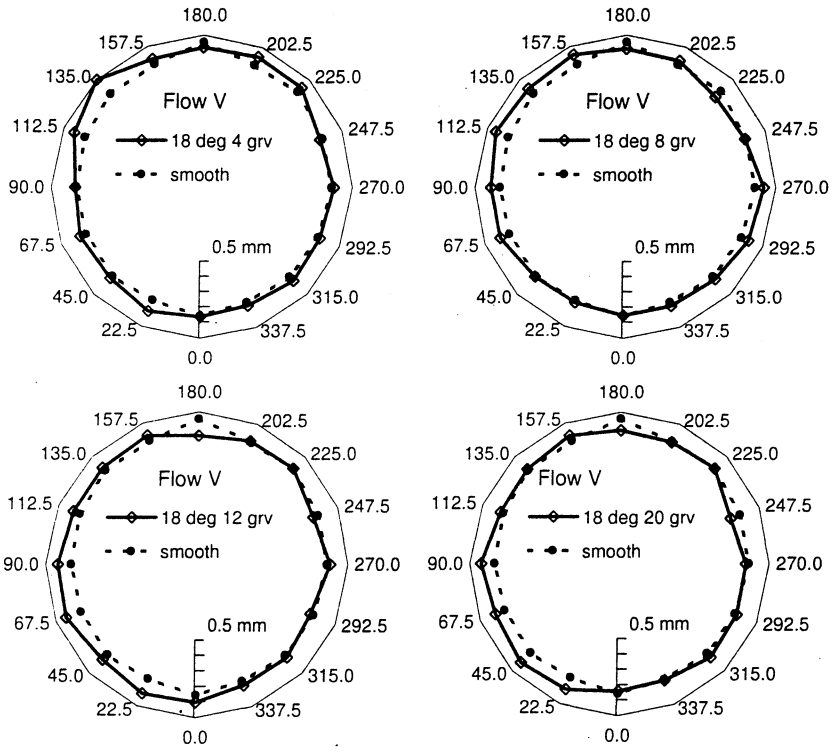

Figure 6.7: Film thickness profiles in tubes with 4, 8, 12 and 20 18 degree helix grooves for Flow V.

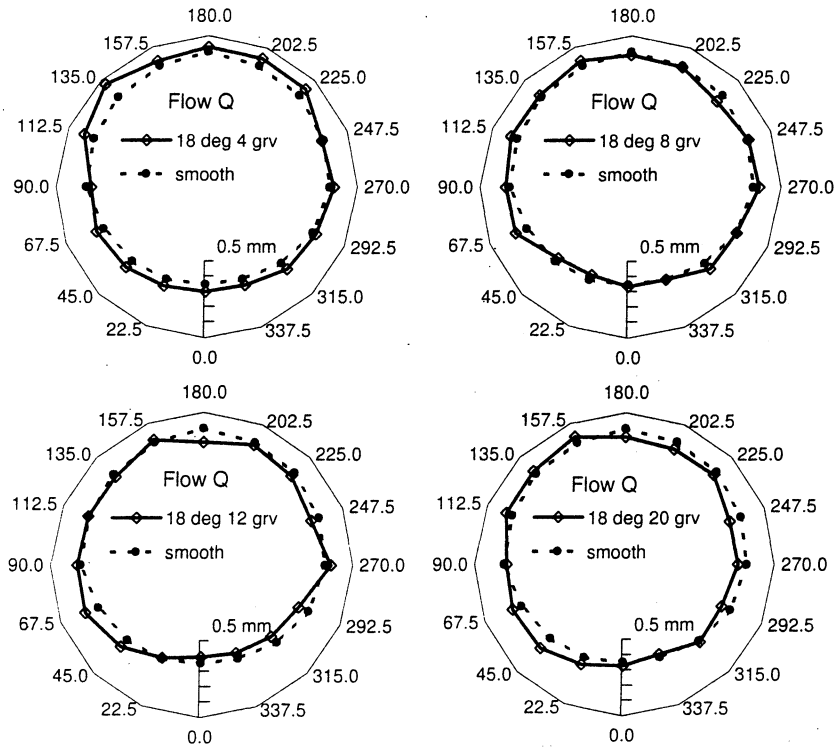

Figure 6.8: Film thickness profiles in tubes with 4, 8, 12 and 20 18 degree helix grooves for Flow Q.

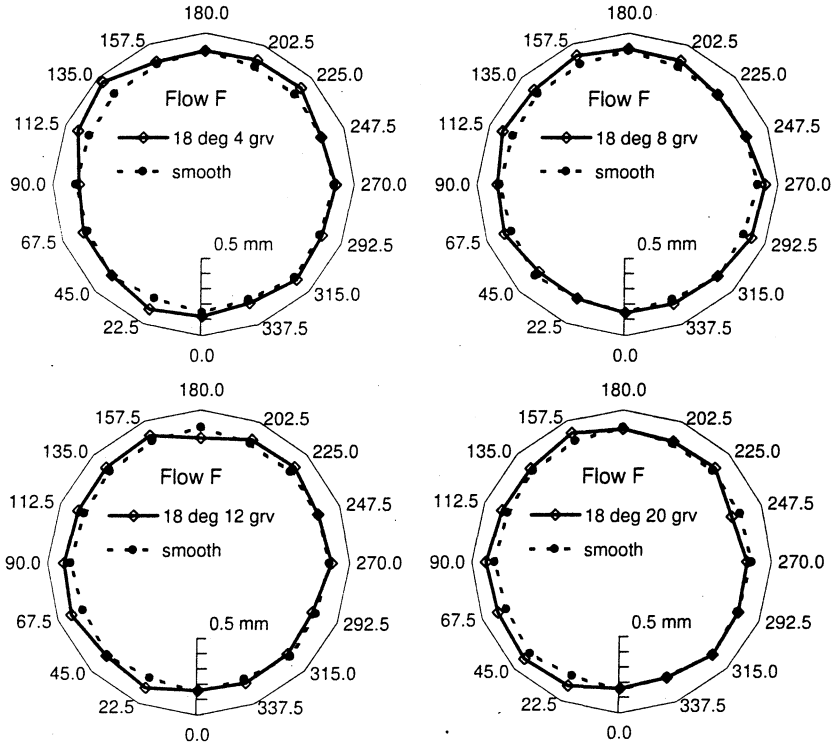

Figure 6.9: Film thickness profiles in tubes with 4, 8, 12 and 20 18 degree helix grooves for Flow F.

6.6 Quantifying the film rotation

It is apparent from the plots of the film profiles in the tube with helical grooves that the film appears to have been rotated; i.e. the thinnest and thickest parts of the film appear to have been shifted counterclockwise from the top and bottom center locations, respectively. Manual approximations of the angle through which the film was rotated proved to be very difficult and inconsistent, however. As a means of quantifying the rotation, a cross-correlation scheme was developed whereby an "ideal" film was rotated on top of the experimental data and the angle at which the highest correlation resulted was defined as the rotation angle of the film. The ideal film was a circle representing a uniform annular film that was then shifted upward slightly with respect to the tube wall. Initially placed at 0 degrees, the values of this eccentric circle at each of the data locations (every 22.5 degrees) was multiplied with the data and the sum of these products was found. The eccentric circle was then rotated 0.5 degrees and the process was repeated through 359.5 degrees.

The resulting correlation data contained a minimum and a maximum which, if the experimental data were truly a rotated form of the symmetrical smooth tube profile, would be separated by 180 degrees. In practice, the separation was between 175 and 185 degrees. As a general observation, flows with markedly thicker films on the bottom, such as T and Q, show less of a rotation within the thicker region than in the thinner region, thus leading to a greater separation between the angles of rotation at the maximum and minimum film locations. The final definition of the film rotation angle was the average of the angles through which the minimum and maximum were rotated from their center positions.

Counterclockwise rotation was defined to be positive in agreement with the direction of the helical grooves in the tube.

This method appeared to be very effective and produced results that seemed to agree with visual inspection of the plots. However the determination of the angle of rotation of the more uniform films was quite sensitive to small variations in thickness. For example, a change of 0.01 mm at one location of a Flow G profile could change the rotation by 10 degrees or more.

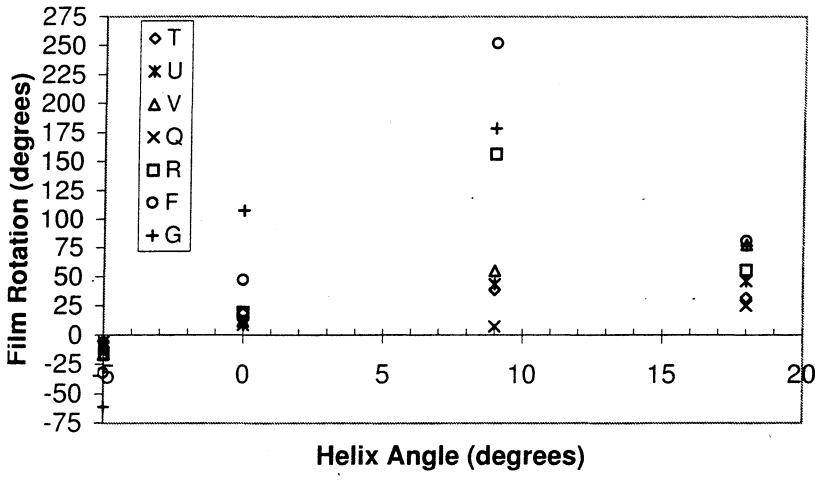

Figure 6.10: Film rotation versus helix angle. Positive rotation angle indicates a counterclockwise rotation. The data on the Y-axis represent the smooth tube film rotation.

6.7 Rotation of the film and the groove helix angle

Figure 6.10 shows how the film rotation angle, γ, determined by the cross-correlation method just described, varies with tube helix angle for each of the flows. At each helix angle, the film rotation is generally proportional to the vapor velocity. No clear trends are evident from this data as to the relation of helix angle to film rotation. Inspection of the film profile plots will confirm that the large rotation angles of the 9 degree data appear to be physically reasonable. No explanation can be offered for this inversion of the film.

An interesting observation from this plot is that the smooth tube data was never perfectly symmetrical with the vertical. The negative rotation angle indicates that the films were rotated clockwise with respect to a vertically symmetric film. It is possible that the magnitude of the very large rotations for Flows F and G (-32 and -61 degrees, respectively) are not the true film rotations due to the sensitivity of the correlation method when applied to these relatively uniform films. However, close inspection of the plots and film thickness data (See Appendix B) indicate that, indeed, the axis of vertical symmetry in the film has been rotated, and that changes of the film thickness on the order of the standard error (about 0.003 mm) would have little effect on the profiles or the symmetry.

There is no reason to suspect that an annular film would tend to have a clockwise

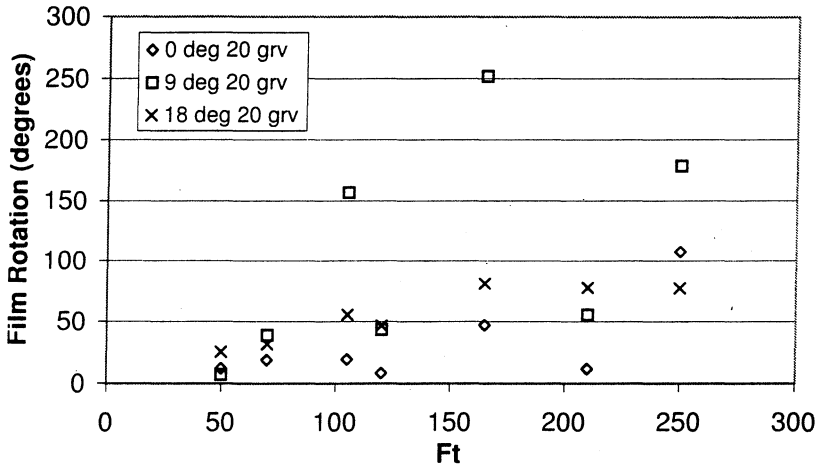

Figure 6.11: Film rotation versus Froude rate (Ft) with helix angle as a parameter.

rotation in general. It is likely that this rotation is related to small variations in the vapor and liquid flow induced by the particular orientation and construction of the flow loop. While it is usually assumed that the liquid film in annular flow through smooth tubes drains under the influence of gravity in a symmetrical manner down either side, a small variation in the flow could cause the film to preferentially drain to one side or the other. Thus, while it is almost universally assumed that the liquid film profiles in horizontal smooth tubes are vertically symmetrical it appears that, in fact, this may be the exception rather than the rule.

Figure 6.11 presents the film rotation plotted against the Froude rate for each of the different helix angles. The data are sufficiently scattered that no real trend may be extracted.

6.8 Film thickness and the groove helix angle

The relation of the groove helix angle to the average film thickness over the wetted tube perimeter is shown in Figure 6.12. It is interesting to note that, except at the lowest Froude rates (50, 70; Flows T and Q, the most asymmetrical flows), the 18 degree helix tube consistently has a lower average film thickness. The absolute differences in film thickness between the smooth and the 18 degree tube are on the order of 0.030 mm for the upper four flows, a difference of about 20%. This is also significantly greater than the standard error for the measurements.

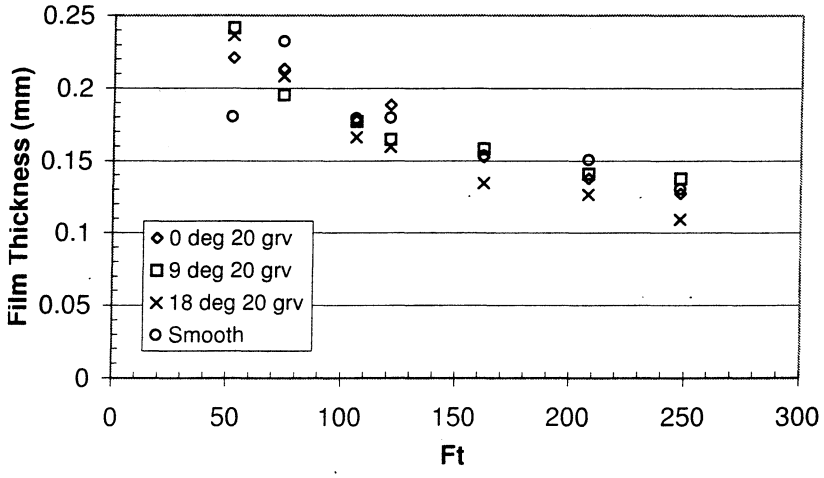

Figure 6.12: Average film thickness over the wetted perimeter plotted against Froude rate.

Visual observation of the flow did not indicate any significant difference in behavior between the 18 degree tube and the others, other than the increased wetting of the walls. However, the 9 degree, and to some extent, the 0 degree, tubes showed increased wetting as well, yet the average film thickness did not fall as far in those tubes.

Figure 6.13 presents the standard error of the film thickness measurements versus the non-dimensional film thickness, h^+, for all seven flows in the four tubes. The determination of h^+ is discussed in Chapter 3. Since the film thickness was measured using light reflected from the surface fluctuations in the surface of the liquid will cause variations in the reflection. The standard error reported here includes the scattering of light due to the passage of large waves on the liquid film. Hence, these plots provide some indication as to the waviness of the liquid surface.

Two interesting trends are apparent in the film thickness standard error plots. One, the general level of standard error rises with angle from the smooth to the 0, 9, and 18 degree tubes. This trend generally coincides with the thinner average film results reported in Figure 6.12. Thus, it appears possible that additional liquid mass is being carried by wave structures, leaving behind less film in the base layer. In addition, Figure 6.13 indicates that the error level rises for thinner films as the angle increases for the 9 and 18 degree tubes. The error level appears nearly constant for the 0 degree tube across the span of film thickness. This possibly indicates that

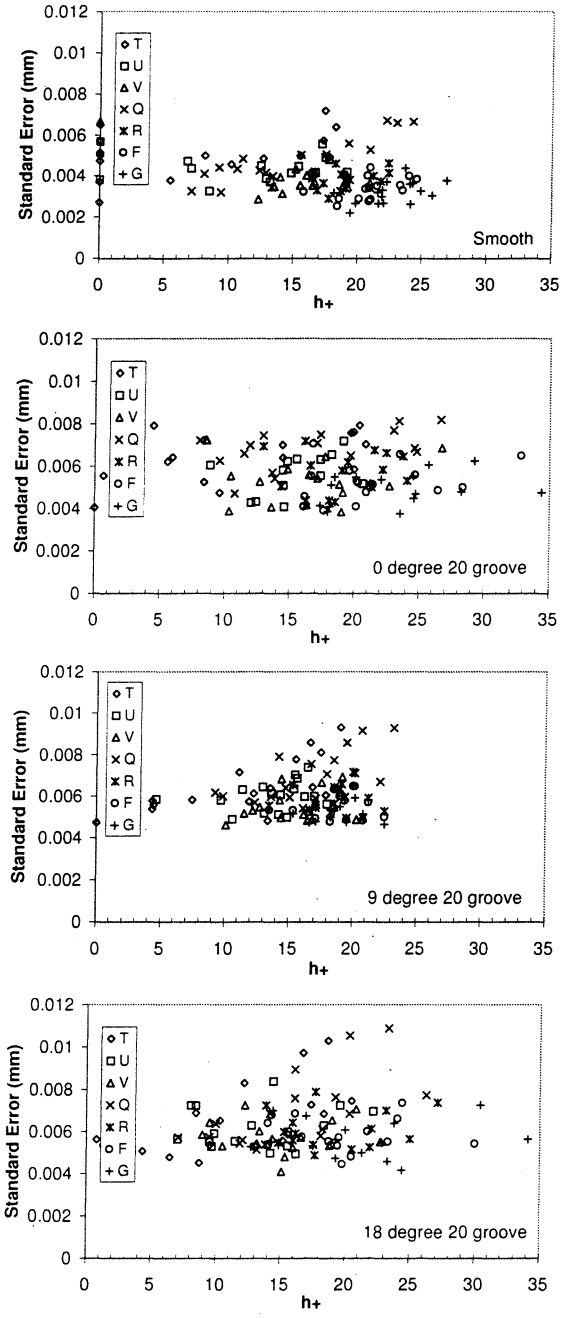

Figure 6.13: Plots of the standard errors in the optical film thickness measurements versus the non-dimensional film thickness, h^+.

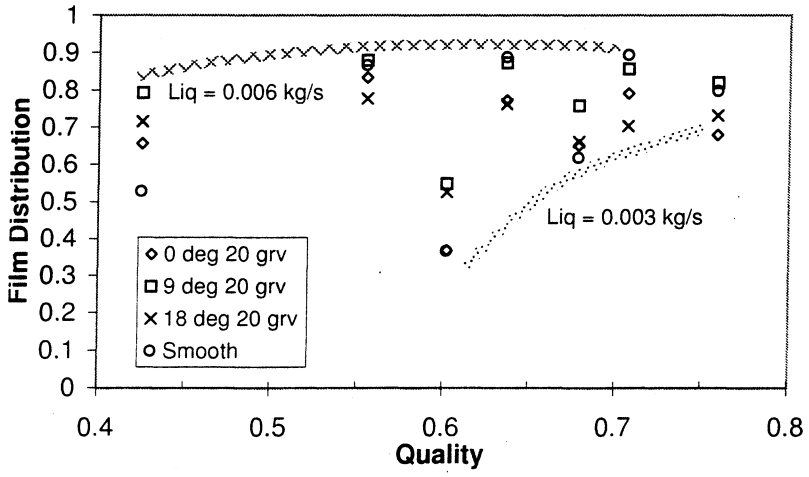

Figure 6.14: Film distribution versus mass quality with groove helix angle as a parameter. Thick lines indicate groupings of data by liquid mass flow rate.

waves become more uniformly distributed around the tube, or at least that their characteristics become circumferentially more uniform.

The film distribution parameter is plotted against mass quality in Figure 6.14 with groove helix angle as a parameter. The 9 degree tube tended to show consistently better distribution across all flow conditions than any of the other tubes, although the 18 degree tube consistently had the thinnest average film thickness. Of particular interest is the observation that the smooth tube performs significantly worse than the grooved tubes at the lowest quality condition for each liquid mass flow. This is consistent with heat transfer data showing that grooved tubes show greatest enhancement over smooth at lower qualities and mass flux. This is apparently due to the increased wetting of the wall by the action of the grooves and somewhat increased uniformity. At higher qualities where the smooth tube annular film becomes more uniform, the heat transfer enhancement diminishes significantly and a similar trend could be inferred from the film distribution data presented here.

6.9 Film rotation and the number of grooves

When the angle of film rotation is plotted against the number of grooves in the tube for the same helix angle (18 degrees), some basic behaviors become apparent, as shown in Figure 6.15. Generally, the rotation angle increases with number of

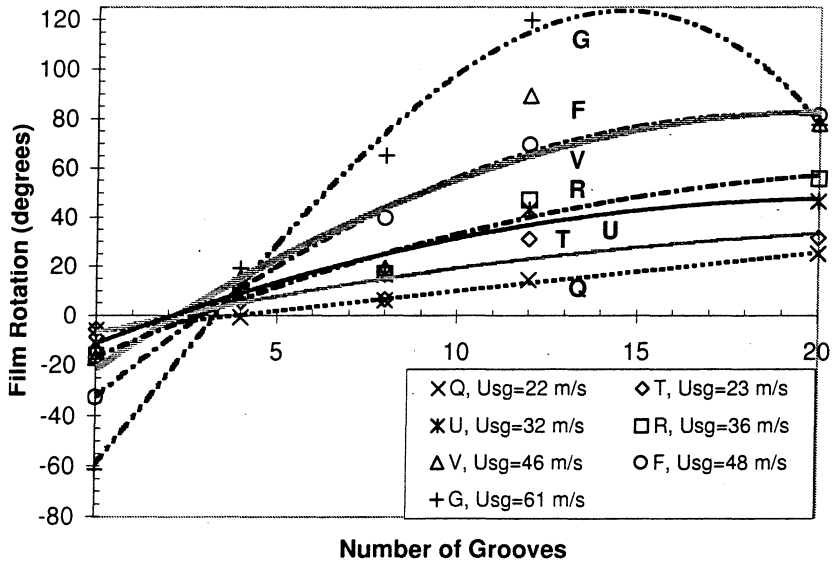

Figure 6.15: Film rotation versus number of helical grooves. The grooves in each case had a helix angle of 18 degrees. Smooth tube data is shown on the y-axis. Patterned lines are polynomial curve fits of the raw data to better bring out trends.

grooves. It is not clear why a peak should occur in the 12 groove data. When a polynomial fit was applied to the data for each flow, the angle of rotation appeared to be directly related to the vapor velocity.

In Figure 6.16, the relation of film rotation to vapor velocity is evident. However, it appears that the rotation reaches a limiting condition at 12 grooves. The 12 and 20 groove tubes have essentially the same behavior. A relation between the film rotation, γ, and the gas velocity and number of grooves, n, was determined to be

$$\gamma(n, U_{sg}) = A_1(n)U_{sg} + B_1(n) \tag{6.1}$$

where

$$A_1 = 0.22n - 0.46 \tag{6.2}$$

$$B_1 = 4.67 - 3n. \tag{6.3}$$

The predictions based on this equation are plotted in Figure 6.16 as solid lines.

While the data were well-correlated by the vapor velocity alone, it was found that including a liquid mass flow effect through the Froude rate was somewhat more effective, as shown in Figure 6.17. A predictive relation based on Ft is

$$\gamma(n, Ft) = A_2(n)Ft + B_2(n) \tag{6.4}$$

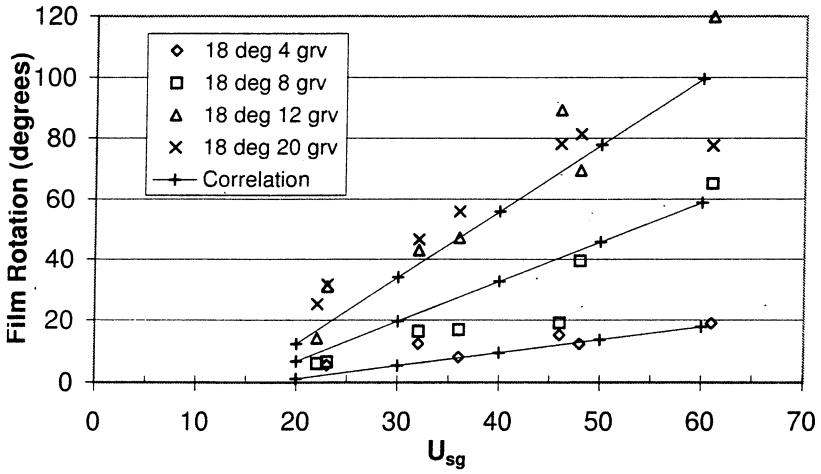

Figure 6.16: Film rotation versus the superficial gas velocity, U_{sg}.

where

$$A_2 = 0.051n - 0.13 \tag{6.5}$$

$$B_2 = 2.41 - 0.98n. \tag{6.6}$$

The predictions based on this equation are plotted in Figure 6.17 as solid lines.

6.10 Film thickness and the number of grooves

The effect of the number of grooves on the mean base film thickness is investigated through Figure 6.18. Similarly to the film thickness behavior with variation in helix angle, the base film is thicker in the grooved tubes for the lowest, stratified-annular flow condition. The remaining data, however, show that the grooves act in some manner to thin the base layer. No definite trend exists with respect to the number of grooves, but the 8 groove tube often generated the thinnest film. From inspection of the film thickness standard error plots in Figure 6.19, it seems that the waviness of the film is increased in the 8 groove tube over that in the 20 groove and that the film thinning may be related to this increased surface activity.

At most of the flow conditions tested, the number of grooves appeared to have little effect on the flow distribution as displayed in Figure 6.20. At the lowest vapor flow rates for each of the two liquid flows, however, the distribution improves in the 20 groove tube by almost 50% over the smooth tube. In addition, the 0.006

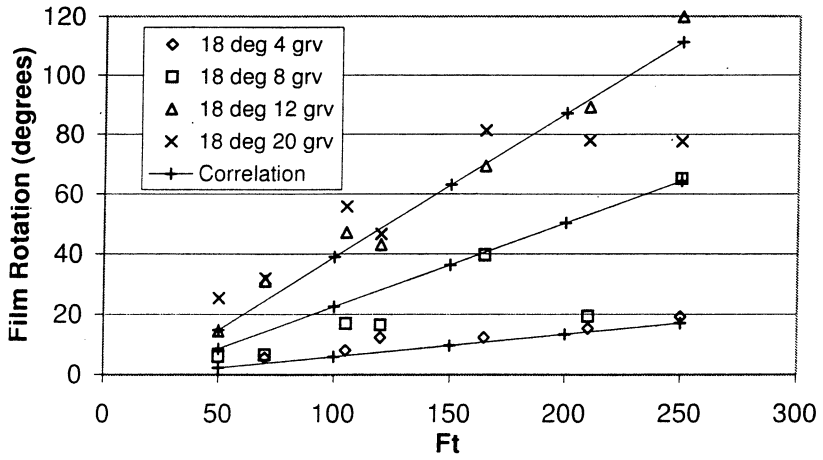

Figure 6.17: Film rotation versus Froude rate with varying numbers of grooves.

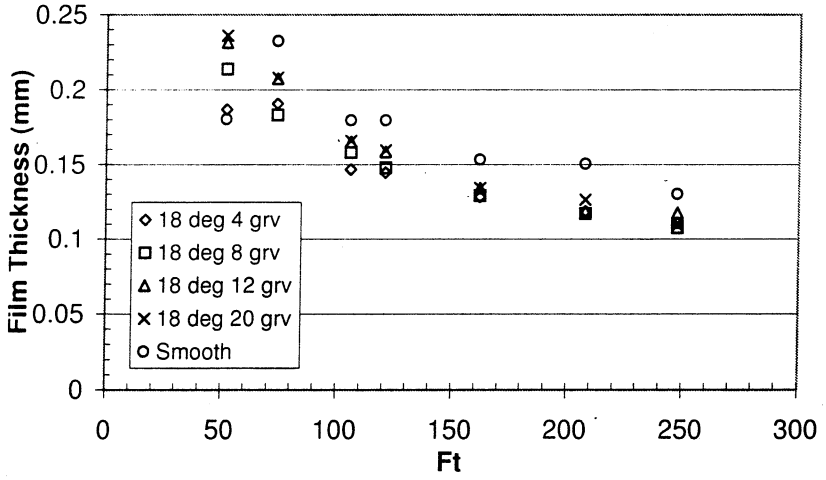

Figure 6.18: Film thickness versus Froude rate and different numbers of grooves.

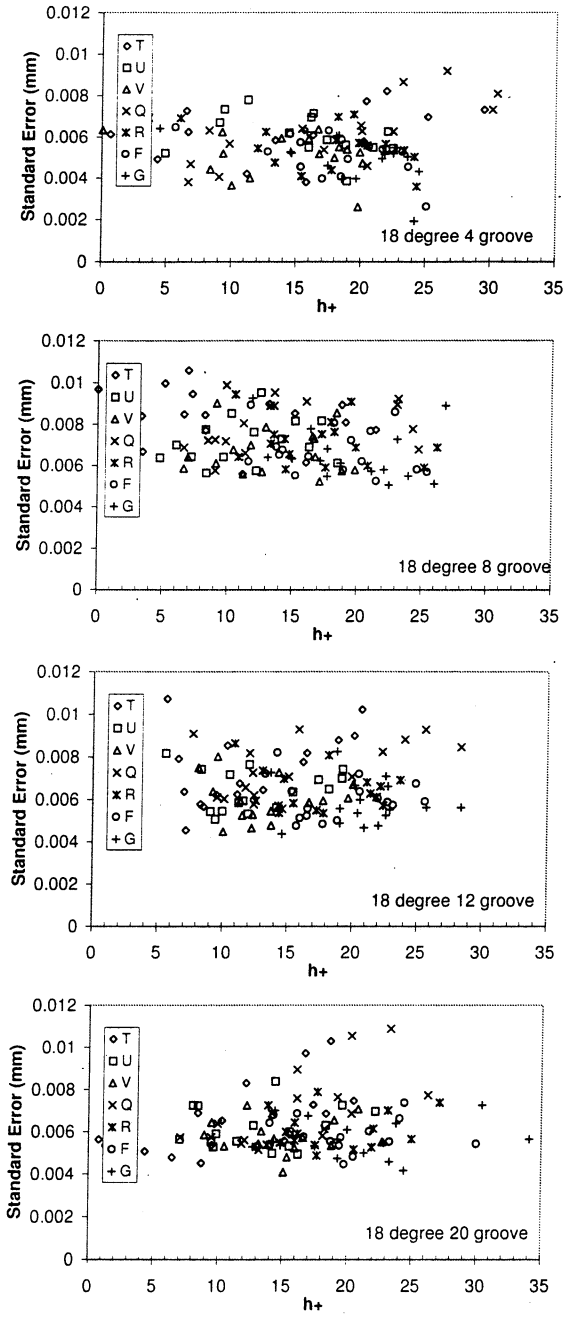

Figure 6.19: Plots of the standard errors in the optical film thickness measurements versus the non-dimensional film thickness, h^+, as the number of grooves increases.

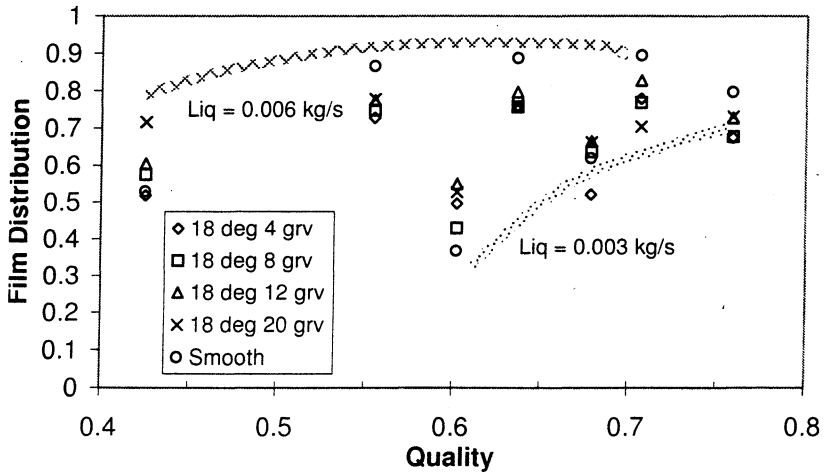

Figure 6.20: Film distribution versus quality with varying number of grooves.

kg/s, 0.42 quality data show that the distribution is directly related to the number of grooves.

6.11 Pressure drop

Figure 6.21 plots the friction factors of the various tubes against the Lockhart-Martinelli parameter, X_{tt}. Clearly the presence of the grooves has only a minor effect on the pressure loss in the tubes. Groove angle appears to have only a small effect which is more pronounced in the higher liquid flow data. If the axial groove points are excluded, the friction factor is essentially directly proportional to the groove angle for three of the 0.006 kg/s flows. No clear pattern exists in the 0.003 kg/s data except at the lowest X_{tt} point where the pattern follows the 0.006 kg/s data. Pressure loss in the axial groove tube tends to coincide with the 18 degree data.

Although the effect is small, the friction factor is more directly related to groove number. As shown in Figure 6.22, frictional loss increases with groove number for all but two of the 0.003 kg/s data points. It is believed that at these two points where the 4 groove tube presents the highest friction factors, the results are influenced by a poorly formed joint in the test section. At these lowest flows, the vapor flow is sensitive to this gap between tubes and the pressure drop shows this. When the liquid flow is greater or more evenly distributed, the small gap is filled with liquid

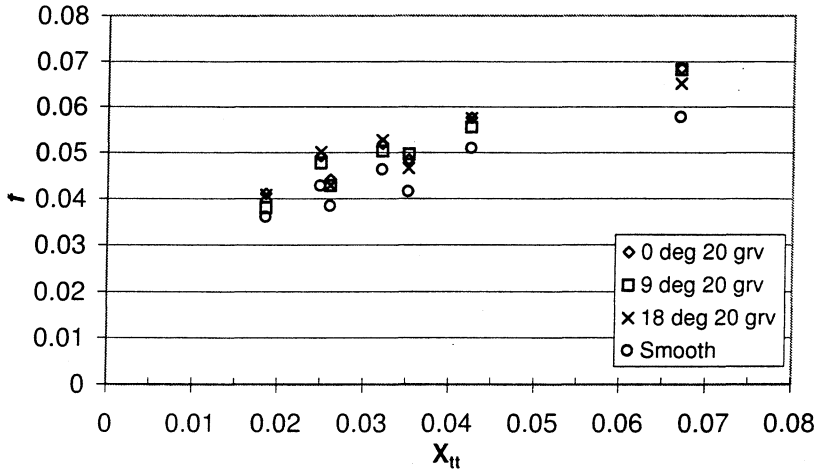

Figure 6.21: Friction factor versus X_{tt} for tubes with different angles of grooves.

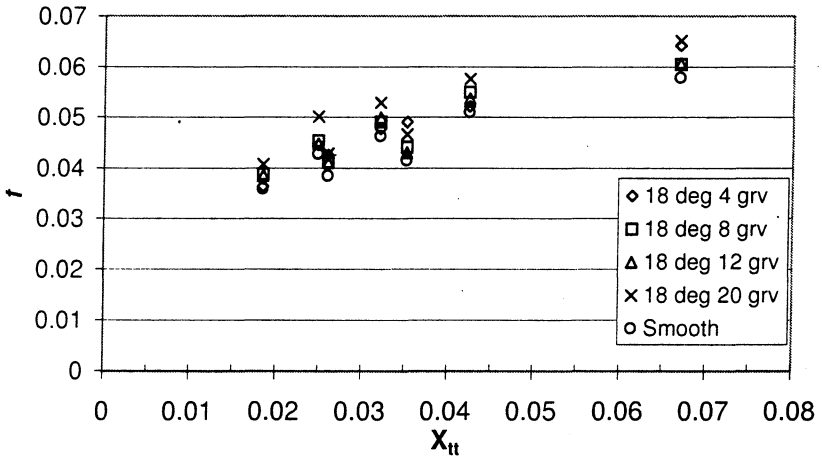

Figure 6.22: Friction factor versus X_{tt} for tubes with different numbers of grooves.

and the vapor flow is minimally affected.

6.12 Summary

The key findings of this work are:

- A relatively small number of grooves are necessary to redistribute the liquid film; this redistribution can be correlated with vapor phase velocity
- The grooves act in some manner so as to affect the stability of the liquid interface
- The grooves can alter the flow such that lower mean film thickness values result
- The pressure loss is directly related to the number of grooves in the tube, at least for these small numbers

No clear relationship was found between groove angle and film rotation. Clearer understanding may be gained by using tubes with a wider variation of helix angles. Effects of large numbers of grooves such as used in commercial products have not been addressed by this study. In addition, the impact of the grooves on the film stability warrants further investigation. Better knowledge of these areas could provide direction for optimizing the patterns used to improve the performance of future heat transfer tubing.

6.13 References

D. Butterworth. Note on fully-developed, horizontal, annular two-phase flow. *Chemical Engineering Science*, 24:1832–1834, 1969.

L. M. Chamra, R. L. Webb, and M. R. Randlett. Advanced micro-fin tubes for condensation. *International Journal of Heat and Mass Transfer*, 39(9):1839–1846, 1996b.

L. M. Chamra, R. L. Webb, and M. R. Randlett. Advanced micro-fin tubes for evaporation. *International Journal of Heat and Mass Transfer*, 39(9):1827–1838, 1996a.

R. Chiang. Heat transfer and pressure drop during evaporation and condensation of Refrigerant-22 in 7.5 mm and 10 mm diameter axial and helical grooved tubes. *Heat Transfer – Atlanta 1993*, 89(295):205–210, 1993.

K. Fujie, M. Itoh, T. Innami, H. Kimura, W. Nakayama, and T. Yanagida. Heat transfer pipe. U.S. Patent Number 4,044,797, 1977.

D. Graham, J. C. Chato, and T. A. Newell. Heat transfer and pressure drop during condensation of Refrigerant 134a in an axially grooved tube. *International Journal of Heat and Mass Transfer*, 42(11):1935–1944, June 1999.

E. T. Hurlburt and T. A. Newell. Prediction of the circumferential film thickness distribution in horizontal annular gas-liquid flow. *Journal of Fluids Engineering – Transactions of the ASME*, 122:1–7, 2000.

M. Ito and H. Kimura. Boiling heat transfer and pressure drop in internal spiral-grooved tubes. *Bulletin of the JSME*, 22(171):1251–1257, September 1979.

J. C. Khanpara, A. E. Bergles, and M. B. Pate. Augmentation of R-113 in-tube evaporation with micro-fin tubes. *ASHRAE Transactions*, 92(2B):506–524, 1986.

H. Kimura and M. Ito. Evaporating heat transfer in horizontal internal spiral-grooved tubes in the region of low flow rates. *Bulletin of the JSME*, 24(195): 1602–1607, September 1981.

S. Y. Oh and A. E. Bergles. Experimental study of the effects of the spiral angle on evaporative heat transfer enhancement in microfin tubes. *ASHRAE Transactions*, 104(2):1137–1143, 1998.

L. M. Schlager, M. B. Pate, and A. E. Bergles. Heat transfer and pressure drop during evaporation and condensation of R22 in horizontal micro-fin tubes. *International Journal of Refrigeration*, 12:6–14, January 1989.

L. M. Schlager, M. B. Pate, and A. E. Bergles. Evaporation and condensation heat transfer and pressure drop in horizontal, 12.7-mm microfin tubes with refrigerant 22. *Journal of Heat Transfer – Transactions of the ASME*, 112:1041–1047, November 1990.

Y. Shinohara, K. Oizumi, Y. Itoh, and M. Hori. Heat-transfer tubes with grooved inner surface. U.S. Patent Number 4,658,892, 1987. Ammended 1990.

S. Yoshida, T. Matsunaga, H. P. Hong, and K. Nishikawa. Heat transfer enhancement in horizontal, spirally grooved evaporator tubes. *JSME International Journal*, 31(3):505–512, 1988. Series II.

7

Thin film particle image velocimetry

7.1 Introduction

A review of horizontal two-phase annular flow literature will reveal that there exists no clear agreement on the mechanisms responsible for the distribution of the liquid film. Evidence has been gathered to support a number of different theories with some success. The wave spreading action suggested by Butterworth [1972] has received some support from an analysis of film thickness measurements by Jayanti et al. [1990]. Fukano and Ousaka [1989] suggest that disturbance waves play a dominant role through a pumping action caused by a gradient in static pressure within the wave. Clearly, the ability to quantify local flow behavior within the liquid film itself would be of great utility in modeling the liquid film flow, after which more general models of pressure loss and heat transfer could be built.

Several efforts have been made to study the nature of the velocity field within the thin liquid film. Photochromic dye tracing was used to obtain axial flow profiles by Hewitt et al. [1990]. Sutharshan et al. [1995] and Kawaji [1998] implemented the photochromic dye technique to obtain axial velocity profiles in stratified films (> 5 mm) as well as average circumferential base film flow velocities in annular flow. These measurements, together with qualitative analysis of the dye movement, provided evidence for the upward flow of liquid during the passage of a disturbance wave. Paras and Karabelas [1992] used Laser Doppler Anemometry in thick (4 - 5 mm) stratified and stratified-annular liquid films to obtain axial velocity profiles and turbulence statistics, while Nasr-Esfahany and Kawaji [1996] did the same using hot film anemometry in much thicker liquid flows (about 20 mm).

Oxide powders have been used by Fukano et al. [1985] and Hagiwara et al.

[1982] to obtain the velocity of the liquid film surface. A particle tracking technique was implemented by Hagiwara et al. [1995] in annular flow to give some indication of circumferential velocity components within the liquid film.

The present work describes the application of Particle Image Velocimetry (PIV) to the measurement of velocity fields in the liquid film. PIV has been applied to two-phase bubbly flows in the past, but apparently not to thin film flows [Oakley et al., 1997]. Promising results have been generated, but the method is still in development. This paper will describe the methods developed for seeding the liquid film, capturing multiple particle images and processing the images to produce velocity vectors. Important issues need to be resolved, including how the velocities of the particles relate to velocities within the film and the effect of particles on the film turbulence.

7.2 Thin film PIV

Particle Image Velocimetry is a well-established technique for determining instantaneous velocity flow fields [Adrian, 1991, Raffel et al., 1998]. Current two-dimensional implementations illuminate seed particles in a three dimensional flow field with a sheet of light to ensure that only movements within a plane are recorded by the digital or conventional camera. This light sheet needs to be pulsed at least two times and needs to be of high intensity so that enough light is scattered from the particles to be captured by the film or video camera. In two-phase annular flow, however, the films are frequently much less than a millimeter thick – typical films in this study are no more than 350 μm thick, though disturbance waves are thought to be about five times this – so particles in the liquid layer are essentially restricted to movement in two-dimensions. Instead of a pulsed laser, then, a stroboscope provides regular pulses of light which doubly or triply expose the particles.

Thin film PIV is being developed on an air/water loop that is described in detail in Chapter 5. Figure 7.1 shows the setup used to inject small (0.05 to 0.08 mm diameter) glass spheres into the liquid flow. A pressurized air stream mixes with particles as it passes through particle container. The air/particle mixture is joined to the water feed just before the liquid enters the test section. Liquid flows into the test section through holes in the test section wall and forms an annular film.

This particle injection scheme was determined to be most effective after at-

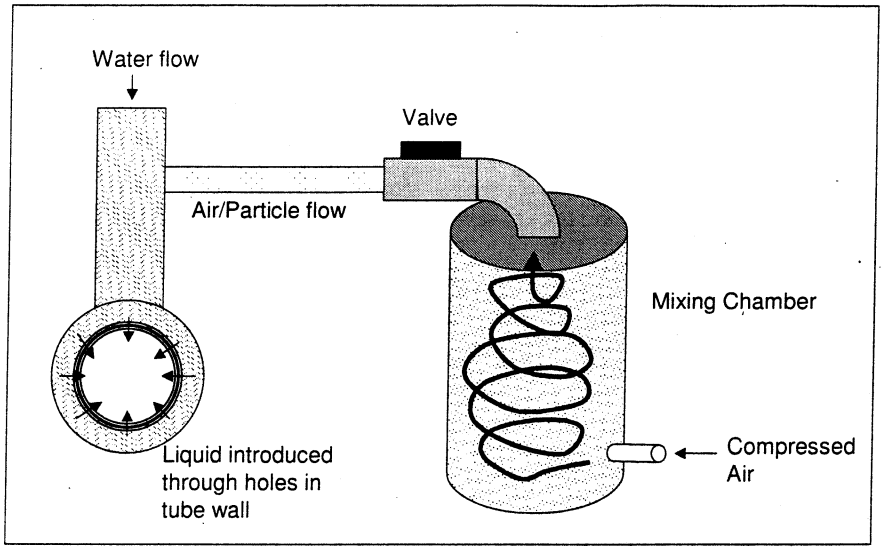

Figure 7.1: Schematic of particle injection system.

tempting several other methods. Mixing the particles directly with liquid was problematic due to the very low liquid flow rates used. Particles would quickly collect at any constriction and clog the flow. Though the total mass flow of air used to transport the particles is quite small, the velocity is high enough to keep particles from collecting. This setup allowed some control of particle density, as well, using the valve at the outlet of the particle container. On an experimental setup with a more sophisticated liquid feed, it may be easier to directly mix the particles with the liquid without the problems experienced here.

At the measurement location, the film is illuminated by a constant series of strobe pulses timed so that 2 or 3 images of each particle are captured in each frame of video. The experimental video setup is shown in Figure 7.2. The position of the light source was found to be important; a position approximately 45 degrees above or below the tube on the side opposite the camera worked well. The light was adjusted for the best contrast by viewing the flow through the camera display. At some angles, the particles were not visible at all. It is believed that the light enters the liquid film from the rear if the tube and travels through the film to the front in the same manner that light is carried by a fiber optic. Light striking a particle from the rear (with respect to the camera) will tend to scatter forward according to Mie scattering theory [Raffel et al., 1998], which appears to explain why this position for the light source works best.

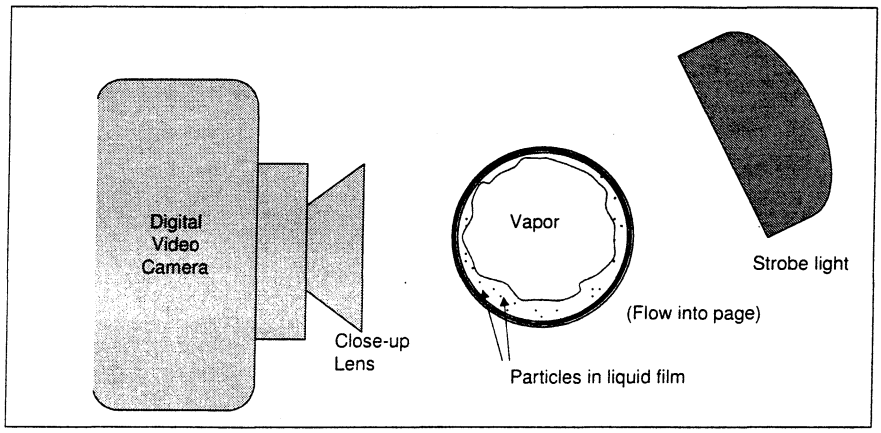

Figure 7.2: Schematic of the lighting and video setup.

For the initial work, a consumer-grade digital video camera (Sony TRV510) with an optional close-up lens was used to capture the flow images. The resolution of the output was fairly poor (640 by 480 pixels), but for a 10 mm by 7.5 mm region the particles used occupied a region of about 4 by 4 pixels, which made them easy to distinguish and isolate.

A typical particle-filled image is shown at the top of Figure 7.3. As is evident from this picture, the frame is filled with visual "noise" that must be removed before it can be processed using traditional interrogation methods. Essentially three steps are performed using a commercial image processing software package: low-pass filtering, particle isolation and thresholding. The result of the image processing algorithm is shown at the bottom of Figure 7.3. This algorithm was found to isolate particles with very high accuracy with very low generation of false "particles".

The first step was to adjust the brightness and contrast of the image so that the particles could be clearly seen. The next step is to remove large-scale structure in the image. This is accomplished by making a copy of the image, applying a low-pass (blurring) filter to it, then subtracting the blurred copy from the original. After enhancing the contrast of the image (contrast stretch), a selective band-pass filter is applied which was designed by trial and error to amplify equal-intensity regions of approximately 4 pixels by 4 pixels, while removing larger homogeneous regions. At this point, virtually all the particle images have been isolated, but some spurious artifacts remain. It was found that these artifacts are almost always at a significantly lower intensity after the filtering than the "real" particle images, so a thresholding operation removes these "false" particles and sets all the remaining

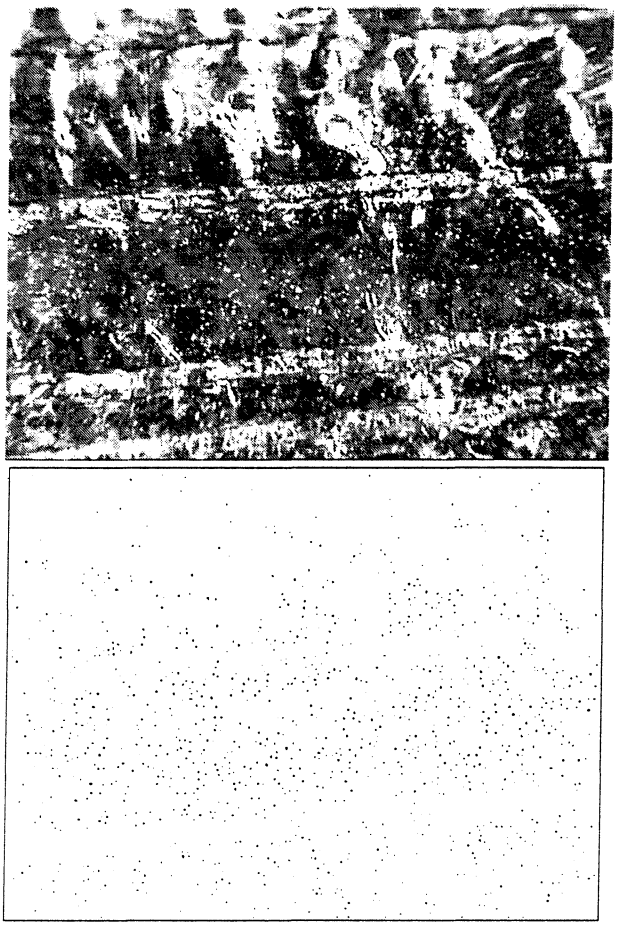

Figure 7.3: Example of image processing results.

pixels to maximum brightness. The final particle image is overlaid on the original as a check of the process. If significant errors are apparent, the filters are adjusted and the image re-processed. An introduction to these image processing techniques may be found in Crane [1997] with Gonzalez and Woods [1992] covering the topic in more detail.

The resulting image of the multiply-exposed particles (see the bottom of Figure 7.3) is then interrogated using PIV Sleuth, a software package developed at the University of Illinois [Christensen et al., 2000]. Flow vectors have been superimposed on the original image in Figure 7.4. See Raffel et al. [1998] for specific information about PIV interrogation techniques. Care was taken to inspect the resulting vector images for consistency with the original image as attractive vector fields are easily generated that bear no relation to the flow field.

7.3 Results

A series of five consecutive video images, each separated by 30 ms, is presented in Figures 7.4, 7.6 and 7.7. An interpretation of where in a hypothetical annular flow these images were taken is shown in Figure 7.5. The average base film thickness for this flow at this location is about 0.2 mm (see Appendix B, Flow Q, 9 degree helix, 90 degrees).

These images represent about a 10 mm wide by 7.5 mm tall section at the midpoint of the side of a 15.1 mm I.D. round tube. As can be seen, the tube has small grooves inscribed in it (20 in total) which are approximately 0.2 mm deep and 0.5 mm wide on average. This investigation was part of a larger work studying annular flow in helical microgrooved tubes (see Chapters 5 and 6).

Figure 7.4 contains velocity vectors for flow within a disturbance wave. Note the very clear upward flow, providing support to the theory of Fukano et al., that disturbance waves "pump" liquid up the wall of the tube. In contrast, the frames following the disturbance wave indicate a very smooth film. Careful inspection of these images shows that the film is smooth enough to clearly see the narrow grooves on the opposite side of the tube, though they are out of focus. The flow is generally downward in these base film flow images, though not necessarily following the groove angle closely. Note the change in character of the flow vectors as a wave approaches from the right side of the 60 ms image in Figure 7.6.

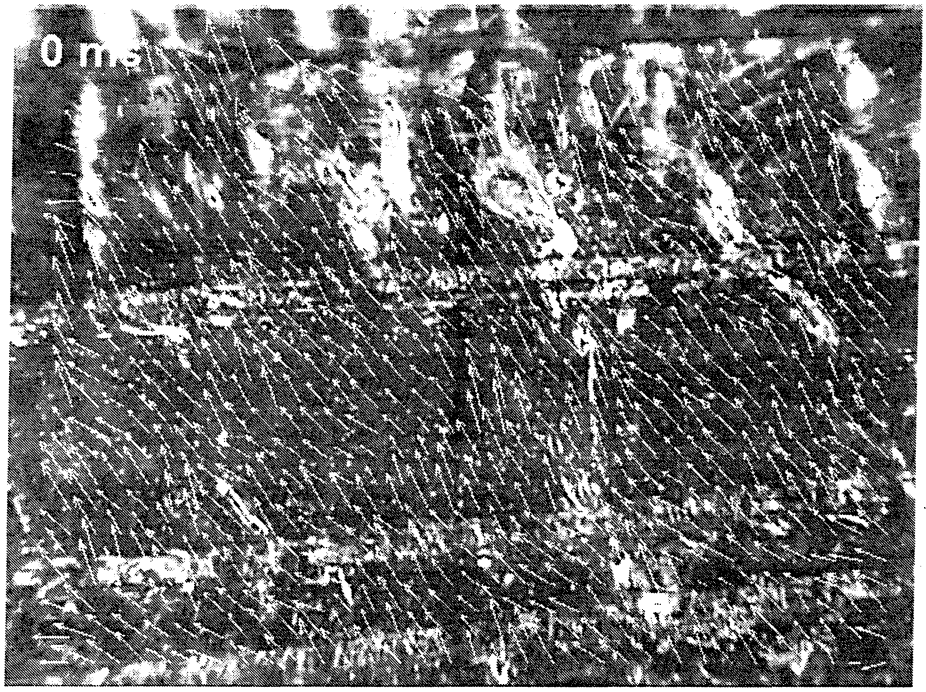

Figure 7.4: Results of PIV interrogation on example image.

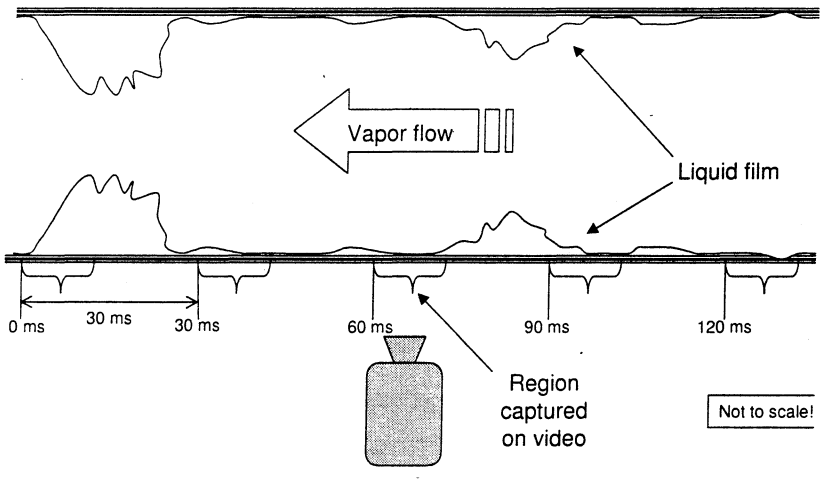

Figure 7.5: Schematic of the relative positions of the sample images in the flow.

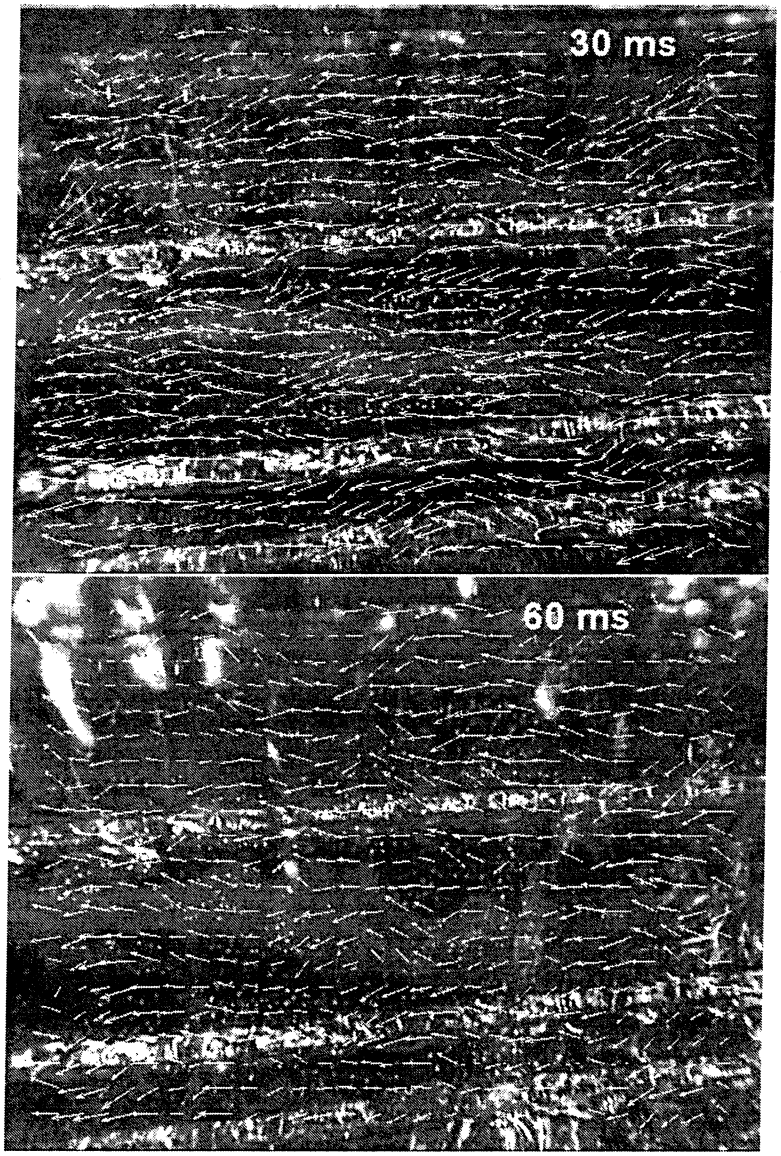

Figure 7.6: Qualitative flow vectors at 30 ms and 60 ms as defined in Figure 7.5.

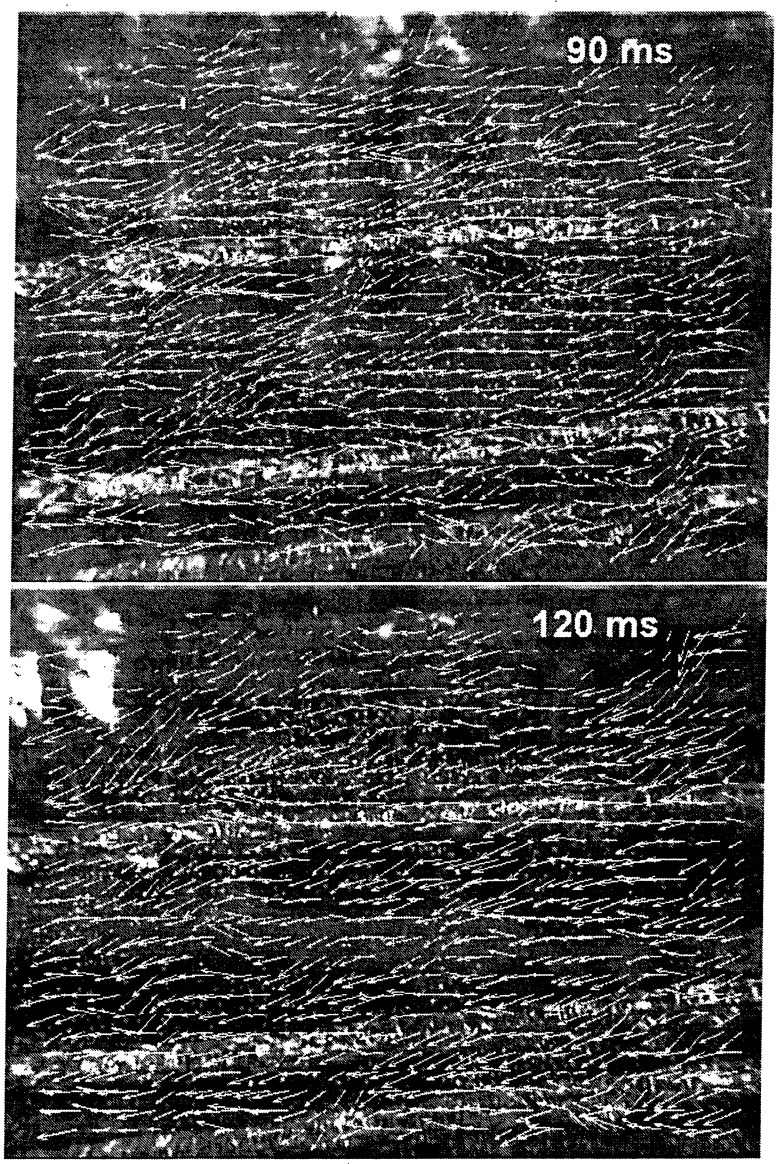

Figure 7.7: Qualitative flow vectors at 90 ms and 120 ms as defined in Figure 7.5.

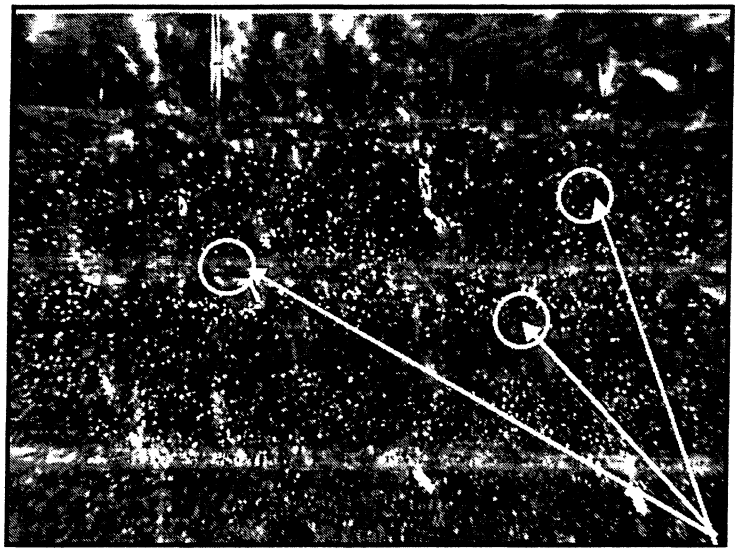

Figure 7.8: Flow image used to illustrate the use of thin film PIV in locating local fluctuations in the film. The analysis of this image is shown in Figure 7.9

This is very much in agreement with the work of Sutharshan et al. [1995] who used light-activated dye to study the flow of liquid film. Upward circumferential flow was noted within disturbance waves, while in between waves, the relatively smooth base film showed a consistent downward draining flow. The dye spots in the base film remained fairly coherent over the span of each video sample (13 ms), which indicated a lack of turbulent mixing or eddy motion within the film itself.

PIV Sleuth also provides the capability of subtracting out the mean velocities, thus allowing for the determination of local turbulent fluctuations. An example of this is shown in Figures 7.8 and 7.9. The original particle image is shown in Figure 7.8 with three areas highlighted. Next, the processed vector image is presented at the top of Figure 7.9. Nothing particularly noteworthy occurs in this image in the highlighted regions. When the average velocities are subtracted however, local outflows from the circled regions appear. Careful inspection of the original image suggests that the groove edge may have a protruding burr near the leftmost highlighted region generating a disruption in the flow at that point. A possible explanation for the behavior at the other locations is that these may be sites of the impact of turbulent vapor eddies imparting momentum to the liquid film. Further work is necessary, however, to correctly interpret this data.

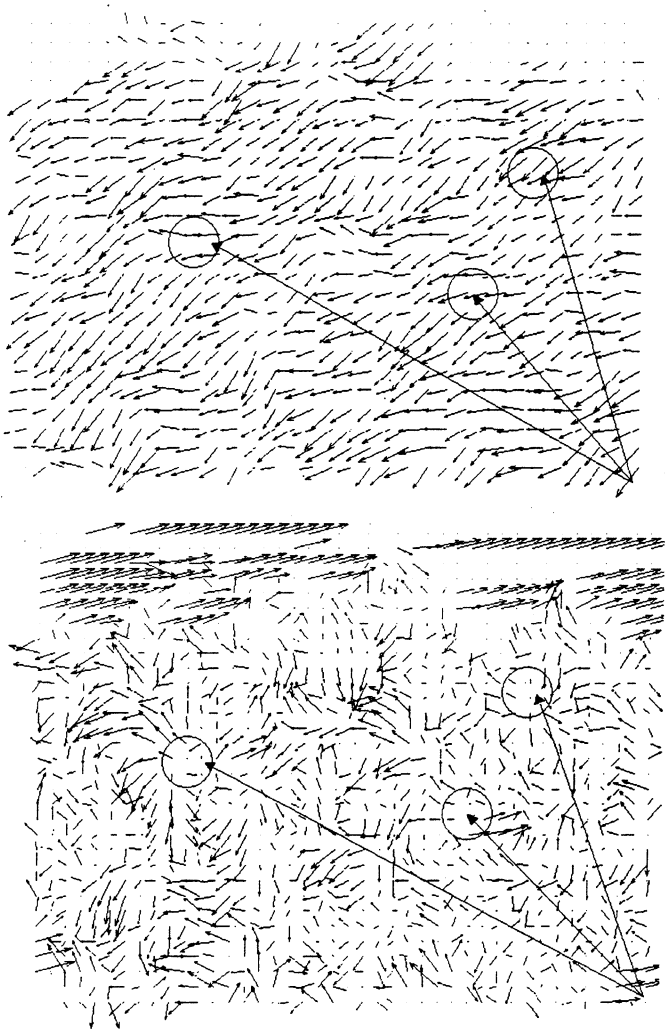

Figure 7.9: An example of how Thin Film PIV could provide information about local surface fluctuations.

One interesting phenomenon observed was the grouping of particles into chains of 3 or more. Other irregular groupings were noticed as well. This is consistent with observations of Segré and Silbergerg [1962] who found that spheres at high enough concentrations in Poiseuille pipe flow would tend to form long chains or "necklaces". Care must be taken when interpreting the particle images in order to not mistake a chain of particles for a series of multiply exposed images. These linear groupings appeared to form along streamlines.

7.4 Discussion

Although these initial results are quite promising, they are still considered qualitative and preliminary. Several issues must be resolved before quantitative velocities and turbulence statistics can be obtained using Thin Film PIV. Particle density should be increased to achieve accurate, quantitative results. The diameter of the particles used here comprises a significant portion of the base liquid film. This limits the particle density which can be achieved and may have a direct impact on the flow behavior of the film. In addition, the solid glass spheres may be prevented from following small-scale fluctuations due to inertial effects. This can be addressed with smaller, neutrally-buoyant particles.

Another source of error in the current setup is due to the curvature of the tube. This will tend to exaggerate vertical movements, particularly as particles move further from the tube centerline. It is estimated that this error was on the order of one particle diameter for the setup used in this experiment since the field of view was limited to 3.75 mm above and below the tube center.

As well, it is unclear exactly where the particles are flowing in the axial velocity field. Vand [1962] found that, in dense suspensions of particles in laminar flow, a small region next to the wall approximately equal to the diameter of a particle, remains particle-free. In agreement with this observation, it was noted by Mei and Hu [1999] that particles tend to move away from regions of high levels of vorticity. Experiments in laminar Poiseuille flow indicated that spherical particles migrate away from both the wall and the center to flow at an equilibrium point about 40% of the radius from the wall [Segré and Silbergerg, 1962]. Further work by Eichhorn and Small [1964] confirmed that spherical particles rotate as they move in the shear field, generating a lift force. Jeffrey and Pearson [1965] indicate that when particles

move more slowly than the mean liquid velocity, they migrate to the tube axis and, conversely, faster traveling particles move toward the wall. They postulated that the equilibrium position is achieved through a balance of the rotation-generated lift force and the drag.

Theoretical models have been constructed which reproduce these experimental results and study parameters which affect the equilibrium position of particles in the flow [Saffman, 1965, Vasseur and Cox, 1976, Cox and Hsu, 1977]. Apparently, particle size has only a minor influence, but the effective viscosity and particle density with respect to the fluid play significant roles. The theoretical work of Ho and Leal [1974] found that spheres in a simple shear flow (Couette flow) tend to flow at a point halfway between the walls. This analysis led to the conclusion that this result was justified by energy dissipation considerations and that it was the effective viscosity difference between the particle and the fluid , rather than the density difference, that was primarily responsible for the final equilibrium position.

The photochromic dye traces of Hewitt et al. [1990] indicate that the velocity profile in the thin base film of annular flow is approximately linear across much of the film thickness, similar to the simple shear flow examined by Ho and Leal. Thus, it seems reasonable to assume that particles imaged in the base layer are flowing approximately midway between the interface and the wall and are providing an indication of the mean velocity of the film.

In the experiments of Sutharshan et al. [1995], the photochromic dye did not immediately disperse upon the passage of a disturbance wave. The authors speculate that laser light penetrated only through the depth of the base layer, and thus movement of exposed dye represented flow within the base film rather than the highly turbulent parts of disturbance waves. The dye migration was determined to have a circumferential component of approximately 0.2 to 0.4 m/s during the passage of a wave. Tracking of particle groups in the present results indicate that the circumferential velocity of these particles may be almost double this velocity range, indicating that they are most likely flowing with the turbulent liquid in the wave and outside of the base film region at that point. However, due to the complexity of the motions within the film in this situation, it is possible that particles are flowing within different regions of the film and may be flowing in different directions within the same image. The use of cross-correlation camera technology could eliminate this ambiguity and increase the confidence in the resulting flow vectors.

Another significant issue is the impact of the particles on the flow field within the liquid. The dampening of fluid turbulence by rigid particles is well documented [Yarin and Hetsroni, 1994, Crowe et al., 1996, Chen and Pereira, 1999, Ooms and Jansen, 2000] and the effect of tracer particles on the annular liquid film distribution should be investigated. Visual inspection of the flow during PIV runs did not indicate any significant change of flow behavior from the particle-free runs, however, quantitative measurements of film thickness and wave behavior were not made on particle-laden flows.

7.5 References

R. J. Adrian. Particle–imaging techniques for experimental fluid mechanics. *Annual Review of Fluid Mechanics*, 23:261–304, 1991.

D. Butterworth. Air-water annular flow in a horizontal tube. *Progress in Heat and Mass Transfer*, 6:235–251, 1972.

X.-Q. Chen and J. C. F. Pereira. Two-way coupling: effects on two-phase flwo predictions. In G. P. Celata, P. Di Marco, and R. K. Shah, editors, *Two-Phase Flow Modelling and Experimentation 1999*, volume 3, pages 1153–1160, Rome, Italy, May 1999. Edizioni ETS, Pisa.

K. T. Christensen, S. M. Soloff, and R. J. Adrian. *PIV Sleuth*: Integrated Particle Image Velocimetry Interrogation/Validation Software. TAM Report 943, Department of Theoretical and Applied Mechanics, University of Illinois at Urbana-Champaign, 2000.

R. G. Cox and S. K. Hsu. The lateral migration of solid particles in a laminar flow near a plane. *International Journal of Multiphase Flow*, 3:201–222, 1977.

R. Crane. *A Simplified Approach to Image Processing*. Prentice Hall PTR, Upper Saddle River, NJ, first edition, 1997.

C. T. Crowe, T. R. Troutt, and J. N. Chung. Numerical models for two-phase turbulent flows. *Annual Review of Fluid Mechanics*, 28:11–43, 1996.

R. Eichhorn and S. Small. Experiments on the lift and drag of spheres suspended in a Poiseuille flow. *Journal of Fluid Mechanics*, 20(3):513–527, 1964.

T. Fukano, A. Itoh, and A. Ousaka. Breakdown of a liquid film flowing concurrently with gas in a horizontal line. *PCH: PhysicoChemical Hydrodynamics*, 6(1/2):23–47, 1985.

T. Fukano and A. Ousaka. Prediction of the circumferential distribution of film thickness in horizontal and near-horizontal gas-liquid annular flows. *International Journal of Multiphase Flow*, 15(3):403–419, 1989.

Rafael C Gonzalez and Richard E Woods. *Digital Image Processing*. Addison-Wesley, Reading, MA, third edition, 1992.

Y. Hagiwara, K. Suzuki, and T. Sato. Studies on thin liquid film of annular-mist two-phase flow I. wave characteristics and heat transfer. *Memoirs of the Faculty of Engineering, Kyoto University*, 44:309–328, 1982.

Y. Hagiwara, S. Yamaguchi, and K. Suzuki. Interfacial wave structure and its effect on transport phenomena in horizontal wavy/annular two-phase flows. In S. Morioka and L. van Wijngaarden, editors, *IUTAM Sumposium on Waves in Liquid/Gas and Liquid/Vapour Two-Phase Systems*, pages 257–267. Kluwer Academic Publishers, The Netherlands, 1995.

G. F. Hewitt, S. Jayanti, and C. B. Hope. Structure of thin liquid films in gas–liquid horizontal flow. *International Journal of Multiphase Flow*, 16(6):951–957, 1990.

B. P. Ho and L. G. Leal. Inertial migration of rigid spheres in two-dimensional unidirectional flows. *Journal of Fluid Mechanics*, 65(2):365–400, 1974.

S. Jayanti, G. F. Hewitt, and S. P. White. Time-dependent behavior of the liquid film in horizontal annular flow. *International Journal of Multiphase Flow*, 16(6): 1097–1116, 1990.

R. C. Jeffrey and J. R. A. Pearson. Particle motion in laminar vertical tube flow. *Journal of Fluid Mechanics*, 22(4):721–735, 1965.

M. Kawaji. Two-phase flow measurements using a photochromatic dye activation technique. *Nuclear Engineering and Design*, 184:379–392, 1998.

R. Mei and K. C. Hu. Particle concentration non-uniformity in turbulent flow. In G. P. Celata, P. Di Marco, and R. K. Shah, editors, *Two-Phase Flow Modelling and Experimentation 1999*, volume 2, pages 1171–1179, Rome, Italy, May 1999. Edizioni ETS, Pisa.

M. Nasr-Esfahany and M. Kawaji. Turbulence structure under a typical shear induced wave at a liquid/gas interface. In M. S. El-Genk, editor, *Heat Transfer – 1996*, volume 92 of *AIChE Symposium Series*, pages 203–210, Houston, TX, 1996. AIChE.

T. R. Oakley, E. Loth, and R. J. Adrian. A two-phase cinematic PIV method for bubbly flows. *Journal of Fluids Engineering – Transactions of the ASME*, 119: 707–712, September 1997.

G. Ooms and G. H. Jansen. Particles-turbulence interaction in stationary, homogeneous, isotropic turbulence. *International Journal of Multiphase Flow*, 26: 1831–1850, November 2000.

S. V. Paras and A. J. Karabelas. Measurements of local velocities inside thin liquid films in horizontal two-phase flow. *EIF*, 13:190–198, 1992.

M. Raffel, C. Willert, and J. Kompenhans. *Particle Image Velocimetry: A Practical Guide*. Springer-Verlag, Berlin, 1998.

P. G. Saffman. The lift on a small sphere in a slow shear flow. *Journal of Fluid Mechanics*, 22(2):385–400, 1965.

G. Segré and A. Silbergerg. Behavior of macroscopic rigid spheres in Poiseuille flow, parts 1 and 2. *Journal of Fluid Mechanics*, 14:115–157, 1962.

B. Sutharshan, M. Kawaji, and A. Ousaka. Measurement of circumferential and axial liquid film velocities in horizontal annular flow. *International Journal of Multiphase Flow*, 21(2):193–206, 1995.

V. Vand. Viscosity of solutions and suspensions. *Journal of Physical and Colloid Chemistry*, 52:277–210, 1962.

P. Vasseur and R. G. Cox. The lateral migration of a spherical particle in two-dimensional shear flows. *Journal of Fluid Mechanics*, 78(2):385–413, 1976.

L. P. Yarin and G. Hetsroni. Turbulence intensity in dilute two-phase flows – parts 1-3. *International Journal of Multiphase Flow*, 20(1):1–44, 1994.

8

Concluding remarks

The purpose of this investigation was to present a broad survey of detailed film thickness results in a variety of geometries for which film thickness data was not available. Beyond this, analysis of these data have made additional unique contributions to the understanding of annular two-phase flow.

In light of the issues in annular flow modeling presented in the Introduction, the detailed film data presented in Chapters 2 and 5 will provide new data with which to examine existing theories and on which to build new models.

Three important issues were addressed in Chapter 3: the structure of the base film, dryout and the application of vertical interfacial shear correlations locally to horizontal flow. From this work, and supported by the standard error data presented in Chapter 6 for the grooved tubes, it appears that the velocity profile in the liquid film behaves in a manner somewhat analogous to the Von Karman, or Law of the Wall profile in wall-bounded turbulent flow. It also appears that a film whose thickness lies wholly within the viscous region of that profile is unable to sustain itself against gravity, leading to dryout. Finally, the detailed film thickness profiles provided a test of the assumption that vertical interfacial shear correlations could be applied locally. One correlation was found to apply quite generally to the round, square and diamond flows with only minor modification, thus indicating that, indeed, the flow behavior in vertical and horizontal situations is similar enough to apply correlations from one to the other.

The striking behavior of the liquid film in square tubes lead to a more thorough investigation of secondary flows under two-phase conditions in Chapter 4. An analysis based on single-phase flow near a corner was extended to the more general case of turbulent flow in the presence of boundaries which cause curved isotachs. This

then explained the origin of secondary flows in round tube with liquid/vapor flow and suggests that secondary flows may play a significant role in annular flow that is not well-understood or modeled to this point.

Decades of research into the enhanced heat transfer of microgrooved tubes has lead to several theories to explain this behavior. The flow visualization of Chapter 5 provides evidence for the enhance wetting characteristics of helically grooved tubes. These profiles give significant insight as to the measured circumferential temperature distributions as well as the different levels of enhancement that occur at different mass qualities and mass flux conditions.

In an effort to quantify the film rotation and redistribution behavior noted in Chapter 5, Chapter 6 presents the efforts undertaken to determine how the groove angle and number impact the liquid film. While more study is needed, it was found that a close relationship existed between the film rotation, the number of grooves and the vapor velocity. In addition, this study brought to light the thinning of the film in grooved tubes with respect to the smooth. The standard error analysis suggests that perhaps the grooves act to decrease the stability of the liquid film allowing more liquid to be carried in waves leaving a thinner base film. Further research in these areas could lead to the design of tube wall patterns which provide enhance performance over current tubes.

Finally, each of the investigations emphasized that while knowledge of the film thickness is important and much can be learned from these profiles, significantly more information is needed about the film behavior. For this reason, a new diagnostic is under development, Thin Film PIV, described in Chapter 7. This tool could provide quantitative evidence of which of the mechanisms involved in the liquid film distribution, as outlined in the Introduction, are significant. And perhaps uncover new behaviors previous undetectable.

While helping to further the understanding of this important flow condition, this survey has also shown how much more there is to know. It is hoped that this work will be of assistance to future efforts in this area.

A

Film thickness data for the round, square, diamond and triangle tubes

Local Film Thickness – 25.4 mm Round					
Position	A	B	C	D	E
0	0.176	0.219	0.392	0.501	0.409
22.5	0.155	0.207	0.347	0.432	0.335
45	0.171	0.216	0.394	0.448	0.376
67.5	0.156	0.209	0.317	0.357	0.329
90	0.138	0.179	0.235	0.237	0.199
112.5	0.020	0.173	0.194	0.192	0.118
135	0.019	0.161	0.190	0.178	0.176
157.5	-0.002	0.163	0.186	0.180	0.168
180	0.034	0.162	0.185	0.160	0.139
202.5	0.022	0.159	0.173	0.149	0.134
225	0.017	0.171	0.195	0.183	0.172
247.5	0.143	0.174	0.226	0.233	0.187
270	0.125	0.163	0.230	0.257	0.193
292.5	0.175	0.211	0.328	0.408	0.300
315	0.186	0.242	0.372	0.538	0.395
337.5	0.189	0.251	0.404	0.506	0.419
Average	0.108	0.191	0.273	0.310	0.253
Error	± 0.006	±0.006	± 0.012	± 0.016	± 0.016

Table A.1: Film thickness at 16 circumferential positions for the five flow conditions tested. All values in millimeters.

Local Film Thickness – 12.7 mm Round						
Position	A	B	C	D	E	F
0	0.207	0.255	0.368	0.345	0.316	0.215
22.5	0.184	0.233	0.341	0.325	0.281	0.216
45	0.180	0.222	0.294	0.299	0.276	0.224
67.5	0.156	0.190	0.229	0.231	0.209	0.212
90	0.138	0.159	0.215	0.203	0.183	0.153
112.5	0.107	0.138	0.162	0.144	0.145	0.131
135	0.101	0.131	0.148	0.143	0.136	0.126
157.5	0.000	0.143	0.153	0.140	0.142	0.136
180	0.000	0.123	0.128	0.135	0.131	0.124
202.5	0.000	0.129	0.143	0.133	0.135	0.129
225	0.000	0.143	0.146	0.142	0.141	0.143
247.5	0.119	0.147	0.166	0.159	0.157	0.138
270	0.157	0.177	0.229	0.209	0.199	0.180
292.5	0.151	0.168	0.236	0.216	0.203	0.161
315	0.176	0.202	0.278	0.291	0.222	0.186
337.5	0.178	0.209	0.315	0.285	0.265	0.199
Average	0.116	0.173	0.222	0.213	0.196	0.167
Error	± 0.005	± 0.007	± 0.012	± 0.012	± 0.010	± 0.007

Table A.2: Film thickness at 16 circumferential positions for the five flow conditions tested. All values in millimeters.

Local Film Thickness – 22.1 mm Square							
Position	LSA	LSB	LSC	LSD	LSE	LSF	LSG
B1	0.186	0.196	0.207	0.261	0.281	0.232	0.214
B2	0.149	0.193	0.241	0.272	0.314	0.274	0.250
B3	0.173	0.209	0.285	0.311	0.397	0.292	0.254
B4	0.142	0.184	0.231	0.274	0.385	0.278	0.230
B5	0.158	0.174	0.193	0.223	0.305	0.234	0.186
R1	0.158	0.167	0.187	0.217	0.238	0.183	0.156
R2	0.128	0.172	0.197	0.227	0.257	0.208	0.164
R3	0.000	0.141	0.170	0.193	0.204	0.171	0.017
R4	0.000	0.164	0.196	0.218	0.210	0.159	0.042
R5	0.000	0.087	0.113	0.123	0.103	0.000	0.000
T1	0.000	0.022	0.147	0.157	0.142	0.000	0.044
T2	0.000	0.000	0.122	0.148	0.167	0.137	0.050
T3	0.000	0.025	0.147	0.186	0.189	0.172	0.000
T4	0.000	0.009	0.146	0.164	0.181	0.145	0.000
T5	0.000	0.005	0.107	0.109	0.130	0.113	0.022
L1	0.000	0.122	0.126	0.123	0.107	0.085	0.000
L2	0.000	0.175	0.208	0.224	0.194	0.156	0.002
L3	0.000	0.119	0.143	0.158	0.174	0.136	0.057
L4	0.071	0.140	0.167	0.200	0.232	0.162	0.115
L5	0.105	0.121	0.137	0.149	0.179	0.128	0.122
Average	0.064	0.121	0.173	0.197	0.219	0.163	0.096
Error	±0.002	±0.002	±0.003	±0.004	±0.005	±0.004	±0.003

Table A.3: Film thickness at 20 locations along the sides of the 22.1 mm square. Data progressess in a counter clockwise fashion from B1 (leftmost of bottom side) to L5 (bottom of left side) for the seven flow conditions tested. All values in millimeters.

Local Film Thickness – 15.2 mm Square						
Position	SSA	SSB	SSC	SSD	SSE	SSF
B1	0.126	0.149	0.156	0.203	0.207	0.158
B2	0.149	0.210	0.242	0.270	0.307	0.249
B3	0.175	0.214	0.221	0.249	0.263	0.227
B4	0.166	0.168	0.162	0.189	0.216	0.201
R1	0.101	0.116	0.126	0.163	0.161	0.133
R2	0.117	0.162	0.177	0.200	0.190	0.180
R3	0.015	0.116	0.118	0.124	0.124	0.119
R4	0.011	0.119	0.116	0.120	0.111	0.099
T1	0.004	0.050	0.053	0.085	0.084	0.064
T2	0.000	0.111	0.130	0.149	0.146	0.124
T3	0.008	0.155	0.170	0.190	0.200	0.171
T4	0.001	0.088	0.093	0.094	0.090	0.074
L1	0.017	0.055	0.065	0.087	0.104	0.067
L2	0.016	0.175	0.179	0.192	0.195	0.182
L3	0.081	0.175	0.191	0.217	0.209	0.191
L4	0.102	0.132	0.137	0.162	0.171	0.140
Average	0.068	0.137	0.146	0.168	0.174	0.149
Error	±0.002	±0.002	±0.003	±0.003	±0.003	±0.003

Table A.4: Film thickness at 16 locations along the sides of the 15.2 mm square. Data progressess in a counter clockwise fashion from B1 (leftmost of bottom side) to L4 (bottom of left side) for the six flow conditions tested. All values in millimeters.

Local Film Thickness – 22.1 mm Diamond							
Position	LDA	LDB	LDC	LDD	LDE	LDF	LDG
LR1	0.166	0.171	0.202	0.255	0.357	0.232	0.187
LR2	0.185	0.196	0.244	0.334	0.421	0.268	0.002
LR3	0.144	0.166	0.200	0.258	0.339	0.233	0.053
LR4	0.187	0.176	0.226	0.272	0.302	0.260	0.000
LR5	0.133	0.137	0.146	0.185	0.223	0.138	0.000
UR1	0.057	0.166	0.176	0.204	0.220	0.173	0.000
UR2	0.003	0.116	0.157	0.195	0.206	0.146	0.000
UR3	0.007	0.106	0.149	0.176	0.151	0.026	0.002
UR4	0.002	0.007	0.145	0.163	0.145	0.006	0.015
UR5	0.001	0.008	0.093	0.104	0.081	0.000	0.005
UL1	0.000	0.004	0.037	0.075	0.036	0.001	0.000
UL2	0.000	0.000	0.145	0.167	0.110	0.010	0.000
UL3	0.000	0.002	0.165	0.182	0.181	0.128	0.000
UL4	0.000	0.129	0.168	0.203	0.198	0.013	0.007
UL5	0.005	0.137	0.185	0.211	0.202	0.013	0.002
LL1	0.096	0.100	0.126	0.149	0.166	0.104	0.000
LL2	0.210	0.224	0.277	0.306	0.319	0.129	0.191
LL3	0.163	0.175	0.230	0.265	0.301	0.234	0.202
LL4	0.173	0.176	0.241	0.285	0.348	0.251	0.163
LL5	0.152	0.157	0.194	0.260	0.376	0.192	0.192
Average	0.084	0.118	0.175	0.212	0.234	0.128	0.051
Error	±0.002	±0.002	±0.003	±0.004	±0.005	±0.004	±0.003

Table A.5: Film thickness at 20 locations along the sides of the 22.1 mm diamond. Data progressess in a counter clockwise fashion from LR1 (bottom, lower right sided) to LL5 (bottom lower left side) for the seven flow conditions tested. All values in millimeters.

Local Film Thickness – 15.2 mm Diamond						
Position	SDA	SDB	SDC	SDD	SDE	SDF
LR1	0.144	0.169	0.192	0.271	0.368	0.253
LR2	0.077	0.102	0.111	0.132	0.146	0.127
LR3	0.110	0.170	0.167	0.206	0.236	0.185
LR4	0.020	0.188	0.192	0.211	0.212	0.191
UR1	0.002	0.087	0.109	0.139	0.204	0.167
UR2	0.004	0.191	0.211	0.237	0.239	0.224
UR3	0.006	0.152	0.196	0.206	0.203	0.187
UR4	0.018	0.089	0.098	0.105	0.092	0.075
UL1	0.000	0.002	0.004	0.007	0.008	0.002
UL2	0.000	0.109	0.113	0.119	0.100	0.083
UL3	0.000	0.128	0.142	0.172	0.170	0.135
UL4	0.000	0.140	0.147	0.173	0.164	0.143
LL1	0.090	0.108	0.127	0.202	0.241	0.167
LL2	0.091	0.137	0.147	0.200	0.188	0.173
LL3	0.148	0.213	0.238	0.297	0.311	0.257
LL4	0.103	0.132	0.147	0.296	0.305	0.178
Average	0.051	0.132	0.146	0.186	0.199	0.159
Error	±0.002	±0.003	±0.003	±0.004	±0.005	±0.004

Table A.6: Film thickness at 16 locations along the sides of the 15.2 mm diamond. Data progressess in a counter clockwise fashion from LR1 (bottom of lower right side) to LL4 (bottom of lower left side) for the six flow conditions tested. All values in millimeters.

Local Film Thickness – 40 mm Triangle, Apex Up						
Position	TU-A	TU-B	TU-C	TU-D	TU-E	TU-F
B1	0.197	0.213	0.240	0.289	0.316	0.273
B2	0.190	0.213	0.251	0.300	0.353	0.303
B3	0.184	0.202	0.240	0.293	0.335	0.287
B4	0.191	0.216	0.236	0.260	0.285	0.246
R1	0.010	0.184	0.214	0.226	0.226	0.207
R2	0.000	0.125	0.152	0.173	0.165	0.136
R3	0.000	0.000	0.055	0.098	0.036	0.000
R4	0.000	0.016	0.021	0.068	0.018	0.014
L1	0.000	0.006	0.020	0.052	0.047	0.016
L2	0.006	0.022	0.101	0.141	0.107	0.019
L3	0.006	0.139	0.173	0.206	0.203	0.174
L4	0.012	0.163	0.191	0.214	0.217	0.197
Average	0.066	0.125	0.158	0.193	0.192	0.156
Error	±0.002	±0.002	±0.006	±0.003	±0.005	±0.004

Table A.7: Film thickness at 12 locations along the sides of the triangular tube in the apex-up configuration. Data progressess in a counter clockwise fashion from B1 (left bottom) to L4 (bottom of left side) for the six flow conditions tested. All values in millimeters.

Local Film Thickness – 40 mm Triangle, Apex Down						
Position	TD-A	TD-B	TD-C	TD-D	TD-E	TD-F
R1	0.192	0.221	0.245	0.272	0.317	0.288
R2	0.153	0.201	0.224	0.264	0.286	0.258
R3	0.008	0.168	0.192	0.221	0.223	0.179
R4	0.001	0.035	0.147	0.178	0.101	0.035
T1	0.005	0.092	0.106	0.143	0.121	0.099
T2	0.066	0.134	0.137	0.176	0.169	0.145
T3	0.006	0.095	0.120	0.158	0.143	0.127
T4	0.004	0.059	0.097	0.136	0.070	0.023
L1	0.014	0.117	0.156	0.173	0.133	0.092
L2	0.112	0.161	0.191	0.222	0.251	0.226
L3	0.162	0.209	0.248	0.284	0.335	0.317
L4	0.133	0.191	0.232	0.227	0.275	0.256
Average	0.071	0.140	0.174	0.205	0.202	0.170
Error	±0.002	±0.002	±0.002	±0.005	±0.004	±0.004

Table A.8: Film thickness at 12 locations along the sides of the triangular tube in the apex-down configuration. Data progressess in a counter clockwise fashion from R1 (bottom of right side) to L4 (bottom of left side) for the six flow conditions tested. All values in millimeters.

B

Film thickness data for the smooth, 0, 9 and 18 degree tubes

Local Film Thickness – 15.1 mm Smooth							
Position	T	U	V	Q	R	F	G
0	0.309	0.221	0.145	0.360	0.199	0.154	0.126
22.5	0.317	0.241	0.188	0.335	0.220	0.182	0.155
45	0.300	0.227	0.170	0.310	0.196	0.147	0.122
67.5	0.222	0.210	0.175	0.265	0.202	0.174	0.146
90	0.143	0.192	0.167	0.198	0.179	0.151	0.126
112.5	0.016	0.165	0.152	0.181	0.188	0.170	0.144
135	0.051	0.109	0.130	0.157	0.165	0.151	0.127
157.5	0.038	0.085	0.126	0.134	0.156	0.141	0.128
180	0.015	0.091	0.045	0.106	0.128	0.115	0.104
202.5	0.001	0.031	0.124	0.126	0.161	0.154	0.140
225	0.066	0.020	0.110	0.140	0.165	0.154	0.135
247.5	0.017	0.157	0.138	0.167	0.174	0.155	0.140
270	0.098	0.163	0.135	0.183	0.159	0.133	0.111
292.5	0.174	0.195	0.154	0.228	0.182	0.154	0.125
315	0.263	0.215	0.163	0.287	0.176	0.134	0.111
337.5	0.312	0.236	0.177	0.340	0.218	0.178	0.141
Average	0.146	0.160	0.144	0.220	0.179	0.153	0.130
Error	± 0.017	± 0.016	± 0.015	± 0.018	± 0.016	± 0.015	± 0.015

Table B.1: Film thickness at 16 circumferential positions for the seven flow conditions tested. All values in millimeters.

Local Film Thickness – 0 Degree Helix							
Position	T	U	V	Q	R	F	G
0	0.309	0.221	0.145	0.360	0.199	0.154	0.126
22.5	0.317	0.241	0.188	0.335	0.220	0.182	0.155
45	0.300	0.227	0.170	0.310	0.196	0.147	0.122
67.5	0.222	0.210	0.175	0.265	0.202	0.174	0.146
90	0.143	0.192	0.167	0.198	0.179	0.151	0.126
112.5	0.016	0.165	0.152	0.181	0.188	0.170	0.144
135	0.051	0.109	0.130	0.157	0.165	0.151	0.127
157.5	0.038	0.085	0.126	0.134	0.156	0.141	0.128
180	0.015	0.091	0.045	0.106	0.128	0.115	0.104
202.5	0.001	0.031	0.124	0.126	0.161	0.154	0.140
225	0.066	0.020	0.110	0.140	0.165	0.154	0.135
247.5	0.017	0.157	0.138	0.167	0.174	0.155	0.140
270	0.098	0.163	0.135	0.183	0.159	0.133	0.111
292.5	0.174	0.195	0.154	0.228	0.182	0.154	0.125
315	0.263	0.215	0.163	0.287	0.176	0.134	0.111
337.5	0.312	0.236	0.177	0.340	0.218	0.178	0.141
Average	0.146	0.160	0.144	0.220	0.179	0.153	0.130
Error	± 0.017	± 0.016	± 0.015	± 0.018	± 0.016	± 0.015	± 0.015

Table B.2: Film thickness at 16 circumferential positions for the seven flow conditions tested. All values in millimeters.

Local Film Thickness – 9 Degree Helix							
Position	T	U	V	Q	R	F	G
0	0.273	0.190	0.134	0.278	0.181	0.148	0.119
22.5	0.299	0.217	0.147	0.317	0.212	0.163	0.127
45	0.247	0.188	0.164	0.257	0.195	0.175	0.144
67.5	0.185	0.156	0.154	0.245	0.186	0.171	0.144
90	0.000	0.056	0.102	0.203	0.155	0.134	0.114
112.5	0.066	0.128	0.128	0.193	0.173	0.163	0.147
135	0.066	0.157	0.093	0.185	0.162	0.149	0.133
157.5	0.070	0.139	0.172	0.141	0.178	0.183	0.156
180	0.201	0.179	0.180	0.236	0.201	0.193	0.170
202.5	0.201	0.181	0.149	0.213	0.178	0.169	0.151
235	0.265	0.191	0.114	0.243	0.146	0.127	0.129
247.5	0.123	0.114	0.113	0.132	0.127	0.118	0.110
270	0.175	0.164	0.153	0.213	0.178	0.168	0.166
292.5	0.208	0.177	0.158	0.245	0.186	0.153	0.129
315	0.281	0.196	0.160	0.314	0.188	0.171	0.159
337.5	0.269	0.199	0.134	0.291	0.190	0.147	0.107
Average	0.183	0.164	0.141	0.232	0.177	0.158	0.138
Error	± 0.017	± 0.016	± 0.014	± 0.018	± 0.015	± 0.014	± 0.014

Table B.3: Film thickness at 16 circumferential positions for the seven flow conditions tested. All values in millimeters.

Local Film Thickness – 18 Degree Helix							
Position	T	U	V	Q	R	F	G
0	0.305	0.238	0.162	0.332	0.203	0.163	0.126
22.5	0.283	0.173	0.102	0.287	0.154	0.110	0.089
45	0.188	0.095	0.080	0.220	0.119	0.095	0.074
67.5	0.170	0.115	0.113	0.201	0.138	0.115	0.100
90	0.145	0.151	0.075	0.214	0.145	0.095	0.075
112.5	0.071	0.114	0.133	0.139	0.154	0.130	0.067
135	0.021	0.100	0.117	0.132	0.145	0.132	0.119
157.5	0.012	0.088	0.088	0.094	0.121	0.089	0.077
180	0.103	0.139	0.119	0.158	0.142	0.125	0.092
202.5	0.132	0.167	0.129	0.174	0.162	0.141	0.127
225	0.144	0.117	0.109	0.165	0.131	0.127	0.101
247.5	0.240	0.190	0.202	0.247	0.223	0.210	0.184
270	0.231	0.189	0.153	0.240	0.190	0.161	0.114
292.5	0.279	0.223	0.143	0.292	0.199	0.148	0.107
315	0.281	0.183	0.128	0.277	0.185	0.133	0.130
337.5	0.339	0.269	0.171	0.361	0.242	0.174	0.164
Average	0.184	0.159	0.127	0.221	0.166	0.134	0.109
Error	± 0.017	± 0.016	± 0.015	± 0.018	± 0.016	± 0.015	± 0.015

Table B.4: Film thickness at 16 circumferential positions for the seven flow conditions tested. All values in millimeters.

C

Film thickness data and film profiles for the 4, 8 and 12 groove tubes

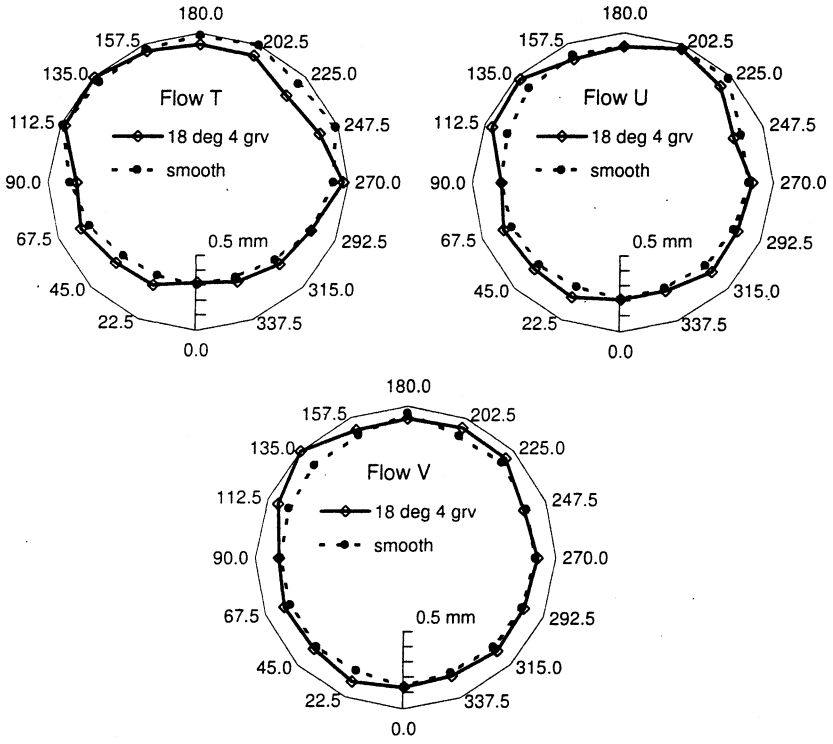

Figure C.1: Film thickness profiles in the 4 groove 18 degree helix tubes for Flows T, U and V.

Local Film Thickness – 4 Groove 18 Degree Helix							
Position	T	U	V	Q	R	F	G
0	0.323	0.216	0.140	0.307	0.184	0.126	0.118
22.5	0.248	0.165	0.110	0.291	0.158	0.104	0.082
45	0.231	0.183	0.150	0.249	0.165	0.148	0.126
67.5	0.161	0.154	0.133	0.215	0.170	0.148	0.133
90	0.189	0.193	0.159	0.232	0.204	0.174	0.139
112.5	0.027	0.051	0.076	0.111	0.101	0.091	0.085
135	0.007	0.027	0.000	0.038	0.050	0.040	0.025
157.5	0.050	0.113	0.091	0.100	0.149	0.128	0.111
180	0.077	0.093	0.081	0.073	0.129	0.117	0.105
202.5	0.079	0.032	0.068	0.075	0.114	0.108	0.101
225	0.177	0.089	0.071	0.082	0.101	0.096	0.086
247.5	0.129	0.206	0.157	0.177	0.197	0.161	0.136
270	0.032	0.140	0.121	0.155	0.144	0.121	0.098
292.5	0.175	0.167	0.142	0.203	0.160	0.138	0.126
315	0.222	0.154	0.126	0.232	0.143	0.113	0.099
337.5	0.275	0.216	0.156	0.300	0.178	0.152	0.121
Average	0.150	0.137	0.111	0.177	0.147	0.123	0.106
Error	± 0.017	± 0.016	± 0.015	± 0.018	± 0.016	± 0.015	± 0.015

Table C.1: Film thickness at 16 circumferential positions for the seven flow conditions tested. All values in millimeters.

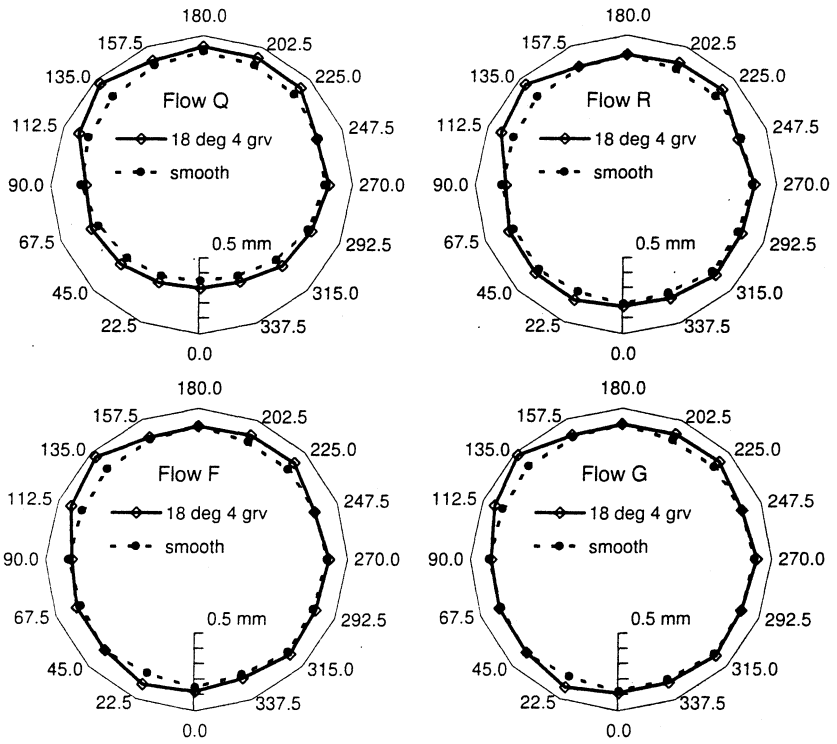

Figure C.2: Film thickness profiles in the 4 groove 18 degree helix tubes for Flows Q, R, F and G.

Local Film Thickness – 8 Groove 18 Degree Helix							
Position	T	U	V	Q	R	F	G
0	0.310	0.201	0.151	0.344	0.186	0.151	0.124
22.5	0.375	0.234	0.172	0.369	0.233	0.177	0.146
45	0.263	0.211	0.163	0.335	0.230	0.181	0.133
67.5	0.114	0.148	0.110	0.186	0.165	0.126	0.091
90	0.058	0.119	0.108	0.173	0.160	0.137	0.117
112.5	0.113	0.059	0.061	0.137	0.137	0.098	0.083
135	0.190	0.091	0.079	0.142	0.129	0.116	0.109
157.5	0.059	0.076	0.058	0.097	0.097	0.082	0.098
180	0.088	0.102	0.090	0.126	0.130	0.102	0.084
202.5	0.034	0.130	0.100	0.136	0.137	0.111	0.101
225	0.147	0.188	0.160	0.194	0.179	0.162	0.147
247.5	0.135	0.155	0.144	0.158	0.173	0.152	0.130
270	0.124	0.102	0.078	0.144	0.096	0.084	0.066
292.5	0.229	0.152	0.104	0.226	0.132	0.101	0.074
315	0.228	0.172	0.142	0.237	0.159	0.137	0.096
337.5	0.316	0.222	0.153	0.340	0.187	0.148	0.124
Average	0.174	0.148	0.117	0.209	0.158	0.129	0.108
Error	± 0.017	± 0.016	± 0.015	± 0.018	± 0.016	± 0.015	± 0.015

Table C.2: Film thickness at 16 circumferential positions for the seven flow conditions tested. All values in millimeters.

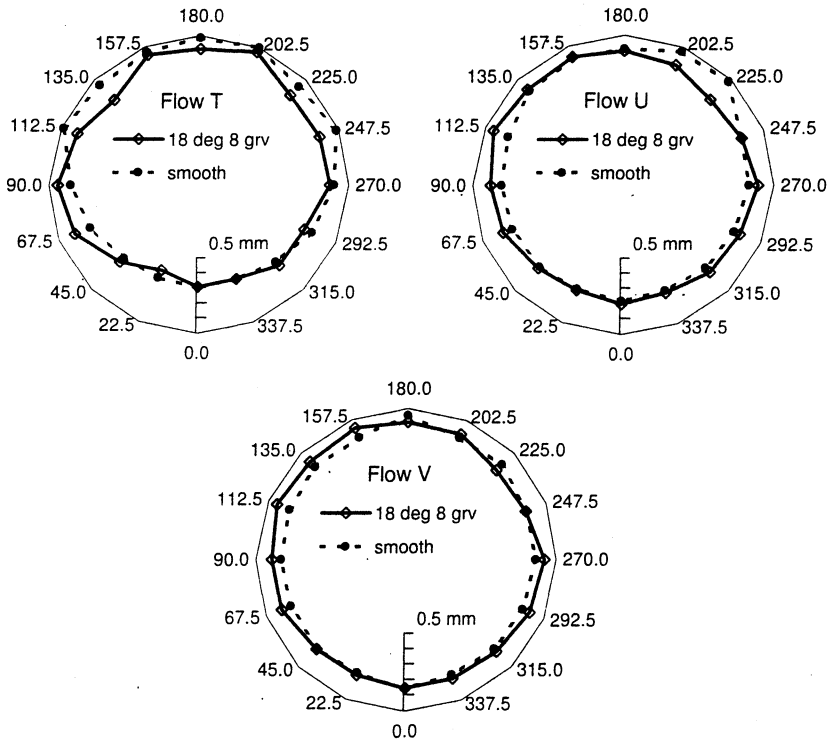

Figure C.3: Film thickness profiles in the 8 groove 18 degree helix tubes for Flows T, U and V.

Local Film Thickness – 12 Groove 18 Degree Helix							
Position	T	U	V	Q	R	F	G
0	0.348	0.230	0.099	0.397	0.204	0.161	0.126
22.5	0.332	0.145	0.089	0.343	0.161	0.111	0.083
45	0.178	0.147	0.124	0.248	0.165	0.144	0.126
67.5	0.103	0.100	0.071	0.173	0.123	0.094	0.076
90	0.110	0.128	0.081	0.178	0.137	0.110	0.115
112.5	0.118	0.147	0.106	0.177	0.165	0.127	0.117
135	0.185	0.109	0.099	0.180	0.145	0.116	0.114
157.5	0.096	0.073	0.087	0.113	0.102	0.101	0.105
180	0.205	0.176	0.156	0.195	0.209	0.183	0.159
202.5	0.185	0.120	0.119	0.142	0.139	0.127	0.127
225	0.148	0.138	0.108	0.173	0.132	0.114	0.107
247.5	0.201	0.189	0.172	0.224	0.205	0.154	0.130
270	0.129	0.123	0.117	0.142	0.128	0.118	0.106
292.5	0.304	0.247	0.178	0.299	0.228	0.177	0.129
315	0.323	0.228	0.145	0.342	0.199	0.159	0.142
337.5	0.351	0.237	0.147	0.380	0.195	0.147	0.117
Average	0.207	0.159	0.119	0.232	0.165	0.134	0.117
Error	± 0.017	± 0.016	± 0.015	± 0.018	± 0.016	± 0.015	± 0.015

Table C.3: Film thickness at 16 circumferential positions for the seven flow conditions tested. All values in millimeters.

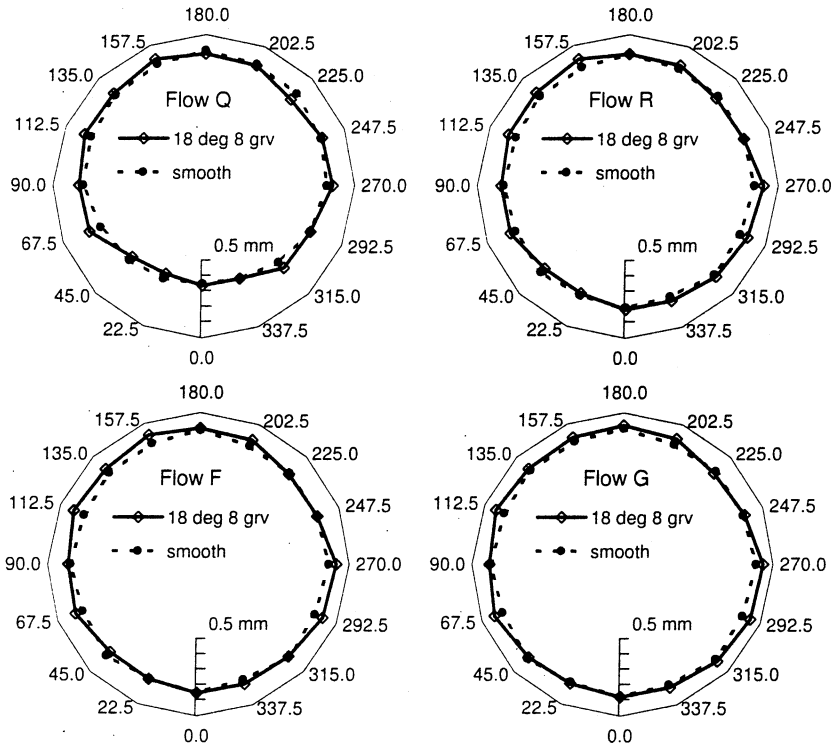

Figure C.4: Film thickness profiles in the 8 groove 18 degree helix tubes for Flows Q, R, F and G.

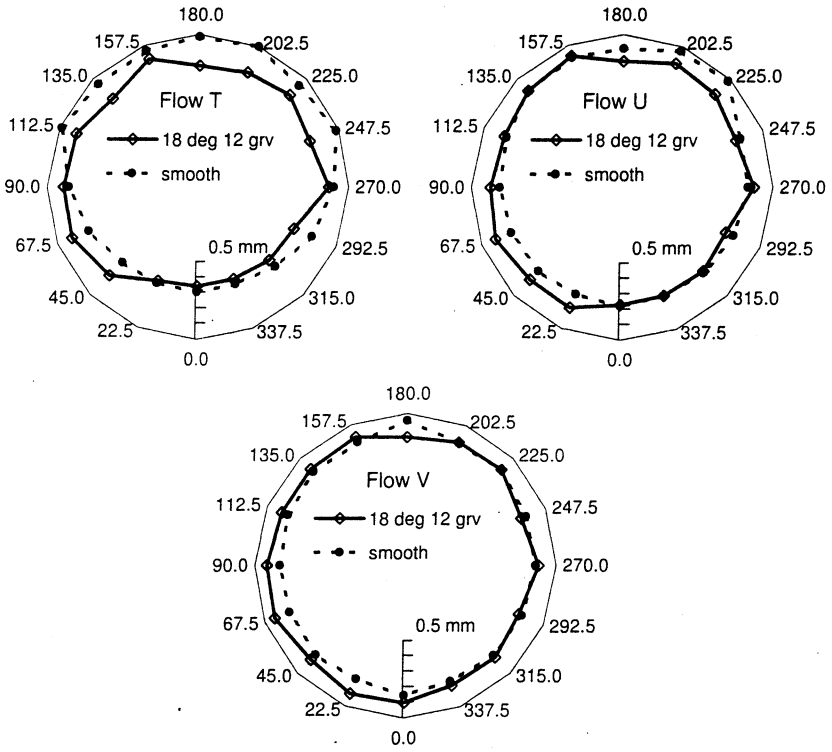

Figure C.5: Film thickness profiles in the 12 groove 18 degree helix tubes for Flows T, U and V.

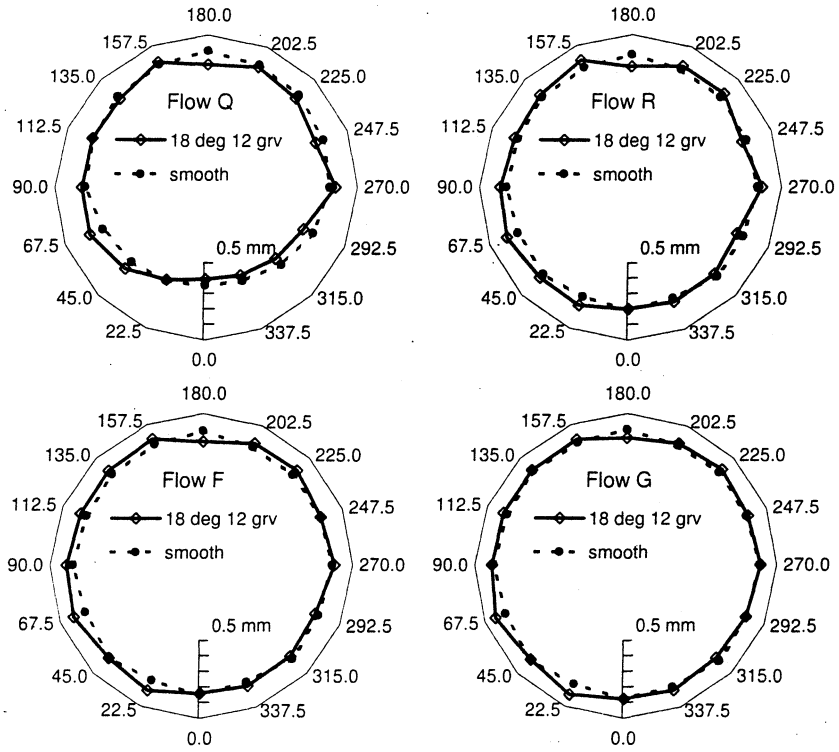

Figure C.6: Film thickness profiles in the 12 groove 18 degree helix tubes for Flows Q, R, F and G.

Vita

Timothy Allen Shedd

Timothy Allen Shedd was born in Springfield, MO, on December 8, 1969, to Glenroy and Shirley Shedd. He grew up in Springfield and graduated from Kickapoo High School where he was drum major of the marching band and active leader in a number of organizations. In his junior year, he won second prize at the International Science and Engineering Fair for his analysis of hand-stopping the French horn. Tim then attended Purdue University, West Lafayette, IN, and participated in the Co-Op program, working in the Semiconductor Engineering Group of Digital Equipment Corporation. After graduating with a BSEE in 1992, he took a position full time with the group, working on the Alpha 21164 and 21264 microprocessors, the former being the first commercial CPU to sustain one billion instructions per second. In August 1995, Tim began work on a MS degree in Mechanical Engineering at the University of Illinois at Urbana-Champaign, which he received in 1998 under Professor Ty Newell. For his masters work, he developed an automated, non-intrusive, optical film thickness measurement system for use in understanding annular two-phase flow. He applied this to the analysis of two-phase vapor-liquid flows in several unique tube geometries during his PhD work, also under Professor Newell. Throughout his masters and PhD research, Tim supervised 10 undergraduate and high school students on various independent research projects. As a consultant, Tim as provided technical training services to the Alpha Development Group of Compaq Corporation. During his time at UIUC, Tim has been very active in the campus and community, serving as a coordinator of hands-on science activities for a local children's program (BOAST), volunteering in the public schools, working on gender equity issues with the Women In Engineering office, participating in WIMSE activities, and serving as a CPR/First Aid/AED instructor and committee

member for the American Red Cross. He was recognized for these efforts with one of the first UIUC Campus Awards for Excellence in Public Service in September 2000. Tim has accepted a position as Assistant Professor of Mechanical Engineering at the University of Wisconsin, Madison beginning in March of 2001.